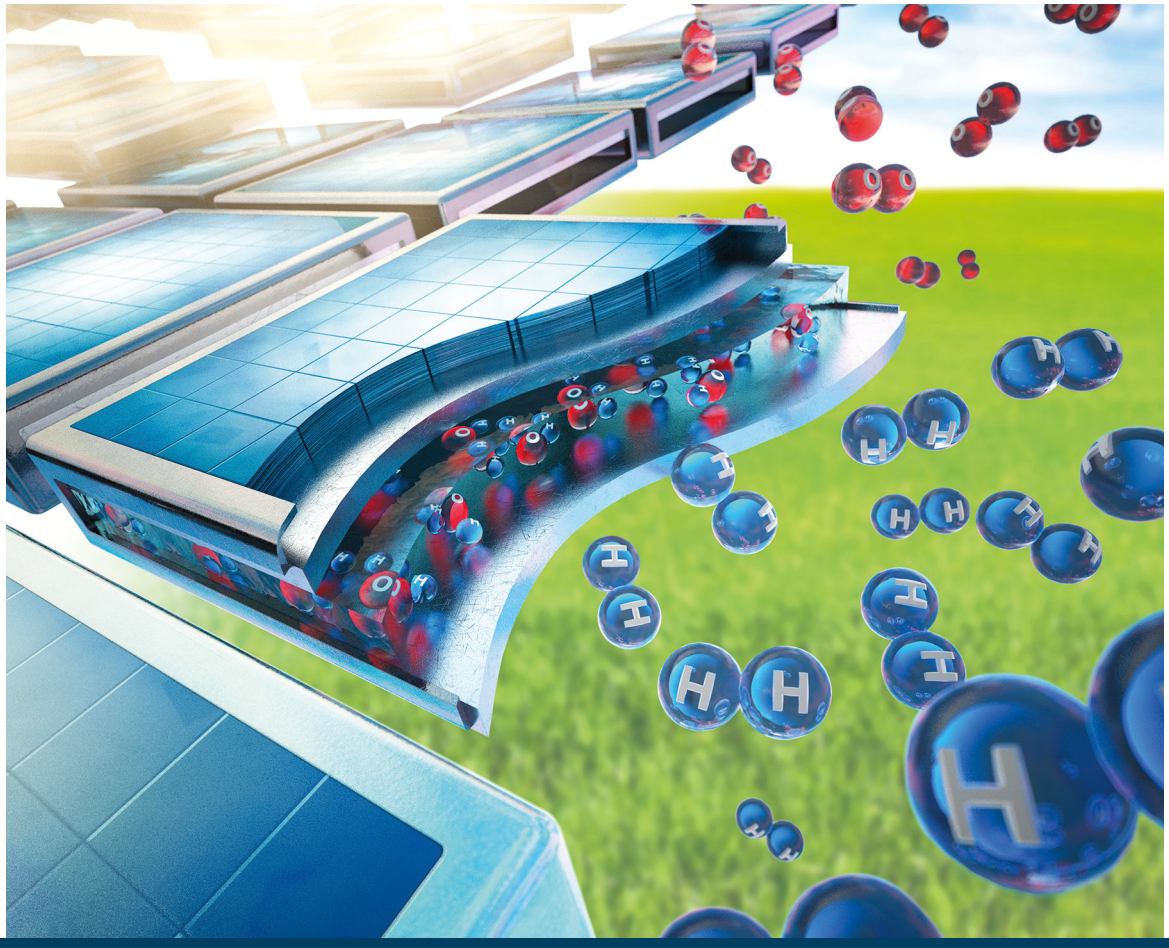

Solar driven water electrolysis based on silicon solar cells and earth-abundant catalysts

Katharina Welter

Energie & Umwelt / Energy & Environment
Band / Volume 508
ISBN 978-3-95806-495-9

Mitglied der Helmholtz-Gemeinschaft

JÜLICH
Forschungszentrum

Schriften des Forschungszentrums Jülich
Reihe Energie & Umwelt / Energy & Environment Band / Volume 508

Forschungszentrum Jülich GmbH
Institut für Energie- und Klimaforschung
IEK-5 Photovoltaik

Solar driven water electrolysis based on silicon solar cells and earth-abundant catalysts

Katharina Welter

Schriften des Forschungszentrums Jülich
Reihe Energie & Umwelt / Energy & Environment Band / Volume 508

ISSN 1866-1793 ISBN 978-3-95806-495-9

Bibliografische Information der Deutschen Nationalbibliothek.
Die Deutsche Nationalbibliothek verzeichnet diese Publikation in der
Deutschen Nationalbibliografie; detaillierte Bibliografische Daten
sind im Internet über http://dnb.d-nb.de abrufbar.

Herausgeber und Vertrieb:	Forschungszentrum Jülich GmbH Zentralbibliothek, Verlag 52425 Jülich Tel.: +49 2461 61-5368 Fax: +49 2461 61-6103 zb-publikation@fz-juelich.de www.fz-juelich.de/zb
Umschlaggestaltung:	Grafische Medien, Forschungszentrum Jülich GmbH
Titelbild:	© aligator kommunikation GmbH
Druck:	Grafische Medien, Forschungszentrum Jülich GmbH
Copyright:	Forschungszentrum Jülich 2020

Schriften des Forschungszentrums Jülich
Reihe Energie & Umwelt / Energy & Environment, Band / Volume 508

D 17 (Diss. TU Darmstadt, 2020)

ISSN 1866-1793
ISBN 978-3-95806-495-9

Vollständig frei verfügbar über das Publikationsportal des Forschungszentrums Jülich (JuSER)
unter www.fz-juelich.de/zb/openaccess.

Solar driven water electrolysis based on silicon solar cells and earth-abundant catalysts

Solarbetriebene Wasserelektrolyse auf der Basis von Silizium-Solarzellen und erdreichen Katalysatormaterialien

Genehmigte Dissertation von Dipl.-Chem. Katharina Welter aus Georgsmarienhütte

1. Gutachten: Prof. Dr. Wolfram Jaegermann
2. Gutachten: Prof. Dr. Uwe Rau

Tag der Einreichung: 09.10.2019
Tag der Prüfung: 23.01.2020

Darmstadt 2020

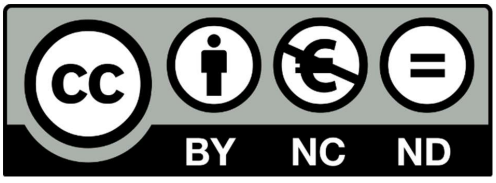

Content

Erklärung zur Dissertation

Hiermit versichere ich, die vorliegende Dissertation ohne Hilfe Dritter nur mit den angegebenen Quellen und Hilfsmitteln angefertigt zu haben. Alle Stellen, die aus Quellen entnommen wurden, sind als solche kenntlich gemacht. Diese Arbeit hat in gleicher oder ähnlicher Form noch keiner Prüfungsbehörde vorgelegen.

Darmstadt, den

(Katharina Welter)

Abstract

In the present work “proof of concept” upscaling steps were taken for a PV-EC device of 100 cm² substrate size. The active thin film silicon solar cell area was increased to 64 cm², while earth-abundant nickel based catalysts were scaled up by a factor of 100 to electrode areas of 50.3 cm². Implementing the thin film silicon solar cell into the PV-EC device in combination with the earth-abundant catalysts yielded a solar-to-hydrogen efficiency of 5.1 %, which is significantly improved compared to a PV-EC device based on nickel electrodes. It is shown that noble metal catalysts can be replaced by earth-abundant materials without performance losses. The long-term stable operation of the scaled up PV-EC devices is ensured by the use of metal sheet electrodes serving as substrate for the catalyst deposition. Regarding the catalyst stability, an excellent performance over 4 days under day-night-cycling was found for the earth-abundant nickel based system. Furthermore, the characterization of integrated PV-EC devices was expanded to illumination conditions similar to those obtained outdoors. All components used in water splitting devices are usually optimized under standard test conditions in the laboratory, which only represent one set of a wide range of possible outdoor operating conditions. For a combined PV-EC system the generation of hydrogen will only occur for output voltages above a certain value (thermodynamic potential + overpotential losses). This means, any illumination conditions shifting the illuminated current-voltage curve of the coupled system such that the voltage at the operating point is too low, will switch the system off. The influence of the operating temperature has been investigated prior to the present work, but studies concerning other possible illumination conditions were missing and therefore investigated in the present work. Additionally, a first estimation of the annual hydrogen output is given to compare devices based on different multi-junction cells and employing different catalyst systems for spectral data reported in literature.

Zusammenfassung

In der vorliegenden Arbeit wurden Aufskalierungsschritte als "Proof of Concept" für ein PV-EC Bauteil der Substratgröße von 100 cm² durchgeführt. Die Fläche der aktiven Dünnschichtsilizium-Solarzellen wurde auf 64 cm² erhöht, während nickel-basierte Katalysatoren um den Faktor 100 vergrößert wurden (Elektrodenflächen = 50,3 cm²). Die Implementierung der Dünnschichtsilizium-Solarzelle in das PV-EC Bauteil kombiniert mit nickel- basierten Katalysatoren ergab einen Gesamtwirkungsgrad von Solar zu Wasserstoff von 5,1 %, welcher im Vergleich zu einem auf Nickelelektroden basierenden PV-EC Bauteil deutlich verbessert ist. In der vorliegenden Arbeit wird gezeigt, dass Edelmetallkatalysatoren ohne Leistungsverluste durch erdreichere Materialien ersetzt werden können. Der langzeitstabile Betrieb der aufskalierten PV-EC Elemente wird durch die Verwendung von Metallblechen als Elektroden gewährleistet, die zudem als Substrat für die Katalysatorabscheidung dienen. In Bezug auf die Katalysatorstabilität, welche in einem Tag-Nacht-Zyklus evaluiert wurde, wurde eine hervorragende Leistung über vier Tage für das nickelbasierte Katalysatorsystem gefunden. Darüber hinaus wurde die Charakterisierung integrierter PV-EC Bauteile auf Beleuchtungsbedingungen erweitert, welche ähnlich sind zu den Bedingungen, die im Freien erwartet werden. Alle Komponenten, die in Wasserspaltungsbauteilen verwendet werden, werden normalerweise unter Standardtestbedingungen im Labor optimiert. Diese stellen allerdings nur einen Satz einer Vielzahl möglicher Betriebsbedingungen im Freien dar. Für kombinierte PV-EC Systeme tritt die Wasserstofferzeugung nur für Ausgangsspannungen oberhalb eines bestimmten Werts (thermodynamisches Potential + Überspannungsverluste) auf. Das bedeutet, dass alle Beleuchtungsbedingungen das PV-EC System ausschalten, die die Strom-Spannungs-Kurve des gekoppelten Systems unter Beleuchtung so verschieben, dass die Spannung am Arbeitspunkt zu niedrig ist. Der Einfluss der Betriebstemperatur wurde in einer vorherigen Arbeit untersucht. Studien zu weiteren möglichen Beleuchtungsbedingungen wurden in der vorliegenden Arbeit ergänzt. Zusätzlich wird eine Schätzung der jährlichen Wasserstoffausbeute für in der Literatur

beschriebene Spektraldaten angegeben, aufgrund welcher Bauelemente basierend auf verschiedenen Mehrfachzellen und unterschiedlichen Katalysatorsystemen verglichen werden.

2 Introduction

In times of man-made climate change and a yet still increasing global energy demand (+2.8 % in 2017[1]), renewable fuels and energy sources become more and more prominent to the global community. However, nowadays 80% of the global energy production is based on carbon-based fossil fuels such as oil, coal and natural gas.[1]

In general, fossil fuels describe fuels containing energy originated in ancient photosynthesis that are made by natural processes such as the anaerobic decomposition of organisms[2], which died and had been buried millions of years ago[3]. These carbon based fossil fuels have been preserved in the earth crust for millions of years, but since the industrial revolution, fossil fuels are widely used to generate electricity[1,4]. In fossil fuel power plants, the fuels are burned in order to operate turbines, which then generate electricity[5]. However, the resources of fossil fuels are limited and will soon be exhausted. Estimations which are made, considering a constant production rate of fossil fuels and known reservoirs showing a reasonable certainty of being recovered in the future (not necessarily proven reserves at company level), show that natural gas will be fully consumed in 53 years, oil in 50 years and coal in 134 years (2017[1]). By combusting fossil fuels, one of the side products emitted is carbon dioxide[6,7]. The intensive use of fossil fuels since the industrial revolution has led to a severe increase of the atmospheric carbon dioxide level (from ~280 ppm in 1750 to ~405 ppm in 2017) [8–10], which is considered to be responsible to the man-made climate change and the subsequent temperature rise.[11–13]

Hence, alternative, carbon dioxide neutral and renewable fuels are needed to fully replace fossil fuels. One possible option to be used as renewable fuel is hydrogen, which has the highest mass energy density among all chemical fuels[14], is storable[15] and can be used in fuel cells to generate electricity[14–16]. One additional positive aspect of using hydrogen as fuel in fuel cells, is that water and energy are the only products of the water formation reaction and no other side products, such as e.g. carbon dioxide, are emitted[17]. Currently, fossil fuels are the main source for industrial hydrogen production based on mostly steam reforming, accounting for 96 % of the four main sources (natural gas 48 %, oil 30 %, and coal 18 %)[18]. The remaining 4 % are covered by hydrogen produced from electrolysis[18]. During the electrolysis, a current-voltage source is used to drive the splitting of water into hydrogen and oxygen. To drive the reaction, a thermodynamic potential difference of 1.23 V has to be overcome. Compared to the fossil fuel based hydrogen production, water is used as hydrogen source and no other products than hydrogen and oxygen are emitted in the electrolysis:[19]

$$2\,H_2O \xrightarrow[1.23\,V]{} 2\,H_2 + O_2 \qquad (1)$$

Generally, if water electrolysis should become competitive to the steam reforming method, the technique has to be highly-efficient, low-cost and carbon dioxide neutral.[14] To perform the water splitting reaction, an electrolyser can be used with the current supplied from the plug socket, referred to in the following as “power + EC”. In this case, the origin of the power taken from the plug socket could be based on any kind of technology, such as combustion of fossil fuels, renewable energies or nuclear energy.[14] Two main electrolyser technologies are prominent on the current market, the alkaline and the proton exchange membrane (PEM) electrolyser. Alkaline electrolysers are cheaper in terms of materials used (usually nickel catalysts) and show an efficiency of about 70%[20]. PEM electrolysers are more expensive due to the use of platinum-group metal catalysts, but can operate at higher current densities and the efficiency can reach to around 80%[20]. In order to generate carbon neutral, renewable hydrogen, fossil fuels have to be eliminated from this cycle and the energy to split water should use only from non-carbon based sources, such as wind energy, hydropower or photovoltaic systems.[14]

The splitting of water into oxygen and hydrogen requires 237 kJ/mol, which equals 1.23 eV per electron transferred during the reaction. This amount of energy can be provided by photons from the solar spectrum with wavelengths λ below 1008 nm as can be extracted from the following equation:

$$\lambda = \frac{hc}{E} = \frac{6.626 \cdot 10^{-34} Js \cdot 299792458 \frac{m}{s}}{1.23\ eV} = 1008\ \text{nm} \quad (2)$$

with the speed of light c, the Planck constant h and the energy E, which equals 1.23 eV in this case. By using photovoltaic cells for the water splitting reaction, the electrical power generated is used to form the hydrogen bonds created during the reaction. In order to drive the water splitting reaction, the photovoltaic cells have to generate voltages exceeding the thermodynamic potential (1.23 V) plus overpotentials occurring at the electrodes during the electrochemical reaction. The overpotential is a kinetic phenomenon describing the difference between thermodynamically calculated potential and the measured potential to drive the reaction. If a single photoabsorber were to be used for the entire water splitting reaction, the band gap of the semiconductor has to exceed 1.23 eV.[21] In this case, overpotential losses obtained for both half-cell reactions, recombination effects and band bending effects of the semiconductor due to the emersion in the electrolyte are not yet considered.[22] Including the loss factors, the band gap of the semiconductor used for unbiased water splitting increases to >2 eV.[23] Additionally, if the unbiased water splitting process should be driven by solar light, the band gap has to be lower than 3 eV in order to be suitable for solar light absorption. Thus, leaving a small range of 1 eV (between 2 – 3 eV) for materials with suitable band gaps for the overall solar driven water splitting reaction with one photoabsorber. One possibility to overcome the small range of suitable band gap energies for semiconductor materials is the formation of multi-junctions consisting of materials with different band gaps. Regarding the multi-junction feasibility of different solar cell technologies, thin film silicon can be highlighted as one technology, which allows to deposit a number of sub cells of hydrogenated amorphous and microcrystalline silicon with different band gap energies in a multi-junction configuration. So far photovoltaic cells with output voltages in the range of 1.5 – 2.8 V have already been produced.[24] Employing photovoltaic cells in a water splitting device offers the side effect of storing solar energy in the form of chemical energy, making the energy available if sunlight is not provided (day-night-cycle). The concept of light induced water splitting has first been shown by Honda and Fujishima in 1972 employing TiO_2 as photoabsorbing material.[25] Since then the technology of solar driven water electrolysis has been of substantial interest and several technologies and materials are available on different levels of the technological readiness level.[26]

The easiest way to split water by using photovoltaic cells is the combination of commercially available and widely used crystalline silicon photovoltaics wired to commercially available electrolysers, referred to as "PV+EC" in the following.[26,27] The combination of both technologies is currently also considered as the most advanced system on the technological readiness level scale way. In this case, the system efficiency is determined by the individual efficiencies of the photovoltaic cell η_{PV}, of the electrolyser η_{EC} and of additional transformers η_{trans} (if used) in the setup and calculated as follows:

$$\eta_{PV+EC} = \eta_{PV} \cdot \eta_{EC} \cdot \eta_{trans} \quad (3)$$

Considering for example the case of a commercially available, crystalline silicon solar cell with an efficiency of η_{PV} = 20 % combined with a PEM electrolyser with η_{EC} = 80 % via a transformer with an efficiency of η_{trans} = 99 %[28], the system efficiency η_{PV+EC} would add up to 15.8 %. For the use of an alkaline electrolyser, the system efficiency η_{PV+EC} is reduced to 13.8 %. For the use of highly efficient crystalline silicon heterojunction solar cells the overall efficiency exceeds the above calculated values.

The application of the "PV+EC" concept was described in literature. It was calculated that using three crystalline silicon solar cells as single band gap photoabsorber operating at 100 % quantum efficiency under 1 sun illumination, with several loss channels included, lead to a solar-to-hydrogen efficiency of 18.1 %.[29,30] The combination of three crystalline silicon heterojunction cells connected in series (η_{PV} = 25.6 %) with an alkaline electrolyser yields a solar-to-hydrogen efficiency of 14.2 %.[27] For a silicon triple heterojunction solar cell with interdigitated back contacts (series connection) combined with an electrolyser consisting of platinum and ruthenium oxide in acidic media, a solar-to-hydrogen efficiency of 14.5 % was reported.[29] As mentioned

before, the combination of the two existing technologies is currently most advanced on the technology readiness level, however it might not be the cheapest method for solar hydrogen production as suggested in literature.[26]

One possible step towards a lower cost solution for solar driven hydrogen production could be the integration of the solar cell into the device in order to save place, additional wiring and transformers. This approach of integrated solar water splitting devices is referred to as "PV-EC" in the following. To reach a sufficient solar cell output voltage and to reduce ohmic losses occurring in a series connection of several solar cells, a suitable approach is the integrated series connection of multiple junctions within one solar cell. Therefore, absorber materials with different band gap energies are stacked vertically to make efficient use of the incident solar irradiation. Solar-to-hydrogen efficiencies were reported in literature for an AlGaAs/c-Si tandem junction yielding 18.3 %[31] and for a tandem junction made of GaInP/GaInAs showing a solar-to-hydrogen efficiency of 19.3 %[32]. Another possible approach yielding high solar-to-hydrogen efficiencies is based on the use of an InGaP/GaAs/GaInNAsSb triple junction solar cell connected in series to two electrolysers under 42 fold illumination, yielding 30 % of solar-to-hydrogen efficiency.[33] However, the solar cells consist of toxic and rare materials and rely on a cost-intensive fabrication.

Earth-abundant, low cost multi-junction solar cells can be obtained using amorphous and microcrystalline thin film silicon as absorber materials. The development of thin film silicon multi-junction solar cells and their application in integrated water splitting devices have been shown in the PhD thesis of F. Urbain conducted at Forschungszentrum Jülich GmbH.[34] By combining hydrogenated amorphous silicon layers with hydrogenated microcrystalline silicon layers in an a-Si:H/a-Si:H/µc-Si:H triple junction solar cell and employing this cell with platinum and ruthenium oxide in alkaline media, a solar-to-hydrogen efficiency of 9.5 % was obtained, which is very close to the possible maximum performance value employing thin film silicon solar cells combined with an alkaline electrolyser (η_{PV} = 14 %, η_{EC} = 70 %, η_{trans} = 99 % → $\eta_{PV\text{-}EC,max}$ = 9.7 %).[24,35] In the scope of the previous work on thin film silicon multi-junction based water splitting devices, different questions and challenges arose[34], which were the starting point and basis for the present work and the resulting PhD thesis.

The first chapter following the introduction provides the fundamentals based on which the results of the present thesis are evaluated (**chapter (2)**). In **chapter (3)**, the experimental techniques and methods are introduced that were used to produce and evaluate solar cells and catalyst materials, respectively.

One question arising following the previous PhD thesis was, whether a triple junction configuration of an a-Si:H/µc-Si:H/µc-Si:H layer stack could be developed that generates a photocurrent, which exceeds the photocurrent yielded by the a-Si:H/a-Si:H/µc-Si:H triple junction solar cell as theoretically predicted[34]. In order to increase the sum of the sub cell current densities and the short circuit current density of the cell stack, the thickness of the cells were varied. In **chapter (4)**, the results aiming to maximize the current densities depending on the sub cell thickness are given and discussed. Additionally, a theoretical prediction of the performance of an a-Si:H/µc-Si:H/µc-Si:H based water splitting device is given.

Another critical duty which has to be realized was the setup of an electrochemical workplace allowing different measurements and the quantification of the evolved gas as well as the further development and improvement of the used photoelectrochemical device. One major focus of the device development was the modularity, so that each part can be easily exchanged and measured individually. A detailed overview of the setup of the electrochemical workplace and the developed device for the measurement of standard sized samples (up to 1.5 x 1.5 cm²) will be given in **chapter (5)**.

As mentioned before, the currently highest solar-to-hydrogen efficiency for thin film silicon multi-junction based water splitting devices was obtained using platinum and ruthenium oxide as catalysts. In order to provide a fully earth-abundant, low cost device, different catalyst systems have to be implemented into the device and used for alkaline water splitting. Different nickel based catalysts were synthesized according to literature[36–40] and compared regarding their water splitting potential (**chapter (6)**). For the synthesis, different methods, such as hydrothermal deposition and electrodeposition, as well as different substrates were used. The catalysts are

compared regarding their potential of upscaling their area leading to the next task, which was named in the previous work, the upscaling of the light induced water splitting devices.

The previously investigated active device area was of 0.5 cm² size[34], which equals the standard laboratory size used in the present work. However, if a solar driven water splitting device were to be used as stand-alone device for the efficient generation of hydrogen from sunlight as intended, the area of the device has to be scaled up significantly and a number of scientific and technological challenges have to be met. These are the scale-up of active solar cell area, an increase in efficiency, the stability under long-term operation, costs, which are to a large extent related to the choice of materials for catalysts, and ease of preparation for the individual components and the entire systems. In **chapter (6)**, the challenges of this stepwise upscaling process of the integrated device and its components are discussed in detail with respect to the previously named demands. Ideally, the active solar cell, catalyst and device areas should account for m² in the technically applied device, however in a "proof of concept" upscaling step, the active photovoltaic cell area was increased from 0.5 cm² to 64 cm² using thin film silicon based solar cells, while the earth-abundant catalyst areas were increased by a factor of 100, from 0.5 cm² to 50.3 cm². In order to prove the modularity of the upscaled PV-EC device, a solar module based on shingled crystalline heterojunction solar cells was implemented for comparison.

The last point addressed in the present work (**chapter (7)**) is the characterization of integrated PV-EC devices under illumination conditions similar to those obtained outdoors. All components used in water splitting devices are optimized under standard test conditions in the laboratory[41], which only represent one set of a wide range of possible outdoor operating conditions. For example, due to clouds the illumination intensity can be below 1 sun, the incident illumination angle changes during the season and the day and on sunny days system temperatures of 60°C or more can occur.[42,43] Furthermore, the spectral quality of the incident illumination spectrum can change during the season[44,45] and the day[46] and can differ for geographical locations.[44,45] Variations in both shape and intensity of the incident illumination spectrum lead, not surprisingly, to an influence of the electrical parameters of thin film silicon solar cells.[42,43,47–49] Photovoltaic cells and modules have been already investigated under simulated and real outdoor conditions in great detail[50–53]. For the combined PV-EC systems, the influence of the operating temperature has been investigated before[54], but studies concerning other possible illumination conditions were missing and are investigated in the present work[55,56]. In this context it is important to note that it is not sufficient to extrapolate the outdoor results on PV systems directly to combined PV-EC systems because in a PV system, power can be drawn out at all points of the illuminated current-voltage curve of the device as long as the product $|J| \cdot V \cdot FF$ is > 0 independent of the illumination conditions. For a combined PV-EC system instead the generation of hydrogen will only occur for output voltages above a certain value (thermodynamic potential + overpotential losses). This means, any illumination conditions shifting the illuminated JV curve of the coupled system such that the voltage at the operating point is too low, will switch the system off. Additionally, the electrochemical part of the device will be influenced by outdoor conditions with considerable variation in temperature as well as day-night-cycling. The additional effects on the EC part of the combined PV-EC system can be detrimental or beneficial to the total device performance. It is therefore required to study these effects on the combined system as well[54,56]. Finally, an estimation of the annual hydrogen output based on the results presented in **chapter (7)** is given to compare devices based on different multi-junction cells and employing different catalyst systems.

3 Fundamentals of photoelectrochemical solar energy conversion

This section begins with a short introduction into different semiconductor junctions and the principle of solar energy conversion into electrical energy, followed by the principals and kinetics of electrochemical reactions. Furthermore, the basics on solar water splitting and buried junction devices will be introduced. Finally, an overview of different illumination conditions and their known influences on the photovoltaic cell will be given.

3.1 Principles of photovoltaics

3.1.1 Light absorption in semiconductor junctions

Semiconductor describes a material whose electrical conductivity and light absorption are between conductors and insulators.[57] Regarding the band energy structure, the gap between valence and conduction band is sufficiently small such that electrons can pass from the valence into the conduction band at normal temperatures.[58,59] The Fermi level, which lies approximately in the middle of the band gap for intrinsic (undoped) semiconductors, can also be translated to a thermodynamic work that is required to add one electron to the semiconductor.[59–61] If the equilibrium in the semiconductor is disturbed, e.g. by light excitation, the electron and hole levels are increased above their equilibrium level. Thus, the initial Fermi levels defined in equilibrium cannot be used to determine the electron and hole concentration and it becomes inevitable to define quasi-Fermi levels for both types of charge carriers upon light excitation (E_{Fn} and E_{Fp}).

If a photon hits the surface of a semiconductor, one of three different processes can proceed. Either the photon passes through the semiconductor without interaction, the photon is reflected off the surface, or the photon is absorbed in the semiconductor. If the photon energy is lower than the band gap energy, the photon either passes through the semiconductor or is reflected at the surface. The absorption of the photon takes place if the energy provided by the photon is higher than or equal to the band gap energy E_{gap} of the semiconductor:

$$E_{gap} = \frac{hc}{\lambda} \tag{4}$$

with h the Planck constant and c the speed of light and λ the wavelength of the electromagnetic wave. An electron-hole pair is generated upon the absorption of the photon, since an electron is excited into the conduction band, where it is free to move around, leaving behind a hole in the valence band.[58,61]

For photon energies which equal the band gap energy, transition path 1 in Figure 2.1 takes place in case of the photon absorption. For photon energies exceeding the band gap energy, transition path 2 takes place and the electron is excited into a higher energy level of the conduction band. Within approximately 10^{-12} to 10^{-13} s the excited electron is thermalized from the higher energy states to the lower edge of the conduction band[62]. In the case of direct semiconductors, such as gallium arsenide, the electron can directly emit a photon due to the identical crystal momentum of electrons and holes in the conduction and valence band edges leading to direct band-to-band transitions. In the case of an indirect semiconductor, such as silicon, the direct emission of a photon by the electron is not possible due to different crystal momentums. The electron in the conduction band must pass through an intermediate state and transfer momentum into the crystal lattice. Band-to-band transitions can only occur if a phonon is emitted simultaneously. For the transition paths 3 to 5, the photon energies are lower than the band gap energy. The transition paths 3 and 5 are possible if impurities are incorporated in the semiconductor lattice (e.g. doping) or if the corresponding energy of intrinsic defects (e.g. dangling bonds) lies within the band gap. For instance, the excitation of an electron from the valence band into the impurity donor level E_D within the band gap becomes possible and can then be followed by the excitation into the conduction band (transition path 3 and 5). In highly doped semiconductors also transition path 4 can occur.[62] Here, electrons in the conduction band are further excited into higher energy states by the absorption of low energy photons (intraband transition). The relaxation of the excited electron into the ground energy state of the conduction band takes place under emission of phonons.

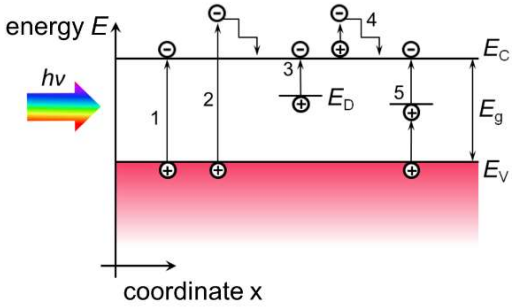

Figure 2.1: Different transition paths for electrons excited upon light illumination. The electron is excited from the valence band into the conduction band and has therefore absorbed a photon with energy equal to or above the band gap (E_g, transition paths 1 and 2). If the photon energy is below the band gap energy, the transition paths 3, 4 and 5 can take place. For further details see the text. Illustration taken from reference[34].

For the recombination of the excited electron in the conduction band and the hole in the valence band, different processes exist. The electron can recombine under emission of a photon (+ phonon for indirect semiconductors) (radiative recombination) or without radiation by recombining through trap states within the band gap (Shockley-Read-Hall recombination)[63,64]. Alternatively, the excess energy of the excited electron can be transferred to another free electron in the conduction band (Auger recombination)[65]. The lifetime of electrons in the conduction band in, for example, crystalline silicon may reach values of 10^{-3} seconds before recombination, which allows the conversion of electron energy into electric energy.[61]

If two differently doped semiconductors are brought into close contact, the electrons diffuse from regions with high electron concentration (n-type doped semiconductor) into regions with low electron concentration (p-type doped semiconductor). The electrons which diffuse across the p-n junction can recombine with holes on the p-type side and holes can recombine with electrons on the n-type side. The diffusion current is proportional to the concentration gradient between the two semiconductors. This process is limited by the build-up of charges and the creation of an electric field within the p-n junction if an external circuit is absent. The created electric field promotes the drift current, which is a charge flow opposing the diffusion current. Drift current and diffusion current balance out the diffusion of electrons and holes, reaching thermal equilibrium, which is also indicated by a constant Fermi level. The region where the charge carrier diffused through the junction into the oppositely doped side is called depletion region. In the depletion region, the ionized donor and acceptor atoms are left behind as immobile impurities and no mobile charge carriers are available. [61,66]

If two layers of similar semiconductor material with equal band gaps but different doping are brought into contact, a p-n homojunction is formed. In most cases, the p-n homojunction is called p-n junction. Heterojunctions in contrary describe junctions of materials with different band gap energies (e.g. crystalline and amorphous silicon)[67]. The different band gap energies cause a discontinuity in the edges of the valence and conduction bands at the junction (see also Figure 2.2). This discontinuity contrarily affects the effective field for the two charge carriers in the junction. For example, the field driving electrons to the n-side can be increased, whereas the field driving holes to the p-side is decreased. In p-i-n junctions, the doped n- and p-layer are separated by an intrinsic, undoped layer. By introducing the intrinsic layer, the electric field and the depletion region are extended over a wider region. The solar cells used in this work are either thin film silicon solar cells with a p-i-n junction or crystalline silicon heterojunction solar cells.

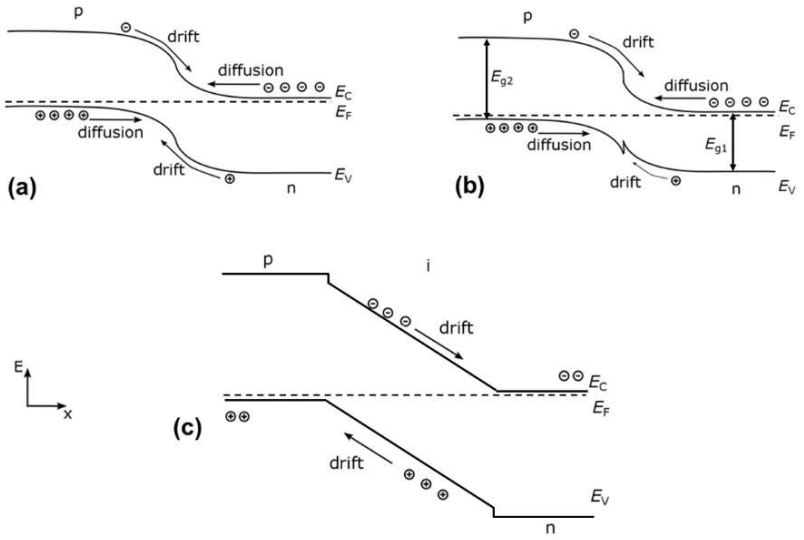

Figure 2.2: Energy band diagrams at equilibrium conditions for a) a p-n junction, b) a p-n heterojunction and c) a p-i-n junction, taken from reference[34].

3.1.2 Thin film silicon solar cells

The solar cells employed in this work are mainly thin film silicon multi-junction solar cells with p-i-n junctions. Therefore, hydrogenated amorphous silicon layers were combined with hydrogenated microcrystalline silicon layers to form the multi-junction cell structure. In the following, a short overview of the two different material properties as well as the working principle of p-i-n junction solar cells and multi-junction solar cells will be given.

a-Si:H and µc-Si:H layers – Structure

In contrast to crystalline silicon, atoms in amorphous silicon do not show a long range ordered crystal structure. Most atoms in amorphous silicon are tetrahedrally bonded and fourfold coordinated as in crystalline silicon, but the bonding lengths and angles are distorted resulting in highly strained bonds. In some cases, the highly strained bonds break leading to the so called dangling bonds within the network (threefold-coordination). This defect occurring in amorphous silicon is not known for the crystalline analogue.

The electronic structure of amorphous silicon can be described using the density of states function $N(E)$. As shown in Figure 2.3, three different states can be indicated: (1) extended band-like states, which result from overlapping electronic wave functions of non- or only slighty distorted bonds and which are similar to the conduction and valence band in crystalline silicon. (2) Localized band-like states forming the band tails, which are due to more strongly distorted and therefore weak bonds. Here, no overlap of the wave functions is observed. At normal temperatures, charge carriers located in the band tails are excited to the conduction band and recaptured, which results in a reduced mobility. Hence, mobility edges are formed at the transition from the band tails to the localized states, as shown in Figure 2.3. The mobility gap serves as an equivalent to the band gap in crystalline silicon. Since the mobility edges are not sharp due to the band-tails, the value determined for the mobility gap depends on the definition and evaluation.[68] The mobility gap, whose energy depends on the deposition conditions, corresponds to the optical band gap of the material.[68,69] Also a distinct definition for the optical gap does not exist. Different approaches for the definition of the optical gap are reported, for example, the photon energy at which the absorption coefficient equals 10^4 cm^{-1} defined as E_{04}.[68,69] Although, mobility gap is the correct terminology for amorphous silicon, it will be named in a more common

way as band gap in the present work. (3) Localized defect states distributed in the mobility gap resulting from highly distorted or unsaturated dangling bonds, which can serve as recombination center for charge carriers and disturb the charge carrier transport. In order to enable amorphous silicon for the application in optoelectronic devices, the dangling bonds have to be saturated. Therefore, hydrogen is incorporated into the material, which partially saturates the dangling bonds, decreasing the defect density from 10^{19} cm^{-3} in amorphous silicon to 10^{15} – 10^{16} cm^{-3} in hydrogenated amorphous silicon.

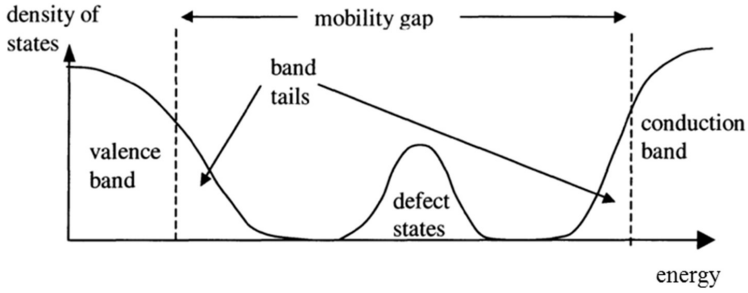

Figure 2.3: A schematic of the density of states in a-Si with: (1) extended band-like states, which form the conduction and valence band, (2) localized band-like states forming the band tails, (3) localized defect states distributed in the energy gap resulting from unsaturated dangling bonds, taken from reference [68].

Hydrogenated microcrystalline silicon describes a mixture of amorphous and microcrystalline phases in various volume fractions. A schematic model of hydrogenated microcrystalline silicon shows the microstructure of the material deposited using plasma-enhanced chemical vapor deposition (see Figure 2.4). The volume fraction of the microcrystalline structure and the properties of the film strongly depend on various deposition parameters as investigated in the references.[34,70,71] This is indicated by the decreasing crystalline volume fraction from left to right in Figure 2.4. The grains between the columns depicted in Figure 2.4 are ideally passivated by surrounding amorphous material, reducing the number of electrically active defects and preventing atmospheric in-diffusion after the deposition process.

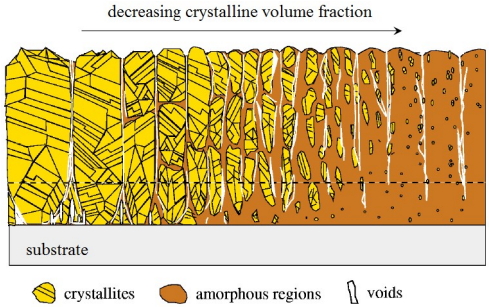

Figure 2.4: Schematic model of microcrystalline material deposited on glass substrate using plasma-enhanced chemical vapor deposition. The crystalline volume fraction decreases from the left side to the right side.[71]

Optical absorption

Figure 2.5 shows the absorption coefficient α_{abs} depending on the incident photon energy E_{ph} for a-Si:H[72], µc-Si:H[73] and c-Si[74]. For c-Si and µc-Si:H material, the absorption coefficients show an overlap in the range of 1.2 eV – 1.55 eV. The optical band gap of crystalline silicon is 1.1 eV.[75,76] For photon energies exceeding 1.85 eV, a-Si:H material shows in this case the highest absorption coefficient. Thus for thin layers, a-Si:H can mainly be used to absorb light in the short wavelength range, while µc-Si:H layers are preferably employed to

absorb light in the long wavelength range. Defects in the sub-gap region of amorphous and microcrystalline silicon cause the absorption for photon energies below 1.0 eV. These defects are not observed in nearly defect-free crystalline silicon, which hence shows no absorption below 1 eV. Due to the long-range disorder in the amorphous material, the momentum conservation law for a direct band-to-band transition of an electron from the valence into the conduction band are relaxed and no additional phonon has to be involved for the transition. Thus, amorphous silicon behaves more like a direct semiconductor.[77] By varying the deposition parameters such as the hydrogen dilution or the deposition temperature, the optical gap can be shifted over (a few) 100 mV[78,79]. Optical gaps above 2.0 eV can be achieved by incorporating carbon (SiC) or oxygen (SiO_X), whereas the incorporation of germanium leads to a reduction of the optical gap[80–82].

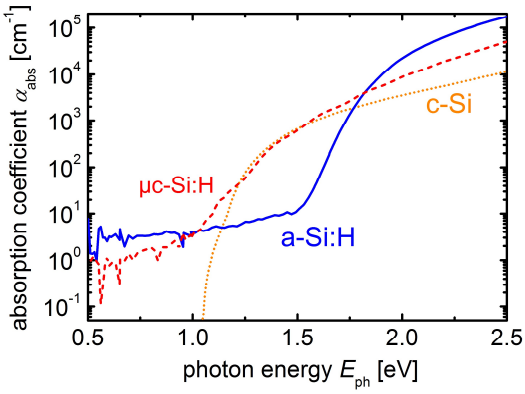

Figure 2.5: Absorption coefficient α_{abs} depending on the incident photon energy E_{ph} for a-Si:H (blue solid curve), µc-Si:H (red dashed curve) and c-Si (orange dotted curve), taken from reference[34].

General principles of thin film silicon solar cells

Figure 2.6 shows the layer structure of a p-i-n single junction solar cell. The light enters the solar cell through a glass substrate coated with a transparent conductive oxide (TCO), which serves as front contact of the solar cell. Depending on the deposition sequence of the layers, thin film solar cells are classified as p-i-n (p-layer is the first deposited layer) or n-i-p (n-layer is the first deposited layer) cells. Details on the deposition process of n-i-p thin film solar cells can be found in the literature[83,84]. Solar cells used in the present work were deposited in the p-i-n configuration. Additionally, superstrate configuration was used, hence the glass substrate is used as window for the illumination and as part of the solar cell encapsulation. In general, thin film silicon solar cells should be illuminated through the p-layer, especially if hydrogenated amorphous silicon is used, because the electron mobility is approximately 1 to 2 orders of magnitude higher than the hole mobility.[85] If the solar cell is illuminated through the p-layer, the majority charge carriers crossing the junction are electrons and the holes have to travel a shorter distance directly to the p-contact. In order to prolong the light path in the absorbing i-layer, the front contact TCO as well as the back contact electrode are structured. Thus, the incoming light is scattered randomly at the interfaces. The back contact consists of aluminum doped zinc oxide (ZnO:Al) and thermally evaporated silver (Ag)[84,86]. Further details on the preparation of thin film silicon solar cells can be found in chapter (4).

If light is absorbed in the i-layer, electron-hole pairs are generated. The photogenerated charge carriers are separated due to the electric field generated by the n- and p-layer of the solar cell. Electrons are driven to the n-side, whereas holes are driven to the p-side of the solar cell. The separation of charge carriers lead to a build-up of voltage between the two doped layers, which is called photovoltage and defined by the quasi-Fermi level splitting (E_{Fn} an E_{Fp}, see also section 3.1.1)[60,61]. In the case of open-circuit conditions, the photovoltage is

named open-circuit voltage V_{OC}. A photocurrent can be extracted from the p-i-n solar cell, if the n- and p-layers are connected by electrodes through an external circuit. In the case of short-circuit conditions, the generated photocurrent is called short-circuit current I_{SC}. Further details about the different photovoltaic parameters and their relation is given in chapter (3).

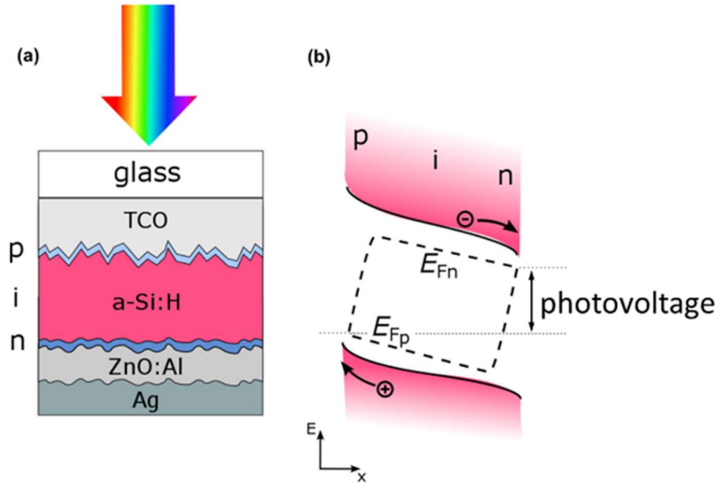

Figure 2.6: Structure (a) and band diagram (b) of a p-i-n a-Si:H single junction solar cell. The solar cell is deposited in the superstrate configuration, thus, the light enters through the glass substrate coated with a transparent conductive oxide. The rear contact consists of ZnO:Al/Ag, which also serves as back reflector. The band diagram is shown under illuminated conditions. The doped layers (*n* and *p*) generate an electric field, which leads to the separation of the charge carriers generated upon light absorption in the intrinsic layer. Electrons move to the n-side of the solar cell and holes accordingly to the p-side. The quasi-Fermi levels for electrons and holes are indicated, taken from reference[34].

Multi-junction thin film silicon solar cells

In the case of single band gap absorbers, such as crystalline silicon solar cells or a-Si:H p-i-n single junction solar cells, the absorption of photons leads to output voltages of approximately 700 mV or 900 mV, respectively, which is not sufficient to drive the water splitting reaction. Therefore, several cells have to be connected in series in order to exceed the required voltage. As described in the introduction, thin film silicon solar cells can be stacked vertically on one another in order to reach a sufficient solar cell output voltage and to reduce ohmic losses occurring in a series connection of several solar cells. As absorber materials with different band gap energies hydrogenated amorphous and microcrystalline silicon can be deposited on top of each other to generate various types of p-i-n thin film multi-junction cells (so far reported: tandem, triple and quadruple junctions)[24,78,87,88]. The sub cells are directly connected in series. Different band gap energies facilitate an efficient use of the solar spectrum, ideally photons of all energies can be absorbed within the multi-junction cell stack. In such a multi-junction cell stack, the sub cell with the highest band gap energy is placed as top cell on the glass TCO superstrate, in order to absorb the short wavelength light first, while the long wavelength light can pass through. The highest band gap energies are provided by a-Si:H sub cells (~1.9 eV) absorbing light mostly in the wavelength region of 400 – 600 nm. Light with longer wavelengths is absorbed in the middle and/or bottom sub cell, which are either made of hydrogenated amorphous silicon with a band gap of 1.8 eV or of hydrogenated microcrystalline silicon (optical band gap 1.1 eV). For a better overview, the solar spectrum at sea level is shown in Figure 2.7(a). Additionally, the external quantum efficiencies extracted for a quadruple junction solar cell are shown in Figure 2.7(b), indicating the main wavelength regions absorbed in the sub cells with different band gap energies. The solar spectrum shows a sharp spectral irradiance maximum in the visible wavelength range (300 – 700 nm). The external quantum efficiencies of the quadruple

junction solar cell (Figure 2.7(b)) indicate that the band gaps of the sub cells are matched to the intensity distribution occurring in the solar spectrum.

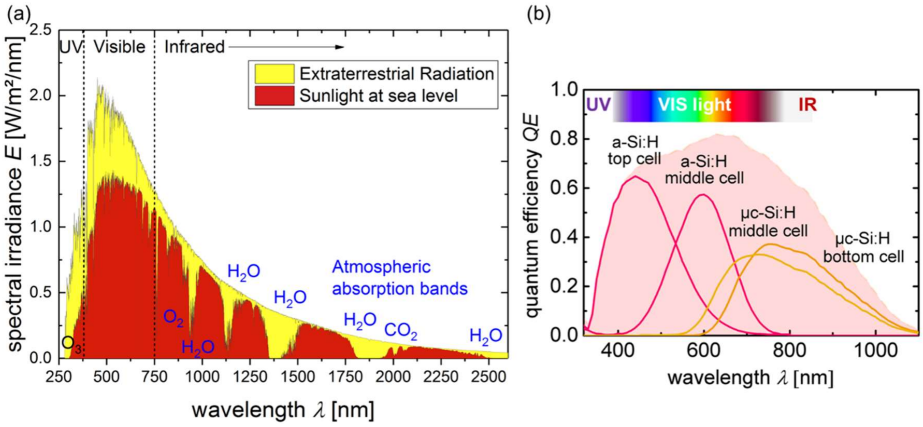

Figure 2.7: (a) Solar irradiance spectrum at different atmosphere levels. The radiation at sea level corresponds to the air-mass 1.5 G spectrum. The different absorption bands are indicated, taken from reference[89]. (b) Quantum efficiency curves of a quadruple junction solar cell. The different sub cells are indicated, as well as the sum of the quantum efficiencies and the visible light wavelength range. Adapted from reference[34].

The absorption process of the different wavelength light in the sub cells is schematically shown in Figure 2.8. The back contact also serves as back reflector to prolong the light path in the multi-junction cell stack. Studies show that an increase in the amount of sub cells can lead to higher theoretical limits of the electrical conversion efficiency.[90–92]

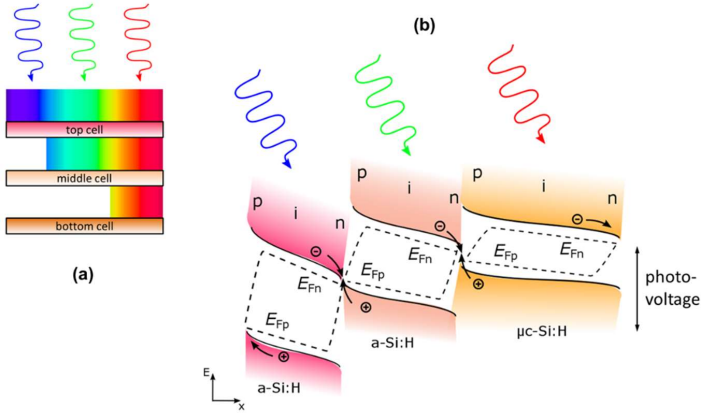

Figure 2.8: (a) Schematic illustration of the light absorption in a triple junction cell. (b) Band diagram of a triple junction cell consisting of a-Si:H/a-Si:H/µc-Si:H layers under illumination. Electrons and holes have to recombine at the sub cell interfaces in order to ensure a current transport along the junction (recombination junctions). The quasi-Fermi levels are indicated for each sub cell. The sum of the quasi-Fermi levels of the sub cells defines the photovoltage of the cell stack, taken from reference[34].

The electrical series connection between the sub cells is established by recombination junctions as shown in Figure 2.8(b). In the a-Si:H top cell, the holes travel to the p-contact, which is in this case the front contact (TCO), while the electrons move to the n-layer, which is directly in contact with the middle cell p-layer. The same movement of charge carriers accounts for the middle and bottom cell. In order to establish a current transport through the cell stack, the electrons and holes at the p/n interface have to recombine. High recombination rates at the p/n interfaces and sufficient density of states are assured by high doping

concentrations in the respective layers.[93,94] Based on the assumption that no voltage is lost in the recombination junction, the stack voltage is the sum of the individual sub cell photovoltages defined by the quasi-Fermi level splitting. In the series connection, the current density of the cell stack is limited by the lowest sub cell current density. Hence, the individual sub cell current densities have to be matched. In the ideal case, the total cell stack current density is equally distributed between the sub cells ("current matched"), ensuring a complete recombination along the recombination junctions and the highest photocurrent possible.[95,96]

3.2 Principles of electrochemistry

Electrochemistry is one branch of physical chemistry dealing with the interaction between electrical energy and chemical change. Reactions investigated in electrochemistry involve electric charges moving between electrodes and an electrolyte or ionic species in a solution, respectively. Electrochemical reactions either consume electrical current supplied externally (electrolysis) or produce electrical current during the reaction (galvanic cell). More specifically, chemical reactions during which electrons are transferred directly between molecules and/or atoms are called redox (reduction-oxidation) reactions. Thus, electrochemistry describes the overall reactions of individual redox reactions connected by an external electric circuit and an electrolyte ensuring the charge transport.

3.2.1 Charge transport in electrolytes and ohmic drop

The charge transport in liquid electrolytes is enabled by ions of positive and negative charge. These charged ions are formed when acids (e.g. H_2SO_4), bases (e.g. KOH) or metal salts (e.g. NaCl) are diluted or dissolved in water. Both ionic charges are present in the same concentration in the electrolyte solution. Strong electrolytes, such as KOH and H_2SO_4, are theoretically completely dissociated in solution. The conductivity σ of a strong electrolyte follows Kohlrausch's Law:

$$\sigma = Fcz_e(b_+ + b_-) \tag{5}$$

with the Faraday constant F, the concentration c [mol/cm³], the respective ion charge z_e and the ion mobilities b_+ and b_- [cm²/Vs]. Most ion mobilities are in the order of 10^{-4} cm²/Vs. Compared to the electron and hole mobility in crystalline semiconductors, the mobility of ions in an electrolyte is approximately 5-6 orders of magnitude smaller.[97–99] The electrolyte conductivity is of interest, since it is inversely proportional to the electrolyte resistance and thus, directly influences the performance of (photo)electrochemical measurements and devices.[100,101] The conductivity of pure water is not sufficient for the use as electrolyte. For current flowing in an electrochemical cell, the potential between the reference/counter electrode and the working electrode drops due to the electrolyte resistance according to Ohm's law ($U = iR$). The Ohmic potential drop is directly proportional to the distance of the electrodes, which is ideally as small as possible, the electrolyte conductivity and the magnitude of the current.[101] The electrolyte resistance can be determined by means of electrical impedance spectroscopy (EIS, see chapter (3)). Knowing the electrolyte resistance and the current flowing in the electrochemical cell, the measured potential can be corrected for the Ohmic drop (iR correction). This iR correction is for example used for the comparison of different electrode materials regarding their potential towards a specific electrochemical reaction.[102]

3.2.2 Standard potential of redox systems

During redox reactions, electrons are transferred directly between molecules and/or atoms such that the oxidation state is changed. The corresponding reaction between the redox couple is:

$$Ox + ze^- \rightarrow Red \tag{6}$$

with Ox as oxidized species (increased oxidation state, e.g. H^+) and Red as reduced species (decreased oxidation state, e.g. H_2). The amount of electrons e^- transferred is given by z.

The amount of energy needed to increase the number of one ion type from z_a to z_e in a system under constant temperature T, constant amount of all other materials within the system N and constant pressure p can be expressed in terms of the electrochemical potential $\bar{\mu}$, which is defined as the chemical potential of that ion in an electrical potential. It can be described using the Gibbs free energy G of the substance[103]:

$$\bar{\mu}_i = \left(\frac{\partial G}{\partial N_i}\right)_{p,T} = \mu_i + z_i F \varphi \tag{7}$$

with the chemical potential μ_i, the charge of the ion z_i, the Faraday constant F and the local electrical potential of the material φ. If no charged particles are present, the electrochemical potential $\bar{\mu}$ equals the chemical potential μ. All chemical and electrochemical potentials are given in joule per mol (J/mol).

The standard potential of a redox couple is the measured electrical potential between the standard hydrogen electrode (SHE) and the half-cell of the examined redox couple under standard test conditions (T = 25°C, activity a = 1 mol/L for all involved species, p = 101325 Pa). The potential of the redox couple H_2/H^+ is set to 0 V and used as reference to determine the standard potentials of all redox couples. The Nernst equation is used to relate the reduction potential of a redox reaction, as written in equation (9), to the standard electrode potential, temperature and activities of the chemical redox species in equilibrium conditions. The activities of the species are often approximated by the concentrations of the oxidized and reduced species. The Nernst equation can be derived from the standard changes in the Gibbs free energy related to an electrochemical transformation:

$$\Delta G = -zF\Delta E \text{ and } \Delta G = \Delta G^0 + RT \ln Q \tag{8}$$

with Q the reaction quotient defined as ratio of activities of the reduced and oxidized species, which can be approximated by the respective concentrations. By using the two expressions given in equation (8) the Nernst equation (9) follows[104]:

$$E_{redox} = E^0_{redox} - \frac{RT}{zF} \ln\left(\frac{c_{red}}{c_{ox}}\right) \tag{9}$$

Here, the concentrations c of the reduced and oxidized species are used, R is the universal gas constant, F the Faraday constant, T is the temperature and z the amount of electrons transferred in the redox process. E_{redox} is the half-cell reduction potential at the condition of interest and E^0_{redox} is the half-cell reduction potential measured at standard conditions. The Nernst equation can be expressed using base-10 logarithm and summarizing the constants involved at a temperature of 25 °C as follows:

$$E_{redox} = E^0_{redox} + \frac{0.059\,V}{z} \log_{10}\left(\frac{c_{ox}}{c_{red}}\right) \tag{10}$$

The reversible hydrogen electrode represents a special type of standard hydrogen electrodes, whose potential does not change with the pH of the electrolyte solution. It can directly be used in the electrolyte in contrast to the standard hydrogen electrode. The concentration of the oxidized species H^+ (c_{ox}) in the solution is hence not 1, but correlates to the H^+ concentration in the electrolyte and a stable potential within changing pH values can be achieved, c_{red} equals unity. For the redox couple H_2/H^+, the term E^0_{redox} equals zero, as defined previously. The potential of the redox couple H_2/H^+ versus the reversible hydrogen electrode and the pH correlate as follows:

$$E_{RHE} = E^0_{redox} + 0.059\,V \log_{10}(c_{ox}) = -0.059\,V \cdot pH \tag{11}$$

The pH value is defined as the inverse base-10 logarithm of the H^+ concentration in the electrolyte, which equals the concentration of the oxidized species.[102]

$$pH = -\log_{10}(c_{H^+}) \tag{12}$$

3.2.3 Electrochemical reaction kinetics at electrode surfaces

The foregoing discussion and introduction of the Nernst equation (9) relate to redox systems in thermodynamic equilibrium, such that the cathodic (*red*) and anodic (*ox*) reaction path show the same reaction rate.

$$0 = r_{red} = r_{ox} = k_{red} c_{ox}^{s} - k_{ox} c_{red}^{s} \tag{13}$$

Here, r is the reaction rate, k_{red} and k_{ox} are the rate constants (cm/s) of the reduction and oxidation reaction and c^s stands for the surface concentration. Assuming Arrhenius formalism, the rate constant follows:

$$k_x = A_x e^{-\Delta G_{x,a}^{\ddagger}/RT} \tag{14}$$

x denotes either the reduced or oxidized species, A_x is the pre-exponential (frequency) factor, R is the universal gas constant, T is the temperature and $\Delta G_{x,a}^{\ddagger}$ is the reaction's activation energy. In equilibrium conditions, the reaction rate is zero ($r = 0$). A change in electrode potential can be interpreted as change in chemical potential and thus in the free energy of either of the species. Figure 2.9 shows the redox system in equilibrium (at E^0) where the reaction rate is zero resulting in equal free energies of the reduced/oxidized species $\Delta G_{0c}^{\ddagger} = \Delta G_{0a}^{\ddagger}$. A positive shift in electrode potential leads to a shift towards the oxidation and the curves at E, for which the standard free energy of the reduction $\Delta G_c^{\ddagger}$ is increased, while the standard free energy for the oxidation $\Delta G_a^{\ddagger}$ is reduced. For the standard free energy of the electrodes (c denotes the cathode and a the anode, respectively) follows:[104]

$$\Delta G_c^{\ddagger} = \Delta G_{0c}^{\ddagger} + \alpha F(E - E^0) \tag{15}$$

$$\Delta G_a^{\ddagger} = \Delta G_{0a}^{\ddagger} - (1 - \alpha) F(E - E^0) \tag{16}$$

with the standard free energy in equilibrium conditions $\Delta G_{0x}^{\ddagger}$, the Faraday constant F and the potential change $\Delta E = (E - E^0)$. The quantity α is named charge transfer coefficient, whose value lies between zero and unity and depends on the shape of the intersection region.[104]

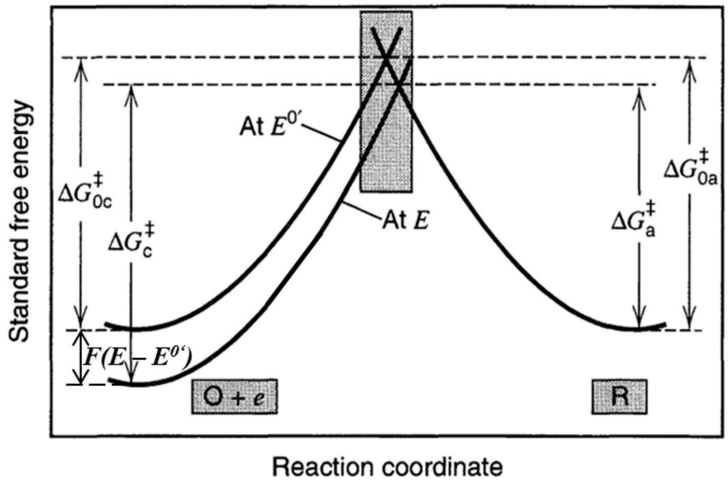

Figure 2.9: The redox system is in equilibrium at E^0, such that the standard free energies of the electrodes are equal $\Delta G_{0c}^{\ddagger} = \Delta G_{0a}^{\ddagger}$. The electrode potential is changed by the value of $\Delta E > 0$, resulting in a shift of the reaction equilibrium towards the oxidation (at E). For the oxidation reaction the standard free energy is reduced by a fraction of $(1-\alpha)F\Delta E$, while the reduction standard free energy is increased by the fraction $\alpha F \Delta E$, adapted from reference [104].

Electrochemical reactions can best be described using steady-state current-potential curves. The overpotential is a kinetic phenomenon of electrode materials and describes the difference between thermodynamically calculated potential E_{eq} and measured potential E at which the electrochemical reaction occurs ($\eta = E - E_{thermo}$). For example, the higher the current drawn out of an electrochemical cell, the higher the voltage over the thermodynamic cell voltage is needed.[102,104] The relation between the overpotential η and the current i is given by the Butler-Volmer equation[105]:

$$i = i_0 \left(e^{-\frac{\alpha z F \eta}{RT}} - e^{\frac{(1-\alpha) z F \eta}{RT}} \right) \tag{17}$$

At equilibrium conditions, the inherent rate of oxidation or reduction is defined as exchange current density i_0, which describes the rate and reversibility of an electrode reaction. Good reference electrodes show high exchange current densities.

For large overpotentials (negative or positive), one of the exponential expressions in equation (17) can be neglected. For example, in the case of negative overpotentials $e^{-\frac{\alpha z F \eta}{RT}} >> e^{\frac{(1-\alpha) z F \eta}{RT}}$ follows for the overpotential-current relation, according to the above written equation (17):

$$\eta = \frac{RT}{\alpha z F} \ln(i_0) - \frac{RT}{\alpha z F} \ln(|i|) \tag{18}$$

While for large positive overpotentials $e^{\frac{(1-\alpha) z F \eta}{RT}} >> e^{-\frac{\alpha z F \eta}{RT}}$, the following expression is obtained:

$$\eta = \frac{RT}{(1-\alpha) z F} \ln(i_0) - \frac{RT}{(1-\alpha) z F} \ln(|i|) \tag{19}$$

The above written equations (18) and (19) are the so called Tafel equations, which are often empirically simplified to:

$$\eta = a + b \log(i) \tag{20}$$

With the experimental constants a and b. The Tafel slope b, which equals $-\left(\frac{RT}{\alpha z F}\right)$ for high negative overpotentials and $-\left(\frac{RT}{(1-\alpha) z F}\right)$ in the case of high positive overpotentials, describes the change in potential per decade of current (mV/dec) and contains information about the reaction mechanism and the rate determining step of the overall reaction.[104]

3.2.4 Catalysts

Catalysts describe materials that enhance the reaction kinetics by lowering the activation energy of a chemical reaction without being consumed. The reaction kinetics are equally enhanced in both directions (oxidation and reduction of a redox couple), meaning that the kinetics are changed while the thermodynamics are constant. During the catalysis, the reactant is bound to the catalyst surface as intermediate and the product is released from the catalyst surface afterwards, leaving the catalyst surface unchanged. The ability of materials, e.g. metals, to serve as catalysts in the hydrogen evolution reaction is depicted in the so called Vulcano plot (Figure 2.10) showing the exchange current density depending on the adsorption enthalpy.[106,107] For low adsorption enthalpies, the hydrogen is weakly bound to the surface and does not reside long enough for the reaction to proceed. If the adsorption enthalpy is high, hydrogen is tightly bound to the surface and the reaction does not proceed further than the adsorption. The best catalyst materials show adsorption enthalpies that are neither too low nor too high. Considering metallic materials in acidic media, the best hydrogen evolution catalysts are found in the platinum group, showing adsorption enthalpies of around 60 kcal/mol. Since these materials are rather expensive and not earth-abundant, other catalyst materials are investigated. Promising alternatives in alkaline media have been found especially for compounds and alloys of nickel and cobalt[39,40,108,109], showing

overpotentials of 0.34 – 0.47 V for the oxygen evolution and between -0.07 to -0.30 V for the hydrogen evolution reaction side. The preparation and properties of earth-abundant catalysts will be discussed further in chapter (6).

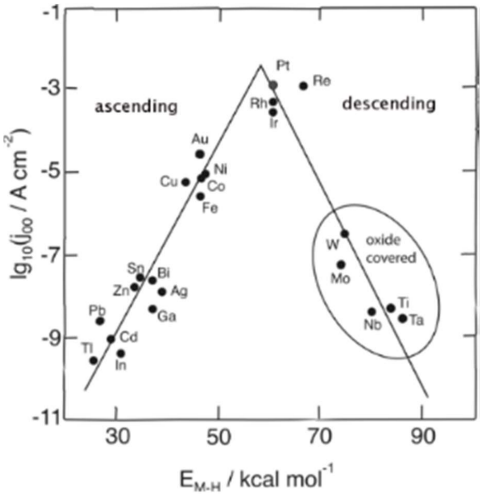

Figure 2.10: Vulcano plot for HER catalysts in acidic solutions showing the exchange current density depending on the adsorption enthalpy, taken from reference [106].

3.3 Principles of photoelectrochemical water splitting

3.3.1 Basics of solar water splitting

As described in section 2, liquid water can be split into gaseous hydrogen and gaseous oxygen using electrical current. Photovoltaic systems offer a clean way to produce hydrogen via electrolysis rather than nuclear power or fossil fuels. Additionally, the hydrogen generation via solar driven water splitting can be understood as storing solar energy in the form of molecular hydrogen. One mol of hydrogen and a half-mol of oxygen are produced upon the splitting of one mol of water:

$$H_2O_{(liquid)} + h\nu \rightarrow H_{2(gaseous)} + \frac{1}{2}O_{2(gaseous)} \tag{21}$$

The half-cell reactions and standard potentials versus standard hydrogen electrode (SHE) and potentials versus the pH independent reversible hydrogen electrode (RHE) in acidic media (pH = 0), where an excess of protons is present, are:

$$2\,H^+ + 2\,e^- \rightarrow H_2 \qquad E^0 = 0 \text{ V vs. RHE} \qquad E^0 = 0 \text{ V vs. SHE} \tag{22}$$

$$2\,H_2O \rightarrow O_2 + 4\,H^+ + 4\,e^- \qquad E^0 = 1.23 \text{ V vs. RHE} \qquad E^0 = 1.23 \text{ V vs. SHE} \tag{23}$$

In alkaline media (pH = 14), an excess of hydroxide ions is present, therefore, the half-cell reactions are written as follows:

$$2\,H_2O + 2\,e^- \rightarrow H_2 + 2\,OH^- \qquad E^0 = -0.826 \text{ V vs. RHE} \tag{24}$$

$$4\,OH^- \rightarrow O_2 + 4\,e^- + 2\,H_2O \qquad E^0 = 0.404 \text{ V vs. RHE} \tag{25}$$

The thermodynamic potential difference ΔE for redox reactions is calculated according to:

$$\Delta E = E^0_{anode} - E^0_{cathode} \tag{26}$$

The water reduction (reaction at cathode) is a two-electron transfer, whereas during the water oxidation (reaction at anode) four electrons are generated to form one mol of oxygen. Hence, for a balanced redox reaction, the hydrogen reduction half-cell reaction has to be multiplied by two. Thus, twice the amount of hydrogen compared to oxygen is yielded during the splitting of water. The free-energy change of the endergonic reaction ΔG^0 is 237.2 kJ/mol under standard conditions, meaning a constant temperature of 298 K, a concentration of 1 mol/L and a pressure of 101325 Pa. The free-energy change of the reaction corresponds to 2.46 eV per molecule of H_2O, hence 1.23 eV per transferred electron in the two-electron process. If a single photoabsorber were to be used for the entire water splitting reaction, the band gap of the semiconductor has to exceed 1.23 eV considerably.[21] If overpotential losses obtained for both half-cell reactions, recombination effects and band banding effects of the semiconductor due to the emersion in the electrolyte are considered[22], the band gap of the semiconductor, which is supposed to be used for unbiased water splitting, increases to >2 eV.[23] Additionally, if the unbiased water splitting process should be driven by solar light, the band gap has to be lower than 3 eV in order to be suitable for solar light absorption. This leaves a small range of 1 eV (between 2 – 3 eV) for materials with suitable band gaps for the overall solar driven water splitting reaction with one photoabsorber. Materials with suitable band gaps in the region between 2-3 eV exist, but these materials (e.g. Fe_2O_3 (2.3 eV), CdS (2.4 eV), GaP (2.25 eV)) are either not stable in the electrolyte (CdS)[110,111] or the water reduction potential (Fe_2O_3) or the water oxidation potential (GaP), respectively, do not exceed the conduction (for HER) or the valence (for OER) band (see also Figure 2.11)[21]. These criteria leave only a small amount of semiconductors, which can thermodynamically be used for the unbiased overall water splitting reaction. However, the overpotential of these few semiconductors is significantly higher than for metal electrodes due to the slower charge carrier transfer kinetics[78,112] and the larger potential drop for the electrolyte/semiconductor interface.[113]

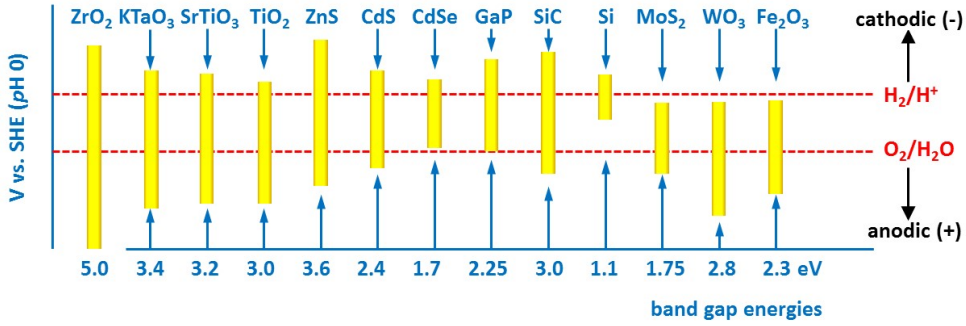

Figure 2.11: Schematic figure illustrating the band gap energies of various photoabsorber materials. The band gap energies are indicated, as well as the position of the band edges with respect to the hydrogen reduction and water oxidation level (pH = 0), taken from reference [21]

The requirements for unbiased solar water splitting can be resolved by using multiple band gap absorber as in a multi-junction thin film silicon solar cell and by efficiently protecting the solar cell against the corrosive electrolyte. For the protection of the solar cell, either protective coatings (e.g. TiO_2[114–117]), thin metal films[24,118]or metal sheets can be used, as it was done in the present work (see also chapter (6)). The processes occurring at the metal-electrolyte interface and the buried junction devices employing multi-junction thin film silicon solar cells are introduced in the following sections.

3.3.2 Helmholtz double layer – metal/electrolyte interface

The Helmholtz double layer at the metal electrode/electrolyte interface consists of the so called Helmholtz layer in the electrolyte and the oppositely charged layer in the electrode surface.[119,120] The Helmholtz layer consists of two parts. The inner Helmholtz layer is a plane parallel to the electrode surface built of ions without hydration shell, such that these ions are directly in contact with the electrode. Those ions are specifically adsorbed on the electrode surface and the resulting inner Helmholtz layer is only a few Angstroms thick (Figure 2.12). The outer Helmholtz layer (OHL) is also a plane parallel to the electrode surface, but it consists of ions with hydration shell. In this case, the hydration shell is in contact with the electrode surface, therefore, the ions are not specifically adsorbed.[121] The diffusion layer is loosely associated with the electrode, the ions of this layer move under the influence of thermal motion and electric attraction. The Helmholtz layer is called rigid layer, although the ions in the Helmholtz layer show diffusion along the layer plane and can be substituted by ions from the diffusion layer (see also Figure 2.12).[119–121]

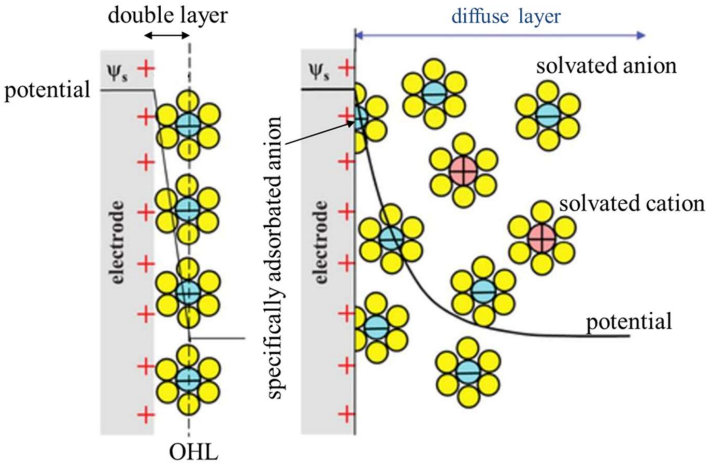

Figure 2.12: Helmholtz model of the metal/electrolyte interface. The Helmholtz layer consists of the inner and outer Helmholtz layer (specifically adsorbated anion (IHL) and OHL) and the diffusion layer. The potential drop across the different layers is indicated, adapted from reference [122].

Due to the opposite charges in the electrode and the Helmholtz layer, a potential difference across the surface/electrolyte interface is built up, leading to an electrical field. The Helmholtz model describes the potential of the electric field as linearly decreasing from the electrode surface to the outer edge of the outer Helmholtz layer, as can be seen in Figure 2.12. The electrical potential for the diffusion layer is considered to decrease exponentially with the distance from the electrode. Due to the high electrical conductivity in the metal electrode, an electrical field within the electrode is not supported, thus the potential drop only occurs within the electrochemical double layer.[119,120] In the case of a semiconductor in contact with the electrolyte, the potential drop not only occurs within the Helmholtz layer but also within the semiconductor. This leads to additional band bending of the valence and conduction band. Similar to the p-n junction discussed in section (3.1.1), a depletion region containing positive charges from ionized donors is built-up near the interface, resulting in a positive band bending at the interface. For further information see reference.[34,116,123]

3.3.3 Buried junction devices

One of the major requirements for solar driven water splitting is to fully protect the solar cell against the corrosive electrolyte.[21] This can for example be achieved by protection layers. Different materials have been investigated as coating layers, e.g. TiO_2 or thin metal films.[116,118] In the present work, 'buried junction' integrated photovoltaic-biased electrochemical devices, as shown in Figure 2.13, were used, consisting of four

main components.[34] The multi-junction thin film silicon solar cell (in Figure 2.13: a-Si:H/a-Si:H/µc-Si:H) is the photovoltage and photocurrent source powering the device. The solar cell is illuminated through the glass substrate, thus, the light directly enters the solar cell and is not absorbed by surrounding electrolyte. The ZnO:Al/Ag rear contact provides excellent optical reflection of the incident light back into the solar cell. Metal sheets are employed directly in contact with the ZnO:Al/Ag rear contact of the solar cell. The metal sheets were not only used as protection against the electrolyte, but also as electrode material, ensuring good electrical conductivity and most important allowing to maintain the optimized ZnO:Al/Ag rear contact for the best solar cell performance and additionally as substrate for higher active catalysts (see also chapter (6)). Mostly nickel sheets were used, in order to provide an active material as fall back solution in the case of catalyst detachment. By using metal sheets, the photovoltage and photocurrent are independent of the semiconductor/electrolyte interface and its additional band bending.[123] At the metal/electrolyte interface, the overpotential of the electrode and/or catalyst play a major role in the performance of the PV-EC device. Therefore, the occurring overpotentials should be as low as possible. The next component is the alkaline or acidic electrolyte, whose conductivity has to be sufficient in order to reduce Ohmic losses as described in section 3.2.1 (pure water is not sufficient as electrolyte). In the present work, potassium hydroxide solutions of 1 mol/L were used. The last component is the counter electrode coated with an OER catalyst, usually a metal oxide layer. In the present work, mainly $NiFeO_X$ has been investigated as earth-abundant material for the use as OER catalyst in integrated PV-EC devices, as discussed in chapter (6). The counter electrode is electrically connected to the front contact TCO layer, thus electrons generated during the water oxidation can travel through the solar cell to the HER catalyst, where the electrons are being consumed in the water reduction reaction. The device consisting of the four different components is modularly built, allowing to individually optimize each component. For example, different catalyst pairs can be combined and measured with the same multi-junction thin film solar cell and vice versa. A more detailed description of the PV-EC devices will be given in chapter (5). Furthermore, the device can be understood as electrical series connection of the photovoltaic and electrochemical cell, as described in the literature[124,125], allowing detailed modeling of the device performance by using the individually measured current density-voltage characteristics, as further described in chapter (3).

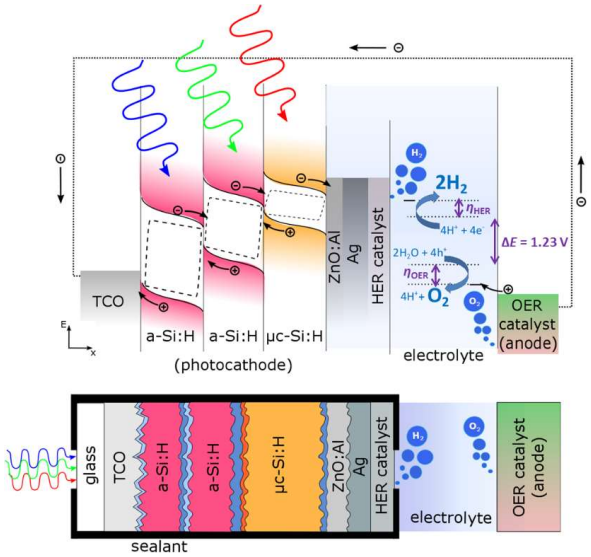

Figure 2.13: Schematic model of the band diagram under illumination and the buried junction device with its components: (1) multi-junction thin film silicon solar cell (in this case a-Si:H/a-Si:H/µc-Si:H, non-biased conditions), (2) hydrogen evolution reaction catalyst, (3) electrolyte and (4) oxygen evolution reaction catalyst. The energy levels of the HER and OER are indicated in the band diagram model. The HER takes place at the solar cell rear side and the OER at the counter electrode. The thermodynamically required potential is 1.23 V. Additionally, the overpotentials of the HER (η_{HER}) and OER (η_{OER}) catalysts have to be overcome for the water splitting reaction, taken from reference[34].

3.4 Standard and non-standard test conditions

As mentioned in the introduction, the performance of solar cells and photovoltaic-biased electrochemical cells are mainly investigated under laboratory standard test conditions (STC)[41,42,100,126]. This means a temperature of 25°C, perpendicular illumination of 1000 W/m² (1 sun) intensity of the AM 1.5G spectrum (shown in Figure 2.14 as radiation at sea level).[41,42,100,126] However, if solar cells and PV-EC devices were to be used outdoors, a wide range of operation conditions appear. The influence of varied temperature, intensity and spectral quality on solar cells has been widely investigated in the past[43–45,51,53], while detailed analysis of the effects on the combined devices have not fully been carried out yet and will be discussed in chapter (7). In the following section, the effects of the varied conditions on solar cells will be briefly discussed.

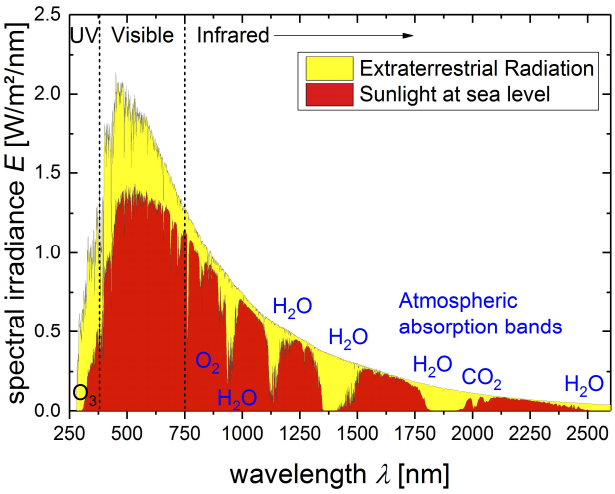

Figure 2.14: Solar irradiance spectrum at different atmosphere levels. The radiation at sea level corresponds to the air-mass 1.5 G spectrum. The different absorption bands are indicated, taken from reference[89].

3.4.1 Temperature

In general, the performance of a solar cell is reduced, if the temperature is increased.[60,61] Regarding the specific parameters, the open circuit voltage V_{OC} is mainly affected by the temperature change and depends as follows on the temperature T:

$$V_{OC} = \frac{E_{gap}}{q} - \frac{n_{id}kT}{q}\ln\left(\frac{J_{00}}{J_{SC}}\right) \tag{27}$$

With E_{gap} as band gap (optical gap)energy, q the elemental charge, n_{id} the ideality factor for the solar cell, k the Boltzmann constant, J_{SC} the short circuit current density and the prefactor j_{00}.[60,61] The open circuit voltage is reduced for increasing temperatures, which is mainly driven by the recombination mechanisms depending on the excess charge carrier concentrations (for further information see [127,128]). The decrease of open circuit voltage for multi-junction thin film silicon cells was reported in literature as approximately 6 mV/°C.[54] The short circuit current density of solar cells generally slightly increases with an increasing temperature, which is due to a decreasing band gap energy upon temperature increase.[127] If the fill factor is not significantly affected, the photovoltaic efficiency of solar cells decrease with increasing temperatures.[54,127] In section (7), the effect of a temperature increase on the PV and PV-EC performance is discussed in detail.[54] Additionally, the observed temperature effects are investigated under varied illumination intensity, assuming that low intensity illumination would lead to lower device temperatures, while high illumination intensities would cause enhanced device temperatures (see section (8.1)).[56]

3.4.2 Incident illumination intensity

Variations of the incident light intensity reaching a solar cell affect all solar cell parameters. The photocurrent density directly depends on the photon flux and therefore J_{SC} depends in most cases linearly on the light intensity.[129,130] For the open circuit voltage, a logarithmic dependence on the incident light intensity is found:

$$V'_{OC} = V_{OC} + \frac{n_{id}kT}{q} \ln X \tag{28}$$

with V_{OC}, the open circuit voltage under standard test conditions (1000 W/m²), n_{id} the ideality factor for the solar cell, k the Boltzmann constant, q the elemental charge, T the temperature and X the light concentration (e.g. 0.8 for measurements under 800 W/m²).[129,130] The effect of a varied intensity onto the PV-EC device performance is discussed in section (8.1), additionally, as mentioned in the previous section, the illumination and temperature variations were combined, investigating the combined effects on the device performance. [56]

3.4.3 Incident illumination angle

Besides the temperature and intensity, the incident illumination angle can have an influence on the performance of the PV-EC device. The incident illumination angle varies during the year and day and depends on the degree of latitude. In Munich (Germany), for example, the difference in the incident angle at noon (12:00) between June 21st (65.3°) and December 21st (18.5°) is approximately 47°. If the illumination angle varies and the PV cell is not adjusted appropriately, the output power is reduced due to the reduced number of incident photons per area and due to reflection losses, as reported in the literature.[53,131–135] A variation in illumination angle could in the worst case possibly lead to an interruption in the hydrogen production. In chapter (8.2), the PV-EC device performance under varied illumination angles will be discussed.

3.4.4 Spectral matching

The spectral matching of a solar cell influences its performance as shown in the literature[51,53,136]. Typically, the sub cell currents of a multi-junction solar cell are adjusted under standard test conditions (air-mass 1.5G illumination) in order to obtain the maximum photocurrent density. For the outdoor use of multi-junction solar cells, different spectra have to be taken into account for the performance of the solar cell.[42,45] The spectral quality of the outdoor spectra can vary in its wavelength share, such that spectra are shifted towards an increase in the short (e.g. during summer) or long (e.g. during winter) wavelength range[44,45]. The spectral quality can be described using the average photon energy of the spectrum, which is defined as the total energy in a spectrum (spectral irradiance) divided by the total number of photons it contains (photon flux density):

$$APE = hc \frac{\int_a^b E(\lambda) d\lambda}{\int_a^b \lambda E(\lambda) d\lambda} \tag{29}$$

Herein, h stands for the Planck constant, c for the speed of light, $E(\lambda)$ is the spectral irradiance and λ is the wavelength. The wavelength range used in the present work is between 300 (a) and 1100 (b) nm.

The different wavelength shares in the spectrum lead to a different enhancement of the individual sub cells, which have different band gap energies, thus resulting in a current mismatch under non-standard test conditions. The current mismatch then leads to an increase in fill factor as described in reference[51]. In the present work, the influence of the spectral quality on triple junction cells and PV-EC devices based on these triple junction solar cells are investigated in further detail (see chapter (8.3)).

4 Experimental techniques and methods

4.1 Techniques and methods to prepare thin film silicon solar cells

4.1.1 Substrates

Prior to the solar cell deposition, the substrate for the deposition has to be chosen and cleaned. In order to ensure a residue-free surface, the substrates were cleaned using DeContam® (ESPI Metals) and an ultrasonic bath for two hours. Afterwards, the substrates were rinsed with deionized water and dried in air. For the a-Si:H/a-Si:H/µc-Si:H triple junction solar cells, substrates of the type "Asahi (VU)" were used. "Asahi (VU)" denotes SnO_2:F coated white glass with low iron content and a pyramidal structure. For triple junction solar cells with an a-Si:H/µc-Si:H/µc-Si:H absorber layer stack, ZnO:Al was used as transparent conductive oxide material. Therefore, an 800 µm thick ZnO:Al layer was deposited by means of magnetron sputtering onto a cleaned Corning type Eagle glass of 1.1 mm thickness. To form a light scattering structure, the ZnO:Al substrates were etched for 40 s in 0.5 molar hydrochloric acid.[137,138] Etched ZnO:Al substrates have larger features and increased scattering properties for long wavelength light as compared to SnO_2:F coated substrates. Particularly for thick microcrystalline sub cells in a-Si:H/µc-Si:H/µc-Si:H triple junction solar cells, it is assumed that etched ZnO:Al substrates provide an improved light scattering.

4.1.2 Plasma-enhanced chemical vapor deposition system ("six-chamber system")

The used thin film silicon solar cells were deposited by means of plasma-enhanced chemical vapor deposition technique in a six-chamber deposition system (MRG Inc., Denver), which is shown as schematic in Figure 3.1. The maximum size of substrates, which can be used for deposition in this system, is 10x10 cm². The six-chamber system consists of one load lock, two transfer locks and six deposition process chambers. Each process chamber is used to deposit different intrinsic and doped layers of material. Therefore, different doping gases are available in the different chambers, while silane, hydrogen and argon are provided in each process chamber. In order to avoid cross contamination and residual doping effects of the layers, the process chambers are separated by transfer valves. The substrate is fixed in face down configuration into a metal carrier, which is transferred through the multi-chamber system by computer-operated transfer arms. The transport rail ensures an electrical grounding of the substrate and carrier. The process temperatures in the deposition chambers are controlled by heating blocks, which are attached only a few centimeters above the carrier with the substrate. The substrate is indirectly heated by the heating blocks. The dependence of substrate temperature on the heater temperature can be found in K. Wilken's diploma thesis[79]. In order to generate a plasma, two electrodes are needed. One electrode is placed on the bottom of the chamber and is powered by a generator with radio-frequency (RF) or with very high frequency (VHF). The substrate in the metal carrier serves as counter electrode and is placed in a fixed distance to the powered electrode. A matchbox is used to capacitively couple the power produced by the generator to the powered electrode in the chamber. The matchbox consists of an inductive coil (L) and two variable capacitors (C1, C2). The capacities have to be manually adjusted such that the matchbox impedance matches the plasma impedance as well as the deposition system components. Besides the capacities, also the generator power has to be adjusted manually, while all other components (e. g. transport arms, valves, deposition parameters) are controlled by a computer based system.

A schematic of the system is shown in Figure 3.1 and further details on the design and operation can be found in the literature.[139,140]

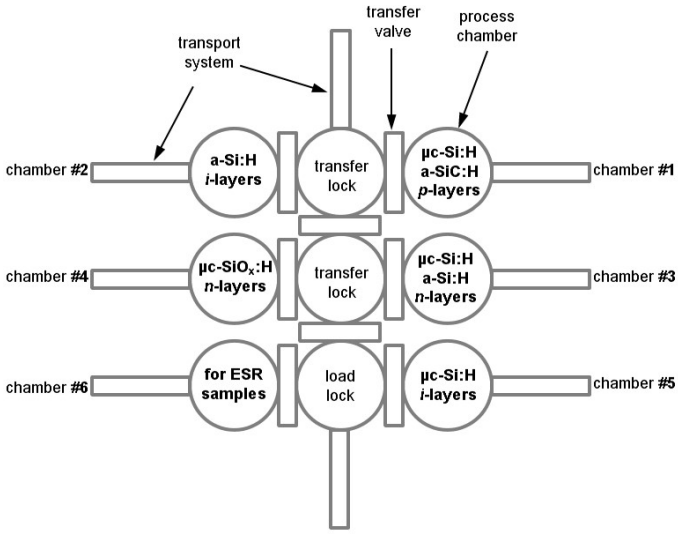

Figure 3.1: Schematic drawing of the six-chamber PE-CVD deposition system used for the thin film silicon solar cell deposition. Each chamber is only used for one layer type, either p-, n-doped or intrinsic layers. The chambers are connected by transfer locks and the load lock in vacuum conditions. Thus, samples can be transferred between the chambers without breaking the vacuum. Transfer valves separate the deposition chambers from the transfer locks. The chamber no. 6 is reserved for ESR samples and was not used in this work, taken from reference [34].

4.1.3 Deposition parameters

For the deposition of the triple junction solar cells prepared in the present work, two different frequencies for the alternating electrical field in the process chambers were used – radio frequency (RF = 13.56 MHz) and very high frequency (VHF = 94.7 MHz). All thin film silicon layers are based on a process gas mixture of silane (SiH_4) and hydrogen (H_2). Trimethylborane (TMB, C_3H_9B) was added for p-type layers and phosphine (PH_3) for n-type layers, respectively. For the intrinsic absorber layers, no additional gas was added to the silane-hydrogen-mixture. Intermediate reflectors or back contact layers made of n-type microcrystalline silicon oxide are deposited by adding carbon dioxide (CO_2) to the respective gas mixture, while methane (CH_4) was added to the first p-type layer in order to enhance the transparency. Silane and hydrogen have a purity of 99.9999 % (6.0). The dopant gases 2 % PH_3 in SiH_4 or 1 % TMB diluted in helium (He) were used with a purity of 5.0. The deposition parameters used for the preparation of the triple junction thin film silicon solar cells in the present work were developed based on previous processes[34] and are listed in Table 3.1.

4.1.4 Rear contact

The deposition of the silicon layers is followed by the deposition of a 80 nm thick ZnO:Al/Ag reflecting back contact[84,86]. The ZnO:Al/Ag layer was deposited by means of magnetron sputtering using a ceramic target with 1 wt.% Al_2O_3. The silver contacts of 700 nm thickness and 1 cm² size were evaporated through stainless steel shadow masks in a thermal evaporation system. ZnO:Al, which is not covered by silver, was etched off by using 0.5 M hydrochloric acid. The solar cell fabrication was finished by annealing the substrate for 30 minutes at 160°C in ambient atmosphere.

Table 3.1: Overview of deposition parameters applied for the deposition of triple junction thin film silicon solar cells.

	Layer	Plasma power density [mW/cm]	Plasma excitation frequency [MHz]	Heater temperature [°C]	Electrode distance [mm]	Deposition pressure [mbar]	SiH_4 flow [sccm]	H_2 flow [sccm]	CH_4 flow [sccm]	He flow [sccm]	CO_2 flow [sccm]	Dopant gas flow [sccm]
p	a-SiC:H	18	13.56	260	20	1.05	12	110	10	11.8	-	0.12
	µc-Si:H	60	94.7	260	20	0.4	1.5	200	-	2	-	0.02
n	a-Si:H	18	13.56	260	20	0.67	84	-	-	-	-	1.2
	µc-Si:H	150	13.56	260	20	4	1	200	-	-	-	0.02
	µc-SiO_X	150	13.56	260	20	4	1	200	-	-	0.75	0.02
i	a-Si:H	15	13.56	186 - 260	12	4	10, 4	90, 96	-	-	-	-
	µc-Si:H	120	94.7	260	12	1.5	4.0 – 6.0	98	-	-	-	-

4.1.5 Laser processing

The electrical contacts of thin film silicon solar cells can also be defined by laser scribing technique. This technique was for example used in chapter (6) to generate the front contact pattern of the upscaled triple junction solar cell. The laser scribing process is performed using a 1064 nm Nd:YVO_4 Q-switched diode-pumped solid state laser source from ROFIN (type PowerLine E). The pulse duration is between 7 and 12 ns (FWHM). The laser scribing process is performed in two steps, which are shown in Figure 3.2. For the first step, the removal of the silicon absorber layer (LP1), and the second step, the insulation of the front contact (LP2), the second harmonic of the Nd:YVO_4 laser and a wavelength of 532 nm were used. For LP1, the pulse frequency was 17 kHz and the average power was 430 mW. The second laser processing step was performed with a pulse frequency of 11.5 kHz and an average power of 290 mW. The feed rate or translation velocity of the laser beam was in both cases 800 mm s^{-1}. A lens system with a focal length of f = 300 mm was used to focus the laser beam in both processing steps. This leads to a beam spot radius of 60 mm. All laser processing steps were performed through the glass substrate side.

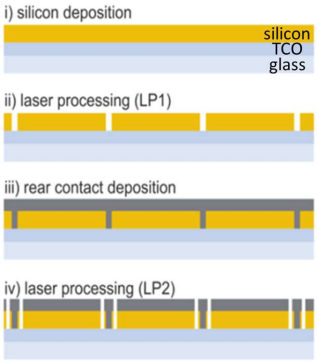

Figure 3.2: Schematic cross section of the laser scribing processing steps. LP1 is the removal of the absorber silicon layer and LP2 is the insulation of the front contact, which defines the solar cell size and shape.

4.2 Solar cell characterization

In the following section, the setups are described to measure current density-voltage curves and external quantum efficiencies of solar cells. The characterizing solar cell parameters, which will be introduced in this section, can be extracted from the current density-voltage curves, while the external quantum efficiency is used to determine the current matching between different sub cells in a multi-junction cell stack arrangement.

4.2.1 Photovoltaic parameters

The current density-voltage curve can be approximated by the superposition of the diode current density-voltage curve in the dark and the generated photocurrent density under illumination J_{photo}.[128] Under illumination charge carriers are generated, which results in a shift of the current density-voltage curve into the fourth quadrant by the value of J_{photo}. The diode equation changes to:

$$J = J_0 \left(e^{\frac{qV_{diode}}{kT}} - 1 \right) - J_{photo} \tag{30}$$

Here, j_0 is the dark saturation current density, q is the elemental charge, V_{diode} is the voltage of the diode, k is the Boltzmann factor and T is the temperature. As mentioned before, the photovoltaic parameters can be derived from the current density-voltage (JV) curve of a solar cell under illumination (see Figure 3.3). The short circuit current density J_{SC} is defined as the intersection of the curve with the axis of ordinates (V = 0 V).

The open circuit voltage V_{OC} describes the intersection of the JV curve with the axis of abscissae (J = 0 mA/cm²). At all points in the fourth quadrant of the current density-voltage curve under illumination, the delivered power density P can be extracted as product of current density and voltage ($J \cdot V$). The highest solar cell power density P is found at the maximum power point MPP with the corresponding current density J_{MPP} and the voltage V_{MPP}. The fill factor is defined as the quotient of $(J_{MPP} \cdot V_{MPP})/(J_{SC} \cdot V_{OC})$ and contains information about the shape of the current density-voltage curve. The most important parameter to characterize solar cells is the conversion efficiency η_{PV}. The conversion efficiency is defined as ratio between maximum power density yielded by the solar cell ($J_{MPP} \cdot V_{MPP}$) and the total integrated power input density P_{in}:[128]

$$\eta_{PV} = \frac{J_{MPP} V_{MPP}}{P_{in}} = \frac{J_{SC} V_{OC} FF}{P_{in}} \tag{31}$$

The total integrated power input density under standard test conditions is 1000 W/m² for the AM 1.5G spectrum. The slopes of the current density-voltage curve under illumination at the intersection points with the axes can be used to calculate the occurring resistances. The series resistance R_S can be extracted at j = 0 mA/cm² and the parallel (shunt) resistance R_P is calculated at V = 0 V.

In the present work, the current density-voltage curves of the solar cells were measured using a class A double source air-mass (AM) 1.5G solar simulator (WACOM sun simulator WXS-140S-Super) at standard test conditions (STC: AM1.5G, 1000 W/m², 25°C), if not stated otherwise. In order to ensure a stable solar cell temperature (± 1 °C), the solar cell was placed on a copper block connected with an electrical heating and water cooling system. A computer-controlled voltage source with the potential to measure the current response was used to conduct the current density-voltage measurements (SMU 238, Keithley). A schematic setup of a sun simulator[128] and the AM1.5G spectrum[141] used for current-voltage measurements can be found in the literature.

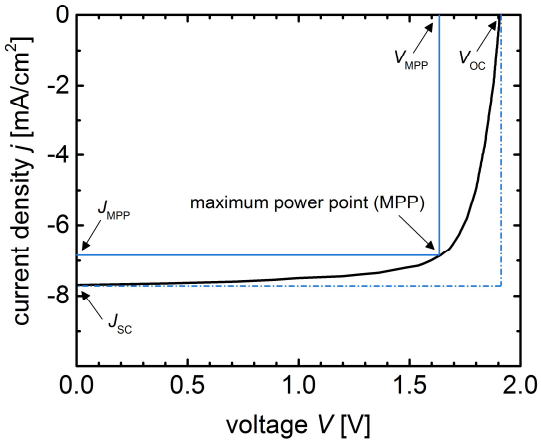

Figure 3.3: Current density-voltage curve of a solar cell under illumination. The following parameters are indicated: short circuit current density J_{SC}, the open circuit voltage V_{OC}, the voltage V_{MPP} and current density J_{MPP} at the maximum power point (MPP). The derivation of the fill factor FF is also shown as ratio between the solid rectangle and the dashed rectangle.

4.2.2 Quantum efficiency

The spectrally resolved external quantum efficiency (EQE) provides information about the optical absorption and charge carrier extraction in a solar cell, since it describes the number of extracted electron-hole pairs upon the number of incident photons shining on the solar cell. The generated electron-hole pair contributes to the extracted photocurrent. The definition of the wavelength dependent quantum efficiency is:

$$EQE(\lambda) = \frac{J_{ph}(\lambda)}{e\,\Phi(\lambda)} \tag{32}$$

Here, J_{ph} is the generated photocurrent density, which directly depends on the number of collected charge carriers, e is the elementary charge and $\Phi(\lambda)$ is the quantum flux per time and unit area for a certain wavelength. The product of $(e \cdot \Phi(\lambda))$ gives the number of photons that impinged the solar cell perpendicularly. One can distinguish between the internal and the external quantum efficiency. The external quantum efficiency takes the total incident light into account, whereas the internal quantum efficiency only takes the light into account that is coupled into the solar cell and does not consider light that is reflected on the glass surface. In the present work, only the external quantum efficiencies were used.

The external quantum efficiency can be extracted from the spectral response, which is measured using the Differential Spectral Response (DSR) method. The spectral response $S(\lambda)$ is defined as the ratio of generated photocurrent density per wavelength $J_{ph}(\lambda)$ and the irradiance $E_{ph}(\lambda)$ of the respective wavelength that reaches the solar cell:

$$S(\lambda) = \frac{J_{ph}(\lambda)}{E_{ph}(\lambda)} \tag{33}$$

By using a reference photodiode with a known spectral response $S_{ref}(\lambda)$, the photocurrent density $J_{ph}(\lambda)$ of the solar cell can be extracted. The quantum efficiency of the solar cell is then extracted from the spectral response $S(\lambda)$ as follows:

$$QE(\lambda) = \frac{S(\lambda)hc}{e\lambda} \tag{34}$$

with the Planck constant h, the speed of light c, the elementary charge e and the wavelength λ.

In the present work, the quantum efficiency measurements were performed using a monochromator in a wavelength range of 300 to 1100 nm. The individual sub cell current densities in a multi-junction solar cell can be determined by applying additional bias light of certain wavelengths to the probing light. The bias light intensity is approximately 1000 times higher than the probing light intensity (approx. 1000 W/m² compared to 1 W/m²). The individual sub cell current densities are calculated by integrating the quantum efficiency $QE(\lambda)$ over the corresponding wavelength λ range:

$$J_{QE} = e \int_{\lambda_{start}}^{\lambda_{end}} QE(\lambda)\Phi(\lambda)\mathrm{d}\lambda \tag{35}$$

e stands for the elemental charge and $\Phi(\lambda)$ is the photon flux density of the AM1.5G spectrum.

In order to determine the individual sub cell current densities of the a-Si:H/µc-Si:H/µc-Si:H triple junction solar cells investigated in the present work, three different bias light settings have to be realized by LEDs and spectrally filtered light from a tungsten lamp. To measure the top sub cell, light of 695 nm has to be applied additionally, such that the middle and bottom cell are saturated and do not limit the cell stack current. In this setting, the cell stack current is then limited by the top cell, which is measured. For the middle cell, two different light sources emitting light of the wavelengths of 470 nm for the top cell saturation and 765 nm for the bottom cell saturation have to be used. The bottom sub cell can be measured if additional bias light with a wavelength of 525 nm is employed, saturating the top and middle sub cells.[34] In order to measure the individual sub cell current densities of an a-Si:H/a-Si:H/µc-Si:H triple junction solar cell, light of 590 nm is used for the top cell evaluation, while the middle cell can be investigated under additional bias light of 400 nm and 780nm. The bias light used for the bottom cell is also of 525 nm as for the a-Si:H/µc-Si:H/µc-Si:H triple junction solar cell.[34] A detailed description of the DSR setup used in the present work is given in reference[142]. Typical quantum efficiency curves are shown in Figure 3.4 for an a-Si:H/a-Si:H/µc-Si:H triple junction solar

cell. The different sub cells are indicated as well as the sub cell current densities, which are evaluated by convolution of the quantum efficiency curves with the AM 1.5 G solar spectrum. Additionally, the sum of the quantum efficiencies is shown as grey plane.

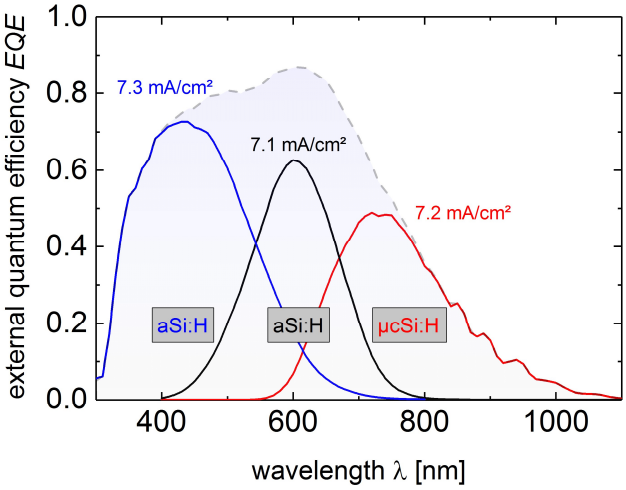

Figure 3.4: Typical quantum efficiency curves of an a-Si:H/a-Si:H/µc-Si:H triple junction solar cell. The different sub cells as well as the sub cell current densities are indicated in the figure. The sum of the quantum efficiencies is shown as grey plane.

4.2.3 Electroluminescence measurement techniques

Electroluminescence measurements are based on the principle of a solar cell as light emitting diode. Instead of shining light on the solar cell, which then generates a voltage, a voltage is applied to the solar cell and a luminescence signal is emitted due to radiative charge carrier combination. Due to the indirect semiconductor nature of silicon, the amount of radiative recombination is relatively low, however the luminescence signal can be registered using different detectors. In the electroluminescence setup used, a silicon CCD camera and an InGaAs camera were used to detect the luminescence signal. Electroluminescence measurements on solar cells are non-disruptive and provide information about the areal uniformity as well as occurring resistances in the solar cell. According to the following equation, the resistance at the position $\boldsymbol{r}$ = (x,y) is defined as:[128,143]

$$R_s(\boldsymbol{r}) = \frac{V_{ext} - V(\boldsymbol{r})}{J(\boldsymbol{r})} \tag{36}$$

with the respective local voltage $V(\mathbf{r})$ and local current density $J(\mathbf{r})$, as well as the externally applied voltage at the contacts V_{ext}.

To perform electroluminescence imaging, a source measurement unit, an illumination source and a camera are needed. As camera, Princeton Instruments Nirvana 640 InGaAs Camera with a resolution of 640 x 512 pixels or an Apogee Imaging System Si-CCD camera with a resolution of 3056 x 3056 pixels was used. For the present work, only the InGaAs camera was used due to the better signal to noise ratio. The integration time of the camera was 1000 ms. The voltage applied was 2.2 V. The light applied was equivalent to 1 sun. The sample stage is placed in a cabinet in order to reduce stray light and to avoid exposure with the laser light source. A Keithley 238 source measurement unit (SMU) was used to detect the electroluminescence signals. The sample is placed on a stage with temperature control and the temperature was maintained at 25 °C. Electrical contacting on the rear side of the solar cell was established using electrically conductive, adhesive silver tape and alligator clips. All parts of the setup are computer controlled using Labview libraries as software. A detailed description of the setup can be found in reference [143].

4.3 Electrodeposition

Electrodeposition (Electroplating) describes a process in which electric current is used to reduce metal cations dissolved in an electrolyte such that they form a coating layer on the working electrode. Electrodeposition is a widely spread method to grow metals, alloys and metal oxides, since the layers are relatively uniform and compact and the required equipment is rather inexpensive.[144–147] The working electrode in the circuit to be plated, is the cathode. As counter electrode a carbon rod or a metal sheet can be used, which are not consumed during the plating process. The dissolved metal ions in the deposition electrolyte are reduced at the interface between the cathode and the solution ("plating out" onto the cathode). The electrolyte, which contains at least one dissolved metal salt as well as other ions, ensures the flow of electricity between the electrodes.[147] Electrodeposition can be performed in continuous or pulsed deposition mode. During the continuous deposition mode, the layer is deposited for a certain amount of time without breaks. In the pulsed deposition mode, the deposition time is partitioned in small pulses during which the deposition current is applied.[39] Pulsed deposition mode is reported to create a more homogeneous atom distribution in the film, to improve the connectivity of the films, and to eliminate the decrease in effective activity of the respective metal sites, while increasing the mass loading compared to continuous deposition.[39] Factors that can affect the electrodeposition are the deposition temperature, the distance between the electrodes as well as stirring of the electrolyte. In some cases, an increased deposition temperature result in an increased deposition rate due to Arrhenius law. The distance between the electrodes influences the current distribution and should be kept constant if possible. The distance should not be as small as possible, since this could lead to an uneven current distribution between the electrodes and therefore an uneven surface topology. Stirring the electrolyte can lead to a transfer of ions from the bulk electrolyte towards the electrode surface.[39,145–147] The setup and conditions used for electrodeposition are described in detail in chapter (6).

4.4 Electrochemical measurement techniques

A brief description of the electrochemical measurement techniques used in the present work will be given in this section. All catalyst samples were characterized using the presented electrochemical measurement techniques using three-electode configuration in the order the techniques are described (4.4.2 - 4.4.7). For the characterization of the PV-EC device, which was performed in two-electrode configuration, mostly the linear sweep voltammetry measurements as well as the chronopotentiometric and chronoamperometric measurements were used. More detailed descriptions of the techniques can be found in reference[108,148].

All electrochemical measurements were performed using a Gamry Reference 600 (C3, Haar, Germany) potentiostat/galvanostat. The Gamry Reference 600 provides an accuracy of ±0.3 % of the selected ranges for the measured potential/current. The electrolyte used for all measurements was 1 M potassium hydroxide, prepared from deionized water (18 MΩ, Millipore, Schwalbach, Germany) and analytical grade potassium hydroxide. A detailed description of the used (photo)electrochemical measurement cells and the electrochemical workplace can be found in chapter (5).

4.4.1 Two-electrode versus three-electrode measurement technique

Electrochemical measurement setups generally consist of at least two electrodes, the working electrode (WE) and the counter electrode (CE). Additionally, a reference electrode (RE) can be included in order to measure in three-electrode configuration. Three-electrode configuration is preferably used for characterizing the working electrode, for example, if catalysts with different deposition conditions are compared. The reference electrode (e. g. Ag|AgCl) has a constant potential, which serves as reference point for the potential of the working electrode. The potential between reference electrode and working electrode is controlled by a potentiostat, while the current between the WE and CE is measured. The resistance of the reference electrode is in a range that no current flow is enabled through the RE. The CE should not be rate-limiting in the reaction, which can be ensured by highly active electrode material or sufficient electrode surface area. For

standardization, the measured potential is recalculated to the reservible hydrogen electrode (V vs. RHE), as described in section (3.2.2).

In two-electrode configuration, which is preferably used to study the entire electrochemical system, the counter electrode is used as reference electrode. Unlike the potential of the reference electrode, the potential of the counter electrode is not constant troughout the reaction. Since the potential of the counter electrode is not constant, the two-electrode configuration is not suitable to characterize specifically different working electrodes (e.g. catalysts deposited with varying deposition parameters), working electrodes can only be compared as part of the entire electrochemical system.

Figure 3.5 shows a schematic setup of the electrode and measurement arrangement for two- and three-electrode configuration.[104] The following measurement sequence (4.4.2 - 4.4.7) can be performed in three-electrode configuration (used for catalyst characterization) or two-electrode configuration (used for PV-EC device characterization). The specific electrode configurations used for the measurements shown in chapter (6) are mentioned specifically in the respective sections.

4.4.2 Open circuit potential

The open circuit potential (OCP) is a parameter for the stability of the potential of the electrodes in the electrolyte. The OCP is the potential at which no current is flowing (compare to the solar cell open circuit voltage V_{OC}) and is equal to the electrochemical potential of the solution. At equilibrium, the open circuit potential is constant.[148] In the present work, the open circuit potential is measured for 600 s.

4.4.3 Electrochemical impedance spectroscopy

Electrochemical impedance spectroscopy (EIS) is used to determine the electrolyte resistance, which is needed to perform the iR correction (see chapter (3.2.1)). The impedance is measured between 100 kHz and 0.01 Hz applying an AC amplitude of 10 mV superimposed over a DC potential of interest.[148]

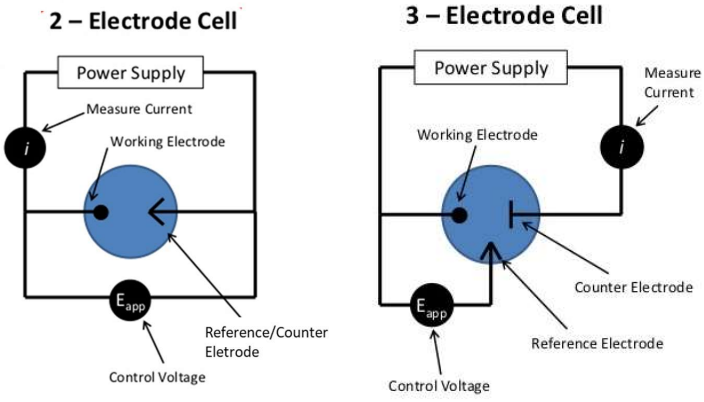

Figure 3.5: Schematic setup of two- and three-electrode measurement configuration. The different electrodes are indicated as well as the control voltage and the current that is measured, adapted from reference[104].

4.4.4 Cyclic voltammetry measurements and electrochemically active surface area

During cyclic voltammetry (CV) measurements, a potential is applied to the working electrode and changed linearly with time until a maximum final potential is reached, afterwards the applied potential is reversed into the opposite direction until a minimum final potential is reached. The current flowing between the working and counter electrode is monitored depending on the applied potential. Cyclic voltammetry measurements show the reversability of the investigated redox reaction.[148] The electrochemically active surface area (ECSA) of an electrode can be investigated by performing cyclic voltammetry measurements in a non-faradaic region with different scan rates[108]. In the non-faradaic region, the electrochemical double layer (see also (3.3.2)) is charged without chemical reactions occurring, only the increase or decrease of electrode charge takes place, leading to a capacitive current. By plotting the difference between the anodic and cathodic current ($i_{an.}$-$i_{cath.}$) extracted from the CV measurements versus the scan rate, information about the ECSA can be obtained. The slope of the current difference versus the scan rate equals the value of double layer capacitance C_{dl}, which divided by the specific capacitance C_s yields the electrochemically active surface area *ECSA*:

$$i_{an} - i_{cath} = \frac{dQ}{dt} = C_{dl}\nu \qquad ECSA = \frac{C_{dl}}{C_s} \tag{37}$$

Here, $i_{an.}$-$i_{cath.}$ is the current difference, Q is the charge, t is the time, C_{dl} is the double layer capacitance, ν is the scan rate, *ECSA* is the electrochemically active surface area and C_s is the specific capacitance, which is reported in the literature to account for 22 – 40 µF/cm² for nickel in alkaline media.[108] The scan rates used in this work were 5, 25, 75, 125, 175 and 200 mV/s.

4.4.5 Linear sweep voltammetry

Linear sweep voltammetry (LSV) is performed similarly to cyclic voltammetry measurements, a potential is applied to the working electrode, which is linearily scanned, and the current between the working and counter electrode is monitored. However, the potential is not reversed after the final maximum/minimum potential is reached. LSV measurements provide information about the current (density)-voltage characteristics of the investigated system (compare IV measurements for PV cells), but they contain no information about the reversibility of the redox reaction. The LSV measurements were performed with a scan rate of 2 mV/s.[148]

4.4.6 Chronopotentiometric measurements

During chronopotentiometric (CP) measurements, a fixed current is applied between working and counter electrode and the potential of the system is measured over time. In the present work, chronopotentometric measurements were conducted for 900 s and a current density of (±)10 mA/cm² was applied.[148]

4.4.7 Chronoamperometric measurements

During chronoamperometric (CA) measurements, a fixed potential is applied between working and counter electrode and the resulting current is monitored over time. For unbiased light induced water splitting employing triple junction thin film silicon solar cells as used in the present work, the applied potential is zero.[148]

4.5 Electrochemical series connection model

In a buried junction PV-EC device as it is used in the present work, the main components (solar cell, hydrogen evolution reaction catalyst, electrolyte and oxygen evolution reaction catalyst) are electrically connected in series, see Figure 3.6. Hence, the current density-voltage curve of the PV-EC device at a specific temperature T can be calculated by merging the current density-voltage curves of the individually measured components at

the specific temperature, as reported in literature[124,125]. The electrical series connection model is expressed by the following equation:

$$V_{PV-EC}(J,T) = V_{PV}(J,T) - \Delta E - \eta_{OER}(-J,T) + \eta_{HER}(J,T) + JR(T) \quad (38)$$

Here, the $V_{PV}(J,T)$ stands for the current density-voltage characteristics of the solar cell at the temperature T, ΔE is the thermodynamic potential difference required for the water splitting reaction and equals 1.23 V at 25°C. The catalyst overpotentials at a certain current density J and temperature T are described as $\eta_{OER}(J,T)$ and $\eta_{HER}(J,T)$. The different sign of the anodic current is taken into account by mirroring the curve at the potential axis and by the substraction. The voltage drop due to the electrolyte and its resistance is described by the factor $JR(T)$.

If only the current density-voltage curve of the PV cell and the electrolysis curve of the entire system (two-electrode configuration) are measured, the above shown equation simplifies to:

$$V_{PV-EC}(J,T) = V_{PV}(J,T) + V_{EC}(J,T) \quad (39)$$

The other factors, such as catalyst overpotentials, electrolyte resistance and thermodynamic potential are then included in the current density-voltage curve measured for the electrolysis. A detailed description of the electrical series connection model and the influences of various parameters can be found in the references [124,125,149].

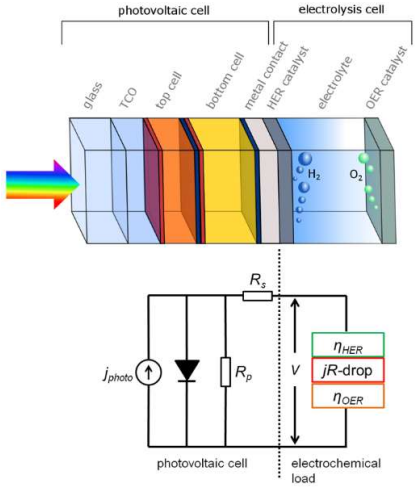

Figure 3.6: Schematic drawing of the buried junction based PV-EC device employing a tandem cell and the corresponding equivalent circuit diagram of the device. The photovoltaic cell is connected in series to the electrochemical cell, which includes the current and temperature depending overpotentials of the catalysts for both electrodes as well as the electrolyte ohmic drop. The equivalent circuit diagram of the photovoltaic cell shows the photocurrent density generated in the PV cell and the diode. The parallel R_P and shunt R_S resistances are indicated, taken from reference [34].

4.6 Solar-to-hydrogen efficiency calculation

The solar-to-hydrogen efficiency describes the ratio of produced hydrogen per total integrated incident power density and can be extracted from the current density-voltage characteristics of the PV-EC device measured in two-electrode configuration. The current at the operating point of the PV-EC device for unbiased light induced water splitting is extracted from the current density-voltage curve at zero volts. The following equation is used to calculate the solar-to-hydrogen efficiency:

$$\eta_{STH} = \frac{\Delta E |J_{OP}| \eta_F}{total\ integrated\ power\ input\ density} \quad (40)$$

Here, $|J_{OP}|$ is the value of the current density at the operating point of the PV-EC device under illumination extracted at zero bias, ΔE is the thermodynamic potential difference (ΔE = 1.23 V), the denominator is the total integrated power input density (1000 W/m² for the AM1.5G spectrum) and η_F is the Faradaic efficiency. The Faradaic efficiency describes the ratio between the hydrogen volume produced by the PV-EC device and the theoretically produced hydrogen volume according to Faraday's law employing the photocurrent density produced by the PV-EC device.

The Faradaic efficiency can be validated by means of volumetric measurements. Therefore, the evolved hydrogen gas is collected and the quantity is determined, for example in an extrusion measurement (see also chapter (5)). The theoretically expected hydrogen volume V_{theo} can be calculated using the ideal gas law in combination with Faraday's law:

$$V_{theo} = \frac{RTIt}{pzF} \quad (41)$$

R stands for the ideal gas constant, T is the temperature, I is the photocurrent, t is the time of the measurement, p is the pressure, F is the Faraday constant and z is the number of electrons transferred per 1 mol of hydrogen in the reaction (z = 2). The Faradaic efficiency is the ratio of the theoretically calculated gas volume V_{theo} and the experimentally measured gas volume V_{meas}.

$$\eta_F = \frac{V_{meas}}{V_{theo}} \quad (42)$$

The determination of the Faradaic efficiency for the used systems is shown in chapter (5) and (6), respectively.

4.7 Spectroscopic characterization methods

4.7.1 Scanning electron microscope

In a scanning electron microscope (SEM), an electron beam is focused on the sample in order to take images of its surface. Images are produced due to the interaction of the electron beam with the atoms in the sample surface. Thus, information about the topography can be obtained by detecting the signals of the interaction. The electron beam is directed in a raster scan pattern across the surface. By combining the electron beam position in the raster pattern and the detected signal, the image of the surface is created. Typically, the secondary electrons, which are emitted due to the interaction of the primary beam electrons and the surface atoms, are used as information source. These secondary electrons can either be detected using a secondary electron detector or an inlens detector. In the present work, mostly the inlens detector was used. The scanning electron microscope was used in the present work to investigate the morphologies of the catalyst surfaces prior and after the electrochemical measurements. For the $NiFeO_X$ samples, an Oxford instrument X-Max^N 150 mm^2 at 20kV was used. The SEM images of the NiMo samples were taken with a Zeiss 1550 SEM. Both scanning electrode microscopes are located at the Helmholtz Nano Facility at the Forschungszentrum Jülich GmbH. The images can be found in chapter (6).

4.7.2 Raman spectroscopy

Raman spectroscopy was used to investigate catalyst materials deposited on nickel foam (chapter (6)). The underlying method is based on inelastic scattering of monochromatic light, provided by a laser source, with molecules or atoms within the material. The interaction of the laser light with the material leads to an energy shift of the laser photons, which provides information about the vibrational modes within the system. For further reading refer to reference[150]. For the Raman spectroscopy, a laser light source of 532 nm (Coherent

sapphire) was used. As camera, a Si-CCD (Andor DU420) was used with an Andor Shamrock SR-303I spectrometer. For magnification of 50 times, an object lens BX-50 was employed. The Raman spectroscopy measurements were performed at the optical laboratories of the Institute for Energy and Climate Research – 5 Photovoltaics (Forschungszentrum Jülich GmbH).

4.7.3 X-ray photoelectron spectroscopy

X-ray photoelectron spectroscopy (XPS) can be used to determine the elemental composition of a sample and the chemical state of the elements detected without destroying the sample. XPS is based on the external photoelectric effect during which photoelectrons are detached from the surface due to the x-ray beam. The photoelectrons derive from the orbitals closest to the nucleus. The photoelectric effect is schematically described in three simplified steps. First, the electron in an orbital close to the nucleus is excited by an incoming photon (1), afterwards the excited electron is transferred to the surface of the atom (2) and finally emitted (3). The binding energy, which can be extracted from the kinetic energy of the electron, is characteristic for the initial orbital of the emitted electron. The kinetic energy of the electron can be detected by using a hemispherical electron energy analyzer. Here, the analyzer settings of electrostatic lenses and counter voltages can be chosen in a way that only electrons with a specific kinetic energy can pass and be detected in the analyzer. If the electrons of a specific energy reach the analyzer, their signal is fed into a photomultiplier such that a spectrum is created. In this spectrum, the intensity is shown depending on the kinetic (binding) energy of the photoelectrons.

In the present work, the samples were measured in an analyzing chamber of an integrated UHV system consisting of a XPS/UPS system (SPECS), equipped with a SPECS Phoibos 150 analyzer and a SPECS Focus 500 x-ray source using the monochromatized AlKα line at 1486.6 eV. The XPS measurements were recorded with the SpecsLab2 software. The measurement area is of 1 mm size and the information depth is approximately 10 nm. The sample placement is assisted by using a camera. The XPS measurements were performed by the Surface Science Group at the Department for Material Science of the Technische Universität Darmstadt.

5 Amorphous/microcrystalline/microcrystalline triple junction cells for solar water splitting

This chapter addresses the further exploration of the potential of a-Si:H/**μc-Si:H**/μc-Si:H triple junction cells regarding the increase of their photocurrent density and the application in water splitting devices. Theoretically, the photocurrent density expected for this cell type should exceed the photocurrent density measured for a-Si:H/**a-Si:H**/μc-Si:H triple junction cells, while providing lower photovoltages.[34] One possibility to further enhance the photocurrent density is the variation of the cell thickness, which will be shown in this section.

The solar cells prepared in the present work are based on the development of the thin film silicon conducted in a previous PhD work[34] by F. Urbain, who addressed the deposition and properties of a-Si:H and μc-Si:H layers and the implementation of these layers into multi-junction thin film silicon solar cells with the focus on high output voltages for the use in PV-EC devices.[24] The concept of multi-junction cells and the use of different band gap absorber materials is described in chapter (3.1.2). Figure 4.1(a) shows the current density-voltage curves of the different thin film silicon multi-junction solar cells (taken from reference [34]). Figure 4.1(b) depicts the current density voltage curves of PV-EC devices based on the solar cells shown in Figure 4.1(a) (taken from reference [34]). The thermodynamic potential required for the water splitting reaction is indicated at 1.23 V in Figure 4.1(a), here, occurring overpotentials at the electrodes (usually in the range of 300 – 500 mV[108]) are not included. In Figure 4.1(b), the operating point for unbiased water splitting is indicated at 0 V, the measurements were performed using platinum and ruthenium oxide as catalyst system in 0.1 M potassium hydroxide solution under AM1.5G illumination.

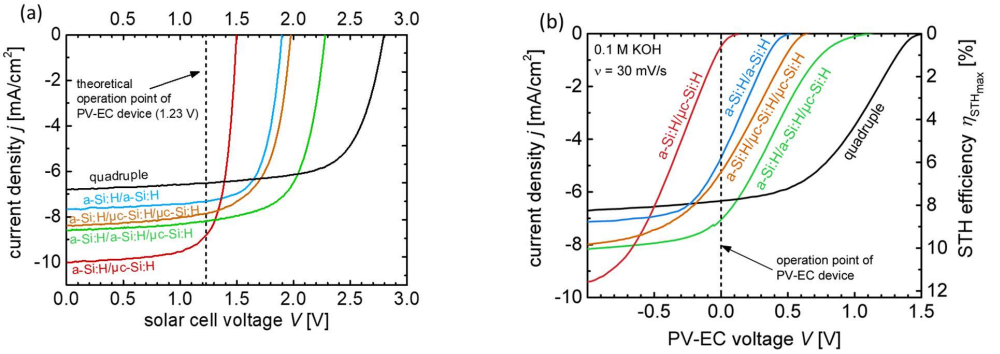

Figure 4.1: (a) Current density-voltage curves for different multi-junction cells under AM1.5G illumination. The thermodynamic water splitting potential is indicated at $E_{thermo.}$ = 1.23 V, adapted from reference [24,34,125]. (b) Current density-voltage curves for PV-EC devices employing different multi-junction cells in 0.1 M KOH under AM1.5G illumination. Platinum and ruthenium oxide were used as catalyst system. The operating voltage (0 V) for unbiased solar driven water splitting is indicated, taken from reference[24,125].

The Figure 4.1(a) and (b) depict the tradeoff between high photocurrent densities and high photovoltages. The highest short circuit photocurrent densities are achieved for the a-Si:H/μc-Si:H tandem cell, which shows the lowest open circuit photovoltage (Figure 4.1(a)). Employing the a-Si:H/μc-Si:H tandem cell in a PV-EC device under the named conditions, the operating current density J_{OP} in the water splitting reaction is below -1 mA/cm², due to the low photovoltage. Tandem cells consisting of an a-Si:H/a-Si:H cell stack deliver a higher output voltage but less photocurrent density compared to a-Si:H/μc-Si:H cells (Figure 4.1(a)). The operating current density obtained for the use of a-Si:H/a-Si:H tandem junction cells is -4.6 mA/cm² (Figure 4.1(b)). The lowest short circuit photocurrent density is measured for the quadruple junction cell (a-Si:H/a-Si:H/μc-Si:H/μc-Si:H), which has the highest open circuit voltage of 2.8 V measured for all multi-junction cells investigated. If quadruple junction cells are employed in water splitting devices, the required voltage is excelled significantly for the used configuration with platinum and ruthenium oxide as catalysts. The use of

quadruple junction cells is mainly beneficial, if catalyst systems with high overpotentials are to be used in the PV-EC device[24]. The best water splitting performances in this configuration were obtained for a-Si:H/a-Si:H/µc-Si:H triple junction cells (Figure 4.1(b)), which offer a reasonable tradeoff between photovoltage and photocurrent density (Figure 4.1(a)), resulting in a high operating current density and hence solar-to-hydrogen efficiency.[24,34] Regarding the a-Si:H/µc-Si:H/µc-Si:H triple junction solar cells, the lower band gap energy of the two microcrystalline sub cells should result in a lower photovoltage, but also in an increased photocurrent density, which should potentially exceed the photocurrent density produced by a-Si:H/a-Si:H/µc-Si:H triple junction cells.[34]

In the present work, the investigation of the a-Si:H/µc-Si:H/µc-Si:H triple junction cells was pursued further to increase the current density by varying the cell thickness without drastically reducing the photovoltage. An open circuit voltage around 1.9 V and a voltage at the maximum power point between 1.5 - 1.6 V should be sufficient for the use of highly active catalyst materials, which are discussed in chapter (6), thus the focus here is on the increase of the current density rather than on the increase of the output voltage. For a further increase of the output voltage, additional buffer layers can be used as shown in the previous PhD thesis.[34] Two different parameters are investigated depending on the cell thickness, which are (i) the sum of the individual sub cell current densities and (ii) the short circuit current density. The sum of the sub cell current densities is the total amount of current that can be produced by the solar cell and is evaluated by external quantum efficiency measurements. The short circuit current density indicates the lowest sub cell current density in the cell stack, which is limiting the device current density, and therefore can provide information about the current matching if combined with the sum of the sub cell current densities. In the ideal case of perfect current matching between the sub cell currents in a series connected multi-junction solar cell, the total amount of photocurrent generated by illumination is divided equally between the individual sub cells (see also chapter (3.1.2)). The starting point for the here deposited cells, is the recipe reported as reference cell in the previous PhD thesis[34], showing the lowest cell thickness of approximately 2700 nm and a conversion efficiency of 10.5 % (cell “Ref.” in Table 4.1).[34] The total solar cell thickness was subsequently increased by varying the deposition time of the intrinsic microcrystalline sub cell layers. A gain in thickness of the intrinsic sub cell layers leads to an increased light absorption in the respective sub cell. If the middle sub cell thickness is increased, the bottom sub cell thickness should also grow in order to compensate for the absorption in the middle cell. The sub cell thicknesses were calculated based on the deposition time and the layer deposition rates. Prior to the variation in thickness, the recipe was used to replicate the results reported previously on a-Si:H/µc-Si:H/µc-Si:H triple junction solar cells[34]. Additionally, the a-Si:H/µc-Si:H/µc-Si:H triple junction cell will be used in the electrical series model (see also chapter (4.5)) to calculate its potential for the water splitting application. The cells developed in this section are used in chapter (7) for the comparison of the annual hydrogen yield of PV-EC devices employing different multi-junction cells.

5.1 Experimental details

The a-Si:H/µc-Si:H/µc-Si:H triple junction solar cells were deposited according to the procedure described in chapter (4.1), using plasma-enhanced chemical vapor deposition technique in a multi chamber system in the p-i-n configuration (see chapter (4.1.2) for further information). As substrate ZnO:Al coated glass (ZnO:Al layer thickness 800 nm, glass thickness 1.1 mm) was used. The cleaning and etching procedure can be found in chapter (4.1.1) as well as the deposition parameters used for the deposition of the amorphous and microcrystalline layers (4.1.3). The intrinsic amorphous silicon layers were deposited at 186°C heater temperature (substrate temperature = 125°C), whereas for the intrinsic microcrystalline layers the heater temperature was 260 °C (substrate temperature = 180°C). The deposition time was varied in a range of 3.7 -5.5 h, resulting in cell thicknesses between 2740 – 4560 nm. After the deposition of the thin film silicon layer stack, ZnO:Al (80 nm) was deposited on the stack by means of magnetron sputtering followed by the thermal evaporation of silver through a stainless steel shadow mask serving as back contact and reflector.

In this chapter, the a-Si:H/µc-Si:H/µc-Si:H cells were characterized by current density-voltage measurements under standard test conditions (25°C, 1000 W/m² (1 sun), AM1.5G) using a Wacom sun simulator WXS-140S-

Super (class AAA). Additionally, external quantum efficiency measurements were performed using a monochromator in the wavelength range of 300 – 1100 nm. The wavelength of the bias light, which was applied for saturation of the individual sub cells, can be found in section (4.2.3). In order to calculate the solar-to-hydrogen efficiency η_{STH} of the PV-EC device employing a-Si:H/µc-Si:H/µc-Si:H cells, the electrical series connection model[124,125] was used, where the operating current density at zero bias (V = 0 V) was extracted. The solar-to-hydrogen efficiency was calculated according to equation (40).

5.2 Results of a-Si:H/µc-Si:H/µc-Si:H triple junction solar cells

Figure 4.2(a) shows the sum of the sub cell current densities, evaluated by external quantum efficiency measurements (details in section (4.2.3)) depending on the cell thickness, while Figure 4.2(b) depicts the short circuit current density versus the cell thickness, which was obtained through current density-voltage measurements at the sun simulator (further details in chapter (4.2.1). The sum of the sub cell current densities increases with increasing cell thickness and is enhanced from 24.9 mA/cm² to 26 mA/cm² (+1.1 mA/cm²). Depending on the cell thickness, the short circuit current density shows a similar trend. With increasing cell thickness the short circuit current density is increased from 7.9 mA/cm² to 8.4 mA/cm² (+0.5 mA/cm²).

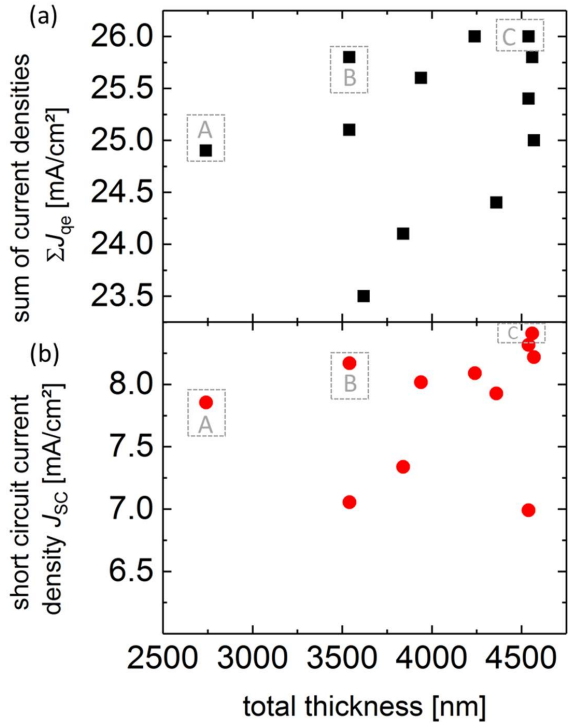

Figure 4.2: (a) Sum of sub cell current densities depending on the total cell thickness and (b) the corresponding short circuit current densities versus the total cell thickness. The cells A-C used for comparison are indicated.

In the following, several cells and their photovoltaic parameters as well as their current matching will be shown and compared in detail. An overview of all a-Si:H/µc-Si:H/µc-Si:H triple junction cells deposited and their photovoltaic parameters can be found in the appendix (Table A1 and Figure A1). Table 4.1 lists the sub cell thicknesses and PV parameters obtained for three different cells A, B and C as well as the reference cell "Ref." deposited previously (data taken from reference [34]). The cells A-C were chosen for comparison, since they show high short circuit current densities and varied cell thicknesses (lowest (A) – intermediate (B) – highest (C)). Additionally, Figure 4.3 shows the corresponding current density-voltage curves of the listed cells. The

reference sample[34] represents the starting point for the thickness variation investigated in the present work (2740 nm). Sample A (2740 nm) was deposited prior to the cell thickness variation according to the recipe reported in the reference and was used to reproduce the values reported for the reference cell.[34] Sample A and the reference cell show slightly different values obtained for all parameters measured except for the current density at the maximum power point.

Table 4.1: Overview of the layer thicknesses and PV parameters (η_{PV}, FF, V_{OC}, J_{SC}, V_{MPP}, J_{MPP}) for the a-Si:H/µc-Si:H/µc-Si:H cells.

Cell	top [nm]	middle [nm]	bottom [nm]	total [nm]	η_{PV} [%]	FF [%]	V_{OC} [V]	J_{SC} [mA/cm²]	V_{MPP} [V]	J_{MPP} [mA/cm²]
Ref. [34]	140	1000	1600	2740	10.5	68.6	1.913	8.0	1.570	6.7
A	140	1000	1600	2740	10.2	68.7	1.890	7.9	1.535	6.7
B	140	1300	2100	3540	11.3	72.2	1.911	8.2	1.570	7.2
C	140	1900	2500	4540	11.9	74.6	1.915	8.4	1.595	7.5

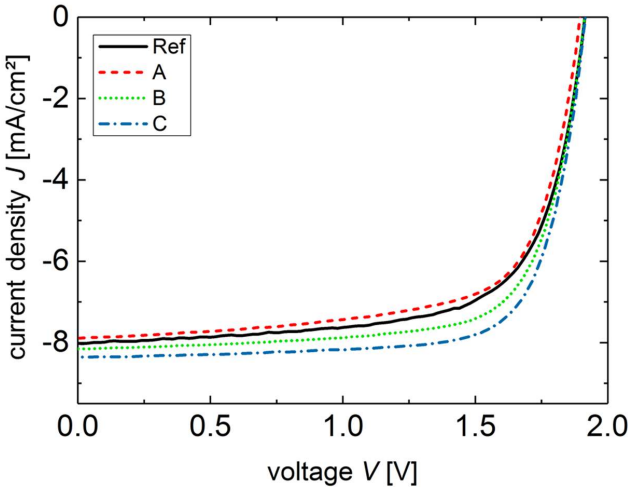

Figure 4.3: Current density-voltage curves of the a-Si:H/µc-Si:H/µc-Si:H triple junction solar cells corresponding to the cells A-C in Table 4.1 with "Ref" as reference cell[34].

Comparing sample A and the reference values[34] to the samples B and C, one can see that the thickness increase of approximately 1800 nm (A → C) leads to an increased conversion efficiency (from 10.2 % (A) to 11.9 % (C)), fill factor (68.7 % → 74.6 %) and current densities (J_{SC}: 7.9 mA/cm² to 8.4 mA/cm² and J_{MPP}: 6.7 → 7.5 mA/cm²), while the open circuit voltage is nearly constant (~1.913 V). Due to the increase in fill factor for sample C, the voltage at the maximum power point V_{MPP} shows also an increase up to 1.595 V compared to the previous samples (V_{MPP} = 1.570 V).

Figure 4.4 shows the external quantum efficiency data for the cells listed in Table 4.1. The data for the reference cell is taken from the previous PhD thesis.[34] The individual sub cell current densities calculated from the EQE measurements are indicated (for further information on external quantum efficiencies see also (4.2.2)).

The top cells show sub cell photocurrent densities in the range of 7.7 mA/cm² ("Ref") to 8.8 mA/cm² (B) and for the middle sub cells photocurrent densities from 8.0 mA/cm² (A) to 9.3 mA/cm² (C) were measured. The bottom sub cell photocurrent densities range from 8.3 mA/cm² (C) to 8.7 mA/cm² (B). Overall, the measured lowest sub cell photocurrent densities are in good agreement with the short circuit current densities determined in the JV measurements. In the following, the obtained results for the a-Si:H/µc-Si:H/µc-Si:H triple junction

solar cells with varied thickness are discussed regarding the current increase, photovoltage and current matching with respect to the variation.

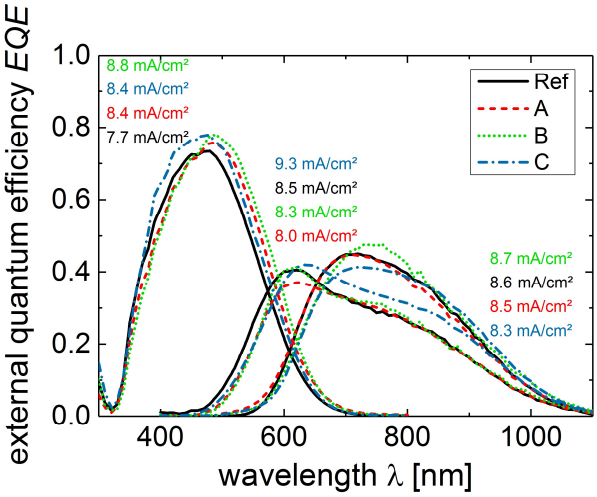

Figure 4.4: External quantum efficiency measurements of the a-Si:H/µc-Si:H/µc-Si:H samples A-C plus the reference data[34]. The calculated sub cell photocurrent densities J_{QE} are indicated and placed near the respective measurements.

5.3 Discussion of the results obtained for a-Si:H/µc-Si:H/µc-Si:H triple junction solar cells

Figure 4.2 shows as highest amount of the total sum of sub cell current densities a value of 26 mA/cm² (cell C). In the case of perfect current matching between the sub cells, the sum of sub cell current densities is equally divided between the three sub cells, as mentioned before. Dividing the highest sum of sub cell current densities obtained (26 mA/cm²) equally among the three sub cells ideally results in a short circuit current density of 8.7 mA/cm². However, the corresponding short circuit current density measured is 8.4 mA/cm². Therefore, the current matching is not ideal, losing 0.3 mA/cm² due to the matching, which will be further discussed in the external quantum efficiency data.

The current density-voltage curves shown in Figure 4.3 for the reference cell[34] and three deposited cells (A-C) and the corresponding values for the photovoltaic parameters listed in Table 4.1 show that the increase in cell thickness leads to an increase of all PV parameters except for the open circuit voltage, which remains constant. Therefore, the output voltage was not drastically reduced while the current density was increased. The differences between the reference cell and the equally deposited cell A can be due to slight changes in the deposition rate, differently enhanced back reflection or differently deposited, treated front contacts. Additionally, systematic errors within the measurements can lead to the slight differences measured for the reference cell and cell A. The output voltage (~1.913 V) should be sufficient for light induced water splitting employing highly active catalysts (introduced in detail in chapter (6)) as a calculation of the water splitting potential suggests (see section (5.4)).

The external quantum efficiency data and the sub cell current densities for the top cells of the investigated solar cells (cell Ref. + cells A-C) show different values, although the top cell thickness has not been varied in the experiment. Different reasons, such as variations in deposition rate, back reflector, front contact or the measurement error bars, are potentially causing the differences observed. The sub cell current densities obtained for the middle cell show a trend depending on the cell thickness, if the reference cell is not taken into account. The highest sub cell current density is generated by the thickest middle cell of cell C with 9.3 mA/cm², while the lowest sub cell current density is yielded by the thinnest middle cell of cell A (8.0 mA/cm²). Regarding the bottom sub cell current density, cell B delivers the highest value obtained and although it is not the thickest bottom cell. This can be due to the influence of the middle cell onto the light absorption in the

bottom cell. For thick middle cells (cell C), less light reaches the bottom sub cell, resulting in a low bottom sub cell current (8.3 mA/cm²). In the case of cell B, the middle cell is not as thick as compared to cell C and more light reaches the bottom sub cell, resulting in a current density of 8.7 mA/cm². This case exemplarily shows the tradeoff between middle and bottom sub cell thickness in order to ensure good current matching between all sub cells in a triple junction cell.

As discussed before, the external quantum efficiency data for cell C confirm the current mismatch that was supposed after evaluating the relation between sum of sub cell current densities and short circuit current density for varied cell thicknesses (Figure 4.2). Thus, the total sum of sub cell current densities was improved due to the cell thickness variation, but the current matching between the sub cells still leaves room for further amendments. The potential of a-Si:H/µc-Si:H/µc-Si:H triple junction solar cells employed in PV-EC devices is investigated further in the following section.

5.4 PV-EC device calculation using a-Si:H/µc-Si:H/µc-Si:H triple junction solar cells

In the following section, the potential of a-Si:H/µc-Si:H/µc-Si:H triple junction solar cells employed in PV-EC devices will be investigated. Therefore, the current density-voltage curve of the reference cell (Ref. cell[34]) and cell C, which showed the best performance (see section (5.2)), are combined with current density-voltages curves of different catalyst systems according to the equivalent series connection model described in chapter (4.5).[124,125,149] As discussed before, the focus of the solar cell thickness variation was on the increase of the photocurrent density rather than the output voltage, since for the use of highly efficient catalysts the output voltage should be sufficient. The catalyst system used in the following are (i) platinum and iridium oxide as noble metal reference system and the earth-abundant systems (ii) cobalt-iron layered double hydroxide (Co-Fe LDH) and nickel molybdenum nitride ($Ni_XMo_YN_Z$) as well as (iii) nickel-iron oxide ($NiFeO_X$) and a nickel molybdenum alloy (NiMo). The earth-abundant catalyst systems, which are highly active in alkaline media, are further discussed and presented in chapter (6). The electrolyte used for all investigated systems in the calculation is 1 M potassium hydroxide solution. Figure 4.5 shows the resulting current density-voltage curves for the PV-EC devices employing a-Si:H/µc-Si:H/µc-Si:H triple junction solar cell C (Table 4.1 in section 5.2) as well as the reference cell combined with the different catalyst systems ((i)-(iii)). The operating point for unbiased water splitting reaction is indicated at 0 V.

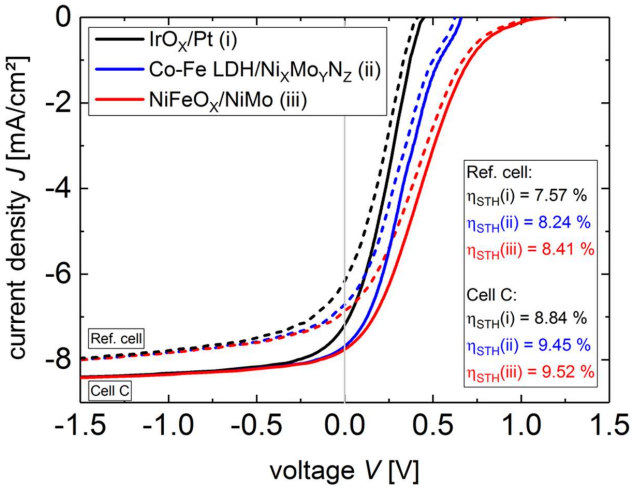

Figure 4.5: Calculated current density-voltage curves for PV-EC devices employing a-Si:H/µc-Si:H/µc-Si:H triple junction cell C (Table 4.1 in section 5.2) or the reference cell combined with different catalyst systems. The respective solar-to-hydrogen efficiencies η_{STH} are indicated for the different solar cells and catalyst systems.

The calculation show the high potential of a-Si:H/µc-Si:H/µc-Si:H triple junction solar cells for the application in water splitting. Especially, if highly active earth-abundant catalyst systems ((ii), (iii)) are used, the overpotentials are sufficiently low (below 400 mV, see chapter (6)), such that the solar-to-hydrogen efficiencies calculated are approximately 9.5 % for cell C. The solar-to-hydrogen efficiency calculated for the use of a noble metal system (i) accounts for 8.8 % (cell C). The lower solar-to-hydrogen efficiency is due to the lower activity of this catalyst system in alkaline media, while the earth-abundant systems are specifically developed for the use in alkaline conditions. This circumstance will be discussed in detail in chapter (6). By comparing the PV-EC devices based on the two different solar cells (C and Ref.), the effect of improved solar cell performance due to the thickness variation can be seen. Cell C based PV-EC devices yield solar-to-hydrogen efficiencies, which are increased by at least 1.1 % compared to the reference cell devices. Further improvement can possibly be made by using an antireflection foil on top of the solar cell as it was applied for the measurement of the a-Si:H/a-Si:H/µc-Si:H triple junction solar cell combined with platinum and ruthenium oxide in alkaline media, which yielded a solar-to-hydrogen efficiency of 9.5 %.[24]

5.5 Summary

The investigation of the a-Si:H/µc-Si:H/µc-Si:H triple junction cells was pursued further to increase the current density by varying the cell thickness without decreasing the output voltage, therefore, the cell thickness was increased by 1800 nm compared to the initial reference cell[34]. The increase in cell thickness resulted in an increase in the sum of the sub cell current densities by +1.1 mA/cm² and an increase in short circuit current density by +0.5 mA/cm². The best a-Si:H/µc-Si:H/µc-Si:H cell deposited in the present work shows a conversion efficiency of 11.9 %, a fill factor of 74.6 %, an open circuit voltage of 1.915 V and a voltage at the maximum power point of 1.595 V, a short circuit current density of 8.4 mA/cm² and a current density at the maximum power point of 7.5 mA/cm². Overall, the variation in thickness successfully increased the current densities, however, the current matching between the sub cells current still has room for improvement. Assuming an ideal current matching for the cell with the highest sum of sub cell currents obtained, would lead to a short circuit current density of 8.7 mA/cm² (measured 8.4 mA/cm²). The current mismatch between the sub cells was also proven in the external quantum efficiency measurements.

The results presented show that both types of triple junction cells, a-Si:H/a-Si:H/µc-Si:H as well as a-Si:H/µc-Si/µc-Si:H, can perform equally well in PV-EC devices, if the overpotential of the catalyst system does not exceed 400 mV, as it is the case for the earth-abundant catalyst systems used in the present work (see also chapter (6)). The calculated solar-to-hydrogen efficiencies for a device based on a-Si:H/µc-Si:H/µc-Si:H triple junction solar cells and earth-abundant catalysts account for 9.5 % in alkaline media, which is similar to the reported solar-to-hydrogen efficiency for a PV-EC device based on a-Si:H/a-Si:H/µc-Si:H triple junction solar cells combined with a noble metal catalyst system in alkaline media.[24]

Overall, the current density for the a-Si:H/µc-Si:H/µc-Si:H triple junction cells investigated in the present work is higher compared to previous reports[34], but does not significantly exceed the current density generated by the a-Si:H/a-Si:H/µc-Si:H triple junction cells[34]. Possible improvements can be made by further increasing the cell thickness or by the application of an antireflection foil on top of the solar cell as it was reported in the reference.[34]

6 Setup of the electrochemical measurement site and development of a fitting PV-EC device

This chapter outlines the development of the advanced photoelectrochemical workplace. Additionally, the design of a photovoltaic-biased electrosynthetic (PV-EC) device for sizes frequently used for sample evaluation is presented in detail. Frequently used sample sizes in the present work are between 0.5 cm² up to 2.25 cm², while increased sample sizes refer to areas above 50 cm². The focus of the designed PV-EC device is flexibility towards exchanging the photovoltaic cells, replacing the electrodes allowing to vary their material, the operation in two- and three-electrode configuration and measurements in stationary or flow state. Additionally, implementing a membrane has to be possible in order to detect and quantify the produced hydrogen gas evolved during the water splitting reaction. Firstly, an overview of the previously used PV-EC devices[34,78,87] and their limitations regarding the advanced setup will be given, followed by the construction process of the new PV-EC device, concluding with the results regarding the newly designed PV-EC device facing the previous limitation problems. The construction of the PV-EC device for frequently used sample sizes was followed by the development of a PV-EC device for increased sample sizes, which will be discussed in detail in the next chapter (6).

6.1 Development of the advanced electrochemical workplace

An advanced electrochemical workplace should be as flexible as possible regarding the measurement conditions, for example in terms of sample exchange, stationary/flow state measurements or two-/three-electrode configuration. Additionally, it should allow to quantify and qualify the gases evolved during the reaction. Measurements in flow state could improve the collection of the evolved gases in the device, which are collected as part of the electrolyte passage. Additionally, pumping the electrolyte could become important for the use of three-dimensional substrates as electrode materials. A schematic figure of the photoelectrochemical workplace is shown in Figure 5.1. In this setup, the PV-EC device (dark yellow element) consists of a photovoltaic cell plus hydrogen evolution reaction catalyst marked in red on the cathode side and an oxygen evolution reaction catalyst on the anode side (marked in purple). A silver silver chloride (Ag|AgCl) reference electrode can be used and implemented for a three-electrode measurement setup. Both half-cells can be separated by a membrane (blue interlayer) and electrolyte (catholyte and anolyte, respectively) can be pumped through the half-cells by a peristaltic pump with two individual pumping channels. The electrolytes and the evolved gases are collected in two different reservoirs. The cathode and anode as well as the reference electrode are electrically connected to the potentiostat, which is controlled by a computer. All measurements are performed with a Gamry Reference 600 potentiostat using the associated software. Additionally, an AM 1.5G sun simulator (Oriel LCS-100 solar simulator, model 94011A, 1000 W/m²) is included in the setup in order to perform the photoelectrochemical measurements under simulated sun light. The evolved gases are separated due to the membrane, collected and quantified in an extrusion measurement. Therefore, the gas/electrolyte outlets are connected to the electrolyte reservoir and the headspace of these reservoirs is connected to a water column (1), which is attached to another water column (2) with an electrical water level indicator. The evolving gas pushes the water in column (1) into column (2). Hence, the water level in column (2) rises, which is detected by the water level indicator yielding a voltage depending on the water level. By using the following experimentally obtained calibration curve, the gas volume V_{gas} can be extracted from the voltage V:

$$V_{gas}\,[\mathrm{mL}] = \frac{V\,[\mathrm{V}]}{0.02884\,\left[\frac{\mathrm{V}}{\mathrm{mL}}\right]} \tag{43}$$

The here described measurement setup addresses some points for the photoelectrochemical device in order to be implemented:

1. Possible connection of a pump for measurements in the stationary or flow state.
2. Implementation of a membrane for gas separation, collection and quantification.

3. Exchange of the working and counter electrodes, two-/three-electrode measurements and implementation of a PV cell as current and voltage source.

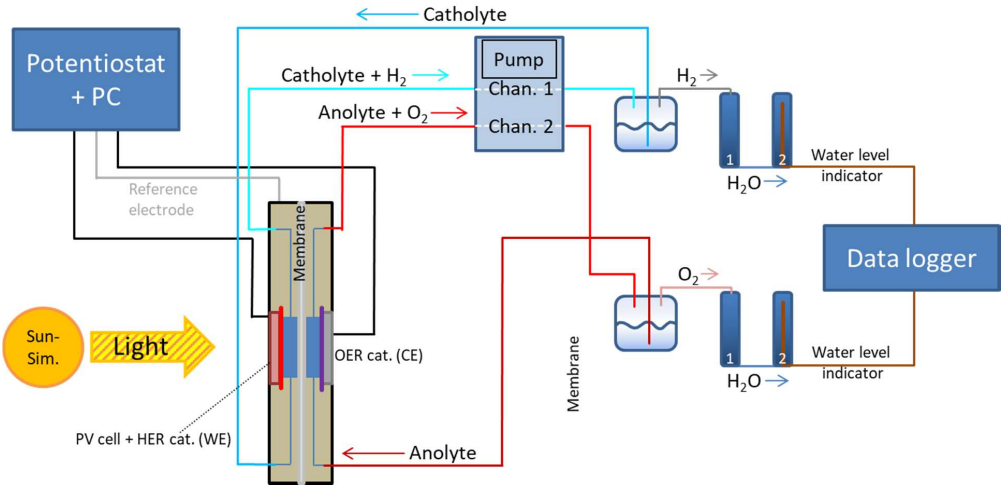

Figure 5.1: Schematic of the photoelectrochemical workplace setup for the PV-EC device with electrolyte flow in both half-cells and collection as well as quantification of the evolved gases.

6.2 PV-EC designs and devices

6.2.1 Previously used PV-EC devices

The Figure 5.2(a) and (b) show the PV-EC devices that have been previously used to investigate light induced water splitting employing multi-junction thin film silicon solar cells[34,78,87]. Both devices have limitations regarding the needs for the implementation in the advanced electrochemical workplace as discussed in detail in the following section. The PV-EC device depicted in Figure 5.2(a) shows an in-house built device consisting of a Teflon cell body with 30 mL electrolyte reservoir. It is described in detail in the previous PhD thesis by F. Urbain (see chapter 4.2.1 in reference [34]). A reference electrode can be placed near the working electrode realizing two- and three-electrode measurements. The working and counter electrode can be easily replaced and the sizes applicable for the working electrode are between 1x1 cm² up to 2.5x2.5 cm². The integration of a PV cell in the device is possible. Therefore, concerning the above named boundary conditions for the implementation in the photoelectrochemical setup, the third point is completely fulfilled. However, the device can only be used in the stationary state and additionally the gases evolving during the reaction can neither be separated nor collected, leaving the first and second condition unfulfilled. Figure 5.2(b) shows a commercially available PV-EC device setup built by Zahner (PECC-2, ZAHNER-elektrik GmbH & Co. KG), which was used for the electrochemical measurements performed in the references[78,87]. Regarding the first point (stationary and flow measurements), the PV-EC device has a gas/electrolyte in- and outlet enabling the connection to a pump. Therefore, stationary and flow measurements are possible. The second point however is not fully achieved, since the gases can be collected but not separated due to the absence of a membrane. In the Zahner device, the working electrode can be exchanged easily and the reference electrode is placed near the working electrode. The integration of a PV cell in the device is possible. However, the counter electrode is not exchangeable and a platinum wire has to be used for all reactions, leading to a high overpotential towards the oxygen evolution reaction (OER).[102] Hence, the third point for the application in the photoelectrochemical workplace, the flexible exchange of all electrodes, is not completely fulfilled and none of the existing devices can be implemented in the advanced electrochemical workplace.

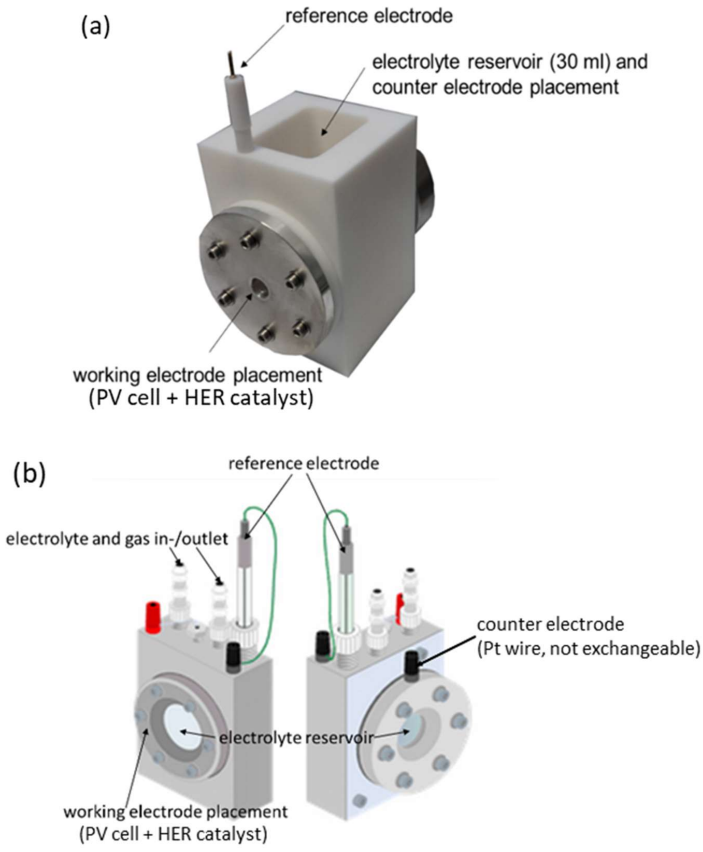

Figure 5.2: (a) In-house built PV-EC device with replaceable working and counter electrode, reference electrode close to the working electrode and 30 mL electrolyte reservoir. No electrolyte flow and gas collection/separation possible, taken from reference [34]. (b) Commercially available PV-EC device built by Zahner (PECC-2, ZAHNER-elektrik GmbH & Co. KG) with replaceable working electrode, reference electrode close to the working electrode. Gas collection and electrolyte flow are possible, but the counter electrode cannot be replaced and the gases cannot be separated.

6.2.2 Newly designed PV-EC device

The here described device was developed in cooperation with the Institute of Complex Systems -Technische und Administrative Infrastruktur Konstruktion - (ICS-TAK) department of the Forschungszentrum Jülich GmbH.

Figure 5.3(a) shows an image of the constructed PV-EC device. The cell body (green), the gas/electrolyte in- and outlets (orange) and the reference electrode enclosure (yellow + purple) are made of polyether ether ketone (PEEK). The sample holder is shown in grey and cased by a metal sample holder retainer with screw threads (blue). A pump can be connected to the gas/electrolyte in- and outlets and electrolyte can be pumped through the cell. Additionally, the in- and outlets can be replaced by a cover in order to use the PV-EC device in stationary state. Leak tightness is ensured by O-ring seals (pink). Figure 5.3(b) shows a cross sectional schematic through one half-cell of the PV-EC device. The electrode (sample), which is shown in light yellow, is pressed against an O-ring (pink) by the metal sample retainer (blue). The sample holder (grey) itself is pressed against an O-ring (pink) by the metal sample holder retainer (blue). In this configuration, it is possible to pump electrolyte through the half-cell. The channels to pump electrolyte can be seen in Figure 5.3(b).

The PV-EC device consists of two almost identical parts allowing separating the two half-cells by the membrane in between (see Figure 5.3(a)). If no membrane is used, leak tightness is ensured by an O-ring seal (pink). For the use of a membrane, flat seal rings have to be used with the membrane inserted in between. By implementing the membrane the evolving gases can be collected separately and quantified using the water extrusion measurement, as described in section (6.1).

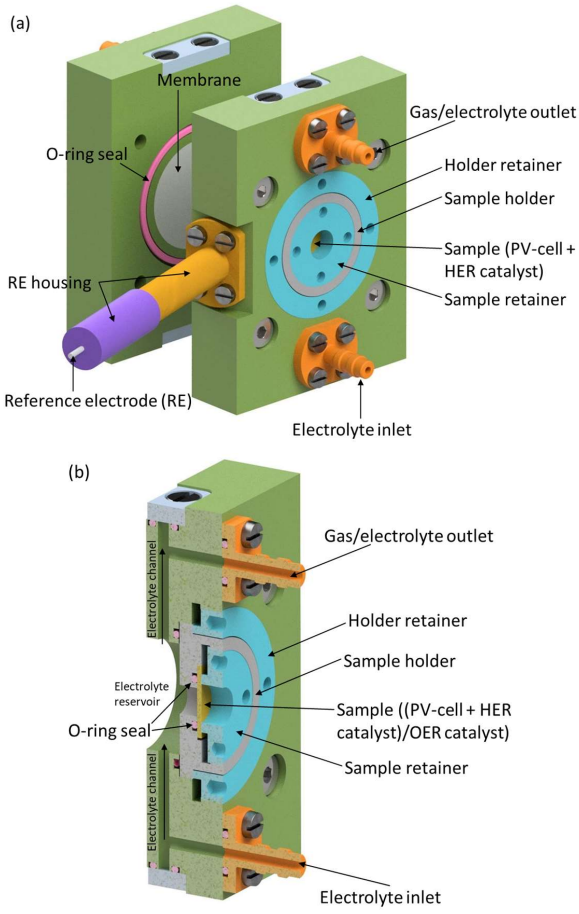

Figure 5.3: (a) Constructed PV-EC device made of polyether ether ketone (PEEK). The gas/electrolyte in- and outlets can be replaced by a cover, allowing electrolyte flow as well as stationary state operation. The reference electrode housing is shown in yellow and purple and can also be replaced by a cover for two- or three-electrode measurements. The two parts allow the implementation of a membrane in order to separate the half-cell reactions. The sample holder is shown in grey and cased by a metal sample holder retainer with screw threads (blue). (b) Schematic cross section through the PV-EC device. The electrode (sample) is shown in light yellow; the sample holder is shown in grey. The two metal retainers are depicted in blue. O-rings are used as sealing and shown in pink. Pumping through the electrolyte channels is possible.

Concerning the flexibility in exchanging all electrodes, switching between two- and three-electrode configuration as well as the implementation of a PV cell into the device, an electrode holder was designed for the working and the counter electrode side, which can be removed separately (shown in grey in Figure 5.3). The electrode in the holder is retained by a metal ring with screw threads (blue in Figure 5.3). Sample sizes for working and counter electrode in the range of 1x1 cm^2 to 1.5x1.5 cm^2, which are frequently used for evaluation and characterization in the present work, fit into the holder. A metal sample holder retainer with screw threads (blue in Figure 5.3) presses the sample against an O-ring seal and provides electrical contact to

the sample. It is also possible to measure porous, shapeable three-dimensional electrode structures using the sample holder due to the closed design and the pressure point between the metal retainer and the O-ring seal. The area in contact with the electrolyte is equal for both sides (0.5 cm²). The sample (PV cell + catalyst) can be illuminated through the aperture of the sample retainer of 0.5 cm² size. Figure 5.4 shows a photograph of the back side of the PV-EC device with counter electrode holder and holder retainer implemented in the device. The working electrode holder and its retainer as well as the sample retainer are placed in front of the device. The sample retainer on the right side is screwed into the PEEK sample holder to hold the sample in place and to ensure the electrical contact to the sample. The sample holder is retained in the device using the metal sample holder retainer ring on the left side, as shown for the counter electrode holder in the device. Additionally, a reference electrode can be placed near the working electrode for three-electrode measurements as can be seen in Figure 5.3 (housing in purple and yellow). For measurements in the two-electrode configuration, the housing is removed and replaced by a cover as shown in Figure 5.4.

Overall, the device meets the demands named in section (6.1) for the application in the photoelectrochemical workplace. In the following, the particular points were tested separately in order to investigate whether the device can be implemented practically.

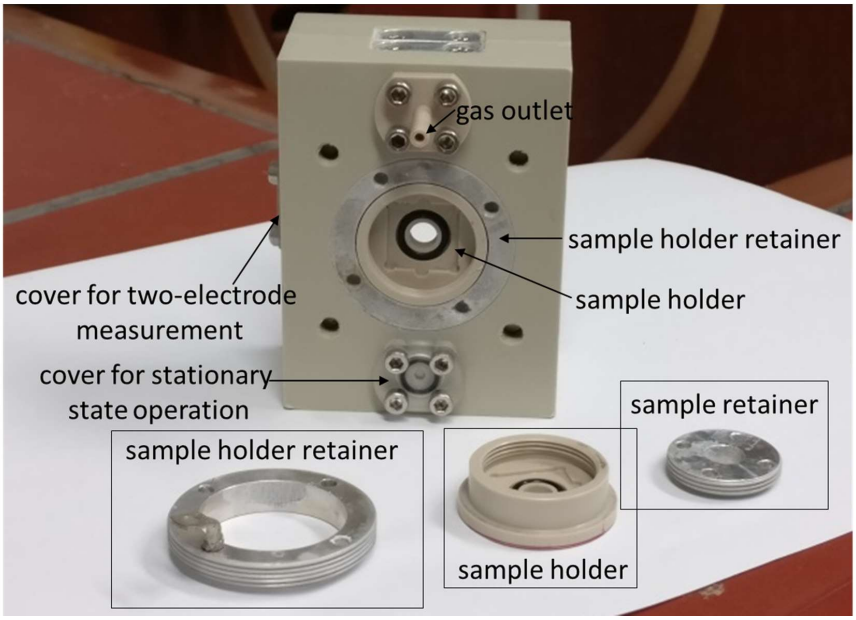

Figure 5.4: Photograph of the PV-EC device in the two-electrode, stationary state configuration. The counter electrode side is shown with an empty counter electrode (sample) holder. The working electrode (sample) holder is placed in front of the device with the sample holder retainer on the left and the sample retainer on the right side.

6.2.3 Test of the constructed device

1. Stationary and flow state measurements

Electrolyte flow through the device could improve the collection of gases independently of the substrate structure. Additionally, measurements with flowing electrolyte could become important if three-dimensional substrates were to be used as electrode materials (see section (6)). To enable electrolyte flow through the system, a peristaltic pump (provided by behr Labor-Technik GmbH) with a two channel pumping head was used. The half-cells, separated by a membrane, were connected to one electrolyte compartment and one pumping channel each (see Figure 5.1). The tubing was set up using polyvinylchloride tubes. Tubing connections were made using Teflon coated tube connectors with the respective diameters. Planar nickel sheets

were used as electrodes in the cyclic voltammetry measurements. The electrolyte used was 1 M potassium hydroxide solution.

Figure 5.5 shows the current-voltage curves of the working electrode for the cyclic voltammetry measurements with different pumping speeds in the range of 0 rpm to 50 rpm (three-electrode configuration). For no pumping (0 rpm, black solid curve) and for a pumping speed of 30 rpm (blue dotted curve), the cyclic voltammetry measurement was repeated twice. Additional data on the current-voltage curves of the device in two-electrode configuration for pumping speeds from 20-60 rpm can be found in the appendix (see Figure A2).

Figure 5.5 shows that generally current-voltage characterization measurements in flow state are possible with the constructed device. Also, no electrolyte leaks could be observed during the experiment. The repeated current density measurements however show differences between the for- and backward scan as well as between the different cycles. This change in electrode performance could be due to degradation and cannot clearly be separated from the possible influence of the pump and pumping speed in this configuration. The obtained results lead to the assumption that one has to take care when measuring with and without pump and using different pumping speeds, since the reasons for the changes observed in the measurement could not clearly be distinguished. The measurements of different catalysts and PV-EC devices were conducted without pumping the electrolyte in order to investigate possible electrode degradation.

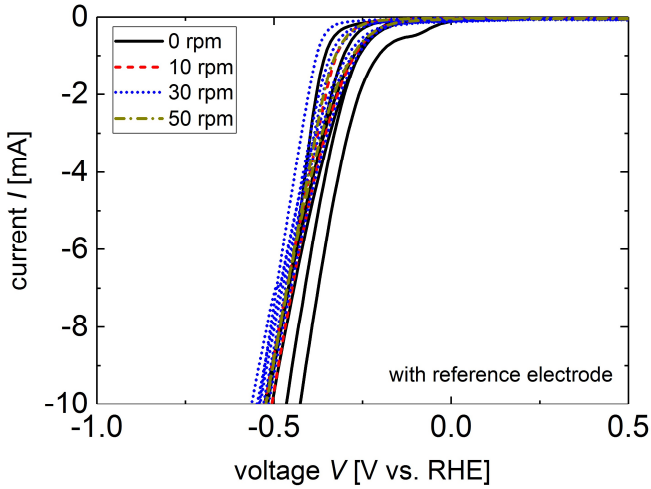

Figure 5.5: Cyclic voltammetry measurements applying different pumping speeds. For no pumping (0 rpm, black solid curve) and for a pumping speed of 30 rpm (blue dotted curve), the cyclic voltammetry measurement was repeated twice. Nickel sheets were used as electrodes on both sides in 1 M KOH in a three-electrode setup with an Ag|AgCl reference electrode.

2. Separation and collection of the evolved gases

In order to separate and quantify the evolving gases hydrogen and oxygen in alkaline media, an anion exchange membrane (fumasep FAA-3PK-130 supplied by FuMa-Tech GmbH) was used. The flat seal rings, which have to be used for the implementation of the membrane, were made of chlorosulfonated polyethylene (CSM, provided by Resogoo GmbH & Co. KG). The current-voltage curves of nickel sheets employed on both electrode sides in 1 M potassium hydroxide solution were measured in cyclic voltammetry measurements (two cycles per membrane configuration) in two-electrode configuration. The two-electrode configuration was used to determine the influence of the membrane onto the entire device performance. The following configurations were applied (1) without membrane, (2) with an unconditioned membrane and (3) with a conditioned membrane. All membranes used in the present work were taken from the same batch. The preconditioning was recommended by the supplier in order to remove additives from the membrane, which could possibly have an

influence on the device performance. Membrane (3) was conditioned for 24 h in 0.5 M sodium chloride (NaCl) solution at 25°C. Figure 5.6 shows the current-voltage curves measured for the different setups (1)-(3).

Figure 5.6 shows higher values of currents at voltages below -1.9 V for the device without membrane compared to the devices employing a membrane. This difference is due to the additional resistance added to the device by using a membrane for gas separation, although membranes should provide high electrical conductivity (see also Figure 5.7). Comparing the unconditioned and conditioned membrane, the current-voltage curves are nearly similar for the hydrogen evolution reaction taking place (V < -1.8 V), since the slight difference observed is within the error range of the measurement. Thus, possible additives in the membrane do not disturb the water splitting reaction and the membranes can be used in the PV-EC device without extra preconditioning.

To investigate the performance of the device including a membrane over time, the potential *E* of the device employing the membrane was monitored for 1 h. Possible changes in the potential could be due to leaks or cracks within the membrane. Additionally, the potential of the system without membrane monitored for 900 s is shown for comparison (see Figure 5.7). The difference of the potentials between the devices with and without membrane is mainly due to the additional resistance added by using the membrane, as was also observed in Figure 5.6 (compare black curve to green and red curve). The additional resistor can be determined by means of electrical impedance spectroscopy and accounts for approximately 8 Ω in the case of the systems shown in Figure 5.7. Both potentials are stable over the investigated times of 3600 s and 900 s and no drastic change in potential is observed. The zigzag curve, which is measured for all systems, is due to the detachment of gas bubbles from the electrode surfaces. Overall, membranes can be successfully implemented into the PV-EC device. In the following step, it was investigated, whether the membrane leads to a complete gas separation, such that the evolving gas can be completely collected and quantified.

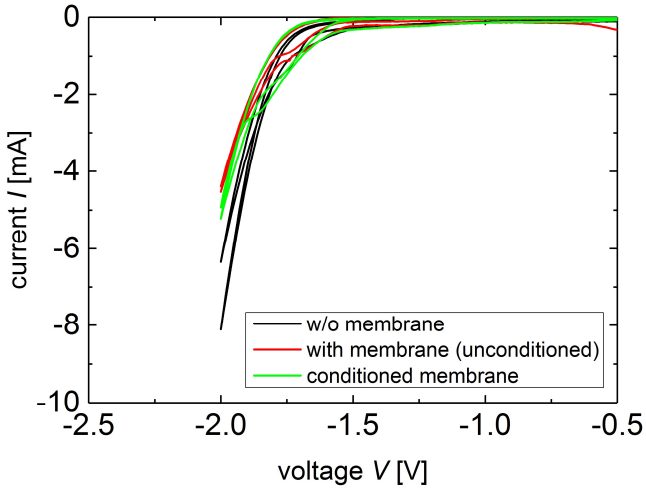

Figure 5.6: Current-voltage curves of PV-EC devices with nickel sheets on both electrode sides in 1 M KOH for the case (1) without membrane, (2) with an unconditioned membrane and (3) with a conditioned membrane (24 h in 0.5 M NaCl solution at 25 °C).

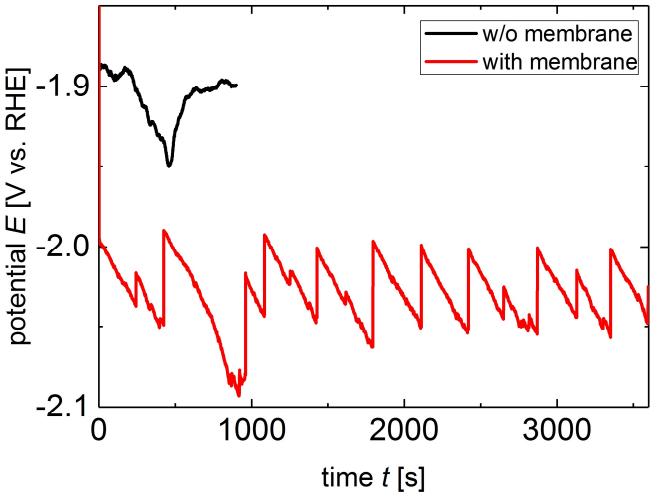

Figure 5.7: Potential over time measured for PV-EC devices employing nickel sheets as electrode in 1 M KOH solution with or without membrane. The device with membrane was monitored for 3600 s and the device without membrane was measured for 900 s. The zigzag shape of the curves is due to the detachment of gas bubbles from the electrode surface.

Therefore, hydrogen evolved during the reaction was collected and compared to the theoretically expected hydrogen volume, as described as definition of the Faradaic efficiency in chapter (4.6). The device employing a membrane was directly connected to the extrusion measurement (see also section (6.1)). A platinum electrode for the hydrogen evolution reaction and a nickel electrode for the oxygen evolution reaction side were used in 1 M potassium hydroxide solution in two-electrode configuration. A current density of 10 mA/cm² was applied for 17000 s in a chronopotentiometric measurement. Figure 5.8 shows the theoretically calculated (red line) hydrogen volume according to the ideal gas law and Faraday's law (41) and the measured hydrogen volume extracted from the extrusion measurement as described in section (6.1). The figure depicts the measured time for the collection of 10 mL of hydrogen.

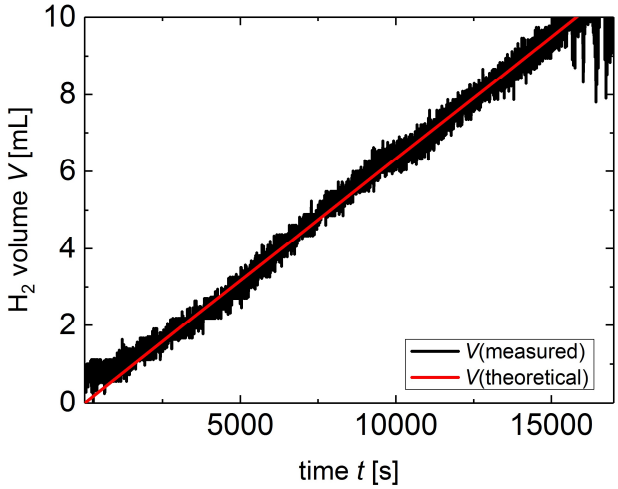

Figure 5.8: Hydrogen volume over time (1) theoretically calculated (red line) and (2) extracted from the extrusion measurement for a PV-EC device consisting of platinum as HER electrode and nickel as OER electrode in 1 M KOH.

The similar slope obtained for both curves (measured and calculated) indicates that hydrogen generated during the water electrolysis is fully collected and quantified using the extrusion measurement. The Faradaic

efficiency η_F for the device in this configuration is equal to unity. The device including a membrane is proven to be gas tight and the gases can fully be separated.

3. Flexibility regarding electrodes and substrate structures

In this section, the flexibility of the constructed PV-EC device towards different electrode material structures and the implementation of a PV cell in the device will be shown. If further improvements of electrodes for light induced water splitting are discussed, one point that is often addressed is the three dimensional structure of the electrodes.[37,109,151] Porous, three-dimensional electrodes provide a higher surface area, leading to improved catalytic behavior. In order to test whether the constructed device can also be used to measure porous, three-dimensional electrodes, two different nickel materials were used as electrodes in 1 M KOH: (1) planar sheets and (2) three-dimensional foam. The nickel foam (1.4 mm thickness, RECEMAT BV, Ni-5763) exhibits a surface-to-volume ratio of 6900 m²/m³. Employing and measuring three-dimensional substrates as electrode material in the constructed device should be possible due to the closed holder structure and the pressure point between the sample retainer and the O-ring seal. For the implementation, the foam has to be cut to a size of ~ 0.55 cm². This size is required such that the foam can be pressed against the O-ring seal by the sample retainer. Thus, only ductile foams can be measured using the device. Additional conductive metal sheets (e.g. nickel sheets) have to be used in order to ensure a good electrical contact to the foam electrode and to prevent leaking through the porous structure. The devices were measured in two-electrode configuration in stationary state.

Figure 5.9 shows the current-voltage curves (repeated CV measurements) of the PV-EC devices employing nickel sheets as electrodes, respectively nickel foam. The measurement shows that both materials can successfully be implemented as electrode material into the constructed device, showing its flexibility towards different structures. Additionally, the effect of an enhanced surface area is visible, since the device using nickel foam electrodes shows a higher current (red dotted curves for repeated CV measurements) for the hydrogen evolution reaction compared to the device with nickel sheet (black solid curves for repeated CV measurements) electrodes (V_{HER} < -1.5 V). Both electrodes are made of the same material (nickel), such that the main difference is the enhanced surface area for the porous foam structure leading to the enhanced current. Please note that the actual surface areas of the nickel foam electrodes are not known. The geometrical surface areas in contact with the electrolyte are in all cases 0.5 cm².

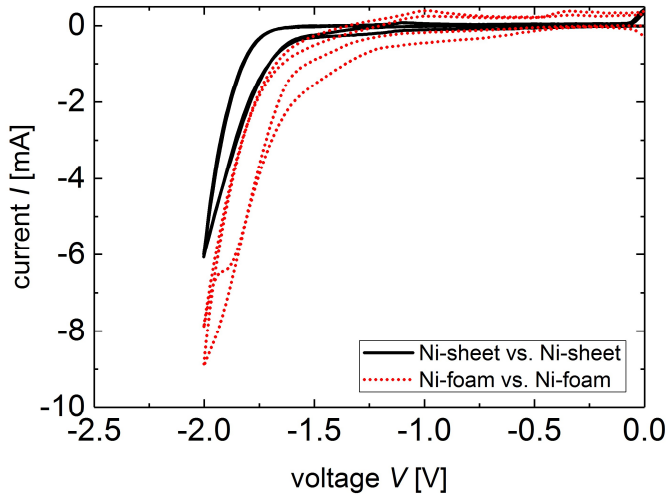

Figure 5.9: Current-voltage curves of PV-EC devices employing different electrode structures (1) planar nickel sheets and (2) three-dimensional nickel foam in 1 M KOH. The geometrical area of all electrodes in contact with the electrolyte is 0.5 cm², which is not equal to the actual surface area in the case of the nickel foam electrodes.

Implementation of a photovoltaic (PV) cell into the PV-EC device

The most important aspect for PV-EC devices is the possibility to include PV cells combined with electrodes and measure the water splitting performance of the entire PV-EC device. In the following section, it was investigated whether a PV cell can be implemented into the device and if the current density-voltage behavior can be characterized. Therefore, an a-Si:H/a-Si:H/µc-Si:H triple junction solar cell of 1.5x1.5 cm² size was combined with platinum as HER catalyst and nickel as OER electrode. Electrical connection between the solar cell's front contact and the sample retainer was ensured by silver paste.

The PV-EC device was filled with 1 M KOH serving as electrolyte and a nickel sheet was used as counter electrode (two-electrode setup). The current density-voltage curve, which can be seen in Figure 5.10, shows the successful measurement of the PV-EC device (shown in Figure 5.3 and Figure 5.4). The operating point of the PV-EC device for unbiased light induced water splitting at zero volts leads to an operating current of ~ 4.4 mA/cm². The measurement shows that PV cells can successfully be used in the constructed PV-EC device and the corresponding current density-voltage curves can be obtained using this setup.

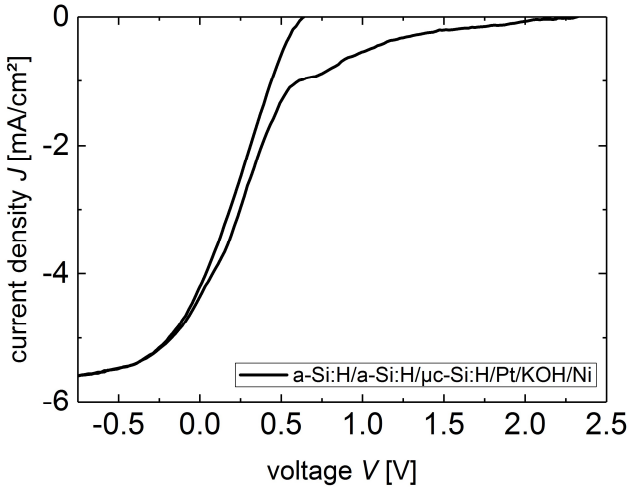

Figure 5.10: Current density-voltage characteristics of the a-Si:H/a-Si:H/µc-Si:H triple junction solar cell based PV-EC device employing platinum (HER) and nickel (OER) in 1 M KOH (two-electrode setup) under simulated solar illumination.

6.3 Summary

Photoelectrochemical devices have to fulfill some demands in order to be used in the advanced photoelectrochemical workplace setup developed in the present work. The previously used PV-EC devices presented in section (6.2.1), were not able to be integrated under the boundary conditions given in the developed setup. Therefore, a new PV-EC device (Figure 5.3 and Figure 5.4) was constructed in order to overcome those limitations and to completely address the points set for the implementation into the advanced electrochemical workplace. In the newly constructed device, electrolyte can be pumped through the PV-EC device and stationary state as well as flow measurements can be performed. Additionally, the two half-cells can be separated by implementing a membrane in between to collect and quantify hydrogen and oxygen evolved during the reaction. The Faradaic efficiency was proven to be equal to unity, ensuring leak and gas tightness. Furthermore, both electrodes in the newly constructed device can easily be exchanged and different electrode morphologies can be used in the PV-EC device. Changing between two- and three-electrode measurements is quickly and easily realizable. Finally, multi-junction solar cells can be implemented in the device and the current-voltage characteristics for light induced water splitting processes can be measured using

the newly constructed device. Therefore, the newly constructed device (Figure 5.3 and Figure 5.4) fully meets the demands for the implementation into the advanced electrochemical workplace. As mentioned in the introduction, the device shown here enables the characterization of sample sizes up to 2.25 cm². The next step for further investigations of PV-EC devices is the upscaling of the device and sample sizes. Thus in the following, a PV-EC device of 100 cm² was designed and constructed, which shows a similar modularity towards the measurement and exchange of the individual parts.[35] The PV-EC device with increased size also allows electrolyte flow within the device, the collection of gases and the implementation of a membrane, as will be presented in the following chapter.

7 Scale-up of PV-EC device by a factor of 100

Practical water splitting device demonstrations are typically performed on device areas of ≤ 1 cm².[41] For a device area of 0.5 cm², the water splitting approach based on thin film silicon multi-junction cells combined with an alkaline electrolyser has been optimized to a very high degree yielding a solar-to-hydrogen efficiency of 9.5 %, which is close to the possible maximum performance value, as shown in chapter (1).[24,35] However, if such a device were to be used as stand-alone device for the efficient generation of hydrogen from sunlight, the area of the device has to be scaled up significantly. Device upscaling is considered to be a stepwise process during which the device and all of its parts are increased in areas, which is not straightforward. The basis for this process is provided by the devices with areas ≤ 1 cm²[41], which are well investigated. The future application targets devices of several square meters[152]. The present work offers a first intermediate "proof of concept" step in the upscaling process, in the frame of which the individual device parts of the PV-EC device are scaled up at least by a factor of 100. The challenges and limitations occurring during the process will be investigated and discussed in the following section for the individual parts and finally for the combined device.

PV-EC devices should provide a multi-functional contact, which offers good electrical and optical properties to make best use of the employed solar cell, as well as of good hydrogen evolution reaction catalyst activities for long-term stable electrochemical performance. In order to increase the degree of freedom for the optimization of upscaled PV-EC devices, the tasks of upscaling the solar cell and the catalysts can be decoupled such that the PV-EC device is modularly built. One possible way of decoupling the individual tasks is the use of sheet metal electrodes in the PV-EC devices. These electrodes offer good electrical properties combined with the solar cell and the optimized optical properties of the solar cell can be maintained. Additionally, the sheet metal electrodes can serve as substrate for catalyst deposition and offer long-term stability due to the thickness of 0.3 mm. The solar cell can effectively be protected against the corrosive electrolyte used in water splitting devices by employing sheet metal electrodes. The device and its properties will be shown and presented in section (7.1).

In section (7.2), the upscaling of photovoltaic cells used in the device will be discussed. One of the major challenges that has to be faced for upscaling the solar cell, is the current collection in the front contact due to the non-negligible sheet resistance of the front contact TCO layer, which results in substantial ohmic losses. Therefore, different front contact patterns are investigated for the use of thin film silicon multi-junction solar cells. If crystalline silicon solar cells were to be integrated into the PV-EC device, three solar cells have to be connected in series. In the present work, silicon heterojunction cells were combined into a module with shingled contacts such that the module can be integrated into the upscaled PV-EC device presented in section (7.1).

The last component to be upscaled is the catalyst system. In order to consider the cost-effectiveness of the PV-EC device for the hydrogen generation, mostly earth-abundant materials should be employed as catalysts. These materials should additionally provide a high catalytic activity in alkaline media and show stable long-term operation under day-night conditions. Finally, the catalyst systems should be easy to prepare. Different materials and their potential towards the water splitting reaction and the upscaling to increased sample areas are characterized and discussed in the sections (7.3), (7.4) and (7.5) of this chapter.

Finally, silicon based solar cells will be combined with earth-abundant catalysts in the upscaled PV-EC device and the full device will be characterized in detail. The focus here was specifically on solar-to-hydrogen efficiencies as well as long-term stabilities, see section (7.6).

7.1 PV-EC device upscaling

Parts of this section have been published in J. P. Becker, B. Turan, V. Smirnov, K. Welter, F. Urbain, J. Wolff, S. Haas, F. Finger, *J. Mater. Chem. A* **2017**, *5*, 4818–4826. The upscaled PV-EC device has similar properties compared to the device developed for samples of frequently used sizes presented in chapter (6.2.2). The device

is modularly built regarding the ease of substituting and measuring the individual device components (PV, EC, PV-EC). Photographs of the device are shown in Figure 6.1, while a schematic of the device is depicted in Figure 6.2. The device body consists of poly(methyl methacrylate) (PMMA) and has the size of 10 x 10 x 3 cm^3. The maximum size for the solar cell substrate is 10 x 10 cm^2, ideally employing as much active area as possible. For the solar cell upscaling process see the following section (7.2). As electrodes, two metal sheets are used as discussed in the introduction of this chapter, physically decoupling the solar cell and the electrode. The area of the two round metal sheets has the size of 50.3 cm^2. The sheet thickness of 0.3 mm ensures a long-term stable performance. A large versatility for the development and investigation of catalyst materials is given by the use of the metal sheet electrodes.

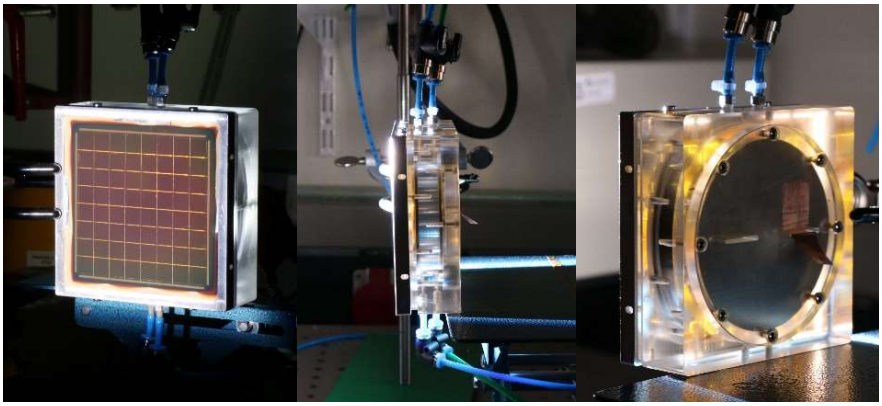

Figure 6.1: Photographs taken of the upscaled PV-EC device, showing the front, side and back view.

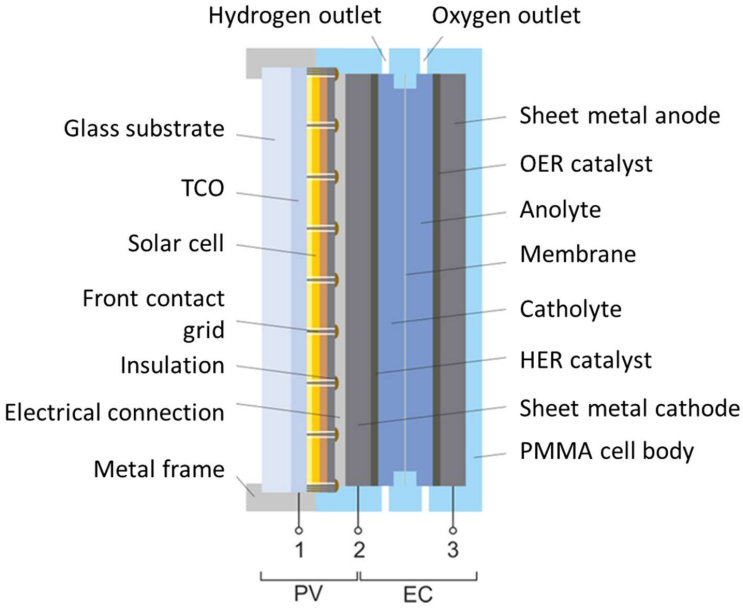

Figure 6.2: Schematic cross section of the upscaled, integrated PV-EC device. The device is modularly built in the sense that each component can be exchanged easily and quickly (e.g. solar cell, catalysts, membrane). The in- and outlets enable stationary state and flow measurements as well as gas collection and quantification. The contact design allows the measurement of the electronic properties of the individual parts (1+2: PV, 2+3: EC, 1+3: PV-EC).

The solar cell as well as the electrodes can be quickly exchanged, allowing to investigate a wide variety of catalysts deposited on metal sheet electrodes or solar cell absorbers. The electrical connection between the solar cell and the sheet metal electrode is established mechanically by pressing the solar cell against the electrode. The hole (front) contact of the solar cell is connected to the metal frame, which is connected to the counter electrode. All contacts (1-3) are designed in a way that each part (PV + EC) can be measured individually. Additionally, the distance between the sheet metal electrodes is kept as small as possible, ideally realizing a zero gap configuration.

Concerning the implementation of the upscaled PV-EC device into the advanced electrochemical workplace, the upscaled device also fulfills all points named in chapter (6.1). Figure 6.1 and Figure 6.2 show the gas/electrolyte in- and outlets, which enable the connection of a pump and thus stationary and flow measurements. The implementation of a membrane for gas separation and quantification is also achieved as Figure 6.3 shows. An anion exchange membrane was glued into an O-ring mount made of polyether ether ketone (PEEK).

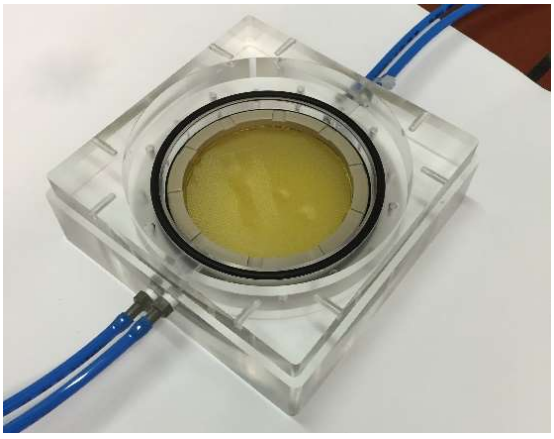

Figure 6.3: Upscaled PV-EC device without electrodes and PV cell, but with implemented anion exchange membrane using the O-ring mount made of PEEK.

The separation and quantification of the evolving gases using an anion exchange membrane was shown using the extrusion measurement setup described in chapter (6.1) (see Figure 6.4(a) and (b)). Figure 6.4(a) shows the hydrogen and oxygen gas volumes collected during an alkaline electrolysis (1 M KOH) at 500 mA employing nickel sheets as both electrodes, while Figure 6.4(b) depicts the corresponding gas evolution rates. The total gas evolution rate is the sum of the individual gas rates. The solid lines represent the theoretically expected gas evolution rates according to Faraday's law. Additionally, the Faradaic efficiency of the device was experimentally determined (see also chapter (4.6)), as shown in Figure 6.4(c). The obtained values scatter around unity, thus the system is proven to be gas tight and the ratio of hydrogen to oxygen, which equals 2, indicates no cross contamination between both gases.

The exchange of electrodes employed in the PV-EC device is depicted in Figure 6.5 showing the use of different electrolyser systems. Here, platinum and iridium oxide in acidic media are used as noble metal system, yielding a solar-to-hydrogen efficiency of 4.8 %. Nickel electrodes in alkaline media are used as earth-abundant system generating a stable operating current of approximately 110 mA, which corresponds to a solar-to-hydrogen efficiency of 2.1 %. For both measurements, the same a-Si:H/a-Si:H/µc-Si:H triple junction cell is used, which will be further discussed in section (7.2) and (7.6). Thus, it was shown that the electrolyzer system can be exchanged. The use of different photovoltaic cells will be shown and discussed in section (7.6). Figure 6.5 also depicts the need to develop earth-abundant catalyst systems that can be used in the upscaled water splitting device (see sections (7.3) and (7.5)), since the used nickel system yields a solar-to-hydrogen efficiency only around 2 %, leaving much room for improvement.

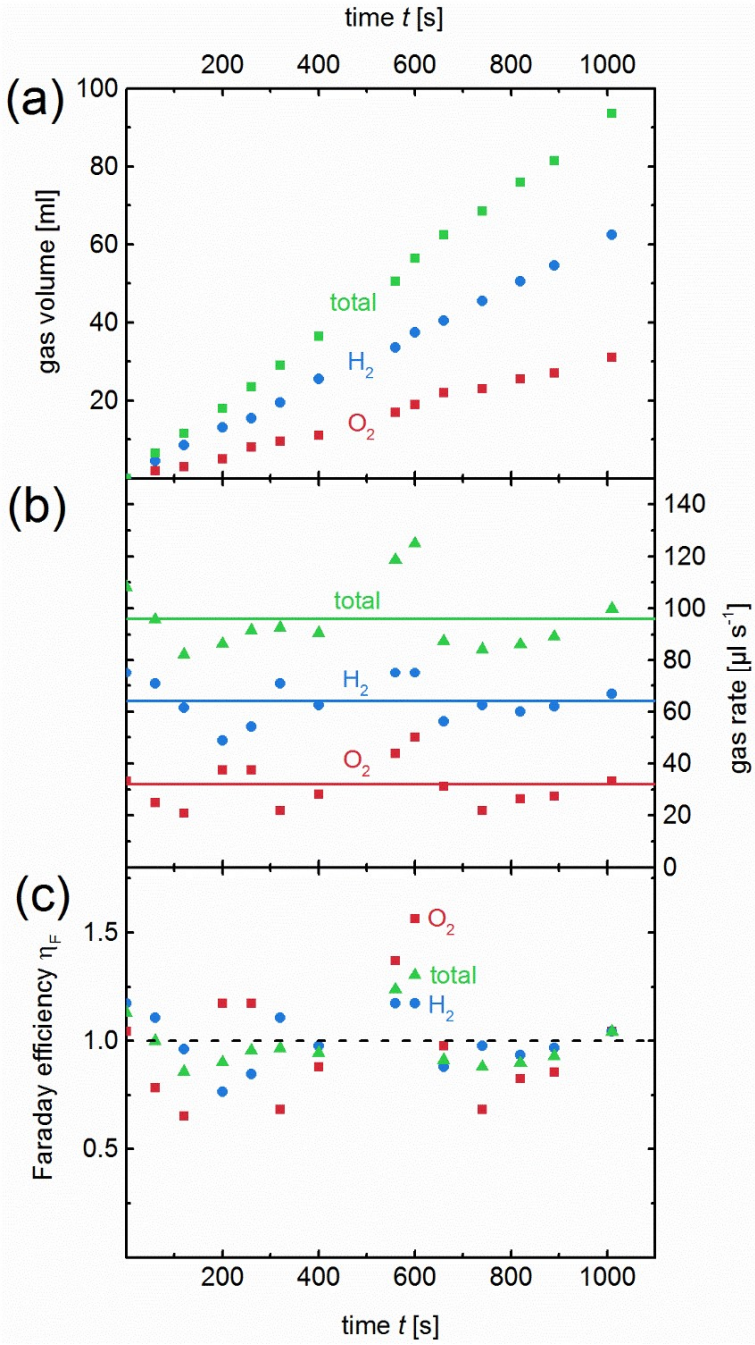

Figure 6.4: (a) Hydrogen and oxygen gas volumes collected during an alkaline electrolysis (1 M KOH) at 500 mA employing nickel sheets as both electrodes using the upscaled PV-EC device with anion exchange membrane implemented. Furthermore, the total sum of both gas volumes is shown. (b) Corresponding gas evolution rates shown for hydrogen and oxygen evolution. The total gas evolution rate is the sum of the individual gas rates. The solid lines represent the theoretically expected gas evolution rates according to Faraday's law. (c) The Faradaic efficiency of the device calculated according to chapter (4.6). The obtained values scatter around unity, indicating the leaks and gas tightness of the device.

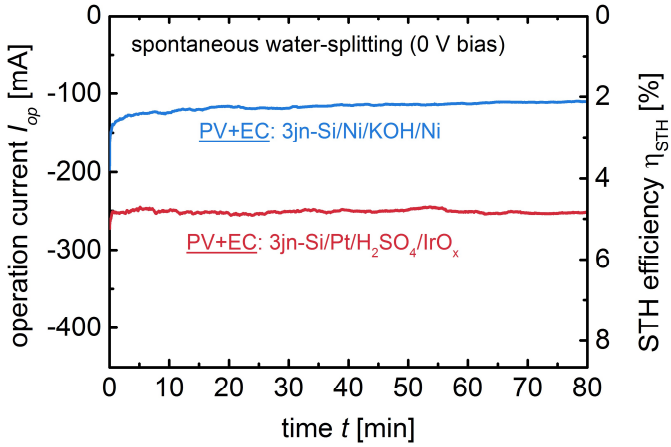

Figure 6.5: Chronoamperometric measurements of the upscaled PV-EC device under bias-free conditions employing (red curve) platinum and iridium oxide on titanium sheet substrates in acidic media (1 M H_2SO_4) and (blue curve) nickel electrodes in alkaline media (1 M KOH).

7.2 Upscaling of the photovoltaic cells

For the application of light induced water splitting devices as hydrogen production source, the light absorber area has to be significantly increased to several square meters as mentioned in the introduction to this chapter.[152] As known from the photovoltaic industry, silicon solar cells can be used in different configurations, such as for example crystalline or amorphous silicon solar modules, to cover areas of several m².[153–156] It has also been shown in literature that three crystalline silicon heterojunction solar cells can be connected in series by wiring[27] or a triple junction silicon heterojunction solar cell with interdigitated back contacts[29] can be used in order to power the water splitting reaction. To establish the series connection of three crystalline silicon heterojunction solar cells by wiring represents an upscaling solution on a low device integration level but with good interconnection.[26,27] For the use of amorphous silicon solar modules, a lateral connection of identical sub cells (side-by-side configuration), as known from the design of large area thin film photovoltaic modules, can be realized to the implementation in water splitting devices.[154–157] In this chapter, the focus will be on the upscaling of earth-abundant silicon solar cells to be integrated into the upscaled water splitting device, hence providing a higher degree of device integration compared to wiring the photovoltaic cells to the electrolyser. Two different silicon solar cell technologies will be compared: (1) thin film silicon solar cells and (2) heterojunction wafer-based silicon solar cells. The use of both technologies should show the flexibility of the upscaled PV-EC device towards different light absorber materials (see also section (7.1)).

As mentioned before, thin film silicon is well upscalable in area[154–156,158]. For the application of thin film silicon solar cells as voltage source for light induced water splitting, multi-junctions are needed due to the high output voltage (chapter (3.1.2)). Upscaling the area of a single solar cell (not module) is not straightforward, since one has to overcome the challenge of current collection through the front electrode with non-negligible sheet resistance resulting in ohmic losses. For example, if the current density of a 1 cm² solar cell accounts for 10 mA/cm², then an increase in solar cell area to 100 cm² would lead to a current of 1 A (factor of 100). Thus, in this section, different front contact designs to support the current collection and reduce the ohmic losses are developed and compared for thin film silicon based solar cells.

If crystalline silicon heterojunction (c-SHJ) solar cells were to be used as current-voltage source in light induced water splitting devices, at least three cells have to be connected in series to generate a sufficient output voltage. The concept and band diagram of silicon wafer-based heterojunction solar cells is described in chapter

(3.1.1). By using c-SHJ solar cells, short circuit photocurrent densities of around 41 mA/cm² can be generated under laboratory conditions[159], which results in a short circuit current density of ~ 13.7 mA/cm² for the use of three solar cells connected in series. For the a-Si:H/a-Si:H/µc-Si:H triple junction cell employed in the PV-EC device yielding a solar-to-hydrogen efficiency of 9.5 %, a short circuit current density of 8.6 mA/cm² was reported[24]. Thus, the use of crystalline silicon heterojunction cells in water splitting devices leads to further increased solar-to-hydrogen efficiencies[27,29]. The connection of the crystalline SHJ solar cells can be achieved via wiring, as mentioned before and reported in the literature[27]. If the cells are integrated into the upscaled water splitting device, in which substrates of maximum 100 cm² can be used, the crystalline silicon heterojunction cells can be shingled into a module in order to fulfill the size conditions (typical M0 wafer size: 239 cm²). In the present work, a module with three shingled crystalline silicon heterojunction solar cells was integrated into the upscaled PV-EC device. The SHJ solar cells were not specifically developed for the water splitting application, since they were deposited in the frame of a project dealing with the baseline production of these cells. The shown device is a first prototype for the integration of crystalline silicon heterojunction solar cells in buried junction PV-EC devices. The preparation process and additional possible improvements regarding the contact design will be discussed in detail in section (7.2.2).

7.2.1 Thin film silicon solar cell

Front contact designs:

The focus of this section is the upscaling of the thin film silicon solar cells employing different front contact designs to overcome the current collection through the front contact and the obtained results for the different designs. One possible way to support the current transport in the transparent conductive oxide (TCO) front contact layer, is the use of evaporated metal front contact grids. Front contact grids are typically used in wafer-based silicon heterojunction solar cells and thin film silicon solar cells deposited in the ”substrate” (n-i-p) configuration, where front contact grids support the lateral conduction of the front TCO layer.[84,86,160] A second approach utilizes parts of the solar cell’s rear contact (ZnO:Al/Ag) in a laser material processing procedure of the solar cell triple junction cell stack to generate a front contact design pattern[35]. The laser generated pattern consists of 64 individual solar cell fractions of 1 cm² size. Additionally, a reference triple junction solar cell without front contact modification was deposited. This reference solar cell is used to compare the influence of front contact design to the solar cell performance. In the case of evaporated metal grids, for example, the metal grid can on the one hand increase the lateral conductance of the TCO layer, but on the other hand, active solar cell area is reduced due to the shading effects caused by the untransparent grid. In the following investigation of different front contact designs, the substrates (glass + TCO) were prepared equally and the silicon deposition was carried out using the same parameters, such that only the front contact design varies.

Figure 6.6(a) shows the processing steps for the evaporated metal front contact grid approach for which the active solar cell area is increased from 1 cm² to 53.3 cm². In the first step (i) SiO_2 (10 nm) was evaporated on the glass substrate using electron-beam evaporation. SiO_2 serves as adhesion-promoting layer for the Ag fingers. In the second step (ii) the silver fingers (250 nm height, 200 µm width, 78 mm length) were deposited on the substrate by thermal evaporation through a stainless steel shadow mask. The distance between two fingers was 2 mm. The fingers were connected by two 3 mm wide, 78 mm long and 250 nm thick Ag busbars evaporated close to the edges of the substrate. The finger deposition was followed by (iii) the deposition of 80 nm ZnO:Al (1 %) at room temperature via radio-frequency magnetron sputtering in order to reduce thermal stress in the Ag fingers. In the next step (iv), 800 nm of ZnO:Al (1 %) were deposited as front contact TCO at a substrate temperature of 350 °C again using magnetron sputtering technique. The TCO was etched for 40 s in diluted hydrochloric acid (0.5 M) prior to the silicon layer deposition to increase the light scattering properties by chemically texturing the TCO. In the (v) step, the a-Si:H/a-Si:H/µc-Si:H (p-i-n) triple junction thin film silicon solar cell deposition was carried out in the multi-chamber system shown in chapter (4.1). The last step was the rear contact deposition, 80 nm of ZnO:Al (1%, sputter deposition at room temperature) and 700 nm thermally evaporated silver serve as rear contact and back reflector forming an active solar cell area

of 53.3 cm². The solar cell without front contact modification was prepared just as described, but without the second step (ii), thus also having an active solar cell area of 53.3 cm².

The alternative approach to generate a front contact grid utilizing the solar cell's rear contact by laser material processing is shown in Figure 6.6(b). Here, the active absorber area is increased from 1 cm² to 64 cm². The substrate was prepared according to the steps (i), (iii) and (iv) of the processing procedure for the evaporated metal front contact grid, thus SiO_2 and ZnO:Al were deposited as TCO layers on a glass substrate and etched afterwards. In the next step (i) (Figure 6.6(b)) the a-Si:H/a-Si:H/µc-Si:H solar cell stack was deposited via plasma-enhanced chemical vapor deposition in the multi-chamber system. The second step (ii) is the laser patterning removing the silicon absorber layers down to the front contact TCO layer, followed by the ZnO:Al/Ag
(80 nm/200 nm, RT) rear contact deposition by magnetron sputtering. The next step (iv) is the second laser processing step insulating the front contact grids, in which the 1 cm² sections are cut and the front contacts are separated from the rear contacts. The front contact grid is electrically insulated using polyimide tape (Kapton, DuPont) (step (v)). In the last step, the 64 individual sections of 1 cm² size were electrically connected in parallel using conductive tape (3M) to form the active solar cell area of 64 cm².[35]

A schematic drawing of the two front contact geometries is shown in Figure 6.6(c) and (d), indicating the active solar cell area, the front contact TCO and the front contact metal grid. Additionally, a reference solar cell without any front contact modification was deposited.

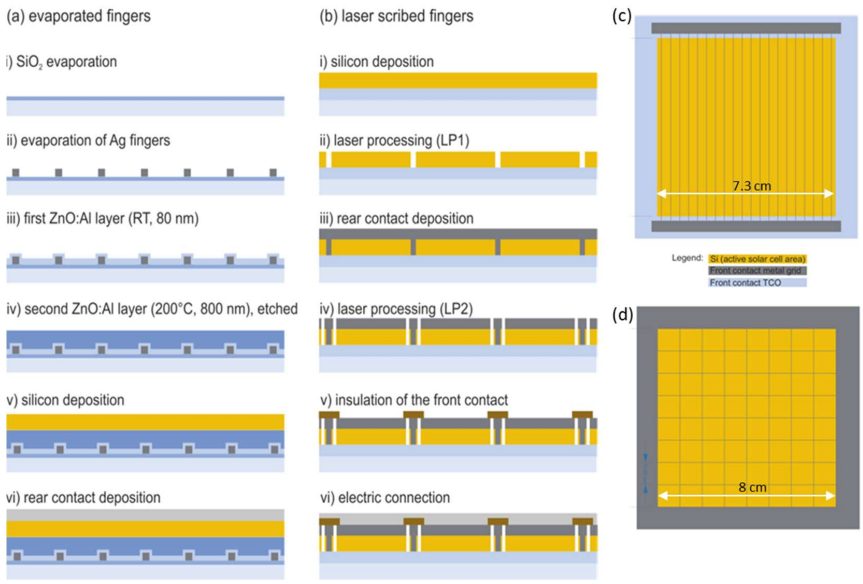

Figure 6.6: Schematic illustration of the two different front contact grid processing ways for (a) the evaporated metal front contact grid and (b) the laser processed front contact grid. In (c) and (d) the top views of the two front contact grid designs are shown (adapted from reference [35]).

Current density-voltage characteristics:

The current density-voltage curves of the three different solar cells (without front contact grid, with evaporated metal front contact grid and with laser processed front contact grid) are shown in Figure 6.7. The corresponding photovoltaic parameters are listed in Table 6.1.

Comparing the cell with and without evaporated metal front contact grid, one can see that the cell with metal grid shows a lower short circuit current density, which is due to the shading losses caused by the grid (without

grid: 5.4 mA/cm², metal grid: 5.2 mA/cm², ~ 4 % loss). The effect of the increased lateral conductance and therefore reduced series resistance in the TCO layer can be seen in the slope at the open circuit voltage[161] in Figure 6.7 and the resistance values in Table 6.1. The series resistance R_S for the solar cell with evaporated metal grid is reduced by 48.5 Ω·cm² compared to the solar cell without front contact modification (from 106.1 Ω·cm² down to 57.6 Ω·cm²). The parallel resistance shows a contrary trend, it is increased for the solar cell with metal front contact grid to 7036 Ω·cm². Additionally, the fill factor is improved for the solar cell with metal front contact grid (without grid: 52.7 %, metal grid: 68.3 %). Thus, the cell with metal front contact grid shows a higher efficiency than the cell without front contact modification (without grid: 6.3 %, metal grid: 7.9 %).

If the solar cell with metal front contact grid is compared to the solar cell with the laser processed front contact pattern, one can see that the short circuit current density is slightly higher for the evaporated metal front contact grid cell (metal grid: 5.2 mA/cm², laser processed: 5.0 mA/cm²), which could possibly be due to the higher total width of the laser processed grids compared to the total width of the metal grids. The series resistance is further reduced employing the laser processed grid (down to 28.3 Ω·cm²), while the parallel resistance is increased (up to 21138 Ω·cm²). The excellent fill factor of 73.6 % for the laser processed cells leads to a high voltage and current density at the operating point. The conversion efficiency η measured for the laser processed cells is the highest obtained in the present study with 8.2 %. Additionally, the laser processed solar cell is less sensitive towards failure. If one of the 64 individual solar cells fails, it can be excluded from the parallel connection, such that the remaining 63 cells can be used. Such a backup solution is not provided for the cells of 53.3 cm² size. If, for example, a shunt occurs in the 53.3 cm² cells, the solar cells cannot be used.

Table 6.1: Overview of the PV parameters (conversion efficiency η, fill factor FF, open circuit voltage V_{OC}, short circuit current density J_{SC}, voltage at the maximum power point V_{MPP}, current density at the maximum power point I_{MPP}, series resistance R_S and parallel resistance R_P) measured for the upscaled PV cells.

Front contact grid	A [cm²]	η [%]	FF [%]	V_{OC} [V]	J_{SC} [mA/cm²]	V_{MPP} [V]	I_{MPP} [mA/cm²]	R_S [Ω·cm²]	R_P [Ω·cm²]
Without	53.3	6.3	52.7	2.22	5.4	1.46	4.3	106.1	4904
Metal grid	53.3	7.9	68.3	2.23	5.2	1.75	4.5	57.6	7036
Laser scribed	64.0	8.2	73.6	2.25	5.0	1.86	4.4	28.3	21138

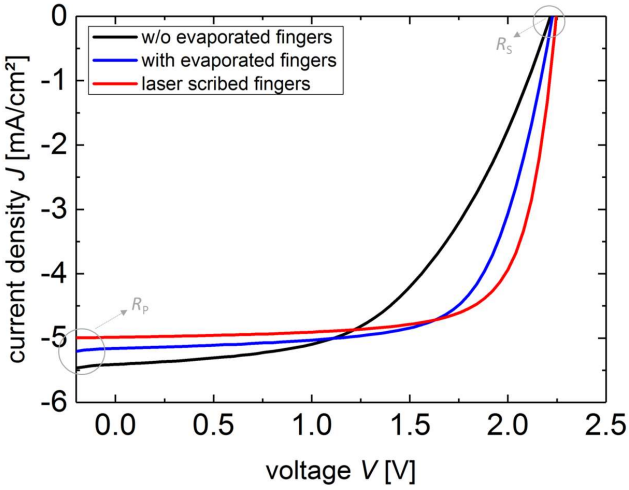

Figure 6.7: Current density-voltage characteristics of upscaled a-Si:H/a-Si:H/µc-Si:H triple junction solar cells employing (1) no front contact grid (w/o evaporated fingers, black curve), (2) an evaporated metal front contact grid (with evaporated fingers, blue curve) and (3) laser processed front contact grid (laser scribed fingers, red curve). The extraction points for the series resistance R_S and the parallel resistance R_P are indicated.

Electroluminescence imaging:

Electroluminescence measurements are based on the principle of a solar cell as light emitting diode. Instead of shining light on the solar cell, which then generates current and voltage, a current or voltage is applied to the solar cell and a luminescence signal is emitted due to radiative charge carrier combination (for further information see also chapter (4.2.3)).

The resistances occurring in the solar cell are represented by an inverse color code. High color values (light colors) stand for low resistances and low color values (dark colors) represent areas of increased resistance values.[143] The electroluminescence images taken for the three different cells with different front contact designs are shown in the following Figure 6.8.

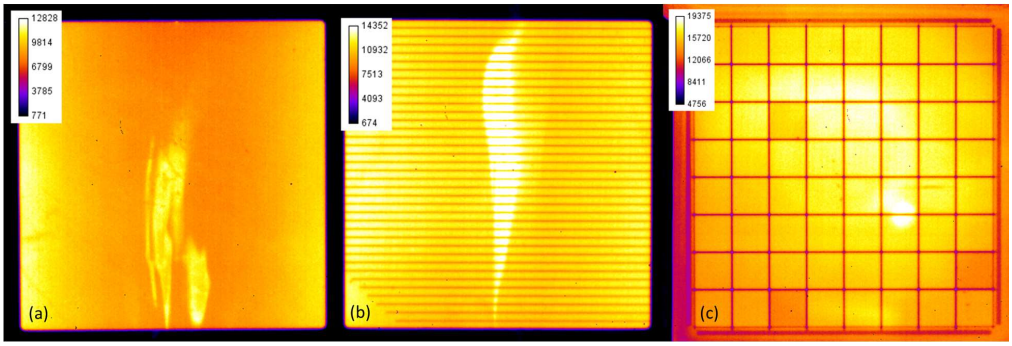

Figure 6.8: Electroluminescence images of the upscaled thin film silicon solar cells with different front contact designs (a) without front contact modification, (b) with evaporated metal front contact and (c) with laser processed front contacts. The color scale indicates the color value. High color values stand for low resistances and low color values represent high resistance values.

In Figure 6.8(a), the solar cell without front contact modification is shown. Hence, only the TCO layer serves as front contact. The image shows lower color values in the middle of the cell compared to the cell edges. Current generated in the middle of the solar cell has to pass from the middle of the cell to the edges in order to be extracted, leading to increased series resistances as indicated. This effect can also be seen in the series resistance value of 106.6 Ω·cm² obtained through the current density-voltage measurement listed in Table 6.1.

The electroluminescence image of the solar cell with evaporated metal front contact grid is shown in Figure 6.8(b). Compared to Figure 6.8(a), the imaged solar cell area in Figure 6.8(b) looks more homogenous. The series resistance appears to be reduced in the solar cell with evaporated metal grid compared to the cell without. The evaporated metal front contact grid supports the TCO layer and increases its conductance. The current generated in the middle of the solar cell can be extracted through the metal grid fingers with less ohmic losses compared to the solar cell without front contact modification. This effect is also seen the series resistance value obtained through the current density-voltage measurement listed in Table 6.1 (57.6 Ω·cm²), and leads to an improved fill factor compared to the cell without front contact modification.

Figure 6.8(c) shows the laser processed front contact grid with 64 individual solar cells of 1 cm² size. Three out of these 64 cells are slightly darker than the remaining 61 cells. The current-voltage curves of all 64 cells can be found in the appendix (see Figure A3). These three cells are not functioning correctly (probably shunted) and have to be excluded from the parallel connection. The remaining 61 cells show a homogenous electroluminescence image and a similar performance.

Summary:

The results obtained in this chapter show the supportive effect of front contact grids for the scale-up of thin film silicon solar cells to areas beyond 1 cm². The lateral conductance of the TCO layer is enhanced and the series resistances are lowered by implementing a front contact modification, as could be seen in the current density-voltage curve and was proven by performing electroluminescence imaging on the solar cells. The different approaches of an evaporated metal front contact grid and the laser processed grids both lead to an improved solar cell performance and can be applied also for areas beyond 53.3 cm² (evaporated grid) and 64 cm² (laser processed), respectively. Although all solar cells prepared in this section can be used in the upscaled water splitting device, solar cells with laser processed front contact grids were mainly used for the following studies and the implementation into the PV-EC device (see chapter (7.6)), since they provide the highest active area investigated in the present work.

7.2.2 Module with three shingled silicon heterojunction solar cells

As described in the introduction to this section, for the use of crystalline silicon heterojunction solar cells in water splitting devices, at least three cells have to be connected in series in order to generate a sufficient output voltage. In order to be integrated into the upscaled PV-EC device presented in section (7.1), the used module consists of three shingled silicon heterojunction solar cells. Figure 6.9 shows schematically the processing steps of silicon heterojunction solar cells. The first step is a cleaned and textured Czochralksi wafer with n-type doping. In the following step, the cleaned, textured wafer is transferred into a plasma-enhanced chemical vapor deposition system, where the hydrogenated amorphous silicon layers are deposited onto the wafer. On one side, intrinsic- and n-type a-Si:H layers are deposited, the other side is coated with intrinsic and p-type a-Si:H silicon layers. The next step is the deposition of indium tin oxide (ITO) by means of DC sputtering on both wafer sides. The preparation process is completed by low temperature screen printing of the silver fingers and busbars on both solar cell sides. Further and more detailed information of the deposition process of crystalline silicon heterojunction solar cells can be found elsewhere.[162,163]

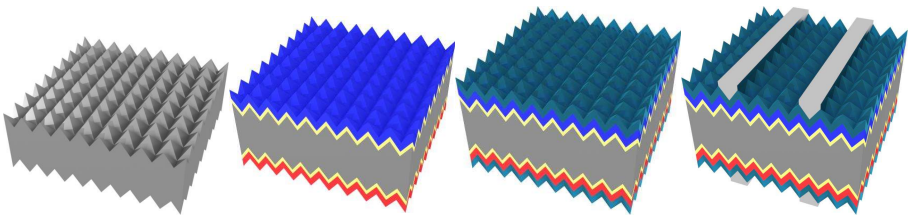

Figure 6.9: 1. Step: textured and cleaned wafer, 2. Step: a-Si:H layer depositions on both sides (yellow = intrinsic, blue = n-type doped, red = p-type doped), 3. Step: ITO deposition on both sides (green = ITO), 4. Step: screen printing of Ag fingers and busbars (grey = Ag). Images made by M. Köhler (Jülich, 2018).

The prepared crystalline silicon heterojunction cells were deposited on wafers of M0 size (239 cm²). Thus, the wafer had to be cut in order to be shingled and integrated into the upscaled PV-EC device. The cutting was performed using a laser system (532 nm, picosecond laser supplied by SCANLAB with f-theta lens). Three of the solar cell parts were connected using silver paste to establish the electrical contact (see also Figure 6.10(b)). Figure 6.10 depicts the arrangement of the solar cells in the shingled module in the photograph (a) and in the schematic (b). The active area of the module accounts for 58.5 cm². One challenge during the preparation process of the module employing shingled heterojunction solar cells, is the electrical connection of the solar cell parts. If silver paste is used, short circuits between front and rear side of the solar cell have to be prevented. For the module shown in Figure 6.10, the contact to the module is established by a 3 mm wide, adhesive metal tape connected to the front and back side respectively. Thus, the current generated in the module is completely discharged through the metal tape connected to either side of the solar module. Improvements regarding the contact design can be made by for example using different contact materials instead of silver paste and adhesive metal tape in order to reduce ohmic losses.

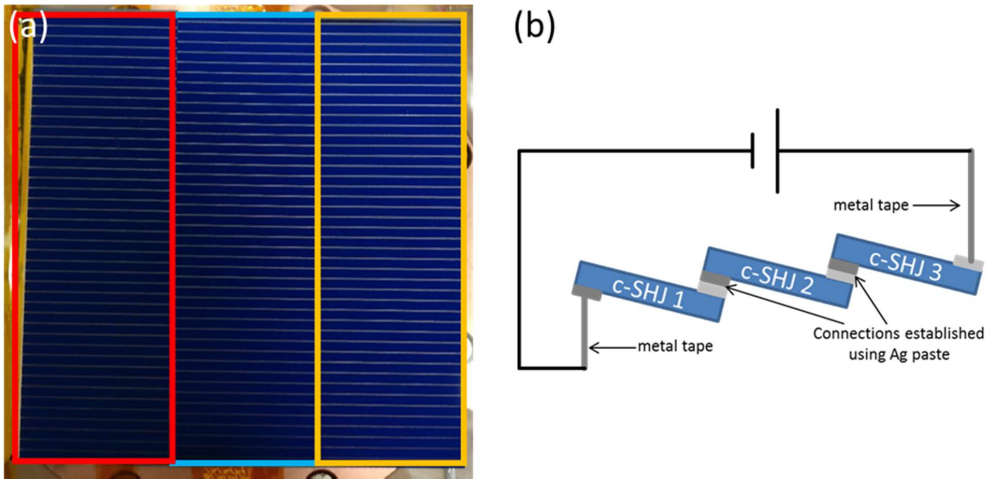

Figure 6.10: (a) Photograph of the module with three shingled crystalline silicon heterojunction solar cells. The different solar cells are indicated and were connected using silver paste. The active area is 58.5 cm².(b) Schematic of the module with shingled crystalline silicon heterojunction solar cells showing the contact arrangement.

Figure 6.11 shows the current density-voltage curve measured under AM1.5G illumination for the module with three shingled crystalline silicon heterojunction solar cells and Table 6.2 lists the photovoltaic parameters obtained. The conversion efficiency of 12.4 % is lower than the values for the individual solar cell parts (η = 20.3 %), which can be due to the electrical contacting needing further improvements. The highest conversion efficiencies of crystalline silicon heterojunction solar cells obtained under laboratory conditions are in the range of 26 %[159], for employing interdigitated back contacts in a monolithic crystalline silicon solar cell an efficiency of 18.7 % was reported[29]. Hence, if the electrical contacting is improved, the conversion efficiency can be increased. The same effects are possibly responsible for the low fill factor of 54.2 % (typical values > 75 %[29,159]). The output voltage generated at open circuit conditions (V_{OC} = 2.07 V) indicate that the module with three shingled crystalline silicon heterojunction solar cells can be used to drive the water splitting reaction, since the required potential is exceeded. Figure 6.12 shows a comparison of the current density-voltage curves for one single crystalline silicon heterojunction solar cell (red dashed curve), the measured curve for the module with three shingled c-SHJ cells (black solid curve) and the ideal case of three c-SHJ cells connected in a module without series resistance losses. The calculation of the ideal module is based on the current density-voltage characteristics of the single c-SHJ cell assuming no resistance losses due to the interconnection. By comparing the black solid and green dotted curve, it becomes evident that the occurring series resistances in the measured module have to be reduced in order to increase the module fill factor, which also directly affects the shape of the corresponding PV-EC device current-voltage curves.

Table 6.2: Overview of PV parameters measured for the module with three shingled heterojunction solar cells.

η [%]	FF [%]	V_{OC} [V]	J_{SC} [mA/cm²]	V_{MPP} [V]	J_{MPP} [mA/cm²]	R_S [Ω·cm²]	R_P [Ω·cm²]
12.4	54.2	2.07	11.1	1.3	9.6	58.5	12139

Overall, the first approach of preparing a module with three shingled crystalline silicon heterojunction solar cells for the integration into the upscaled PV-EC device shows working photovoltaic characteristics, although the comparison to literature and between the calculated, ideal module and the measured module indicates room for improvements. The integration of the module in the PV-EC device and the obtained performance is discussed in detail in chapter (7.6).

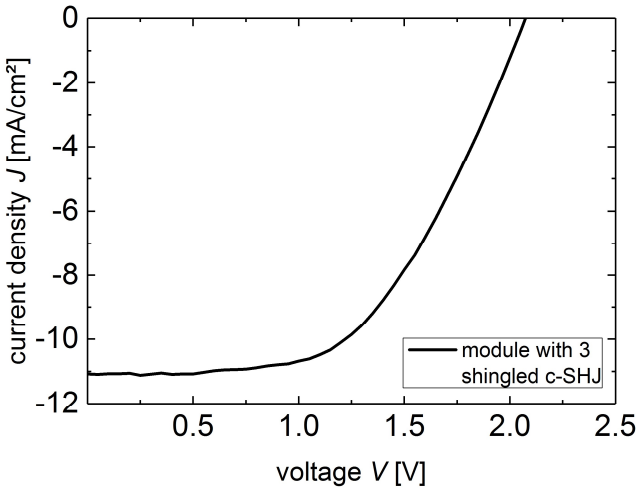

Figure 6.11: Current density-voltage curve of a module with three shingled crystalline silicon heterojunction solar cells measured under AM1.5G illumination.

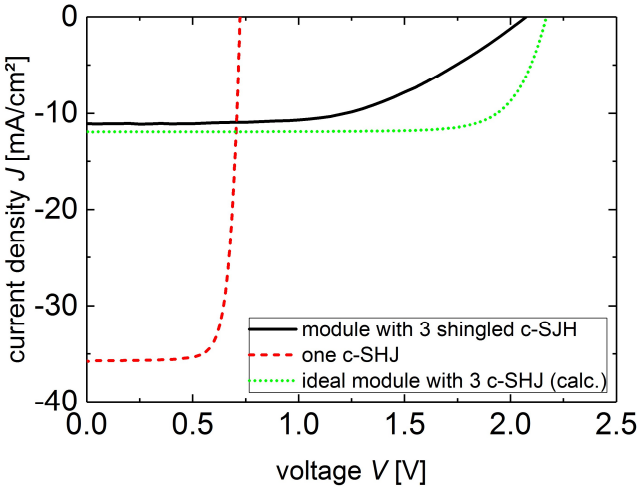

Figure 6.12: Current density-voltage curves of a single crystalline silicon heterojunction (c-SHJ) solar cell (red dashed curve), of the measured module with three shingled crystalline silicon heterojunction (c-SHJ) solar cells (black solid curve) and the ideal module with three crystalline silicon heterojunction (c-SHJ) cells without series resistance losses due to the connection (green dotted curve).

7.3 Earth-abundant catalysts for the use in the upscaled PV-EC device

The previous sections of this chapter focused on the upscaling of the PV-EC device (7.1) and silicon solar cells (7.2), which can be integrated as current-voltage source into the PV-EC device. In this section, the focus lies on the preparation of catalyst materials from earth-abundant materials for both the hydrogen- and the oxygen-evolution reaction side and their application in the upscaled PV-EC device shown in section (7.1). The size restriction for the upscaled, earth-abundant catalyst systems is given by the upscaled PV-EC device and accounts for 50.3 cm².[35] A second upscaling approach based on the lateral interconnection of identical sub cells (side-by-side approach) is briefly discussed for the implementation of nickel foam based electrodes. The required size for the electrode stripes in the latter approach is 50 x 80 mm².[157]

In the previous work, the best light induced water splitting performances and a solar-to-hydrogen efficiency of 9.5 % were obtained using platinum and ruthenium oxide as catalyst system in alkaline media with an area of
0.5 cm².[24,34] But, for the application of the device for efficient generation of hydrogen from sunlight, the device area has to be increased significantly and additionally, the cost-effectiveness of all components has to be considered. Thus, earth-abundant materials are preferably used for the application into PV-EC devices.[26] The application of earth-abundant catalyst systems combined with multi-junction thin film silicon solar cells has been investigated as part of the PhD thesis by F. Urbain as alternative to noble metal catalyst systems.[34] Different metal stacks have been tested regarding their catalytic activity in the hydrogen evolution reaction, while a platinum wire was used as counter electrode[118]. The thin metal stacks (thickness between 300 – 450 nm) were deposited by means of electron beam evaporation and tested on an area of 0.5 cm².[118] However, in the case of metal stack catalysts, an earth-abundant catalyst for the counter electrode was not developed. Additionally, thin metal films of several nanometer thickness do probably not provide long-term stable performances in highly alkaline conditions (1 M potassium hydroxide solution). In the upscaled PV-EC device, different electrolyser systems have been tested as shown in section (7.1) (Figure 6.5). The noble metal system consisting of platinum and iridium oxide yielded a solar-to-hydrogen efficiency of 4.8 %, while for the earth-abundant system of nickel used for both electrodes, a solar-to-hydrogen efficiency of 2.1 % was measured for electrode areas of 50.3 cm².[35] Considering the cost-effectiveness, platinum and iridium oxide should be avoided. The performance of the nickel based system, however, can substantially be increased by using other earth-abundant catalyst materials.[108] A second upscaling approach based on a side-by-side lateral interconnection of identical sub cells employed nickel foam electrode stripes for the water splitting reaction[157], which can potentially be replaced by nickel foam coated with more active materials. In the following, different earth-abundant catalysts were prepared, electrochemically characterized and their potential towards the application in the upscaled PV-EC devices (substrate size of (1) 50.3 cm², (2) 50 x 80 mm²) was evaluated. For the choice of catalyst materials, the extensive research activities on the development of catalysts and their integration into water splitting devices or electrolysers reported in the literature[36,37,108,109,164–170] were consulted. In contrast to the application in electrolysers (typical operating current density J_{OP} in A/cm² range[171]), the current density in a PV-EC device is limited by the solar cell and its current density, which is usually between 5-9 mA/cm² at the operating point[24,87,118] for an output voltage >1.5 V. The requirements for the catalysts employed in PV-EC cells are hence more relaxed compared to the application in electrolysers. Based on these reports, nickel nitride[36] and nanosheets consisting of Ni_3S_2[37,38] were deposited on nickel foam substrates, while nickel sheet electrodes were used for the deposition of nickel iron oxide (OER)[39] and nickel molybdenum (HER)[40,108]. Regarding the substrates, nickel foam provides a high surface area; whereas nickel sheets should ensure a long-term stability of the device. All materials have been studied intensively regarding their electrochemical properties[36–38,108,109,168,171–173], their structure and mechanism[172,174,175] and different synthesis routes[37,38,40,109,171,173] are known. For example, hydrothermally deposited NiMo and $NiFeO_X$, with nickel foam as substrate of 3 cm² size can be combined in an alkaline electrolyser without any performance loss compared to noble metal catalysts.[109] The obtained results for the synthesis and characterization of the different materials on frequently used sample sizes (0.5 – 3 cm²) will be presented in the following sections. Additionally, a brief description of a catalyst system developed in the frame of the joint project “Sustainable Hydrogen” (FKZ 03X3581 of the German Bundesministerium für Bildung und Forschung (BMBF)),

consisting of cobalt-iron layered double hydroxide (Co-Fe LDH) and nickel molybdenum nitride ($Ni_XMo_YN_Z$), will be given due to the use of this system in chapter (7). Both catalyst materials were prepared and measured externally and information concerning the synthesis can be found in the literature.[176–178] Finally, NiMo and $NiFeO_X$ were chosen for the catalyst upscaling and implementation into the PV-EC device described in chapter (7.1) (substrate size of 50.3 cm²). Both materials, NiMo and $NiFeO_X$, can be deposited via electrodepostition[39,40] (see also section (4.3)), an easily feasible and wide spread method for catalyst fabrication, allowing the deposition on areas beyond typical laboratory scale. The synthesis of these materials using electrodeposition has so far been reported on substrates like transparent conductive oxides (TCO) covered with titanium and gold[39] or glassy carbon disks (GC).[108,168] Nickel sheets, which are compatible with the PV-EC design described in section (7.1), should not only serve as substrate for the catalyst deposition but also as a fall back solution, if the catalyst layer is detached. In that case the PV-EC device performance will decrease, but the device is still able to operate due to the active electrode material. Additionally by using nickel sheets as electrodes, the optical and electronic properties of the solar cell are maintained, since modifications concerning the rear contact are not necessary as they are for example compared to the implementation of protective coatings.

7.3.1 Nickel foam substrates

Three-dimensional nickel foam substrates are employed in water splitting devices in order to increase the active electrode area and are used in a zero gap measurement configuration. Additionally, an upscaling approach based on a lateral interconnection of identical sub cells (side-by-side approach), which is described in literature[157], employs uncoated nickel foam electrodes, which can possibly be replaced by materials prepared and investigated in this section. The required electrode size for the implementation in this approach is 50 x 80 mm².[157] The first material discussed is nickel nitride, which can serve as hydrogen and oxygen evolution catalyst[36]. In this work, nickel nitride coated nickel foam was prepared by adding a supramolecular cyanuric acid-melamine-barbituric acid (CMB) complex to nickel foam substrates in a glass ampoule, which was evacuated and heated in an oven. For the synthesis of nanosheets made of Ni_3S_2 on nickel foam, the foam substrates were heated in thiourea solution in a hydrothermal system for several hours.[37] The Ni_3S_2 coated nickel foam electrodes are also bifunctional for the use as oxygen and hydrogen evolution catalyst as reported in literature.[37] The system of cobalt-iron layered double hydroxide and nickel molybdenum nitride was prepared externally.[176–178] In this section, the different synthesis procedures of the materials prepared at the Institute for Energy and Climate Research – 5 are presented and the obtained results regarding the material characterization are discussed. Finally, an overview of the potential use of the materials in the upscaled water splitting devices will be given.

Experimental procedures

All chemicals used for the cleaning, measurements and catalyst depositions were in reagent grade quality. The nickel foam substrates were supplied by RECEMAT BV, Ni-5763.

Nickel nitride

Cleaning:

Prior to the synthesis, the nickel foam substrates of 2 cm² size were cleaned for 5 minutes each in an ultra-sonic bath, using the following solvents i) aceton, ii) isopropanol, iii) deionized water (18 MΩ), iv) 25 % hydrochloric acid and v) deionized water (18 MΩ). Afterwards the samples were dried for 24 h in ambient atmosphere at 160°C.

CMB complex:

The CMB complex was prepared mixing 1 g of cyanuric acid, 1 g of melamine and 0.1 g of barbituric acid in 40 mL of deionized water. The solution was stirred for 4h at room temperature. Afterwards, the complex was filtered using a suction filter and washed with DI water. The powder was dried in air and afterwards dried in vacuum at 60°C until remaining solvent residues were completely removed.

CMB complex + nickel foam:

Three nickel foam substrates of 2 cm² size were mixed with 1 g of the CMB complex in a glass ampoule. The glass ampoule was evacuated, closed and placed in an oven. The oven was heated for 4 h with a heating rate of 2.3 °C/min, afterwards the temperature was maintained at 550°C for 4 h.

Cobalt-iron layered double hydroxide and nickel molybdenum nitride

Both materials were prepared by partners in the frame of the joint project "Sustainable Hydrogen" (FKZ 03X3581 of the German Bundesministerium für Bildung und Forschung (BMBF)). Information regarding the synthesis of both materials can be found in the literature.[176–178]

Nanosheets made of Ni_3S_2

Cleaning:

The nickel foam substrates of 3 cm² size were cleaned for 30 min of sonication prior to the synthesis, using the following solvents i) acetone, followed by rinsing with deionized (DI) water and ii) 3 M HCl solution (mixing HCl (25 %) and DI water). The ultra sonic cleaning was followed by rinsing the samples with deionized water and ethanol. The substrates were dried in nitrogen atmosphere.

Synthesis:

11.1 mg of thiourea were dissolved in 100 mL deionized water (1.445 mM). 30 mL of the thiourea solution were transferred into a 100 mL autoclave together with three nickel foam substrates of 3 cm² size. The autoclave was sealed and heated at 150 °C for 5 h. The hydrothermal system was opened after cooling to room temperature. The nickel foam samples were rinsed three times with ethanol and dried in vacuum.

Results on nickel foam substrates - Nickel nitride

The ampoule was cooled to room temperature before opening. An image of the ampoule prior to opening can be found in the appendix (Figure A4). The CMB complex, which had initially no color, has turned brown during the reaction. The nickel foam substrates show a black brown color after its coating (compared to metallic before). A black, brownish accumulation of material, partially containing crystals, is found at the top of the ampoule. During the opening of the ampoule, the substrate structures broke into several pieces, such that the remaining parts did not provide sufficient area for a detailed electrochemical characterization. In order to fit into the sample holder and to be electrochemically characterized using the PV-EC device shown in chapter (6.2.2), the three-dimensional substrate has to be ductile, which was not given for the obtained material. However, scanning electron microscope images could be taken, showing micrometer rods grown on the nickel foam surface, shown in Figure 6.13.

Regarding the application as electrode in one of the upscaling approaches, the presented synthesis route was not further pursued, since the size requirements given (50.3 cm² or 50 x 80 mm²) could not be fulfilled due to

the brittle product. Thus, further characterizing and analyzing the obtained material was not performed and the nickel nitride composition of the material was not confirmed.

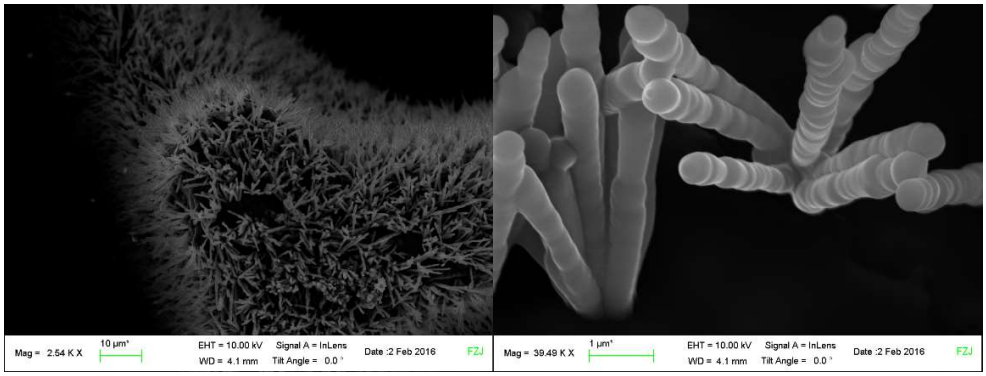

Figure 6.13: Micrometer rods deposited on nickel foam by heating nickel foam substrates with CMB complex in a glass ampoule.

Results on nickel foam substrates - Cobalt-iron layered double hydroxide and nickel molybdenum nitride

The investigated catalyst system consisting of cobalt-iron layered double hydroxide and nickel molybdenum nitride was prepared and measured by partners in the frame of a joint project on "Sustainable Hydrogen" (FKZ 03X3581 of the German Bundesministerium für Bildung und Forschung (BMBF)). The current density-voltage curves shown in Figure 6.14 were measured by Evonik Creavis GmbH. The measurements were performed using three-electrode configuration in a zero gap flow electrolysis cell employing 1 M potassium hydroxide as electrolyte. A schematic of the measurement setup is shown in the appendix (see Figure A5).

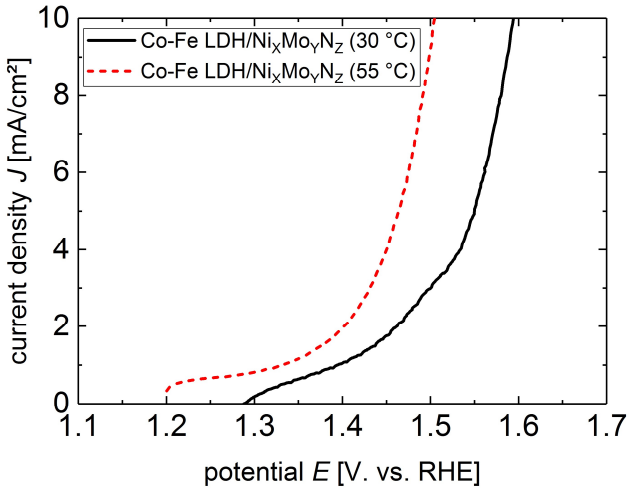

Figure 6.14: Current density-voltage curves of the catalyst system cobalt-iron layered double hydroxide combined with nickel molybdenum nitride developed and measured by partners in the joint project on "Sustainable Hydrogen" (FKZ 03X3581 of the German Bundesministerium für Bildung und Forschung (BMBF)). The measurements were performed using three-electrode configuration in a zero gap flow electrolysis cell employing 1 M potassium hydroxide as electrolyte for two different temperatures. The potential of the catalyst system is decreasing with increasing temperature.

Two different electrolyte temperatures were investigated (30 °C and 55 °C) as shown in the Figure 6.14. The system shows a potential of 1.59 V at 10 mA/cm², which equals to an overpotential of 360 mV. For a temperature of 55 °C, the potential accounts for 1.51 V, which is equal to an overpotential of 280 mV. Thus, the overpotential of the system is reduced for a temperature increase, as expected from the literature[102] and as described in chapter (3.2.3).

The shown current density-voltage curves are used in chapter (7) for the comparison of different illumination conditions on the device performances. The different devices are constructed from various multi-junction cells as well as catalyst systems.

Results on nickel foam substrates - Ni_3S_2 nanosheets

Electrochemical measurements:

After the reaction, the autoclave was cooled to room temperature prior to opening. The obtained nickel sheets after the reaction showed a metallic color and remained ductile. The electrochemical performance obtained by means of cyclic voltammetry (CV) measurements of the coated nickel foam is shown in Figure 6.15 for one sample. A hydrothermally untreated nickel foam reference is shown for comparison, as it was used in the side-by-side upscaling approach[157]. The measurements were performed in 1 M potassium hydroxide solution and platinum served as counter electrode. Additional CV data on other samples are shown in the appendix (see Figure A6).

In Figure 6.15, the current-voltage curves of repeated cyclic voltammetry measurements are shown for untreated and Ni_3S_2 coated nickel foam. The geometric sample area was 0.5 cm², while the actual surface area was not determined. The effect of an increased electrode surface area can be seen for both current-voltage curves depicted, which show currents measured in the range of several 100 mA (shown up to 400mA). Typical currents measured for planar substrates with a geometric sample size of 0.5 cm² are in the range below 50 mA. Comparing the current-voltage curves of hydrothermally untreated nickel foam (black) and the Ni_3S_2 coated nickel foam substrate (red), one can see the improvement due to the hydrothermal treatment, since the current voltage curve of the Ni_3S_2 sample (red) is shifted towards lower potentials. The bifunctionality of the material was not further investigated.

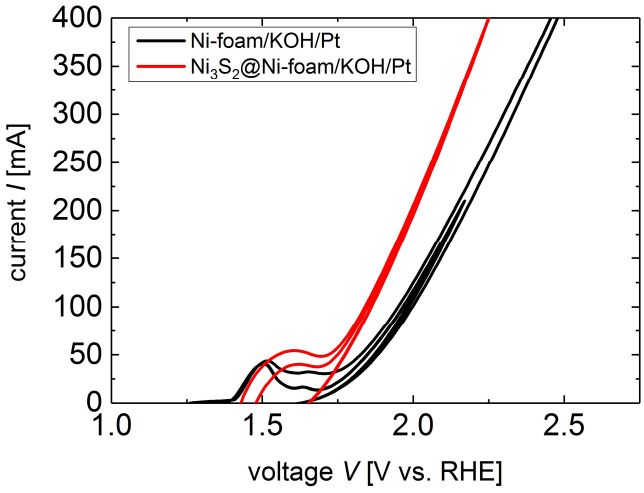

Figure 6.15: Current-voltage curve of Ni_3S_2 deposited on nickel foam in 1 M KOH using platinum as counter electrode. For comparison, the current-voltage curve of untreated nickel foam is shown.

Using the Ni_3S_2 nanosheet coated nickel foam electrodes in the side-by-side upscaling approach could possibly enhance the device performance and should be possible due to the stable foam structure. Additionally, electrode stripes of 50 x 80 mm² size can be coated using the existing hydrothermal treatment system. The preparation of Ni_3S_2 nanosheet coated nickel foam electrodes of increased size is one task for further investigations.

Surface morphology:

In order to investigate the surface morphology of the prepared Ni_3S_2 samples, scanning electron microscope images were taken. The images taken of the Ni_3S_2 samples prepared in the present work are shown in Figure 6.16. The nickel foam structure is preserved after the hydrothermal treatment (see Figure 6.16(a)). Increasing the magnification, a surface coverage of the nickel foam can be seen (Figure 6.16(b) and (c)). For further magnification to the nanometer scale, the nanosheet structure of the deposited coating can be identified. Such a nanosheet morphology is also described in literature.[37]

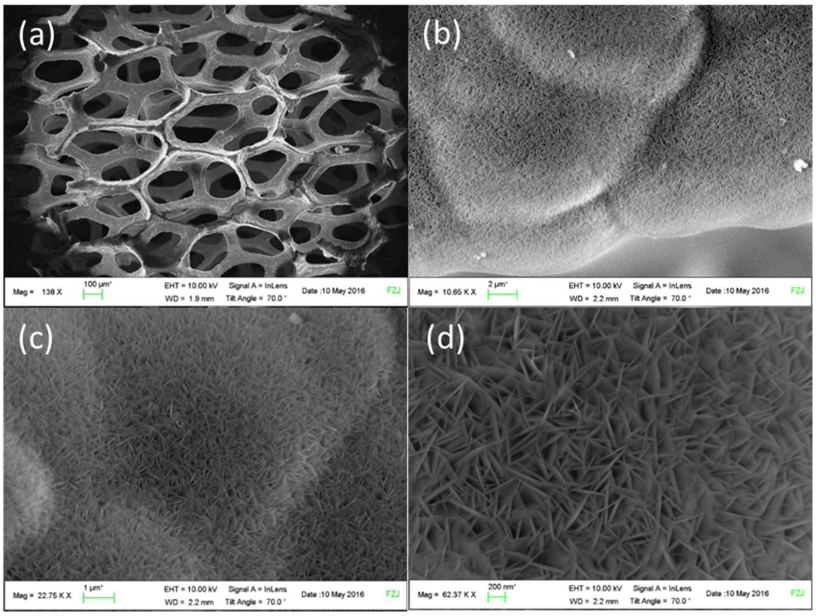

Figure 6.16: Scanning electron microscope images taken for the Ni_3S_2 samples prepared in the present work. The images show a preserved nickel foam structure and complete coverage with nanosheets.

Raman spectroscopy:

To identify the material of the nanosheets deposited on nickel foam, Raman spectroscopy can be used as reported in the literature[37]. The obtained Raman spectra are shown in Figure 6.17, showing the spectra of the Ni_3S_2 coated nickel foam and for comparison hydrothermally untreated nickel foam prior and after the electrochemical characterization.

In Figure 6.17, Raman lines in the range of 200-350 cm^{-1}, can be observed for the hydrothermally treated nickel foam, which are associated to Ni_3S_2 (compare to the literature[37]). The Ni_3S_2 Raman spectra are not changed due to the electrochemical measurement (compare red and green curve). Additionally, a small peak at 450 cm^{-1} is visible, which was not assigned to any compound. The hydrothermally untreated nickel foam substrate shows no significant Raman scattering before the electrochemical measurement, but afterwards, a Raman line of nickel oxide is observed at 475 cm^{-1}[179] and additionally a peak at 540 cm^{-1} was found, which could overlap with the second nickel oxide Raman line at 555 cm^{-1}[179]. The formation of nickel oxide can be due to the use as oxygen evolution electrode in alkaline media and the possible formation of another species on the electrode

surface. The Raman measurement confirmed the successful coating of nickel foam electrodes with Ni_2S_3 nanosheets, which are stable throughout the electrochemical characterization in alkaline media.

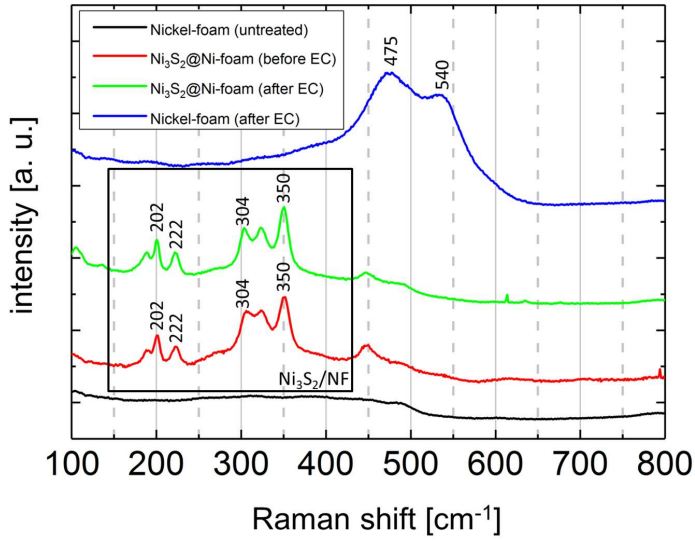

Figure 6.17: Measured Raman spectra for Ni_3S_2 coated nickel foam and for hydrothermally untreated nickel foam prior and after the electrochemical characterization. The measured spectra are in good agreement with the Raman spectra reported in the literature for Ni_3S_2[37], thus they confirm the deposition of Ni_3S_2 nanosheets on nickel foam.

Summary:

Overall, the synthesis of catalyst materials on nickel foam was successfully performed. The Ni_3S_2 nanosheets showed lower overpotentials for the oxygen evolution reaction compared to hydrothermally untreated nickel foam samples. The deposition of Ni_3S_2 material on the nickel foam surface was confirmed by the changed surface morphology in SEM and Raman spectra, which were similar to those reported in literature[37]. Regarding the potential application as electrode in the upscaled PV-EC device, which is shown in section (7.1), the nickel foam substrates of the shown materials have to be increased to a size of 50.3 cm^3, which does not fit into the used hydrothermal treatment system (autoclave). However, the prepared materials on nickel foam electrodes could possibly be implemented into the approach for PV-EC device upscaling, which is based on a lateral connection of identical sub cells (side-by-side connection). The potential of the later approach has been reported in literature employing hydrothermally untreated nickel foam electrode stripes of the size 50 x 80 mm^2.[157] The obtained results show that the performance of the PV-EC device can be enhanced by using Ni_3S_2 coated nickel foam electrode stripes, which can be a task for further investigation regarding PV-EC devices. The required size for the implementation into the side-by-side device can be reached using the available hydrothermal treatment system.

7.3.2 Nickel sheet substrates

In the following section, electrodeposition is used to deposit nickel iron oxide and nickel molybdenum on nickel sheets. Compared to nickel foam substrates, nickel sheet electrodes can be implemented into the upscaled PV-EC device, as described in the introduction to this chapter and shown in section (7.1). First, the samples were deposited on substrates of 1.5 x 1.5 cm² size (deposition area 0.5 cm²) for electrochemical and material characterization. Different deposition parameters, such as the precursor ratio, current density, time and method (pulsed vs. continuous), and their influence on the obtained activity towards the respective gas evolution reactions were investigated. In the next step, both materials were electrodeposited on nickel electrodes of 50.3 cm² size and implemented into the upscaled PV-EC device. In the case of $NiFeO_X$, the results and experiments summarized in this section were carried out in the framework of the master thesis of N. Hamzelui at the Forschungszentrum Jülich GmbH. The master thesis focused on electrodeposition of nickel based catalysts for the oxygen evolution reaction in photoelectrochemical water splitting devices. In the present PhD thesis, the key results of the master thesis will be summarized, highlighted and expanded by detailed X-ray photoelectron spectroscopy measurements. For more details on the fabrication and characterization of $Ni_{1-Y}Fe_YO_X$, the reader is referred to the corresponding master thesis.[180] Parts of the following section concerning the upscaling of earth-abundant catalysts on nickel sheets and their performance implemented into upscaled PV-EC devices have been published in K. Welter, N. Hamzelui, V. Smirnov, J.-P. Becker, W. Jaegermann, F. Finger, *J. Mater. Chem. A* **2018**, 15968–15976.

Experimental procedures

Catalyst deposition

All chemicals used for the cleaning, measurements and catalyst depositions were in reagent grade quality.

Cleaning:

The nickel sheets (99.2%, supplied by Metall Jobst, Germany), which were used as substrates, were cut into 1.5 x 1.5 cm² samples for a deposition area of 0.5 cm² and circular samples with a diameter of 8.5 cm for the deposition area of 50.3 cm². The samples were cleaned for 30 min by sonication prior to the catalyst depositions, using the following solvents i) acetone, followed by rinsing with deionized (DI) water and ii) 3 M HCl solution (mixing HCl (25%) and DI water). The ultra sonic cleaning was followed by rinsing the samples with deionized water and ethanol. The samples were dried using compressed air.

Electrodeposition of $NiFeO_X$ *for OER*:

The electrolyte used for the deposition was a 0.1 M solution consisting of $Ni(NO_3)_2 \cdot 6\ H_2O$ and $FeCl_2 \cdot 4\ H_2O$ dissolved in deionized water. The portions of Ni to Fe were varied from 100:0 to 60:40 (mol:mol). Prior to the film deposition, nitrogen was sparged into the electrolyte for 20 min in order to prevent oxidation of Fe(II) to Fe(III).[39] A Gamry Reference 600 potentiostat in a two-electrode setup was used to perform the electrodeposition. A carbon rod was used as counter electrode for deposition areas of 0.5 cm². For the upscaled sample areas (50.3 cm²), a Ni sheet was employed as counter electrode. All deposition areas were defined by O-ring seals with the respective diameters. Schematic deposition setups are shown in Figure 6.18.

Besides the varied Ni:Fe ratio, different deposition charge densities (-100 mC/cm² – -400 mC/cm²), deposition times between 10 s to 40 s, and deposition methods (continuous vs. pulsed[39]) were investigated. In order to implement the catalyst material into the modular device, the electrodeposition on the 50.3 cm² electrode was carried out using the following deposition parameters: Ni:Fe ratio of 80:20 mol%, J_{dep} = -10 mA/cm², t_{dep} = 40 s, pulsed deposition mode (5 s pulse, 10 s stirring), T_{dep}= room temperature (RT). All samples were cleaned after deposition with DI water in order to remove possible contaminants.

Electrodeposition of NiMo *for HER:*

The electrolyte solution for the electrodeposition of NiMo consists of $NiSO_4 \cdot 6\ H_2O$ (1), $Na_2MoO_4 \cdot 2\ H_2O$ (2) and $Na_3C_6H_5O_7 \cdot 2\ H_2O$ (3) (quantities: 3.16 g (1), 1.92 g (2), 3.52 g (3)[40]) dissolved in 40 mL of NH_4OH[40,108]. The electrodeposition was performed using a Gamry Reference 600 potentiostat in a two-electrode setup. For the depositions on small and increased scale, the same deposition setups and electrode configurations as mentioned for the $NiFeO_X$ electrodepositions were used (see Figure 6.18(a) and (b)). The substrate size of 0.5 cm² was used for the investigation of different deposition times at a constant deposition current density J_{dep} of -160 mA/cm². Additionally, the influence of a constant deposition charge density was investigated, using the sample size of 0.5 cm² (e.g.: $Q = Jt$ = constant → J_{dep1} = -160 mA/cm² for t_{dep1} = 1200s, Q_{dep1} = -192 C/cm²; and J_{dep2} = -1200 mA/cm² for t_{dep2} = 160 s, Q_{dep2} = -192 C/cm²).

The following parameters were used for the deposition of NiMo on nickel sheets of 50.3 cm² size: 80 mL of NH_4OH, 6.32 g of $NiSO_4 \cdot 6\ H_2O$, 3.84 g of $Na_2MoO_4 \cdot 2\ H_2O$, 7.04 g of $Na_3C_6H_5O_7 \cdot 2\ H_2O$, t_{dep} = 19200s, J_{dep}= -10 mA/cm², Q_{dep} = -192 C/cm², T_{dep}= room temperature (RT), stirring 800 rpm, continuous mode.

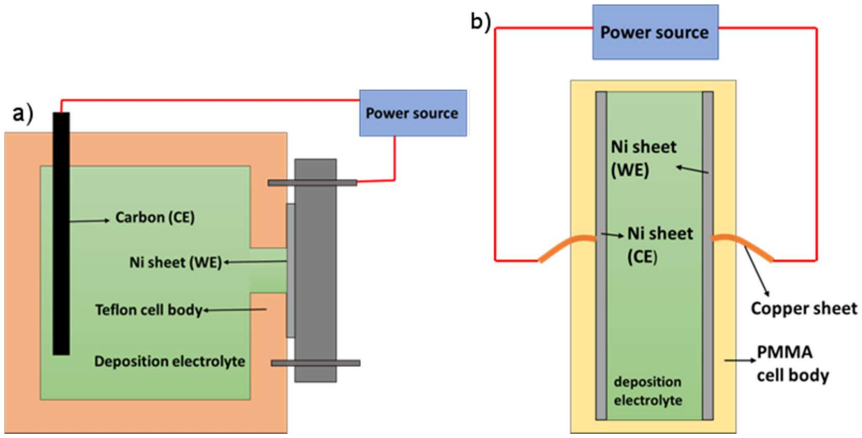

Figure 6.18: Setups for the electrodeposition on a sample area of (a) 0.5 cm² and (b) 50.3 cm². The sample areas are defined by O-rings with the respective diameters. The cell body in (a) is made of Teflon and a carbon rod was employed as counter electrode (CE) (distance between working electrode (WE) and counter electrode (CE): 1.5 cm). The setup shown in (b) consists of polymethylmethacrylat (PMMA). A nickel sheet of 50.3cm² was used as counter electrode (CE) (distance between electrodes: 7 mm).

Electrochemical measurement sequence for accurate catalyst comparison:

All electrochemical measurements were performed using a Gamry Reference 600 potentiostat. The electrolyte was in all cases 1 M potassium hydroxide solution at room temperature. In a three-electrode setup, Ag|AgCl served as reference electrode (see also chapter (4.4.1)). The measurements were performed according to the following measurement sequence (approximately 1.5 h duration):

1. Open circuit potential (OCP) for 600s
2. Electrochemical impedance spectroscopy (EIS) between 100 kHz and 0.01 Hz
3. Cyclic voltammetry (CV) measurements in a non-faradaic region at different scan rates (5, 25, 75, 125, 175, 200 mV/s)
4. Linear sweep voltammetry (LSV) was performed at a scan rate of 2 mV/s
5. Chronopotentiometry (CP) measurements were applied at (±)10 mA/cm² for 900s

The uncompensated cell resistance used for the iR correction (described in chapter (3.2.1)), was calculated from the electrical impedance spectroscopy by using Gamry Echem Analyst software with the included "CPE with diffusion model". The CV measurements were performed in a non-Faradaic region and used to calculate the electrochemically active surface area (ESCA) according to C.C.L. McCrory et al.[108]. For a detailed description of the methods used, see chapter (4.4). The evaluation of the overpotential was performed at current densities where no overlapping reactions occurred. The error bars, which are shown in Figure 6.20, Figure 6.28 and Figure 6.29, were derived from the standard deviation evaluated from measurements of several samples deposited with the same deposition conditions or repeated measurements of the deposited samples, if only one sample was prepared.

Results on nickel sheet substrates - $NiFeO_X$ for OER:

Deposition parameters and electrochemical characterization

The deposition parameters, which were varied for the sample depositions on 0.5 cm² area and whose influence on the overpotential of the catalyst material towards the oxygen evolution reaction was investigated, are the precursor ratio, the charge density, the time and the deposition method (pulsed vs. continuous). The pretests were conducted in order to determine the conditions for the preparation on an increased electrode area of 50.3 cm² size. The conditions for the deposition on an increased area were determined by comparing the overpotential of the samples of 0.5 cm² size evaluated at 20 mA/cm² depending on the varied parameters. Ideally, the conditions yielding the lowest overpotential should be used for the upscaling.

In Figure 6.19, the current density-potential curves of different nickel iron oxide samples are exemplarily shown, which were obtained by means of linear sweep voltammetry measurements according to point 4 of the described measurement sequence. The iron content of the samples shown in Figure 6.19 was varied, while the other deposition parameters were kept constant. The deposition was carried out on an area of 0.5 cm² using the setup shown in Figure 6.18(a). The deposition parameters of the shown samples are listed in Table 6.3. A detailed characterization of the samples prepared under varied conditions and a sample list of all $NiFeO_X$ samples deposited can be found in the reference.[180] Additionally, the current density-potential curves of iridium oxide and nickel are shown as references. All measurements were performed in three-electrode configuration, employing platinum as counter electrode in 1 M potassium hydroxide solution. Figure 6.19 depicts the low overpotentials of the investigated nickel based systems, which outperform the two reference systems. Overpotentials, which are lower for nickel iron oxide materials than for iridium oxide and nickel, have been reported in literature[108] with η_{IrOx} = 390 mV and η_{NiFeOx} in the range of 340 – 380 mV. The overpotential difference between nickel iron oxide and iridium oxide observed in Figure 6.19 is in the range of 100 mV. This increased difference compared to the literature can possibly be due to different surface morphologies, and hence different electrochemically active surface areas, between the deposited nickel iron films and the commercially purchased iridium oxide on titanium substrate. The surface morphology of the nickel iron oxide material is investigated in the following section.

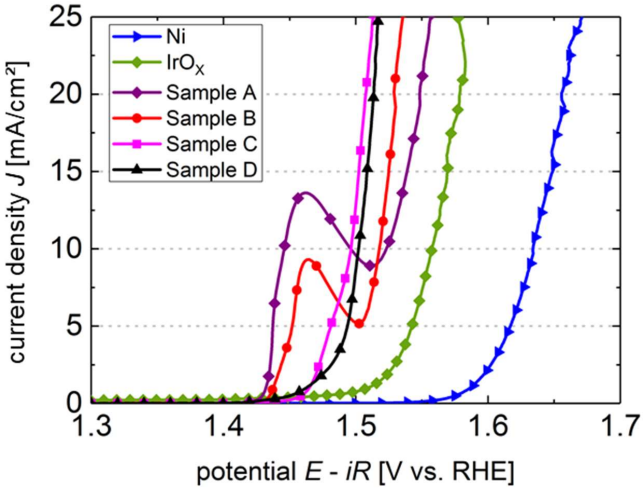

Figure 6.19: Current density-potential curves of three nickel iron oxide samples (exemplarily shown for 0.5 cm² area) and iridium oxide and nickel as references. The measurements were performed in alkaline media (1 M KOH), in three-electrode configuration employing platinum as counter electrode. The investigated nickel based systems show lower overpotentials than the reference systems. For the purple square curve, an overlap between the oxygen evolution reaction and a nickel oxidation peak is observed. The figure is taken from reference [180].

In the case of the nickel iron oxide samples, the overpotentials are evaluated at 20 mA/cm², since in some cases (see purple curve in Figure 6.19) an overlap of the oxygen evolution reaction and a Ni oxidation peak[39] at lower current densities (e.g. at 10 mA/cm²) was observed, such that the two reactions could not be clearly separated.

In Figure 6.20 the potential at 20 mA/cm² and the respective overpotential as a function of iron concentrations are shown (plotted, based on the results in ref. [180]). Continuous vs. pulsed deposition methods as well as different charge densities (constant deposition current densities J_{dep}, varying deposition times t_{dep}) are indicated. A three-electrode setup with platinum as counter electrode was used for the electrochemical catalyst characterization.

Table 6.3: Deposition parameters used for preparation of $NiFeO_X$ samples shown in Figure 6.19. Sample C was used for several studies (SEM, XPS and repeated measurements).

Sample name	c_{Fe} [mol%]	t_{dep} [s]	Q_{dep} [mC/cm²]	T_{dep} [°C]	*mode*
A	5	40	-400	25	pulsed
B	10	40	-400	25	pulsed
C	20	40	-400	25	pulsed
D	25	40	-400	25	pulsed

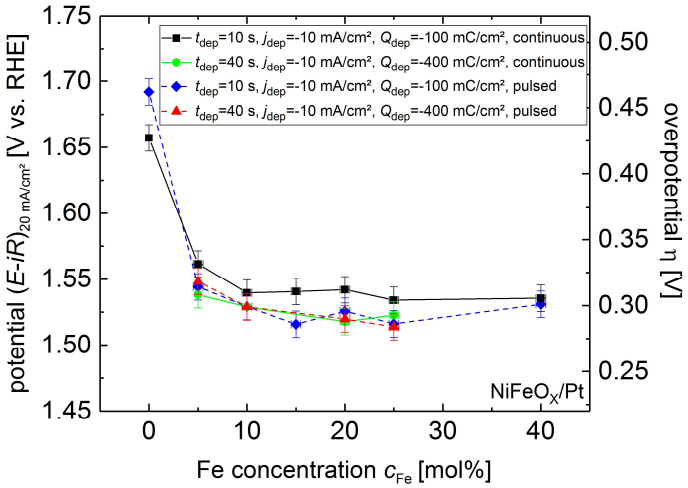

Figure 6.20: Potential of $NiFeO_X$ samples deposited on 0.5 cm² area as a function of the iron concentration evaluated at 20 mA/cm². The respective overpotentials are indicated on the right-hand axis.

The iron to nickel ratio in the deposition solution is one of the key parameters investigated here. In Figure 6.20, one can see that already 5 mol% Fe leads to a reduction in the overpotential by ~ 100 mV. This positive effect of iron incorporation has been extensively investigated and reported in the literature.[168,181–183] Possible reasons for the increase in OER activity are, for example, increases in conductivity; changes in the electronic structure and changes in the Ni-O local environment due to the iron incorporation; and the role of Fe induced partial-charge-transfer mechanism.[168,174,183] In the present study, the lowest overpotentials for the $NiFeO_x$ catalyst are generally found in the iron concentration range from 15 – 25 mol%. The increase of the deposition charge density in the continuous mode by increasing the deposition time (compare the black and green curves) leads to a lower overpotential for all Fe concentrations investigated. This positive effect is probably due to a higher active surface area established during the higher deposition time (10 s vs. 40 s). Regarding the deposition mode for a given charge density/time, one would expect lower overpotentials for the samples prepared in the pulsed deposition mode according to the literature, where the benefits of the pulsed mode over the continuous mode are well investigated and discussed[39,101]. The lower overpotentials measured for samples

made in the continuous mode is related to the lower catalyst packing density due to the deposition mechanism. During the continuous deposition, nitrate is reduced at the surface leading to a local pH gradient and therefore precipitation of metal hydroxides on the electrode surface and on the outer surface layers occurs.[39] Comparing the different deposition modes for a charge density of -100 mC/cm² (compare the black and blue curves in Figure 6.20), the pulsed deposited samples indeed show lower overpotentials. However, if the charge density is increased, (-400 mC/cm²) (green and red curves) no difference between the two modes is observable.

Overall, the lowest overpotentials η in the range of 0.28 V – 0.30 V were found for materials prepared with an iron content of 15 – 25 mol% in the electrolyte for various deposition conditions, such as for example (i) 15 mol% iron content, a charge density of -100 mC/cm² and pulsed mode, (ii) 20 mol% iron content, a charge density of -400 mC/cm² and pulsed mode or (iii) 20 mol% iron content, a charge density of -400 mC/cm² and continuous mode. The electrodeposition on the electrode with a size of 50.3 cm² was carried out using the following parameters (ii): Ni:Fe ratio of 80:20 mol%, J_{dep} = -10 mA/cm², t_{dep} = 40 s, pulsed deposition mode (5 s pulse, 10 s stirring), T_{dep}= room temperature (RT). The performance of the catalyst nickel iron oxide obtained on the 50.3 cm² size electrode is discussed in detail in section (7.5) combined into an electrochemical system with nickel molybdenum. In the following section, the nickel iron oxide films are spectroscopically characterized and the influence of the alkaline media during the electrochemical measurement sequence to the catalyst is investigated.

Spectroscopic characterization and influence of electrochemical measurement sequence

Ideally, a catalyst material should not be consumed during the reaction, as described in chapter (3.2.4). In order to investigate, whether this accounts for the prepared catalyst $NiFeO_X$, different characterization methods were used. Scanning electron microscope images were taken in top-down and cross-section mode in order to investigate the surface morphology and layer cross section before and after the electrochemical measurement sequence. Possible morphology changes can thus be identified. The chemical composition of the catalyst material was evaluated by X-ray photoelectron spectroscopy. Changes in the chemical composition due to the exposure to alkaline media can possibly be differentiated. Repeated linear sweep voltammetry measurements suggest a possible change in performance. The $NiFeO_X$ samples investigated in the following were deposited for 40 s in pulsed mode with a charge density of -400 mC/cm² and an iron content in the deposition electrolyte of 20 mol% (see also sample C in Table 6.3).

SEM studies before and after electrochemical measurements

In Figure 6.21, the top-down and cross-sectional SEM images of the $NiFeO_X$ sample (Table 6.3) are presented. The images (a), (c) and (e) show the sample prior to the electrochemical measurement and (b), (d), and (f) after the electrochemical measurement sequence described in the experimental procedures of this section (7.3.2) (duration around 1.5 h). Comparing the top-down image (a) to (b), the surface structure prior to the EC measurement consists of a cluster like structure with chunks of material on top of the surface. After the EC measurements (b), the surface appears to be flatter and different layers are distinguishable. The images (c) and (e) show the cross-sectional images of the sample before the electrochemical measurement sequence. Different thicknesses are indicated. The sample consists of two different sub layer structures, one dense layer close to the surface (~ 2-3 µm height) with a less dense layer on top (~ 5-9 µm). This two layered structure is preserved after the electrochemical measurement sequence (images (d) and (f)), however, the overall thicknesses of the layers are reduced to ~1 µm for the dense layer and 2 µm for the less dense layer. Therefore, mostly the dense layer exists after the measurements and less of the top layer can be observed.

The morphologies observed in the image shown in (b) are probably due to the deposition in pulsed mode, leading to a higher interconnection and surface coverage. The dense layer (cross-sectional images (c), (e) and (d), (f)), which is directly in contact with the nickel substrate, may show epitaxial film growth on the nickel surface. The structure of the less dense top layer ((c) and (e)) could possibly be caused by a concentration

gradient during the electrodeposition process[39], leading to precipitation of the deposition electrolyte onto the layer surface after electrodeposition.

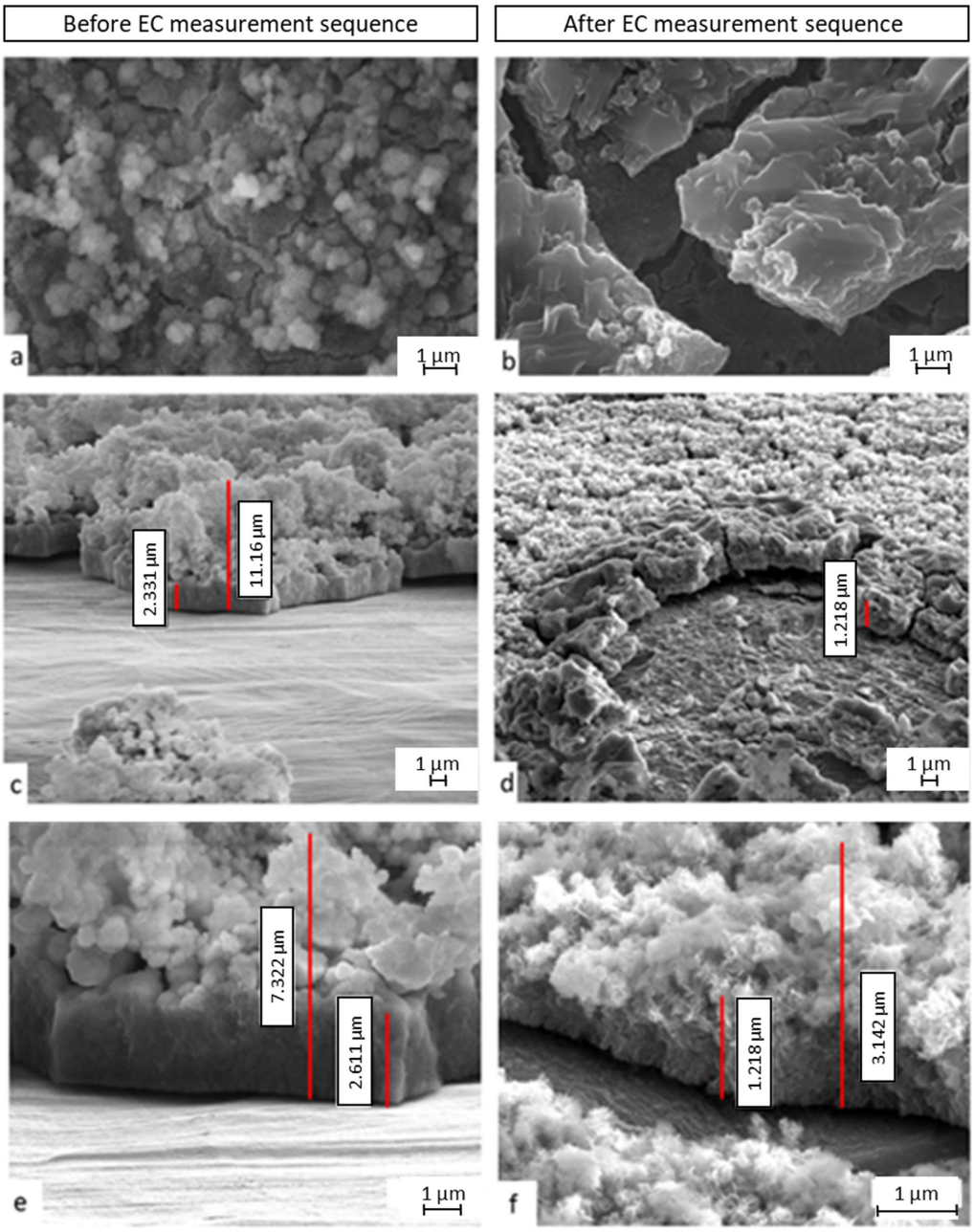

Figure 6.21: SEM images prior and after the electrochemical measurements of $NiFeO_X$ containing 20 mol% iron deposited for 40 s with a charge density of -400 mC in the pulsed deposition mode at room temperature. Figures a, c, and e were taken prior to the electrochemical measurement sequence and b, d and e afterwards. The different thicknesses are indicated in the cross sectional SEM images c-f, the images a and b were taken in the top-down mode.

One possible reason for the thickness reduction, observed in the images (d) and (f), could be due to the dissolution in the electrolyte or the consumption of the film during the oxygen evolution reaction. The less dense top layer possibly has an enhanced surface area in contact with the electrolyte solution and for the oxygen evolution reaction compared to the dense bottom layer, which could lead to the larger thickness decrease. However, the dense bottom layer would also be in contact with the electrolyte, which could lead to the observed thickness decrease for the bottom layer. The thickness change could possibly be resolved by additional scanning electron microscope experiments during the electrochemical measurement sequence. It appears as if the catalyst layer is degrading. For the case of complete detachment, the changes would be indicated in the chemical composition (XPS) and changes in the catalyst performance (repeated LSV measurements and long-term testing). While the results of the XPS measurements and the repeated LSV measurements are discussed in the following section, long-term stability testing was conducted in the combination with nickel molybdenum and is discussed in section (7.6.3).

XPS studies before and after the electrochemical measurement sequence

To investigate the chemical composition of the deposited $NiFeO_X$ materials and to see how far the electrochemical measurement sequence affects the materials, the $NiFeO_X$ catalyst prepared in reference[180] was further investigated by XPS studies in the present thesis. The deposition conditions of the sample C investigated in the XPS studies are given in Table 6.3. The change in surface morphology observed in the SEM images is possibly accompanied by a change in the surface composition. In the following Figure 6.22 -Figure 6.25 the XP spectra for carbon (Figure 6.22), oxygen (Figure 6.23), iron (Figure 6.24) and nickel (Figure 6.25) are shown, comparing the spectrum before the electrochemical measurement sequence (black curve) to the spectrum after the electrochemical measurement sequence (red curve). The peak of the carbon C-C binding energy was used as reference for the XPS measurements and set to 285 eV. The other spectra were corrected with the offset determined from the carbon spectrum.

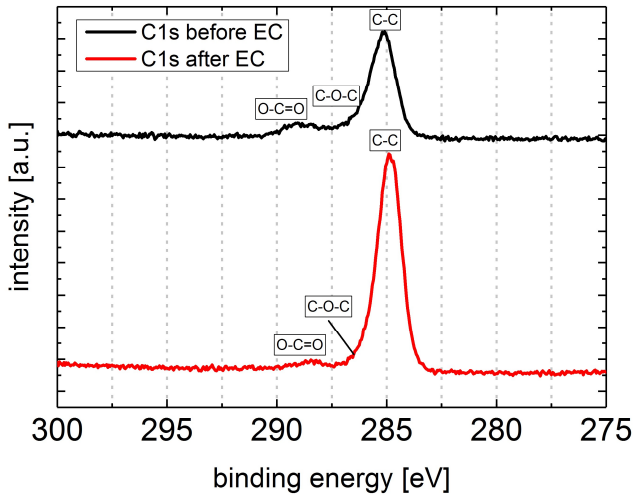

Figure 6.22: XP spectra of carbon before (black curve) and after (red curve) the electrochemical measurement sequence. The C-C carbon peak was used as reference for the XP spectra and set to 285 eV.

The following emissions were identified in the carbon spectra: C-C at 285 eV, C-O-C at 285.7 eV and O-C=O at 288.7 eV.[184,185] The C-C as well as the O-C=O peak can clearly be seen in the spectra. The C-O-C peak overlaps with the C-C peak and can be indicated as asymmetric shoulder. Comparing the spectra before and after the electrochemical measurement sequence shows that the indicated features are found in both spectra. The intensity of the C-C peak is increased after the electrochemical measurement sequence. An increased

intensity could lead to the assumption that the carbon content on the surface is also increased. However, specific reasons for the increase in intensity were not investigated. Generally, the carbon content on the surface is due to the storage and handling of the samples in air causing the accumulation of organic molecules on the surface. The samples were not cleaned by sputtering prior to the measurement in order to keep the surface composition after the electrochemical measurement sequence unchanged.

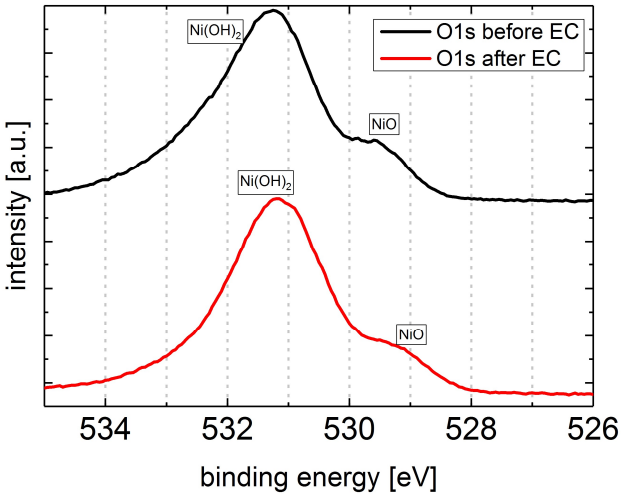

Figure 6.23: XP spectra of oxygen before (black curve) and after (red curve) the electrochemical measurement sequence. Different oxygen species are indicated.

The oxygen XP spectra are shown in Figure 6.23. The following components are identified: NiO species at 529.5 eV and $Ni(OH)_2$ 531.2 eV.[184,185] Both peaks are overlapping but can be clearly determined. Thus, the deposited layers are neither completely oxidic nor completely hydroxidic. The deposited layers can also be denoted as $Ni_XFe_{1-X}O_Y(OH)_Z$. The nickel hydroxide peak at 531.2 eV is overlapping with possible FeO_X related components at 531.7 eV. Comparing the spectra after the exposure to alkaline media, no changes in shape can be determined. Since the intensity of the emission lines does not change after oxygen evolution in alkaline media, one can assume that the oxide hydroxide was located on the layer surface prior to the electrochemical characterization. The oxide hydroxide species is either deposited during the electrodeposition or is formed due to the contact with oxygen during the storage in ambient atmosphere.

The spectra of iron before and after the electrochemical measurement sequence are shown in Figure 6.24 and confirm that iron is incorporated in the catalyst layer. The iron emissions are only slightly visible due to the background caused by the nickel LMM peak in the investigated range from 700 – 750 eV.[184,185].The iron emissions observed are associated to Fe_2O_3 species with binding energies of 711.5 eV for the $2p_{3/2}$ orbital and ~725 eV for the $2p_{1/2}$ orbital.[184,185] A slight change due to the electrochemical measurement sequence is observable, since the peak at 725 eV can be better indicated after the electrochemical measurement sequence. The interpretation of the spectra remains difficult due to the low intensity of the iron peaks.

In Figure 6.25, the XP spectra of nickel are shown. The line shape of the Ni 2p region is more difficult to interpret due to various effects such as multiplet splitting and shake-up structures.[186,187] The following lines can be identified: a $Ni2p_{3/2}$ emission at 852.6 eV and the corresponding $Ni2p_{1/2}$ emission at 871 eV, which are associated with nickel metal (Ni^0).[187] These emissions are clearly visible prior to the exposure to alkaline media and result from the electrodeposition under cathodic conditions.[39] A $Ni(OH)_2$ signal can be seen at 855.6 eV with satellite shake up bands at 862 eV. A NiO species, which was identified in the O 1s spectra (see Figure 6.23), can be seen at 853.7 eV serving as shoulder of the $Ni(OH)_2$ peak. The NiO emission is only slightly visible due to the overlap with the $Ni(OH)_2$ and $Ni2p_{3/2}$ peak.[184,185] Possible emission lines of NiOOH species[187] cannot be distinguished from the identified signals. Based on the measured nickel and oxygen

XP spectra, one may assume that the deposited layer consists of a mixture of nickel metal, NiO and $Ni(OH)_2$ (compare also to the literature[187]). The most evident changes due to the electrochemical measurement sequence can be seen for the metallic nickel species. The $Ni2p_{3/2}$ peak at 852.6 eV (nickel metal) is strongly decreased after the electrochemical measurement sequence, but can still be identified. The same effect is observed for the corresponding $Ni2p_{1/2}$ (Ni^0) peak at 871 eV. The observed peaks for $Ni(OH)_2$ at 855.6 eV and the satellite shake up bands at 862 eV as well as the NiO shoulder remain unchanged after the electrochemical measurement sequence. Hence, after the exposure to alkaline media, the catalyst layer possibly consists of a mixture of nickel metal, NiO and $Ni(OH)_2$, with a strongly decreased Ni^0 share.

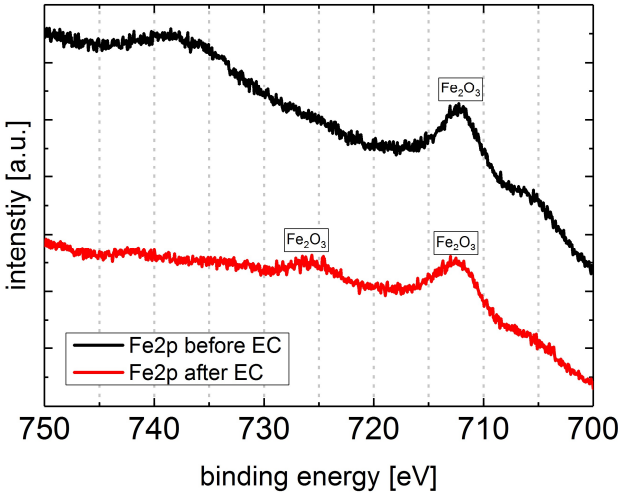

Figure 6.24: XP spectra of iron before (black curve) and after (red curve) the electrochemical measurement sequence. Different iron species are indicated.

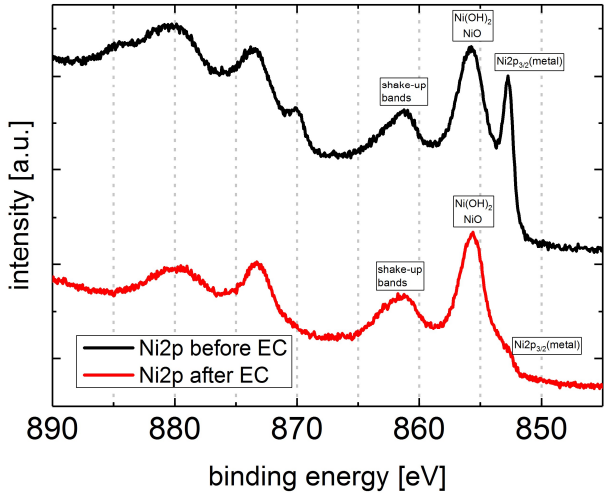

Figure 6.25: XP spectra of nickel before (black curve) and after (red curve) the electrochemical measurement sequence. Different nickel species are indicated. The peaks observed in the range of 870 – 890 eV are the doublets of the peaks in the range of 850 – 865 eV.

Prior to the electrochemical measurement sequence, the nickel XP spectrum shows a clear signal for metallic nickel, which is strongly reduced after the exposure to alkaline media. Combining this result with the scanning electron microscope images taken before and after the electrochemical characterization, which show a height reduction and a strong decrease of less dense top layer material (see previous section), leads to the assumption

that the less dense top layer containes metallic nickel species. Considering the penetration depth and size of the XPS beam (10 nm and 1 mm size), it could also be possible that besides the catalyst layer, a substrate signal (Ni^0) was obtained due to possible microscopic holes in the deposited layer. The active species during the catalytic reaction, which is NiOOH[172], could not be detected in the XP spectrum after the electrochemical measurement sequence. Here, in situ XPS studies performed during the water splitting reaction could show the active NiOOH species.

Summarizing the results obtained by XP spectra, it was confirmed that iron is incorporated into the catalyst layer, which consists of a nickel metal, nickel oxide and nickel hydroxide mixture. The oxide and hydroxide species were clearly distinguished in the oxygen spectra and can also be seen in the nickel spectra. Prior to the electrochemical measurement in alkaline media, an XPS signal assigned to nickel metal was measured caused by the cathodic electrodeposition conditions, which was strongly decreased after the measurement sequence. The observed change correlates to the results from the scanning electron microscope images, showing a height reduction and a decrease of top layer material caused by the exposure to and reactions in alkaline media, leading to the assumption that the top layer contains Ni^0 species. Spectra reported in literature for as deposited nickel iron oxide layers on glassy carbon disk electrodes also show Ni^0 emissions as well as $Ni(OH)_2$ emissions.[108] However, it can also be possible that microscopic holes in the catalyst layer were detected leading to the Ni^0 signal. Further experiments, such as in situ XPS, are needed to clarify the ongoing processes during the oxygen evolution reaction.

Repeated current density-voltage measurements

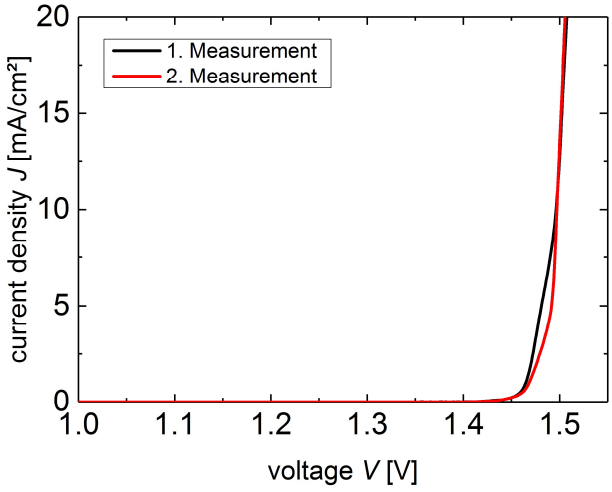

Figure 6.26: Repeated current density-voltage measurements for $NiFeO_X$ (deposition parameters see Table 6.3). No significant differences between both measurements are observed at current densities above 10 mA/cm². The difference between both curves observed for current densities below 10 mA/cm² is probably due to the overlap of oxygen evolution reaction and nickel oxidation peak[39].

To investigate the possible influences on the catalytic activity due to the changes after the contact to alkaline media during the electrochemical measurement sequence ((i), duration approximately 1.5 h), which were observed in the SEM images and XP spectra, repeated current density-voltage measurements were performed as part of a second electrochemical measurement sequence ((ii) directly after (i)), showing the performance of the nickel iron oxide catalyst regarding the oxygen evolution reaction. The measurements are shown in Figure 6.26 for a $NiFeO_X$ sample deposited using the following conditions given in Table 6.3, which were also employed for the samples investigated in the previous SEM and XPS section. The current density-voltage curves do not show significant differences for the potential obtained at 10 mA/cm², respectively 20 mA/cm².

The slight difference for current densities below 10 mA/cm² are possibly due to the overlap between oxygen evolution reaction and nickel oxidation peak, which has been discussed previously (see first section of this sub chapter).[39] The measurement shows the stable catalytic performance of the deposited nickel iron oxide layers. Considering also the results obtained by scanning electron microscope images and X-ray photoelectron spectroscopy, one may assume that the dense catalyst bottom layer consisting of nickel iron oxide/hydroxide shows the catalytic activity in the oxygen evolution reaction. However, long-term testing is needed to reveal the stability of the prepared catalyst films. The long-term performance of the earth-abundant catalyst system $NiFeO_X$ and NiMo is discussed in chapter (7.6.3).

Summary of the results for $NiFeO_X$

Electrodeposition was successfully used to prepare $NiFeO_x$ compounds as oxygen evolution catalysts to be used in water splitting devices. The prepared catalyst layers show a significantly improved performance compared to iridium oxide and nickel as reference systems. The overpotential measured for nickel iron oxide films is reduced by around 100 mV compared to iridium oxide. Overpotentials, which are lower for nickel iron oxide materials than for iridium oxide and nickel, have been reported in literature[108] with η_{IrOx} = 390 mV and η_{NiFeOx} in the range of 340 – 380 mV. The increased difference observed in the present work compared to the literature can possibly be related to different surface morphologies, and hence different electrochemically active surface areas, between the deposited nickel iron films and the commercially purchased iridium oxide on a titanium substrate.

The best performances and hence lowest overpotentials were found for materials deposited with an iron content of 15 – 25 mol% in the electrolyte prepared under various conditions (η in the range of 0.28 V – 0.30 V for samples deposited on 0.5 cm² area). Literature values, as listed in the previous paragraph, were reported for samples of 0.2 cm² substrate size in 1 M sodium hydroxide solution[108], thus the sample size is already increased by a factor of 2.5 in our preliminary experiments enabling a deposition area of 0.5 cm². The deposition on the electrode with a size of 50.3 cm² was carried out using the following deposition parameters: Ni:Fe ratio of 80:20 mol%, J_{dep} = -10 mA/cm², t_{dep} = 40 s, pulsed deposition mode (5 s pulse, 10 s stirring), T_{dep}= room temperature (RT). The results obtained for the deposition on 50.3 cm² electrode size are shown and discussed in section (7.5).

The SEM images show a layered structure for the $NiFeO_X$ catalyst with a dense bottom layer and a less dense top layer, which is nearly completely dissolved after the electrochemical measurement sequence with the dense bottom layer remaining. XPS studies confirm that iron is incorporated into the catalyst layer, which consists of a mixture of nickel metal, nickel oxide and nickel hydroxide species.[187] Prior to the electrochemical exposure to alkaline media, an XPS signal assigned to nickel metal was measured, which was strongly decreased after the measurement sequence. The nickel metal can be deposited due to the cathodic electrodeposition conditions. It can be assumed that the less dense top layer contains Ni^0 species or microscopic holes in the catalyst layer were detected leading to the Ni^0 signal, although the catalyst layer appeared to be dense. Further experiments, such as in situ XPS, are needed to clarify the ongoing processes during the oxygen evolution reaction. Despite the changes in surface morphology and surface composition, the electrochemical performance towards the oxygen evolution reaction is not affected as repeated measurements have shown. Long-term testing of the catalyst combined with nickel molybdenum is discussed in chapter (7.6.3) revealing the stability of the prepared catalyst films.

Results on nickel sheet substrates - NiMo for HER:

Deposition parameters and electrochemical characterization

For the electrodeposition of nickel molybdenum as hydrogen evolution catalyst, the same deposition setups as described and shown in Figure 6.18 were used. The deposition parameters, which were varied for the sample preparations on 0.5 cm² area and whose influence on the overpotential of the catalyst material towards the hydrogen evolution reaction was investigated, are the different times at a constant current density (J_{dep} = -160 mA/cm², varied Q_{dep}) and a constant charge density Q_{dep} (variation of J_{dep} and t_{dep}). The depositions were performed in continuous mode and the precursor ratio was constant. The influence of a constant deposition charge density of Q_{dep} = -192 C/cm²[40] is of interest for the deposition on larger sized electrodes (50.3 cm²) using the Gamry Reference 600 potentiostat as current source (current limit: 600 mA). Due to the limited current and therefore limited current density of the power source, the charge density for increased electrode areas could be kept constant by increasing the deposition time for lower current densities ($Q = Jt$). The conditions for the deposition on increased areas were determined by comparing the overpotential of the samples of 0.5 cm² size evaluated at -10 mA/cm² for the varied parameters obtained through linear sweep voltammetry measurements. The current density-potentials of several nickel molybdenum catalysts with varied parameters are shown in Figure 6.27. The curves of platinum and nickel are shown for comparison. Compared to the nickel reference, the potential of the deposited catalyst films is significantly reduced. Figure 6.27 shows no overlap of the hydrogen evolution reaction with another reduction such that the overpotential of the nickel molybdenum catalysts can be evaluated at -10 mA/cm². In the following section, the results of the varied parameter depositions are presented and discussed. Ideally, conditions yielding low overpotentials should be used for upscaling the catalyst material.

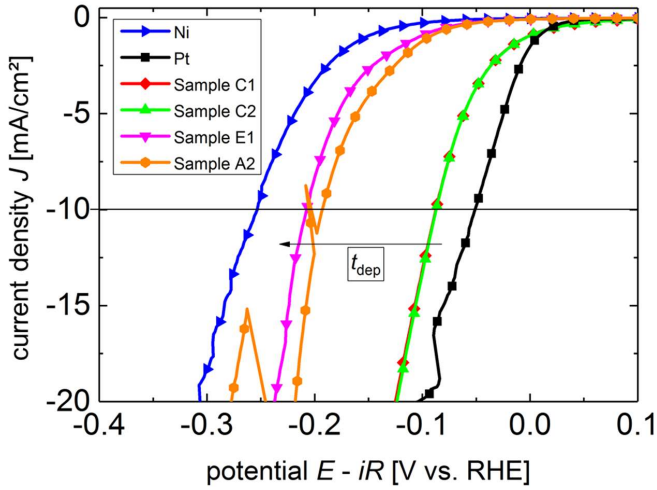

Figure 6.27: Current density-potential curves of different nickel molybdenum catalysts deposited under varied conditions. Nickel and platinum are shown for comparison. The potential of the NiMo catalysts is significantly reduced compared to the nickel reference and no overlapping reactions are observed.

Constant deposition current density

The first parameter to be investigated was the thickness dependence of activity. The samples were deposited using a current density of J_{dep} = -160 mA/cm² as reported in literature[40,108], while the deposition time t_{dep} and therefore the charge density Q_{dep} were varied. The deposition time t_{dep} was varied between 600 s and 1800 s, resulting in a charge density Q_{dep} in the range of -96 C/cm² to -288 C/cm². In the literature a preparation time of 1200 s, hence a charge density of Q_{dep} = -192 C/cm² is reported[40,108]. This first experiment was used to

determine the charge density Q_{dep} for the following variation of preparation conditions, in which the deposition charge density was kept constant. The overpotentials of the resulting samples were evaluated at -10 mA/cm², since no overlapping reaction occurred as shown in Figure 6.28 and listed in Table 6.4. The electrochemical characterization was carried out in a three-electrode setup using IrO_X as counter electrode and Ag|AgCl as reference electrode. 1 M potassium hydroxide solution was used as electrolyte. The overpotentials measured at -10 mA/cm² for nickel and platinum are shown for comparison.

Table 6.4: Overview of deposition parameters (deposition time t_{dep}, deposition current density J_{dep}, deposition charge density Q_{dep}) and overpotentials η for NiMo samples deposited under constant current density conditions (A-E) as well as nickel and platinum.

sample	t_{dep} [s]	J_{dep} [mA/cm²]	Q_{dep} [C/cm²]	η [V vs. RHE]
A1	600	-160	-96	-0.120
A2	600	-160	-96	-0.193
B	900	-160	-144	-0.075
C1	1200	-160	-192	-0.087
C2	1200	-160	-192	-0.087
C3	1200	-160	-192	-0.071
C4	1200	-160	-192	-0.050
C5	1200	-160	-192	-0.086
D	1500	-160	-240	-0.060
E1	1800	-160	-288	-0.066
E2	1800	-160	-288	-0.208
Ni	-	-	-	-0.254
Pt	-	-	-	-0.051

The deposited nickel molybdenum samples show overpotentials in the range of -50 – -208 mV, which are generally lower than the overpotential measured for nickel as reference (-254 mV). The samples A1, A2 and E2 show the highest overpotentials (-120 mV – -208 mV) for the prepared NiMo catalysts. In the case of the samples A1 and A2, this can be due to the low deposition time during which not sufficient material is accumulated on the surface and thus the catalyst layer is too thin. The samples E1 and E2 show quite different overpotentials, which can be due to the mechanical instability of the samples, which was observed during the characterization. In the case of sample E1, the catalyst layer was intact during the measurement sequence, but detached afterwards. Whereas in the case of sample E2 parts of the catalyst layer were detached during the measurement sequence, which could possibly lead to the comparatively high overpotential.

Samples C, which were deposited according to the conditions reported in literature, yielded overpotentials ranging from -50 – -87 mV, giving -76 mV as mean value. The measured overpotentials are close to the overpotential measured for platinum (-51 mV). The overpotentials measured for samples B (-75 mV) and D (-60 mV) are in the same range as for sample C. Overpotentials reported in literature for nickel molybdenum, using nickel(II) sulfate, sodium molybdate and sodium citrate as precursors, are -40 mV. For a second electrodeposition approach using different precursors, the reported overpotential for NiMo accounts for -70 mV.[108] The obtained overpotential values (down to -50 mV) in the present work and the reported overpotential value are in good agreement. The reference values reported in literature were measured for sample sizes of 0.2 cm² in 1 M sodium hydroxide solution.[108] The difference between the reported overpotentials and the measured overpotentials in the present work could be due to the increased sample size of 0.5 cm² used in the present work.

As mentioned in the first paragraph of this section, the experiments conducted under constant current density deposition were used to determine the deposition charge density for the following experiments. A deposition charge density of -192 C/cm² was used, since it showed overall reasonable overpotentials and the lowest overpotential determined for one sample.

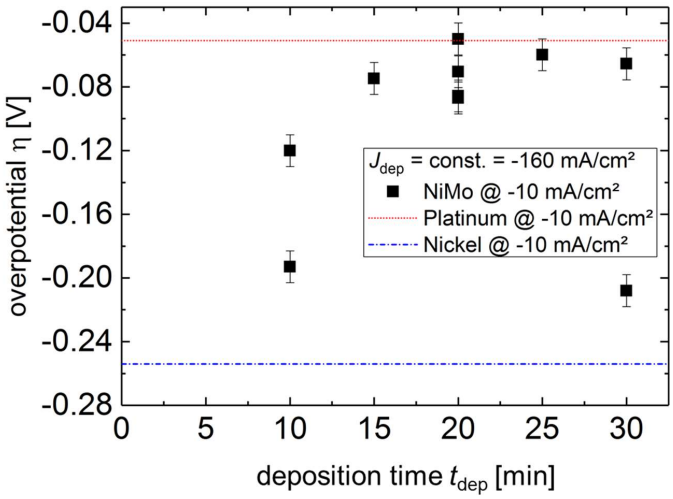

Figure 6.28: Overpotential measured for NiMo samples deposited under constant current density conditions (-160 mA/cm²), varying the deposition time (600 – 1800 s) and thus the deposition charge density. The overpotentials measured for nickel and platinum are shown for comparison.

Constant charge density conditions

In the following section, the electrodeposition of nickel molybdenum was carried out under constant deposition charge density conditions, which was determined in the previous section and accounts for -192 C/cm². In order to deposit with a fixed charge density, the deposition time and deposition current density were varied. The deposition under constant charge density conditions is of interest for the deposition on upscaled electrodes, as described in the introduction to this section.

The samples deposited under constant charge density conditions were compared with respect to their overpotential. The measurements were performed in three-electrode configuration with Ag|AgCl as reference electrode and IrO_X as counter electrode. The deposition conditions and the resulting overpotentials (evaluated at -10 mA/cm²) are shown in Figure 6.29 and in Table 6.5. A current density-potential curve exemplarily showing the results for two samples deposited under constant deposition charge conditions can be found in the appendix (see Figure A7). The samples (F-M) show very similar overpotentials in the range of -50 – -89 mV, which are similar to the reported literature values for NiMo of -40 mV using the same precursors[108] and significantly improved compared to the overpotential measured for nickel (-254 mV). As discussed in the previous section on the constant deposition current density, the difference between the measured and reported overpotential range could be due to an increased sample size from 0.2 cm² (literature[108]) to 0.5 cm² (present work).

Overall, the deposition of nickel molybdenum under constant deposition charge density conditions (Q_{dep} = -192 C/cm²) yields overpotential values in a similar range of -50 – -89 mV. The deposition of nickel molybdenum on increased electrodes with the size of 50.3 cm² was performed using constant deposition charge density conditions with the following parameters: t_{dep} = 19200s, J_{dep}= -10 mA/cm², Q_{dep} = -192 C/cm², T_{dep}= room temperature (RT), stirring 800 rpm, continuous mode. The obtained results are presented and discussed in section (7.5).

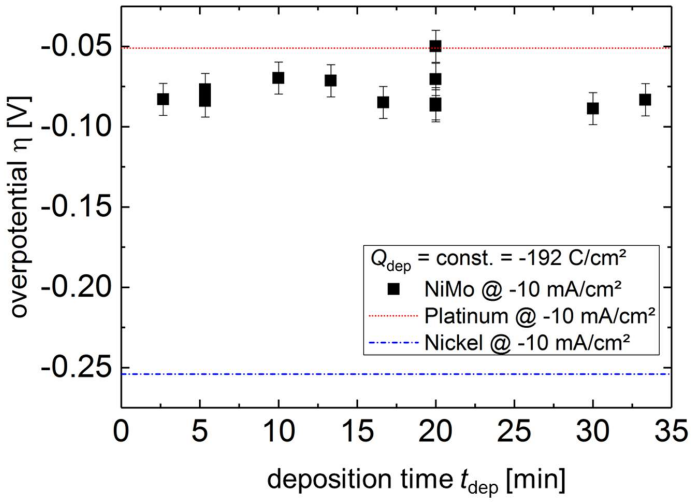

Figure 6.29: Overpotential evaluated at -10 mA/cm² over deposition time for samples deposited under constant charge density conditions (Q_{dep} = -192 C/cm²). The overpotentials of nickel and platinum are indicated for comparison.

Table 6.5: Overview of deposition parameters (deposition time t_{dep}, deposition current density J_{dep}, deposition charge density Q_{dep}) and overpotentials η for NiMo samples deposited under constant charge density conditions (F-M) as well as nickel and platinum.

Sample	t_{dep} [s]	J_{dep} [mA/cm²]	Q_{dep} [C/cm²]	η [V vs. RHE]
F	160	-1200	192	-0.083
G1	320	-600	192	-0.077
G2	320	-600	192	-0.084
H	600	-320	192	-0.070
I	800	-240	192	-0.071
J	1000	-192	192	-0.085
K1	1200	-160	192	-0.087
K2	1200	-160	192	-0.087
K3	1200	-160	192	-0.071
K4	1200	-160	192	-0.050
K5	1200	-160	192	-0.086
L	1800	-107	192	-0.089
M	2000	-96	192	-0.083
Ni	-	-	-	-0.254
Pt	-	-	-	-0.051

Spectroscopic characterization and influence of electrochemical measurement sequence

Since the deposition under constant charge conditions was one of the aspects investigated for the upscaling of material, samples deposited under these conditions were compared regarding their surface morphology and thickness using top-down and cross-sectional scanning electron microscope images. The chemical composition of two samples (G and K, see Table 6.5) deposited under constant deposition charge density conditions is investigated using x-ray photoelectron spectroscopy.

Additionally, the surface morphologies and chemical composition prior and after the electrochemical characterization sequence are compared to indicate possible changes caused by the use as hydrogen evolution catalyst in alkaline media. Ideally, catalyst materials are not consumed during the reaction, as described in

chapter (3.2.4). By comparing the results before and after the electrochemical characterization sequence, it can be evaluated, if this accounts for the prepared nickel molybdenum catalysts. Finally, changes in the electrochemical activity regarding the hydrogen evolution reaction are determined by repeated linear sweep voltammetry measurements.

SEM studies before and after electrochemical measurement sequence

Scanning electron microscope images were taken of different samples (G and K, see Table 6.5) deposited under constant charge density conditions (Q_{dep} = -192 C/cm²), showing possible differences in surface morphology and thickness. The top-down images before and after performing the electrochemical measurement sequence are used to determine possible morphology changes due to the use in alkaline media.

Figure 6.30 shows top-down SEM images of samples deposited under constant charge density conditions (Q_{dep} = -192 C/cm²) for sample G (320 s at -600 mA/cm²) and sample K (1200 s at -160 mA/cm²). The images (a), (b) and (e), (f) show for both samples a cauliflower structure with a high surface area. In both cases, cracks within the catalyst layer are visible. The sizes of the features shown in image (a) (sample G) are slightly smaller than the features seen in image (e) (sample K). The smaller feature sizes observed for sample G could be due to the shorter deposition time and higher deposition current density compared to the parameters used for sample K. In both cases, complete surface coverage with the highly interconnected cauliflower structures were observed.

Comparing the surface morphology prior and after the electrochemical characterization sequence, all images (c), (d) and (g), (h) show no differences in the surface morphology compared to the initial state. The only difference that can be identified, are small residues on the surface structures (probably potassium hydroxide), as can be seen for both samples in the images (d) and (h). Thus, nickel molybdenum materials show a stable morphology for the application as HER catalyst in alkaline media.

The Figure 6.31 show cross-sectional SEM images of samples deposited under constant deposition charge density conditions (Q_{dep} = -192 C/cm²), which were taken to investigate the thickness of the catalyst layers as well as the corresponding features for varied deposition times and current densities. The samples were cut mechanically, which in most cases led to a detachment of the catalyst layers from the substrates at the cutting edge. The following deposition conditions were used to prepare the shown samples (see also Table 6.5): G 320 s at -600 mA/cm², H 600 s at -320 mA/cm², K 1200 s at -160 mA/cm² and L 1800 s at -107 mA/cm². Comparing sample G to sample L, one can identify different feature sizes. For sample G (short deposition time, high deposition current density), the deposited features are smaller and resemble small spheres, while for sample L (long deposition time, low deposition current density) more massive spheres with flatter surfaces can be seen. The samples H and K support the trend that samples with short deposition times and high deposition current densities show smaller features, while samples with increased deposition time and decreased deposition current density show more massive spheres with flatter surfaces. All investigated samples G – L show a complete surface coverage and high surface areas. The layer structure consists of a denser layer of 0.5 – 3 µm height, which is directly in contact with the nickel substrate, followed by an intergrowth into the cauliflower like structure. Total layer thickness in the range of 41 – 96 µm were measured, as indicated in Figure 6.31.

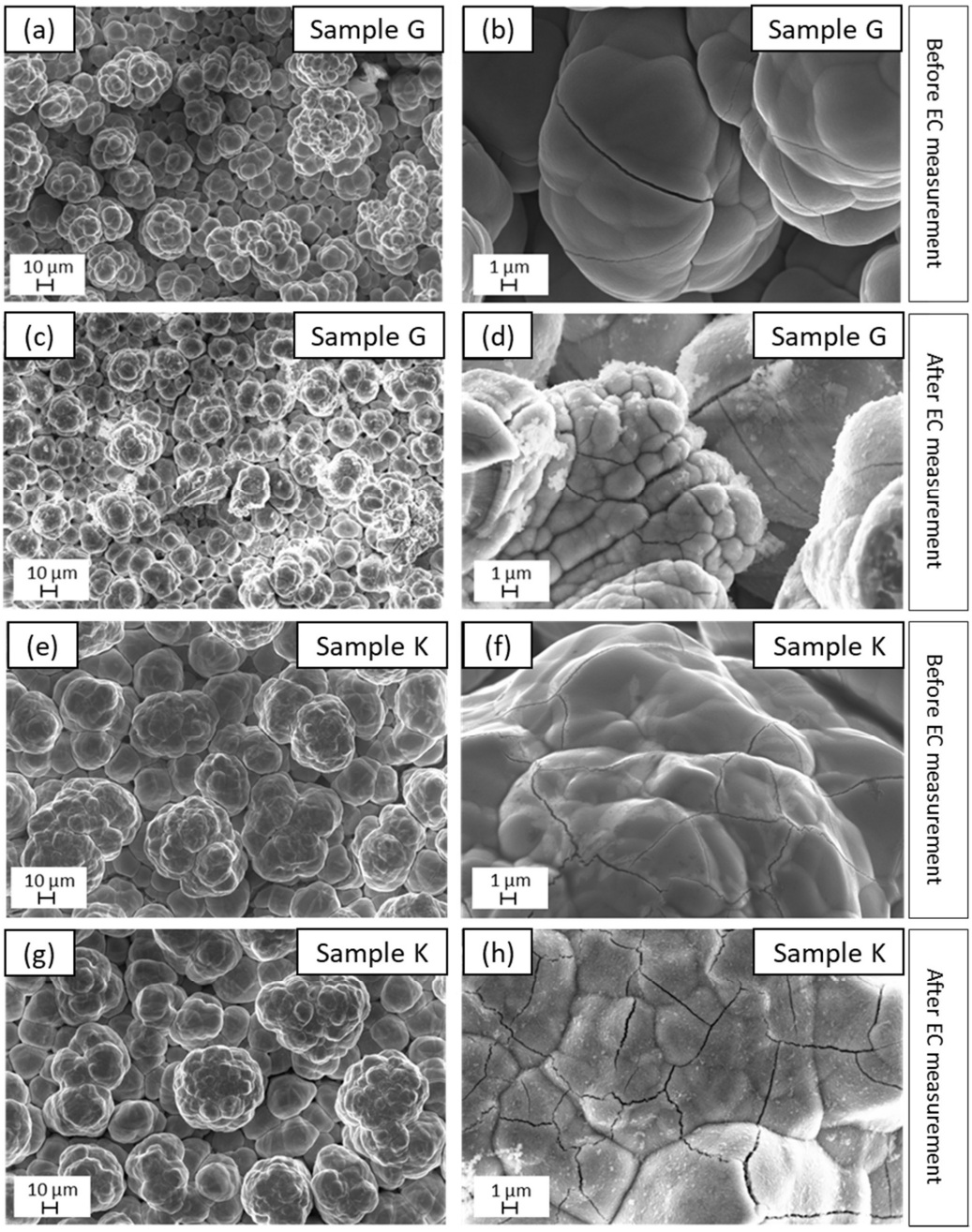

Figure 6.30: Top-down SEM images of two samples deposited under constant charge density conditions before and after the electrochemical measurement sequence: Sample G 320 s at -600 mA/cm² and sample K 1200 s at -160 mA/cm². A cauliflower structure can be seen for both samples, which is well preserved after the electrochemical measurement sequence.

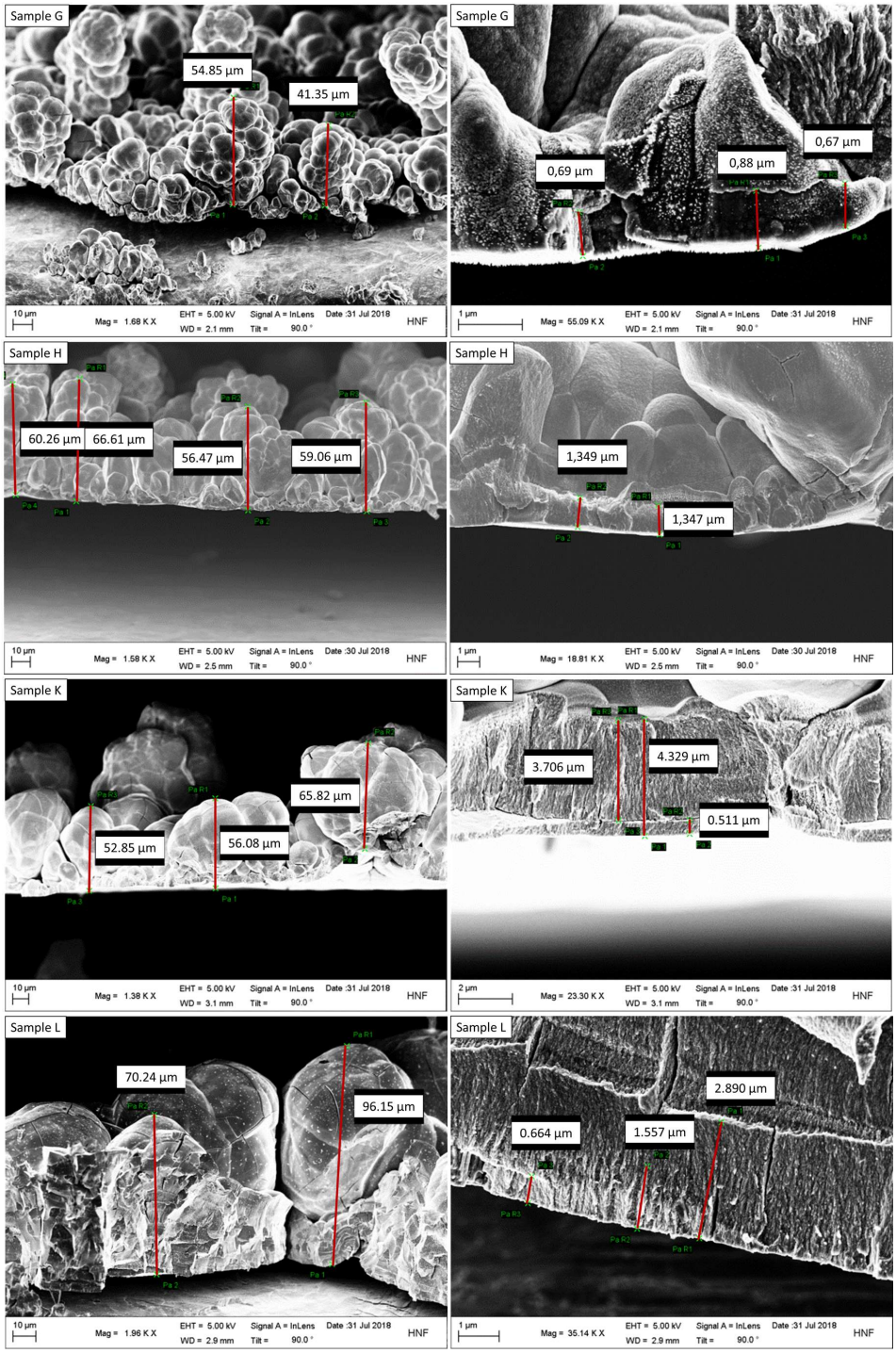

Figure 6.31: Cross sectional SEM images of samples deposited under constant deposition charge density conditions (Q_{dep} = -192 C/cm²). The deposition parameters are listed in Table 6.5 for the samples G, H, K and L.

XPS studies before and after the electrochemical measurement sequence

The chemical composition of the nickel molybdenum films deposited under constant deposition charge density conditions (Q_{dep} = -192 C/cm²) and possible changes due to the use in alkaline media were investigated using X-ray photoelectron spectroscopy. In the following Figure 6.32 - Figure 6.35 the XP spectra for carbon (Figure 6.32), oxygen (Figure 6.33), molybdenum (Figure 6.34) and nickel (Figure 6.35) are shown, comparing the spectra of the differently deposited samples before the electrochemical measurement sequence (black curve) to the spectrum after the electrochemical measurement sequence (red curve). The deposition parameters of the investigated samples G and K can be found in Table 6.5. The emission for the carbon C-C binding energy was used as reference for the XPS measurements and set to 285 eV. The other spectra were corrected with the offset determined from the carbon spectrum.

The following emission lines are visible in the carbon spectra measured for both samples: C-C at 285 eV, C-O-C at 285.7 eV and O-C=O at 288.7 eV.[184,185] The C-C as well as the O-C=O peak can clearly be seen in the spectra. The C-O-C emission overlaps with the C-C peaks and can be identified as asymmetric shoulder in all cases. Comparing the spectra before and after the electrochemical measurement sequence for both samples shows that the observed emission lines are found in all spectra. The intensities of the C-C and the O-C=O peaks are decreased after the electrochemical measurement sequence, which can be due to the removal of deposited electrolyte residues as it contains sodium citrate. In general, the carbon content on the surface can also result from storage and handling of the samples in air causing the accumulation of organic molecules on the surface. The samples were not sputtered for cleaning purposes prior to the measurement in order to keep the surface composition after the electrochemical measurement sequence unchanged.

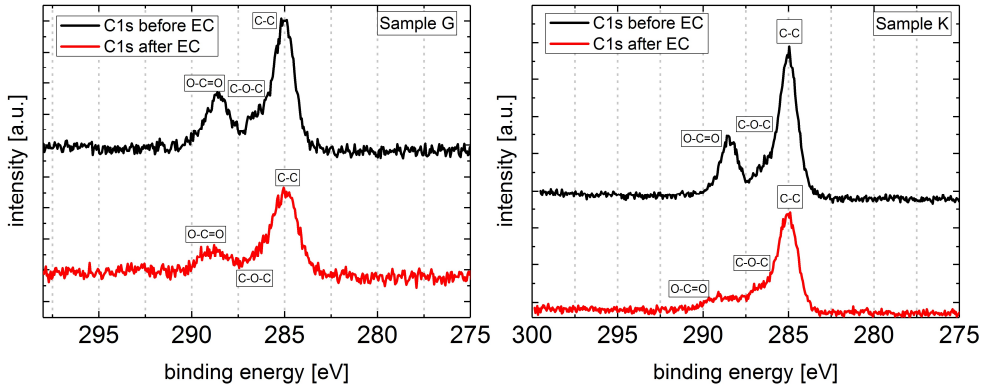

Figure 6.32: Carbon XP spectra of NiMo deposited at constant charge density conditions before and after the electrochemical measurement sequence (for deposition parameters see Table 6.5). Different carbon species are identified.

The oxygen XP spectra are shown in Figure 6.33. The following emission lines are identified for sample G: NiO species at 529.5 eV and $Ni(OH)_2$ 531.2 eV.[184,185] Both lines are overlapping, but can be clearly determined prior and after the electrochemical characterization sequence. Thus, the catalyst layer of sample G is neither completely oxidic nor completely hydroxidic. The intensity of both emissions is increased after the exposure to alkaline media, which can be due to the formation of nickel hydroxide on the surface: the shape of the indicated peaks remains unchanged.

In the case of sample K, the nickel hydroxide ($Ni(OH)_2$) line at 531.2 eV is also clearly visible.[184,185] Additionally, a peak at 536 eV can be seen prior to the electrochemical characterization sequence, which is caused by Auger electrons emitted by sodium (Na KLL) from residues of the deposition electrolyte containing sodium citrate. After the electrochemical characterization sequence, the sodium peak is not observed anymore and the nickel hydroxide shows an asymmetric right shoulder, which can possibly be attributed to the formation of nickel oxide. However, a nickel oxide peak cannot clearly be determined, as for example in the spectra of sample G.

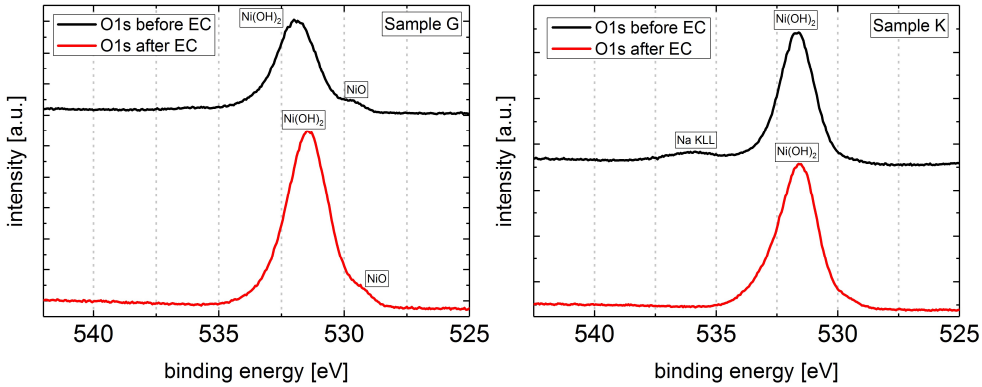

Figure 6.33: Oxygen XP spectra of NiMo deposited at constant charge density conditions before and after the electrochemical measurement sequence (for deposition parameters see Table 6.5). Different oxygen and sodium species are indicated.

Figure 6.34 shows the molybdenum spectra measured before and after the electrochemical measurement sequence for the two samples deposited under constant charge conditions. For sample G, the following emissions are visible in the spectra: MoO_3 at 232.5 and 235.6 eV and Mo^0 at 227.7 eV.[184,185] Comparing the spectra before and after the electrochemical measurement sequence, the intensities of the molybdenum peaks are increased after the characterization sequence. Prior to the sequence, the molybdenum peaks are only slightly visible, but can be identified. Overall, it is confirmed that the deposited catalyst layer of sample G contains molybdenum in the form of MoO_3 and Mo metal.

In the XP spectra of sample K, the peaks identified are: MoO_3 at 232.5 and 235.6 eV and Mo^0 at 227.7 eV.[184,185] In contrast to sample G, the XP spectra of sample K show a contrary effect. After the electrochemical characterization sequence, the intensity of the molybdenum peaks in the XP spectra is decreased such that the peaks are only slightly visible. The reduction of the peak intensities could be caused by deposited electrolyte residues in the form of sodium molybdate, which are removed after the electrochemical characterization sequence. Also for sample K, it is confirmed that molybdenum is incorporated into the catalyst layer in the form of MoO_3 and Mo metal, although the contrary effects as observed for the intensities of the molybdenum species for sample G and K prior and after the electrochemical sequence cannot be explained.

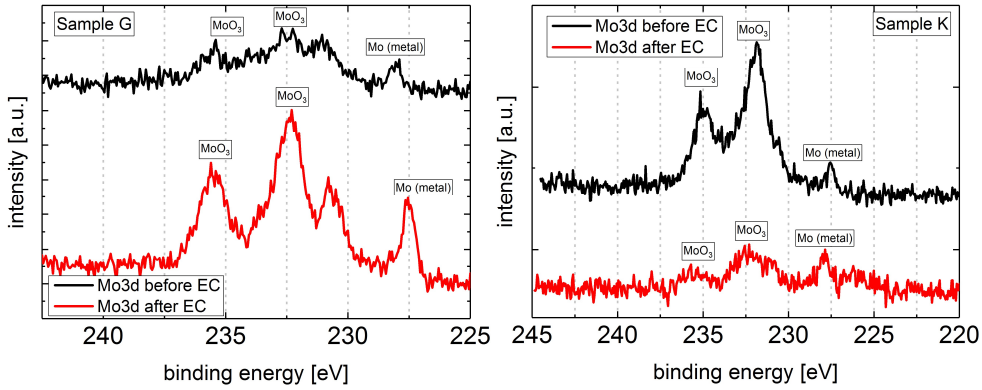

Figure 6.34: Molybdenum XP spectra of NiMo deposited at constant charge density conditions before and after the electrochemical measurement sequence (for deposition parameters see Table 6.5). Different molybdenum species are identified.

The nickel XP spectra are shown in Figure 6.35 for both samples. In the case of sample G, the following emissions are identified: Ni^0 at 852.6 accompanied by a satellite signal at 861 eV (satellite prior to the

electrochemical characterization) and $Ni(OH)_2$/NiO at 855.6 eV with corresponding shake up bands after the electrochemical measurement sequence.[184,185] After the electrochemical measurement sequence, the intensity of the Ni^0 peak is reduced, while the intensity of the $Ni(OH)_2$/NiO peak is increased. Additionally, the Ni^0 satellite peak is overlapped by the $Ni(OH)_2$ shake up bands after the electrochemical characterization sequence. These effects are probably due to the formation of nickel hydroxide on the surface in alkaline media. The same peaks and trends are observed for sample K, as shown in the XP spectra. Overall, the XP spectra for both samples suggest that a nickel alloy (Ni^0 state) with molybdenum is deposited as catalyst layer, which partially forms nickel hydroxide in alkaline media during the reaction. Clearly visible Ni^0 peaks can be identified after the exposure to alkaline media for sample G and K, possibly showing the stability of the alloy during the use as HER catalyst.

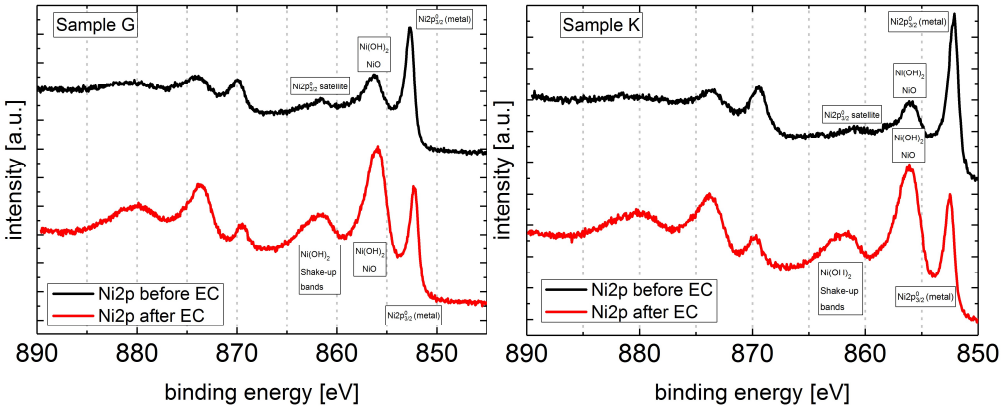

Figure 6.35: Nickel XP spectra of NiMo deposited at constant charge density conditions before and after the electrochemical measurement sequence (for deposition parameters see Table 6.5).

Summarizing the results obtained by XP spectra, it was confirmed that molybdenum is incorporated into the catalyst layer for both samples deposited under constant deposition charge density conditions. In both cases, molybdenum species in the form of MoO_3 and Mo metal were found. The obtained results suggest that both catalyst layers consist of nickel alloy (Ni^0). For sample G (deposition parameters can be found in Table 6.5), nickel oxide and nickel hydroxide peaks were found in the oxygen spectra, while for sample K only nickel hydroxide was found. Comparing the spectra of the samples before and after the electrochemical measurement sequence, in both cases, a small nickel hydroxide signal is observed in the spectra prior to the electrochemical measurement sequence, which is increased after the characterization, while the Ni^0 signal is also obtained. Thus, after the characterization, nickel hydroxide and possibly nickel alloy (Ni^0 state) are present on the catalyst surface layer. In the case of the molybdenum species, contrary effects for both samples were observed regarding the intensity after the electrochemical measurement sequence. In the case of sample G, the intensities of the molybdenum peaks are increased after the sequence, while for sample K the intensities are decreased. No convincing explanation can be given for the contrary effects.

Repeated current density-voltage measurements

To investigate possible influences on the catalytic activity due to the changes after the electrochemical measurement sequence (i) in alkaline media, repeated current density-voltage measurements as part of a second electrochemical measurement sequence (ii) were performed ((ii) directly after (i)), showing the performance of the nickel molybdenum catalyst regarding the hydrogen evolution reaction. Considering the results obtained by X-ray photoelectron spectroscopy and scanning electron microscope images, no performance decrease for nickel molybdenum catalysts is expected. The measurements are shown in Figure 6.36 for NiMo sample K (deposited for 1200 s at -160 mA/cm², see also Table 6.5). The current density-voltage curves do not show

significant differences for the potential obtained at -10 mA/cm². The measurements show the stable catalytic performance of the deposited nickel molybdenum layers. However, long-term testing is needed to investigate the stability of the prepared catalyst films. The long-term performance of the earth-abundant catalyst system $NiFeO_X$ and NiMo is discussed in chapter (7.6.3).

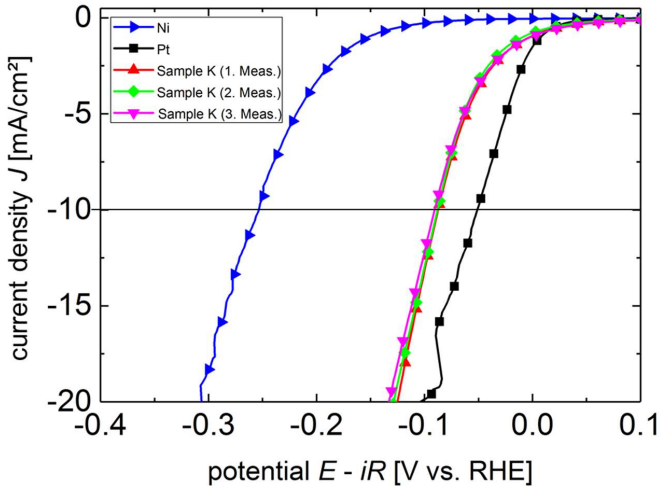

Figure 6.36: Repeated current density-potential measurements for NiMo (sample K, see Table 6.5). No significant differences between both measurements are observed at a current density of -10 mA/cm².

Summary of the results for NiMo

Nickel molybdenum catalyst layers were successfully prepared using electrodeposition. In a first experiment, the deposition current density was kept constant, while the deposition time and thus the charge density were varied. The charge density yielding low overpotentials was used in the second step to investigate if the electrodeposition can be performed under constant deposition charge density conditions. The experiments show that electrodeposited NiMo allows a wide range of electrodeposition conditions, since a varied deposition time at a constant current density or the constant charge density preparation lead to similar overpotentials. The overpotentials measured for the prepared NiMo catalysts, which are in the range of -50 – -208 mV towards the hydrogen evolution reaction, are significantly reduced compared with pure nickel substrates (-254 mV). The lowest overpotentials measured for nickel molybdenum in the present work are in the range of -50 – -89 mV. Overpotentials reported in literature for nickel molybdenum account for -40 mV. The difference between the measured overpotentials in the present work and the reported overpotential could be due to the sample size. The reference values reported in literature were obtained for sample sizes of 0.2 cm² in 1 M sodium hydroxide solution[108], while in the present work a sample size of 0.5 cm² was used. The results suggest that the deposition under constant deposition charge density conditions can be performed without a loss in performance towards the hydrogen evolution reaction. Therefore, the electrodeposition of NiMo on large sized electrodes (50.3 cm²) was performed using the following parameters: t_{dep} = 19200 s, J_{dep} = -10 mA/cm², Q_{dep} = -192 C/cm² and continuous deposition mode (see section (7.5)).

The top-down SEM images (Figure 6.30) of samples G and K (see Table 6.5 for deposition parameters) deposited under constant deposition charge density conditions show in both cases a cauliflower like structure with high surface areas, which is preserved after the electrochemical characterization sequence. Comparing the cross-sectional SEM images (Figure 6.31) of samples deposited under constant deposition charge density conditions, it was observed that samples with short deposition times and high deposition current densities show smaller features, which resemble small spheres, while samples with increased deposition time and decreased deposition current density show more massive spheres with flatter surfaces. In all cases, the layer structure

consists of a denser layer, which is directly in contact with the nickel substrate, followed by an intergrowth into the cauliflower like structure. Total layer thicknesses in the range of 40 – 96 µm were measured.

The XP spectra confirmed that molybdenum is incorporated into the catalyst layer for samples deposited under constant deposition charge density conditions. Molybdenum species in the form of MoO_3 and Mo metal were found. The obtained results suggest that deposited catalyst layers consist of nickel alloy (Ni^0). For the sample with short deposition time and high deposition current density, nickel oxide and nickel hydroxide peaks were found in the oxygen spectra, while only nickel hydroxide was found for the sample prepared with increased deposition time and reduced deposition current density. Comparing the spectra of the samples before and after the electrochemical measurement sequence, in both cases, a small nickel hydroxide signal is observed in the spectra prior to the electrochemical measurement sequence, which is increased after the characterization, while the nickel^0 signal is also obtained. Thus, after the characterization, nickel hydroxide and possibly nickel alloy are present on the catalyst surface layer. In the case of the molybdenum species, contrary effects for the investigated samples G and K (see also Table 6.5) were observed regarding the intensity after the electrochemical measurement sequence. In one case, the intensities of the molybdenum lines are increased after the sequence, while for the other sample, the intensities are decreased. No convincing explanation can be given for this contrary effect. The electrochemical performance towards the hydrogen evolution reaction is constant as repeated measurements showed and one could expect from the results obtained by XPS and SEM. Long-term testing of the catalyst combined with nickel iron oxide is discussed in chapter (7.6.3), revealing the stability of the prepared catalyst films.

7.4 Theoretical calculation of PV-EC device performance using earth-abundant catalysts

The results obtained for earth-abundant catalyst materials on nickel foam or nickel sheets of 0.5 cm² size in the previous section are quite promising for the application in water splitting devices, since the overpotentials are significantly reduced compared to untreated nickel electrodes. In order to estimate the performances of water splitting devices employing the catalyst systems, Co-Fe LDH/$Ni_XMo_YN_Z$ and $NiFeO_X$/NiMo, the current density-voltage curves of the PV-EC devices were calculated. Therefore, the individually measured current density-voltage curve of an a-Si:H/a-Si:H/µc-Si:H triple junction solar cell was combined with the current density-voltage curves of the catalyst systems measured in alkaline media using the electric series connection model described in chapter (4.5). For better comparison to reported values, the calculation was performed using the current density-voltage curve of the a-Si:H/a-Si:H/µc-Si:H triple junction solar cell that was employed in the water splitting device for which a solar-to-hydrogen efficiency of 9.5 % was measured.[24,34] For the use of a-Si:H/µc-Si:H/µc-Si:H triple junction solar cells developed in the present work, the respective calculation and figure can be found in section (5.4). Comparing both triple junction solar cells, the a-Si:H/µc-Si:H/µc-Si:H offers some benefits, such as for instance lower degradation[34], but requires longer deposition times and offers slightly lower photovoltages compared to a-Si:H/a-Si:H/µc-Si:H.

Figure 6.37 shows the current density-voltage characteristics of the PV-EC devices using a-Si:H/a-Si:H/µc-Si:H triple junction solar cell and (i) platinum and iridium as noble metal catalyst system, (ii) cobalt-iron layered double hydroxide (Co-Fe LDH) together with nickel molybdenum nitride and (iii) nickel iron oxide and nickel molybdenum (sample area 0.5 cm²). The respective solar-to-hydrogen efficiencies are calculated at zero bias according to equation (40). The calculation shows that both earth-abundant catalyst systems (ii) and (iii) outperform the noble metal catalyst system (i), supporting the high potential of the prepared earth-abundant catalyst systems. The catalyst system consisting of $NiFeO_X$/NiMo shows the highest calculated solar-to-hydrogen efficiency of 9.7 % on a sample area of 0.5 cm². Compared to the reported solar-to-hydrogen efficiency of 9.5 %, which was achieved for the same triple junction solar cell combined with platinum and ruthenium oxide, the noble metal catalysts can be replaced by the earth-abundant catalysts without performance losses. Thus, a highly active earth-abundant catalyst system may also outperform the noble metal catalyst system on increased scale, as will be discussed in the following section.

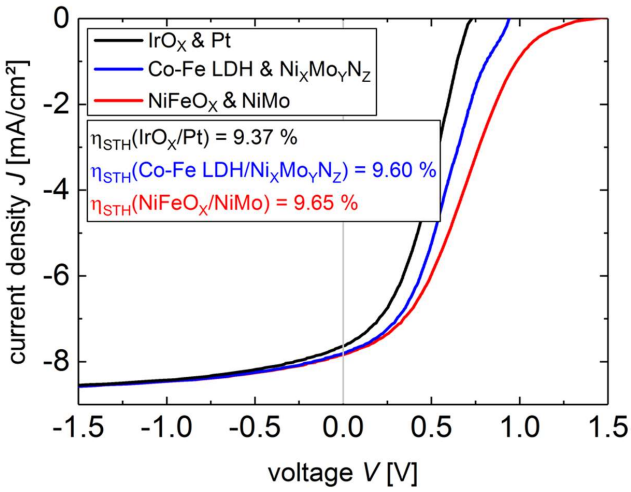

Figure 6.37: Calculated current density-voltage curves for PV-EC devices consisting of an a-Si:H/a-Si:H/µc-Si:H triple junction cell and various catalyst systems ((i) IrO_X/Pt, (ii) Co-Fe LDH/$Ni_XMo_YN_Z$, (iii) $NiFeO_X$/NiMo) on 0.5cm² area.

7.5 Characterization of HER and OER catalysts on electrodes of 50.3 cm²

Deposition conditions and images of NiMo and $NiFeO_X$ on 50.3 cm²

In the previous sections, the oxygen evolution reaction catalyst nickel iron oxide and the hydrogen evolution reaction catalyst nickel molybdenum were tested on sample sizes of 0.5 cm² in order to determine the conditions for the deposition on electrodes of 50.3 cm² size fitting in the modular device.[35] Various deposition parameters, such as the deposition time, the charge density or the mode, were varied and the resulting overpotentials were evaluated depending on these parameters. The following parameters were determined in the previous section to perform the electrodeposition on increased sample sizes:

NiMo: c_{Mo} = 28 mol%, t_{dep} = 19200 s, J_{dep} = -10 mA/cm², Q_{dep} = -192 C/cm² and continuous deposition mode.

$NiFeO_X$: c_{Fe} = 20 mol%, t_{dep} = 40 s, J_{dep} = -10 mA/cm², Q_{dep} = -400 mC/cm² and pulsed deposition mode.

For further information about the determination of the parameters and the overpotentials obtained for the different deposition conditions, please refer to the previous section (7.3.2). The electrodeposition on 50.3 cm² was performed using the setup shown in Figure 6.18 in two-electrode configuration, employing a nickel sheet as counter electrode.

Images of the two catalysts deposited on 50.3 cm² nickel sheet electrodes are shown in Figure 6.38 before (a) and after (b) the use in alkaline media in the upscaled device. Both materials show a good surface coverage, while the nickel iron oxide appears to be more homogeneously deposited. Prior to the contact to alkaline media, nickel iron oxide shows a yellow brown color (a), which changes to black brownish (b) after the use as OER catalyst in alkaline media. The color change can possibly indicate the formation of nickel iron oxide hydroxide (NiFe(O)(OH)) on the surface, which is reported to have a black color and to be the active catalytic species[172]. However, NiFe(O)(OH) could not specifically be determined in the XP spectra of $NiFeO_X$ shown in section (7.3.2). In the case of nickel molybdenum, good, but less homogeneous electrode surface coverage was achieved. Prior to the use in alkaline media, the surface coating is grey and black at the edges, while after the use in alkaline media, the color changes to brownish grey with remaining black color at the edges. The color change could possibly correspond to the increased amount of nickel hydroxide on the surface, which was observed in the XPS analysis in the previous section. The image in Figure 6.38(b) could possibly show the

nickel hydroxide and nickel alloy species obtained in the XP spectra measured for NiMo after the electrochemical measurement sequence.

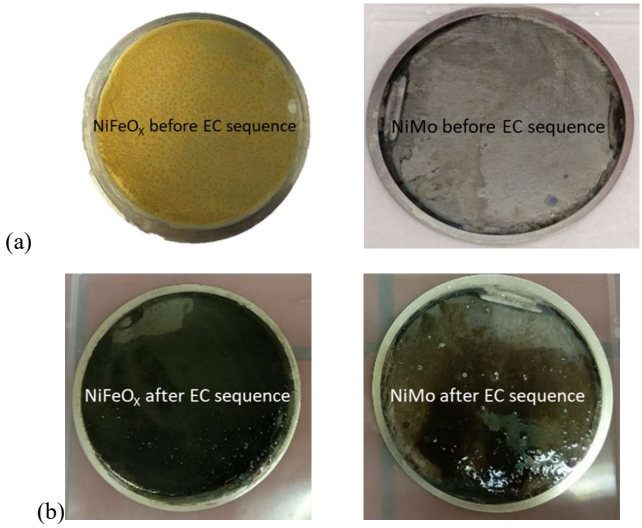

Figure 6.38: Images of the catalyst materials on electrodes on 50.3 cm² size prior (a) and after (b) the use as catalyst in alkaline media.

Electrochemical characterization of catalyst coated electrodes of 50.3 cm² size

Prior to the implementation into the PV-EC device, different catalyst systems were tested regarding their current density-potential curves and their potential over time. The measurements were performed in two-electrode configuration in alkaline media. The catalyst systems include a noble metal reference system of platinum and iridium oxide (both supplied by Metakem and deposited on titanium substrates), earth-abundant catalyst systems nickel/nickel and the prepared nickel iron oxide/nickel molybdenum as well as systems of noble metal catalysts combined with earth-abundant materials.

The current density-potential curves of the various systems are shown in Figure 6.39. The overpotential values of the shown catalyst systems were evaluated at a current density of 8 mA/cm² and not at typically used 10 mA/cm², since for two systems, the current density-potential curve was only measured up to 9 mA/cm². Additionally, the iR correction was not performed because the resistance values could not be determined in all cases.

The highest potential of 2.08 V is measured for the nickel/nickel system, which was expected from literature[108]. By replacing the nickel electrode used for the oxygen evolution reaction side with iridium oxide or nickel iron oxide, the potentials of the catalyst systems are reduced to 1.99 V and 1.85 V, respectively. The lower potentials obtained for the system consisting of nickel iron oxide (OER) and nickel (HER) compared to the system iridium oxide (OER) and nickel (HER) are due to the more active nickel iron oxide species (OER). This effect has also been observed for the catalyst samples deposited on 0.5 cm² size and has been discussed in detail in section (7.3.2). By replacing the nickel electrode on the hydrogen evolution reaction side, the potential of the system IrO_X (OER) and NiMo (HER) is reduced to 1.90 V, while for the system $NiFeO_X$ (OER) and NiMo (HER) a potential of 1.77 V is measured. The obtained potential for the $NiFeO_X$/NiMo system is similar to the measured potential of the noble metal reference system iridium oxide (OER)/platinum (HER) in alkaline media on electrode sizes of 50.3 cm².

The overpotentials at 10 mA/cm² of the main systems nickel/nickel, nickel iron oxide/nickel molybdenum and iridium oxide/platinum were determined using the current density-potential curves with iR correction, which

are shown in Figure 6.40. The thermodynamic water splitting potential of 1.23 V is indicated by the grey vertical guideline, while the potentials at 10 mA/cm² are highlighted by the grey horizontal guideline. For the system of nickel/nickel an overpotential of ~690 mV (vs. 1.23 V, at 10 mA/cm²) was found, while for $NiFeO_X$ and NiMo an overpotential of ~455 mV vs. 1.23 V at 10 mA/cm² was measured. The noble metal reference system consisting of platinum and iridium oxide shows an overpotential of ~450 mV vs. 1.23 V at 10 mA/cm². All values were obtained for catalysts on 50.3 cm² sized electrodes. Thus, the prepared upscaled earth-abundant catalyst system of $NiFeO_X$/NiMo is a very good alternative to noble metal catalyst systems in alkaline media.

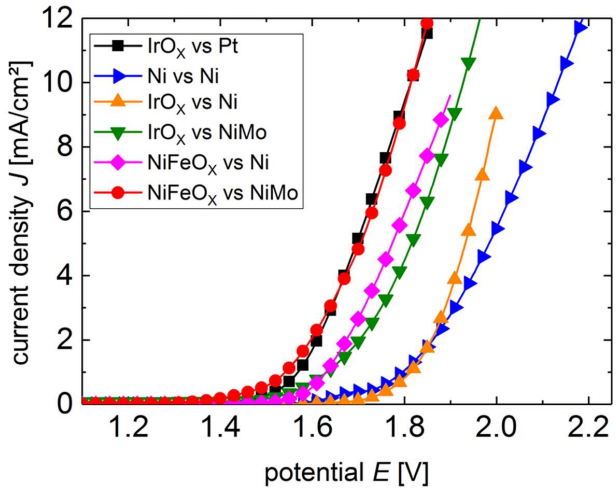

Figure 6.39: Current density-potential curves measured for various catalyst systems in alkaline media for an electrode size of 50.3 cm².

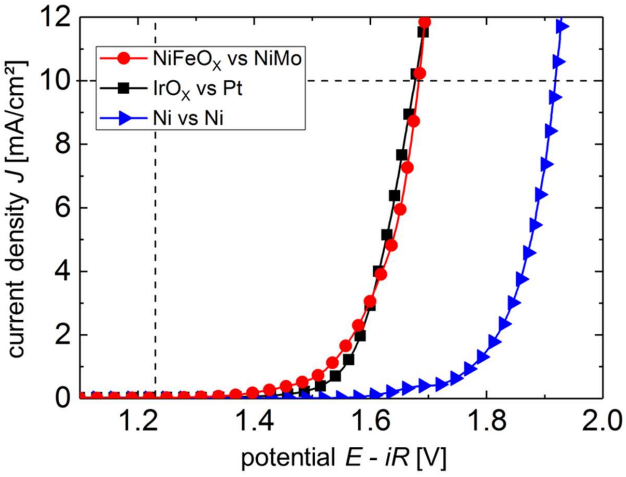

Figure 6.40: Current density-potential curves after iR correction of the main catalyst systems nickel/nickel (blue triangles), IrO_X/Pt (black squares) and $NiFeO_X$/NiMo (red dots) measured for samples of 50.3 cm² size, which were used for the determination of the overpotentials at 10 mA/cm². The thermodynamic water splitting potential is indicated at 1.23 V (vertical guideline) and the potentials at 10 mA/cm² are highlighted by the horizontal guideline.

Chronopotentiometric measurements were performed for the different catalyst systems, which are shown in Figure 6.41. The potential over 900 s was measured for an electrolysis at a current density of -10 mA/cm² in alkaline media. As expected from Figure 6.39, the nickel/nickel system shows the highest absolute potential value of 2.1 V and similarly to the previous figure, the absolute potential values are reduced equally as found

in Figure 6.39 for replacing the electrodes successively. The lowest absolute potential of 1.82 V is found for nickel iron oxide and nickel molybdenum. The investigated catalyst systems show a constant potential over time, only for the noble metal reference system an increasing absolute potential value (from 1.83 V to 1.88 V) was measured.

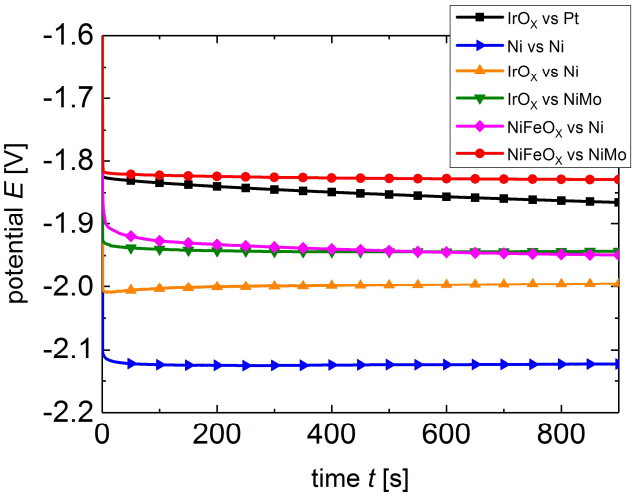

Figure 6.41: Potential measured over time (900 s) for an electrolysis at -10 mA/cm² in alkaline media for various catalyst systems covering an electrode size of 50.3 cm².

Overall, the promising results that were gathered in the previous section (7.3.2) for nickel iron oxide and nickel molybdenum deposited on areas of 0.5 cm² were also confirmed for both catalysts deposited on 50.3 cm² electrode area, which represents a size increase by a factor of 100. The electrodepositions of the earth-abundant materials were successfully carried out using the deposition conditions determined in the previous section (7.3.2). On increased sample sizes of 50.3 cm², the earth-abundant electrodeposited $NiFeO_X$/NiMo system shows similar overpotentials as the noble metal reference system IrO_X/Pt for the application in alkaline media ($\eta_{@10\ mA/cm^2}$(NiMo/$NiFeO_X$) = 455 mV and $\eta_{@10\ mA/cm^2}$(Pt/IrO_X) = 450 mV). Regarding the measured potential over time obtained from chronopotentiometric measurements, the earth-abundant system $NiFeO_X$/NiMo outperforms the other investigated catalyst system with a constant potential of 1.82 V. Further improvements for the reduction of the overpotential of the $NiFeO_X$/NiMo system can be made regarding the substrate structure. For the same catalyst combination hydrothermally deposited on nickel foam (three-dimensional structure, higher surface area), overpotentials of ~300 mV were reported in alkaline media, however, only on 3 cm² geometrical size.[109] The prepared systems can be implemented into the upscaled PV-EC device (7.1) and the overall performance of the device regarding the light induced water splitting reaction can be investigated (section (7.6)).

7.6 PV-EC device performance employing upscaled components

In the previous sections of this chapter the different components were prepared and tested regarding the implementation into the upscaled device, which was presented in section (7.1). Two different solar cell technologies, thin film silicon and crystalline silicon heterojunctions, are available for the integration into the device as shown in section (7.2). Furthermore, different catalyst systems have been tested and nickel molybdenum and nickel iron oxide were successfully upscaled to a deposition area of 50.3 cm², showing excellent current density-potential characteristics, which are similar to noble metal reference systems. Additionally, in section (7.4), the performance of light induced water splitting devices consisting of an a-Si:H/a-Si:H/µc-Si:H triple junction cell combined with (i) noble metal catalysts and (ii) earth-abundant

catalysts has been compared for sample areas of 0.5 cm², showing the high potential of the prepared earth-abundant NiMo/NiFeO$_X$ catalyst system, which outperformed the noble metal reference system. In this section of the chapter, the different components will be combined into the upscaled PV-EC device and the device performances will be compared. Specifically, the a-Si:H/a-Si:H/µc-Si:H thin film solar cell with an active area of 64 cm² will be combined with the noble metal reference system (Pt/IrO$_X$) and with the prepared earth-abundant catalyst system (NiMo/NiFeO$_X$). The a-Si:H/a-Si:H/µc-Si:H triple junction solar cell was used in this section for better comparison of the earth-abundant PV-EC device to the previously reported results[35]. Furthermore, the earth-abundant catalyst system will be employed in combination with the module consisting of three shingled crystalline silicon heterojunction solar cells. Prior to the measurement of the devices, the performances will be examined theoretically and compared to the literature values. Finally, the different devices are measured under illumination and the long-term stability of earth-abundant catalyst systems is investigated in a simulated day-night-cycle.

7.6.1 Theoretical analysis

In order to theoretically calculate the solar-to-hydrogen efficiencies of the various devices, the individually measured current-voltage curves of the photovoltaic cells and the catalyst systems were plotted and the respective currents at the intersection points were extracted, which are the operating currents of the PV-EC devices. The solar-to-hydrogen efficiencies are directly proportional to the operating currents and were calculated according to equation (40). For a better overview, the parameters measured for the photovoltaic cells (a-Si:H/a-Si:H/µc-Si:H triple junction cell (thin film Si) and module with three shingled crystalline silicon heterojunction (SHJ)) and their active areas are listed in Table 6.6. The upscaled a-Si:H/a-Si:H/µc-Si:H triple junction solar cell employed in the present work was also used in previously reported studies[35] and enables better comparison of the obtained results.

Table 6.6: Overview of PV parameters for the 64 cm² triple junction solar cell with a-Si:H/a-Si:H/µc-Si:H absorber layers (thin film Si) and for the module with three shingled crystalline silicon heterojunction (SHJ) cells of 58.5 cm² size.

PV cell	A_{PV} [cm²]	η_{PV} [%]	*FF* [%]	V_{OC} [V]	I_{SC} [mA]	J_{SC} [mA/cm²]
thin film Si	64	7.7	52.5	2.22	426.1	6.7
crystalline SHJ	58.5	12.4	54.2	2.07	649.4	11.1

In Figure 6.42, the IV-curves for both PV cell technologies and both catalyst systems are shown. The corresponding values extracted for the operating current densities and the respective solar-to-hydrogen efficiencies are listed in Table 6.7.

Table 6.7: Overview of obtained operating currents and corresponding solar-to-hydrogen efficiencies for the investigated PV-EC devices based on different PV technologies (thin film Si and crystalline SHJ) combined with a noble metal reference catalyst system (Pt/IrO$_X$) and an earth-abundant catalyst system (NiMo/NiFeO$_X$).

PV cell	A_{PV} [cm²]	η_{PV} [%]	*catalysts*	I_{OP} [mA]	η_{STH} [%]
thin film Si	64	7.7	NiMo/NiFeO$_X$	-265	5.1
thin film Si	64	7.7	Pt/IrO$_X$	-265	5.1
crystalline SHJ	58.5	12.4	NiMo/NiFeO$_X$	-304	6.4
crystalline SHJ	58.5	12.4	Pt/IrO$_X$	-304	6.4

The two catalyst systems show very similar current-voltage characteristics, leading to similar currents at the operating point for both PV cells. For the use of the thin film silicon based PV-EC device, an operating current of $I_{op, PV\text{-}EC}$ = 265 mA was found for both catalyst systems, resulting in solar-to-hydrogen efficiencies of 5.1 % for both devices. Previously reported solar-to-hydrogen efficiencies employing the same a-Si:H/a-Si:H/µc-Si:H triple junction solar cell and platinum/iridium oxide as catalyst system account for a solar-to-hydrogen efficiency of 4.8 % and 2.1 % for the use of nickel/nickel as catalyst system, respectively.[35] Thus, the device

employing the prepared earth-abundant catalysts NiMo/NiFeO$_X$ on 50.3 cm² area is expected to significantly outperform the earth-abundant device previously used, which was based on nickel electrodes.

If the module consisting of three shingled silicon heterojunction solar cells is used as current-voltage source in the device, the absolute value of the operating current is increased to 304 mA, thus leading to solar-to-hydrogen efficiencies of 6.4 % expected for both catalyst systems shown. Regarding solar-to-hydrogen efficiencies reported in literature for the use of crystalline silicon solar cells in water splitting devices[27,29], which account for up to η_{STH} = 14.5 %[29], the here expected value is comparably small. The solar-to-hydrogen efficiency of 6.4 % for the use of crystalline silicon heterojunction solar cells shingled into a module is due to the solar module performance, as also discussed in section (7.2.2). The approach of the shingled solar cells was used in order to integrate the module into the PV-EC device rather than to wire device and PV cells. The obtained conversion efficiency of 12.4 % and especially the fill factor of 54.2 % can significantly be improved (typical values η_{PV} ~22 % and FF ~ 70 – 80 %[29,159]). Possible improvements can be made regarding the decrease of series resistances occurring in the shingled module (R_S = 58.5 Ω·cm², see also Table 6.2). Figure 6.43 shows the current density-voltage curve of a module with three shingled crystalline silicon heterojunction solar cells (produced at IEK-5 Photovoltaics) in the ideal case of no series resistance losses caused by the connection. The ideal solar cell connection shows an improved fill factor FF compared to the measured current density-voltage curve in Figure 6.42, which can be indicated by the more rectangular shape of the current density-voltage curve in Figure 6.43. The solar-to-hydrogen efficiencies extracted from Figure 6.43 add up to 13.5 %. In order to further increase the solar-to-hydrogen efficiencies of PV-EC devices based on crystalline silicon heterojunction solar cells, the catalyst system performance, the solar cell conversion efficiency and the electrical connections within the device can be further improved.

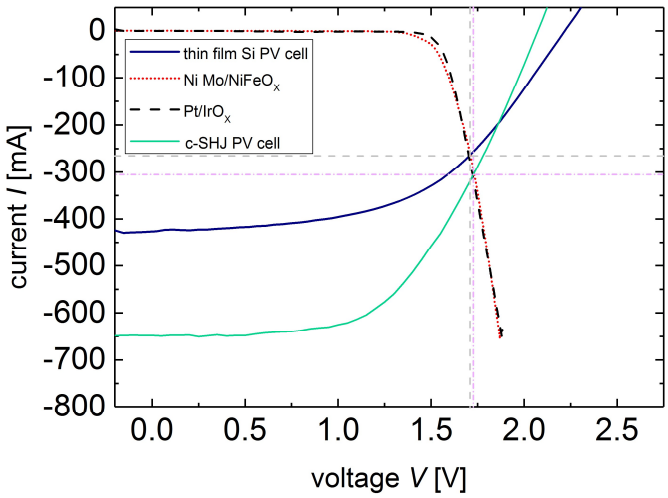

Figure 6.42: Current-voltage curves of (i) a triple junction a-Si:H/a-Si:H/µc-Si:H solar cell (TF-Si, blue solid line) with an active area A_{PV} = 64 cm² under AM1.5G illumination, (ii) current-voltage curve of a module with three shingled silicon hetereojunction solar cells (c-Si, green solid line) with an active area A_{PV} = 58.5 cm² under AM1.5G illumination and (iii) current-voltage curves of the electrochemical (EC) cells with two catalyst pair systems NiMo/NiFeOX (red dotted line) and Pt/IrOX (black dashed line) on 50.3 cm² area in 1 M KOH. The intersection point delivers the currents (265 mA, 304 mA) and voltages (1.7 V, 1.73 V) at the theoretical operating points of the PV-EC devices. Using equation (40), the theoretically expected solar-to-hydrogen efficiencies can be calculated for both systems (η_{STH} = 5.1 % for TF-Si and η_{STH} = 6.4 % for c-Si).

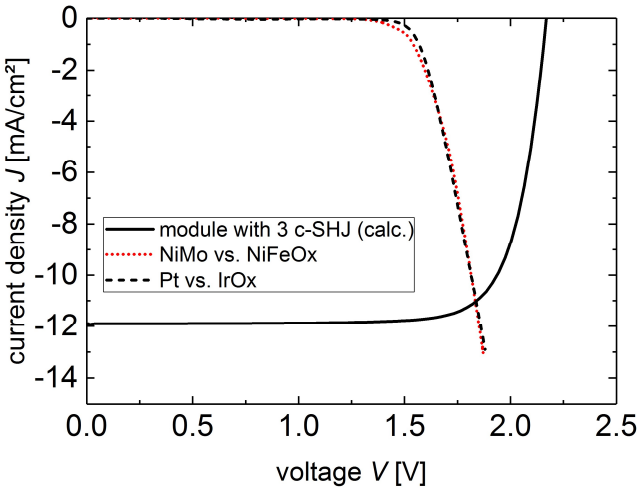

Figure 6.43: Current density-voltage curve of a module with three crystalline silicon heterojunction solar cells (produced at IEK-5 Photovoltaics), in the ideal case without series resistance losses due to the cell connection, plotted together with the curves of two catalyst systems in alkaline media.

7.6.2 Measurements of the upscaled PV-EC device under illumination

The upscaled catalysts systems were integrated in the modular device and combined with the photovoltaic voltage sources. The current-voltage curves of an a-Si:H/a-Si:H/µc-Si:H triple junction thin film silicon solar cell (TF-Si) combined with NiMo/$NiFeO_X$ and Pt/IrO_X were measured under AM 1.5G simulated solar illumination. Additionally, the module with three shingled crystalline silicon heterojunction solar cells was combined with NiMo/$NiFeO_X$ and the current-voltage characteristics were determined under AM 1.5G illumination. In all cases, 1 M potassium hydroxide was used as electrolyte. The measurements performed here are compared to the theoretical analysis given in the previous paragraph.

In Figure 6.44, the current-voltage curves of the PV-EC devices employing the 64 cm² a-Si:H/a-Si:H/µc-Si:H triple junction solar cell combined with the two catalyst systems of Pt/IrO_X (black dotted curve) and NiMo/$NiFeO_X$ (red solid curve) are shown. The currents extracted at 0 V are the operating currents for unbiased light induced water splitting for both catalyst systems. The respective solar-to-hydrogen efficiencies are calculated according to equation (40).

The PV-EC device using the earth-abundant catalyst system NiMo/$NiFeO_X$ in combination with the triple junction thin film silicon solar cell yields a solar-to-hydrogen efficiency η_{STH}(NiMo/$NiFeO_X$) of 5.1 (± 0.1)%, which is similar to the previously expected solar-to-hydrogen efficiency calculated for this device. The here shown PV-EC device (a-Si:H/a-Si:H/µc-Si:H/NiMo/KOH/$NiFeO_X$) is proven to significantly outperform the earth-abundant device previously used, which employed the same triple junction solar cell and was based on nickel electrodes (η_{STH}(Ni/Ni) = 2.1 %)[35]. Additionally, the earth-abundant PV-EC device employing NiMo/$NiFeO_X$ slightly outperforms the noble metal based reference device (a-Si:H/a-Si:H/µc-Si:H/Pt/KOH/IrO_X), which yields a solar-to-hydrogen efficiency η_{STH}(Pt/IrO_X) of 4.8 (± 0.1)%, similar to the reported literature value[35] and slightly lower than the expected solar-to-hydrogen efficiency of 5.1 % (see previous section).

If the module with three shingled crystalline silicon heterojunction solar cells is integrated into the PV-EC device, the following current-voltage curve under 1 sun AM1.5G simulated illumination is measured as shown in Figure 6.45. The earth-abundant catalyst system NiMo/$NiFeO_X$ was used in the PV-EC device and 1 M KOH served as the electrolyte. At zero bias, a current of 298 mA is extracted, resulting in a solar-to-hydrogen efficiency of 6.3 (±0.1) %, which is similar to the previously expected solar-to-hydrogen efficiency of 6.4 %

calculated in the prior section. The measured performances of all investigated PV-EC devices are discussed in the following paragraph.

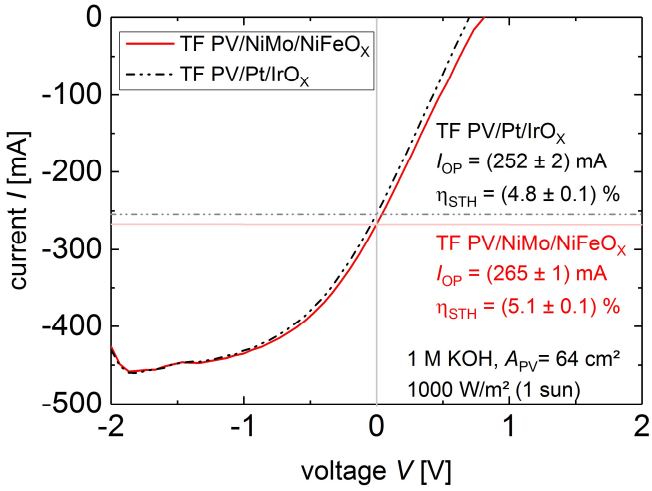

Figure 6.44: Current-voltage curves of the thin film (TF) silicon solar cell (A_{PV} = 64 cm²) based PV-EC devices employing the earth-abundant catalyst system NiMo/NiFeO$_X$ and the noble metal catalyst system Pt/IrO$_X$ under 1 sun illumination in 1 M KOH. The current at zero bias (V = 0 V, vertical guideline) is the operating current for unbiased, light induced water splitting. The different operating currents and resulting solar-to-hydrogen efficiencies are indicated (η_{STH}(NiMo/NiFeO$_X$) = 5.1 (± 0.1)% and η_{STH}(Pt/IrO$_X$) = 4.8 (± 0.1)%).

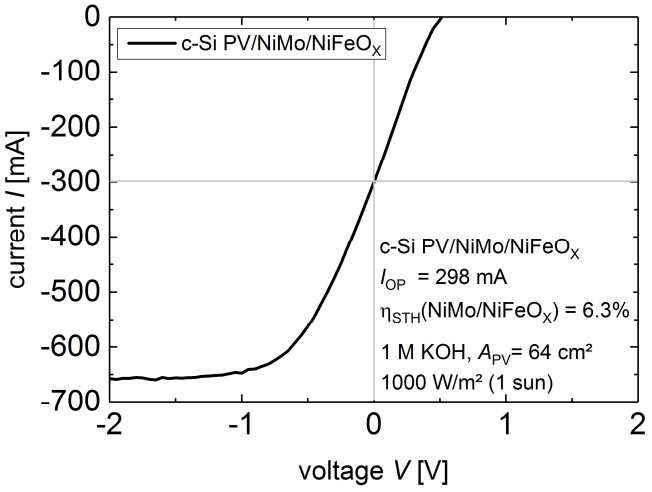

Figure 6.45: Current voltage curves of the PV-EC device consisting of a 58.5 cm² module with three shingled crystalline silicon heterojunction cells and NiMo/NiFeO$_X$ as earth-abundant catalyst system. The current at the operating point is indicated (vertical guideline), resulting in a solar-to-hydrogen efficiency of (6.3±0.1) %.

First of all, the measurements show the modularity of the upscaled PV-EC device towards different solar cell technologies. An upscaled thin film silicon solar cell (active area of 64 cm²) and a module with three shingled crystalline silicon heterojunction solar cells (active area 58.5 cm²) were successfully integrated into the upscaled PV-EC device and used to drive the light induced water splitting reaction. The different approaches of laser processed front contact grids in the case of the thin film solar cell and the shingling of the crystalline silicon heterojunction solar cells were chosen in order to meet the size conditions provided by the upscaled PV-EC device (max. substrate size of 100 cm²). In the case of the module with three shingled crystalline silicon

heterojunction solar cells, the series resistance losses have to be significantly decreased for an increase in PV-EC device performance. As shown in the previous section, by assuming the ideal case of no series resistance losses, the expected solar-to-hydrogen efficiency accounts for 13.5 %. Additionally, series resistance losses within the PV-EC device can be further decreased, for example the contact resistance between the photovoltaic cell and the hydrogen evolution reaction electrode or the electrolyte resistance. The distance between the electrodes can possibly be decreased to a zero gap configuration for a decrease of electrolyte resistance (distance in the used PV-EC device: 11 mm). However, to realize the zero gap configuration, the electrodes have to be porous in order to enable electrolyte flow. Therefore, the catalysts would have to be deposited on a porous substrate, such as nickel foam, of 50.3 cm² substrate size for the implementation in the current PV-EC device. An approach for the hydrothermal deposition of NiMo and $NiFeO_X$ on nickel foam has been reported in the literature, however only on 3 cm² size.[109] In order to increase the PV-EC device performance, one possibility is to further increase the activity of the catalyst systems towards the gas evolution reactions. The results obtained in this section confirm the previous calculation based on the current density-voltage curves for small area devices (a-Si:H/a-Si:H/µc-Si:H triple junction cell, area = 0.5 cm², see section (7.4)), which showed that PV-EC devices using earth-abundant catalysts can outperform noble metal based systems. The increased performances are due to the catalyst systems, which are specifically developed for the use in alkaline media. In addition, the catalytically active surface areas of the electrodeposited catalysts are probably enhanced compared to the commercially purchased noble metal catalysts, which could also increase the catalyst's activity.

Overall, the measurement showed that the developed solar cells/module and upscaled catalysts can successfully be implemented into the upscaled PV-EC device. The earth-abundant device (a-Si:H/a-Si:H/µc-Si:H/NiMo/KOH/$NiFeO_X$) significantly outperforms the previously used device (a-Si:H/a-Si:H/µc-Si:H/Ni/KOH/Ni), while the noble metal reference device was slightly outperformed (η_{STH}(NiMo/$NiFeO_X$) = 5.1 %; η_{STH}(Ni/Ni) = 2.1 %; η_{STH}(Pt/IrO_X) = 4.8 %). For the use of crystalline silicon heterojunction solar cells, a shingled module approach was chosen to meet the size conditions of the PV-EC device. The resulting solar-to-hydrogen efficiency of the shingled module in combination with the earth-abundant catalyst system adds up to 6.3 %. In general, overall improved contact arrangements should reduce the internal series resistance losses and therefore increase the device performance further.[35]

7.6.3 Performance stability of the upscaled, integrated PV-EC device system

As mentioned in the introduction to this chapter, one crucial challenge for the operation of integrated PV-EC devices is their stability against chemical corrosion caused by the electrolyte and additionally the mechanical stability of the layer stack towards oscillating temperatures and illumination conditions. Especially the need of long-term stability testing to investigate a possible catalyst degradation was addressed in the section discussing the scanning electron microscope results of nickel iron oxide, since the SEM images showed a decreased catalyst layer thickness after the electrochemical measurement sequence (section (7.3.2)).

In the first experiment, the stability over time was monitored by measuring the current produced for unbiased conditions (chronoamperometry) under AM1.5G illumination by the a-Si:H/a-Si:/µc-Si:H thin film silicon solar cell PV-EC device employing different catalyst systems for 600 s each (unbiased conditions, see Figure 6.46). The measurements were performed using 1 M potassium hydroxide solution as electrolyte in the upscaled PV-EC device, presented in section (7.1). In agreement with the results observed in the previous section (7.6.2), the earth-abundant catalyst system NiMo/$NiFeO_X$ outperforms the noble metal reference system Pt/IrO_X, showing a slightly higher current throughout the whole measurement duration. The initial decay of the currents of about 10 % of their primary values is followed by stable currents showing noise as a function of time, which can be attributed to the formation and detachment of gas bubbles on the electrode surfaces. Overall, the earth-abundant catalyst system yields an average operating current of I_{OP}(NiMo/$NiFeO_X$) = 214 ± 9 mA, while the noble metal catalyst system delivers I_{OP}(Pt/IrO_X) = 197 ± 38 mA. For comparison, the average operating current reported for the PV-EC device using the same 64 cm² thin film silicon solar cell and nickel/nickel as earth-abundant electrodes is I_{OP}(Ni/Ni) = 110 mA.[35] Thus, the upscaled PV-EC device

employing the thin film silicon triple junction solar cell in combination with the upscaled NiMo/$NiFeO_X$ coated electrodes perform stable over 10 min and yield almost twice as much current at the operating point compared to the previously used earth-abundant catalyst system consisting of nickel on both sides.[35]

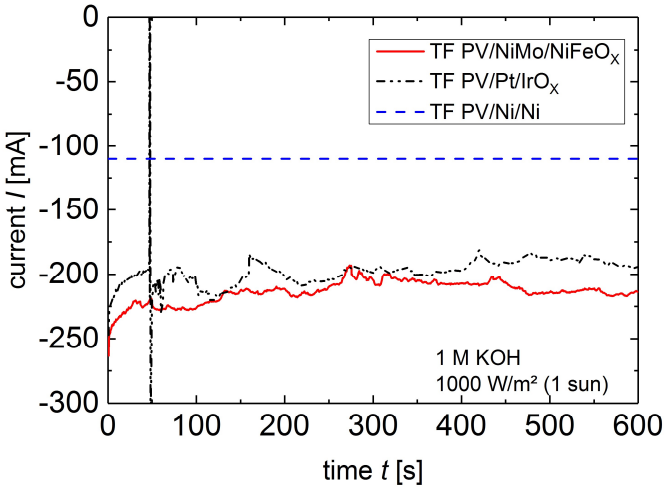

Figure 6.46: Chronoamperometric measurements of the integrated PV-EC device under bias-free conditions featuring different catalyst systems in 1 M KOH and under 1000 W/m² illumination. The reported current over time for the earth-abundant Ni/Ni system is shown for comparison (blue dashed line). [35]

Besides the stability testing of the PV-EC device under illumination, long-term stability measurements of the catalyst systems under simulated day-night-cycles were performed in order to determine possible catalyst degradation caused by the exposure to alkaline media. For example, the catalyst could become instable and detached from the surface or dissolve due to oscillating illumination and related temperature exposure during the working (day) period, leading to a decreasing catalyst performance. The effects of a decreased catalyst performance could then possibly be inverted during the resting (night) period by curing and precipitation on the electrode surfaces, restoring the initial catalyst performance.[188]

Two different earth-abundant catalyst systems (Ni/Ni and NiMo/$NiFeO_X$) were investigated under the following conditions: 6 h of operation at -10 mA/cm² electrolysis provided by the potentiostat simulating the illumination/working period followed by an overnight resting period at open circuit conditions, simulating no illumination and therefore no electrolysis. The system temperature was kept constant during the measurements, although additional heating caused by the illumination is beneficial for the device performance as is discussed in chapter (8).[54,56]

In Figure 6.47, the measured potential over time at -10 mA/cm² for the system employing nickel on both electrodes is shown for four days. During the working period, the potential of the Ni/Ni system decreases, which is possibly due to partial dissolution of the electrode surface in alkaline media or the coverage of the electrode surface with less active material.[189] However, during the resting period this effect is more than inverted, resulting in a decrease of absolute potential values of about 300 mV after 4 days of operating and resting (compare potential at day 1 (black curve) and potential at day 4 (magenta curve)). This observed absolute potential value decrease can be due to the precipitation of a more active species on the electrode surface during the recovery period (e.g. NiO_X) or due to the formation of an increased electrochemically active surface area compared to the initial electrode area.[188] The increase in electrochemically active surface area (ECSA) can be tested by means of cyclic voltammetry measurements with different scan speeds in non-faradaic region and is shown in Figure 6.48. As described in detail in chapter (4.4.4), the slope of the resulting curves (current difference versus scan speed) is directly proportional to the capacity, which is directly proportional to the electrochemically active surface area. Therefore, an increase of the slopes represent an increase in

electrochemically active surface area. The ECSA can also be used to calculate absolute values for the surface area changes, but the method is controversially discussed.[39,108] Hence, in this work, only the ECSA trends are investigated. The increasing ECSA trends are shown in Figure 6.48. The measurements suggest an increase of the electrochemically active surface area.

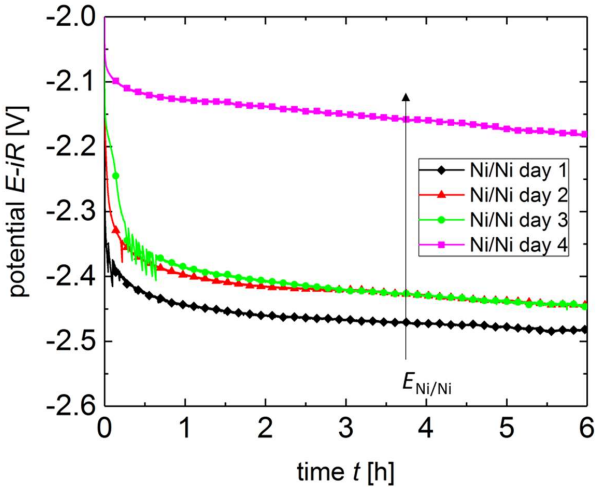

Figure 6.47: Potential over time measured for 6 h for four days at -10 mA/cm² electrolysis for the catalyst system consisting of nickel on both electrodes.

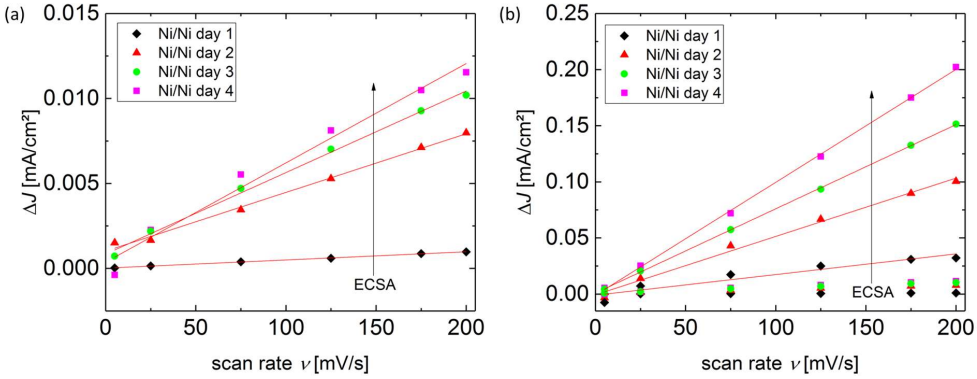

Figure 6.48: Current density difference between anodic and cathodic current plotted versus the scan rate. The slope is directly proportional to the electrochemically active surface area (ECSA) as described in section (4.4.4). The trends for the increasing slopes of the curves and thus the ECSAs are indicated.

The resulting potentials of the day-night-cycling test at -10 mA/cm² for the NiMo/$NiFeO_X$ system are shown in Figure 6.49. For comparison, the potential measured for Ni/Ni at day 4 is also shown in Figure 6.49. In accordance with the above presented data, the potential measured for the NiMo/$NiFeO_X$ system to drive the electrolysis at -10 mA/cm² is significantly lower than the potential measured for Ni/Ni throughout the whole measurement period. In contrast to the Ni/Ni system, the NiMo/$NiFeO_X$ system shows constant potentials during the whole measurement period and no significant changes due to the working/resting periods can be identified. Therefore, the earth-abundant material based NiMo/$NiFeO_X$ catalyst system shows very good stability for the water splitting reaction performed in a simulated day-night-cycle measurement and outperforms considerably the system consisting of Ni/Ni, while showing even slightly better performances than a system employing noble-metal catalysts Pt/IrO_X. Regarding the layer thickness decrease, which was observed in the SEM images of nickel iron oxide, it appears as if the catalyst layer is not completely dissolved

and the thickness decrease possibly terminates at some point in order to ensure the stable performance. This assumption is supported by SEM images taken of both electrodes (Figure 6.50). The SEM image of nickel molybdenum shows a surface morphology, which is similar to the initial morphology (Figure 6.50 (a)). In the SEM image of nickel iron oxide (Figure 6.50(b)), a layer covering the surface can be identified, which is catalytically active, since the performance of the catalyst system is stable over the investigated time frame. The surface layer shows smaller features compared to the initial surface morphology, which would support the assumption that the catalyst layer is partially dissolved correlating to the thickness decrease observed.

In summary, the earth-abundant catalyst system combined with the a-Si:H/a-Si:H/µc-Si:H triple junction cell significantly outperforms the previously used earth-abundant system of the same triple junction solar cell combined with nickel electrodes in the chronoamperometric measurements (current over time, see Figure 6.46). Additionally, the noble metal reference system is also slightly outperformed by the NiMo/$NiFeO_X$ based PV-EC device (Figure 6.46). The constant electrochemical performance of the NiMo/$NiFeO_X$ system measured under day-night-cycle conditions for four days suggests that the observed layers are stable within the investigated time frame. Thus, both materials NiMo and $NiFeO_X$ are applicable in water splitting devices.

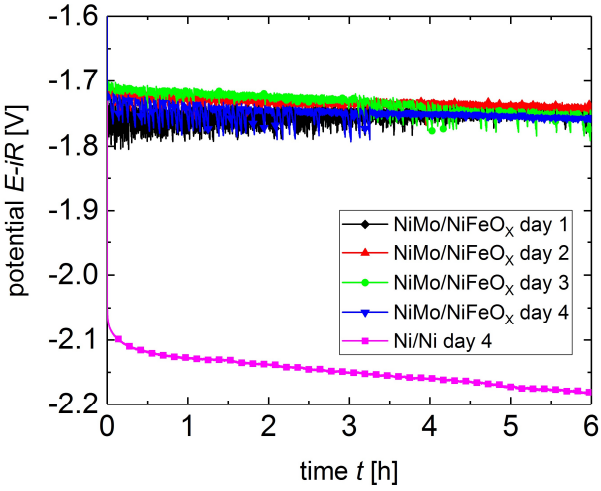

Figure 6.49: Potential over time measured for 6 h for four days at -10 mA/cm² electrolysis for the catalyst system consisting of NiMo/$NiFeO_X$ coated nickel sheet electrodes.

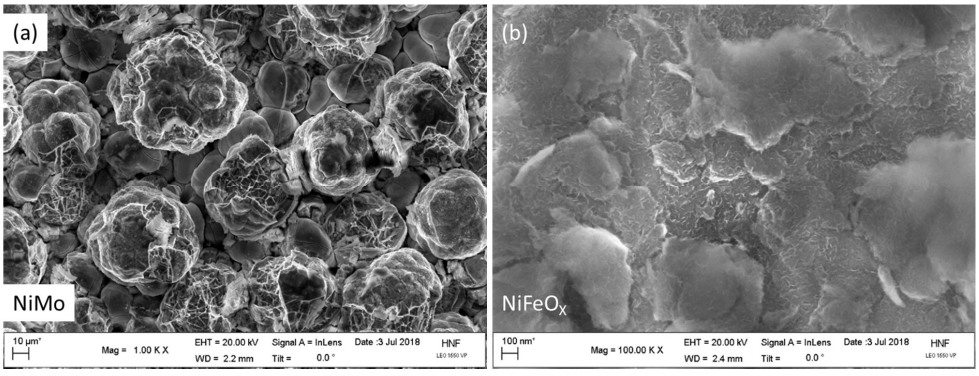

Figure 6.50: SEM images of (a) NiMo and (b) $NiFeO_X$ after a complete day-night-cycle. The initial surface morphologies are preserved in the case of nickel molybdenum. The SEM image of nickel iron oxide shows a layer covering the surface, showing smaller features compared to the initial surface morphology (compare Figure 6.21 and Figure 6.30).

7.7 Summary of upscaling processes

The upscaled PV-EC device can be implemented into the electrochemical workplace set up in chapter (6.1), as presented and described in chapter (7.1). The device was shown to be modular, since different catalyst systems and electrolytes could be employed. The modularity of the PV-EC device is later used to compare the prepared earth-abundant catalysts to a noble metal reference system and to implement photovoltaic cells based on different technologies.

One challenge occurring during the upscaling process in the case of thin film silicon based photovoltaic technology, is the efficient current collection through the front contact TCO layer. Hence, different front contact patterns using laser scribing and evaporated metal front contact grids were investigated to increase the active solar cell area beyond 1 cm². The thin film silicon solar cell finally employed for solar driven water splitting in the device has an active area of 64 cm² created by using a laser patterning approach, which ensured low resistive losses as well as a decreased chance for entire solar cell failure. Alternatively, for the thin film silicon solar cells using an evaporated metal front contact grid, the active area was upscaled to 53.3 cm² and it was shown that the evaporated metal grid enhances the current transport in the front contact TCO layer. Additionally, a module consisting of three shingled crystalline silicon heterojunction solar cells has been tested in the PV-EC device to show its potential for the water splitting application as well as the modularity of the device towards different solar cell technologies (active area of 58.5 cm²).

The synthesis of different catalyst materials was successfully realized. Prepared Ni_3S_2 nanosheets showed lower potentials for the oxygen evolution reaction compared to hydrothermally untreated nickel foam samples and can possibly be implemented in the upscaling approach based on the lateral interconnection of individual sub cells (side-by-side approach).

In order to be compatible with the upscaled PV-EC device presented in section (7.1), the catalysts were in the following deposited on nickel sheet electrodes. The earth-abundant catalysts NiMo (hydrogen evolution reaction catalyst) and $NiFeO_X$ (oxygen evolution reaction catalyst) were chosen as candidates for the catalyst upscaling after intensive literature research. Both materials were first deposited on nickel sheets with a sample size of 0.5 cm² in order to determine the deposition conditions for the upscaling procedure and to investigate the surface morphology changes (SEM) and composition changes (XPS) due to the electrochemical operation sequence. Both catalysts were successfully prepared on geometrical areas of 50.3 cm² using electrodeposition. Prior to the implementation into the PV-EC device, the performance of different upscaled catalyst systems was evaluated, NiMo/$NiFeO_X$ shows a similar performance compared to the noble metal reference system Pt/IrO_X with an overpotential as low as 455 mV at 10 mA/cm² (η(Pt/IrO_X) = 450 mV).

The catalysts were implemented in a PV-EC device using the upscaled laser scribed thin film silicon solar cell as well as the module with three shingled crystalline silicon heterojunction cells. The respective solar-to-hydrogen efficiencies achieved for the thin film silicon solar cell (a-Si:H/a-Si:H/µc-Si:H, A_{PV} = 64 cm²) were η_{STH}(NiMo/$NiFeO_X$) = (5.1 ± 0.1) % and η_{STH}(Pt/IrO_X) = (4.8 ± 0.1) %. Hence, the earth-abundant catalyst system slightly outperforms the noble metal catalyst system. Compared to nickel used for both electrodes (η_{STH}(Ni/Ni) = 2.1 %[35]), the NiMo/$NiFeO_X$ system yields a solar-to-hydrogen efficiency twice as high. For the module with three shingled crystalline silicon heterojunction solar cells, a solar-to-hydrogen efficiency of η_{STH}(NiMo/$NiFeO_X$) = (6.3 ± 0.1) % was achieved for an active area of 58.5 cm².

The NiMo/$NiFeO_X$ catalyst system shows an excellent stability over 4 days under simulated day-night-cycling with a potential of 1.75 V to drive the water splitting reaction at an operating current density of -10 mA/cm². In conclusion, the here developed NiMo/$NiFeO_X$ is suitable for the application in PV-EC devices with areas beyond 1 cm² and shows long term performances close to or even better than systems based on noble metal catalyst systems.

8 Characterization of PV-EC devices under non-standard test conditions

As shown in the previous chapters, multi-junction thin film silicon solar cells are well suitable for the application in photovoltaic-biased electrosynthetic water splitting devices, since they provide reasonably high photocurrent densities at a sufficient photovoltage to drive the water electrolysis. Depending on the number of sub cells connected in series and the respective absorber layer band gaps, the open circuit voltage ranges from 1.5 to 2.8 V.[24,78,87] Each sub cell layer is electrically and optically optimized with respect to standard test conditions, which means in particular for the measurement of the photovoltaic cell: a temperature of 25°C and perpendicular illumination of 1000 W/m² (1 sun) intensity of the AM1.5G spectrum (see also chapter (3.4)).[41,42,100,126]

However, if PV-EC devices were to be used outdoors, the standard test conditions represent only one set of many possible illumination conditions, which can differ significantly from STC conditions. For example, due to clouds the illumination intensity can be below 1 sun, the incident illumination angle changes during the season and the day and on sunny days system temperatures of 60°C or more can occur.[42,43] Furthermore, the spectral quality of the incident illumination spectrum can change during the season[44,45] and the day[46] and can differ for geographical locations. [44,45]

Variations in both shape and intensity of the incident illumination spectrum lead, not surprisingly, to an influence on the electrical parameters and performance of thin film silicon solar cells.[42,43,47–49,190,191] Photovoltaic cells and modules have been already investigated under simulated and real outdoor conditions in great detail, as also briefly shown in chapter (3.4).[50,56] However, advanced studies on combined PV-EC systems have not been carried out in full details yet. In this context it is important to note that it is not sufficient to extrapolate the outdoor results on PV systems directly to combined PV-EC systems for several reasons. These are for example:

In a PV system, one would be able to draw power out of the system at all points of the illuminated current-voltage curve of the device as long as the product $|J| \cdot V \cdot FF > 0$. This would be true for any kind of illumination conditions. For a combined PV-EC system instead, the generation of hydrogen by unbiased light induced water splitting will only occur for output voltages above a certain potential value (thermodynamic potential + overpotential losses). This means, any illumination conditions, which will shift the illuminated current density-voltage curve of the coupled unbiased system such that the output voltage is below the operating point (V = 0 V), will switch the unbiased system off. Figure 7.1 schematically illustrates how varied illumination conditions can potentially shift the current-voltage curves for an unbiased light induced PV-EC device. For the green current-voltage curves, the operating current of the unbiased PV-EC device can be extracted at zero bias, thus hydrogen can be generated. In the case of the red curve, the current-voltage characteristics could possibly be shifted due to various outdoor conditions such that no current at the operating point for unbiased water splitting is obtained. Hence, no hydrogen can be generated and the unbiased PV-EC device is switched off. For practical use this will have serious consequences (and may ask for additional electronic operation point control and/or power back-up solutions).

Outdoor conditions with considerable variation in temperature, also influenced by variation in the illumination conditions together with day-night-cycling will have additional effects on the EC part of the combined PV-EC system, which can be detrimental or beneficial to the total device performance. It is therefore required to study these effects on the combined system as well[54–56]. Studies in the frame of the previous PhD thesis by F. Urbain addressed the beneficial influence of the operating temperature on the device performance[54]. In the present work, the influence of varying illumination conditions on the performance of photovoltaic-biased electrosynthetic water splitting devices based on thin film silicon multi-junction cells is further addressed. The device characterization is expanded towards influences of illumination intensity, the combined effects of illumination intensity and temperature, illumination angle and spectral quality. The various results are presented individually in the following sections. The conditions employed here are significantly different to STC and similar to conditions obtained outdoors. A description of the measurement parameters and the used

setups are given in the respective sections. Furthermore, a first estimation of the annual hydrogen output of PV-EC devices employing various catalyst systems and different multi-junction thin film silicon solar cells is given under varied spectral quality conditions. Parts of the results presented in this chapter are published in K. Welter, V. Smirnov, J.-P. Becker, P. Borowski, S. Hoch, A. Maljusch, W. Jaegermann, F. Finger, *ChemElectroChem* **2017**, *4*, 2099–2108.

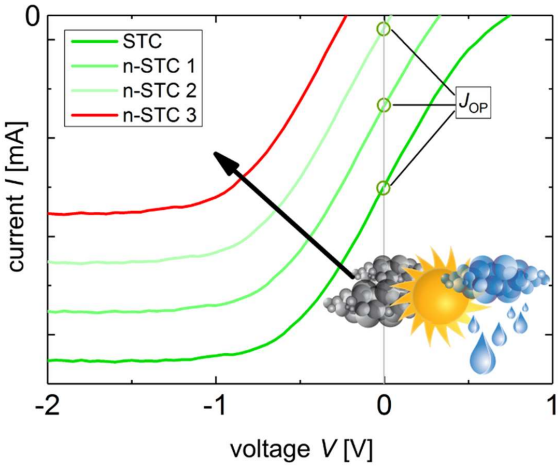

Figure 7.1: Schematic illustration of possible changes of the current-voltage characteristics for unbiased PV-EC devices caused by varying outdoor conditions. For the green IV curves, an operating current at zero bias can be extracted, thus hydrogen can be generated. In the case of the red curve, no operating current can be extracted, therefore the unbiased light induced water splitting device is switched off (no hydrogen production).

8.1 Operating temperature and illumination intensity

In the following, the influences of operating temperature and illumination intensity on the PV-EC device performance are investigated in detail. First, the influences of both parameters on the water splitting PV-EC device performance are investigated separately, before the effects of the combination of both parameters on the performance is addressed. Regarding the outdoor application of the PV-EC device, the operating temperature and illumination intensity are crucial for the device performance and are rarely at 25°C and 1 sun intensity. As reported in literature, an increased operating temperature is to some extend beneficial for the PV-EC device performance, since the decreased PV performance is compensated by increased kinetics during the electrochemical reaction[54]. In addition, one can expect that 1 sun illumination intensity would lead to heating effects within the device resulting in increased operating temperatures, whereas low intensities would yield low operating temperatures. Considering heating effects due to the illumination intensity, the combined influence of operating temperature and illumination intensity on the solar-to-hydrogen efficiency of the device is of interest.

The experiments to determine the operating point of the PV-EC device under varied operating temperature and illumination intensity are performed for a PV-EC device consisting of an a-Si:H/a-Si:H/µc-Si:H triple junction solar cell and platinum/iridium oxide as respective gas evolution reaction catalysts. The current-voltage curves of the photovoltaic cell and the electrochemical cell were individually measured at different temperatures and combined together to evaluate the PV-EC performance. The intersection point between the current-voltage curves of the photovoltaic and electrochemical cell represent the device operating point. The currents at the intersection points are consequently the operating currents of the PV-EC device under the varied intensities and operating temperatures.

8.1.1 Experimental details

Current-voltage measurements were performed under the spectrum corresponding to AM1.5G illumination in order to study the influence of the illumination intensity on the PV cell and the PV-EC device performance. For the variation in illumination intensity, different neutral density filter masks were placed above the solar cell in the light path of the sun simulator. The intensities applied were 0.644, 0.364 and 0.156 sun.[55] The sample temperature was varied in the range of 25°C to 80°C. The electrochemical system investigated here, consists of platinum (99.95% purity, supplied by Goodfellow GmbH, Germany) and iridium oxide (12 g Ir/m^2 on Ni electrode, METAKEM GmbH, Usingen, Germany). The current-voltage behavior of the catalyst system Pt/IrO_X was determined by linear sweep voltammetry measurements (LSV) in 1 M potassium hydroxide solution using a Garmy Reference 600 potentiostat (no stirring, scan rate 50 mV/s, T_{OP} =25 – 80°C).

8.1.2 The influence of the operating temperature

Figure 7.2 shows the current-voltage curves of the a-Si:H/a-Si:H/µc-Si:H triple junction cell (solid lines) and the electrochemical cell (Pt/IrO_X, dashed lines) measured for temperatures in the range of 25°C to 80°C under 1 sun simulated solar irradiation. The photovoltaic performance decreases with increasing temperatures mainly due to the decreasing photovoltage, whereas the electrochemical performance is increased, since the voltage needed to drive the water splitting reaction is reduced. Both effects were expected from reports in literature[54,60,61,102,105] and described in the section (3). The decreased photovoltaic performance is attributed to a decrease in band gap energy and changed recombination kinetics upon temperature increase.[127] Enhanced kinetics and transport effects in the reaction lead to the effect of an increased electrochemical performance (see dashed curves in Figure 7.2).[102,105] The positive current measured for the electrochemical cell in the range from 0 – 1.3 V is unexpected and no convincing explanation can be given to fully understand this observed effect.

Overall, both effects compensate each other for temperatures up to 60°C, since the intersections of the curves for the respective temperatures yield similar currents (J_{OP} = 6.7 ±0.1 mA/cm²) at the operating points. For temperatures of 80°C, the current at the operating point is slightly decreased to J_{OP} = 6.5 mA/cm², which could possibly indicate that the effect of the enhanced electrolysis does no longer compensate the decreased photovoltaic performance. The obtained results are in good agreement with the literature, where a constant performance was found for the temperature range of 25 – 60°C, with the highest performance at 50°C.[54]

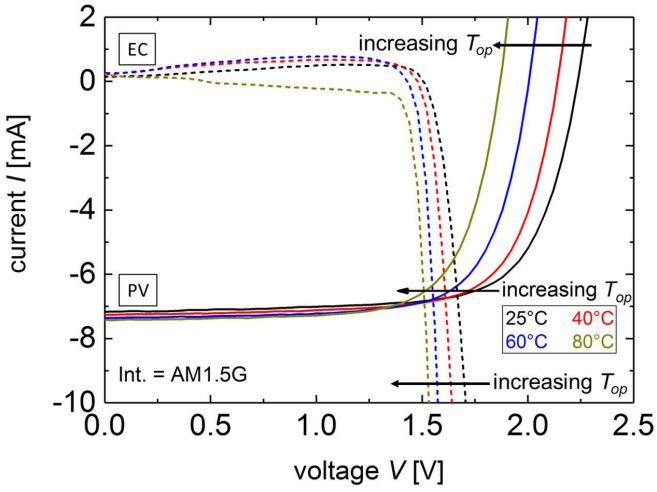

Figure 7.2: Temperature dependence of the current-voltage curves measured for an a-Si:H/a-Si:H/µc-Si:H triple junction cell (solid lines) under 1 sun illumination intensity and the electrolysis cell employing platinum and iridium oxide as catalysts (dashed lines) in 1 M KOH. The operating temperature was varied from 25 – 80 °C.

8.1.3 The influence of the illumination intensity

Figure 7.3 shows the intensity dependence of the photovoltaic cell's current-voltage curves measured at an operating temperature of 25°C plotted together with the electrolysis curve measured at 25°C (for measured positive current, see also Figure 7.2). The intensity was decreased from 1 sun illumination to 0.156 sun illumination. The current-voltage curves measured for the a-Si:H/a-Si:H/µc-Si:H triple junction solar cell show a decreasing short circuit current I_{SC} as well as a decreasing open circuit voltage V_{OC}. The values for the currents extracted at the intersections, which represent the operating currents of the device under varied illumination intensity, are decreased for reduced intensities (from 6.7 to 1.1 mA/cm²). The voltage changes observed for the current-voltages curves of the solar cell (between 2.23 V for 1 sun to 2.06 V for 0.156 sun illumination) are due to a reduced quasi-Fermi level splitting under reduced intensities, as described in the literature[128]. The short circuit current decreases linearly with the intensity changes and is defined by the number of incident photons.

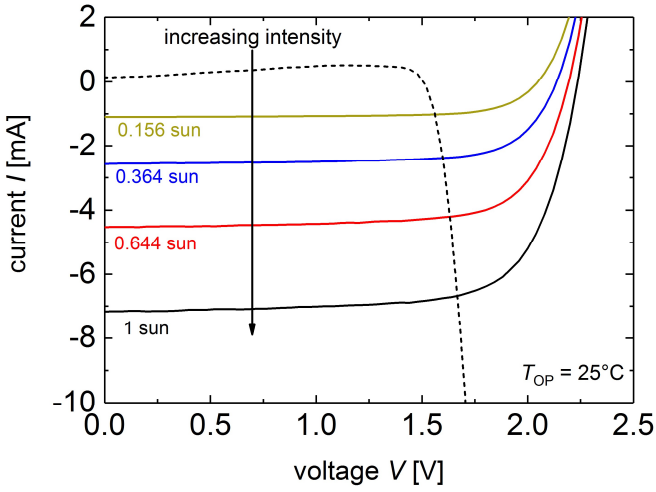

Figure 7.3: Intensity dependence of the current-voltage curves measured for the a-Si:H/a-Si:H/µc-Si:H triple junction cell (also used in section (8.1.2)) for an operating temperature of 25°C plotted together with the electrolysis (Pt/IrO_X) at 25°C.

Regarding the use of different catalyst systems in PV-EC devices under varied illumination intensities, it was found that systems with a high catalytic activity, such as platinum and ruthenium oxide, and systems with less catalytic activity, for example nickel and cobalt(II,III) oxide (Co_3O_4), show differences in operating current under one sun illumination (J_{OP}(Pt/RuO_2) = 6.7 mA/cm² and J_{OP}(Ni/Co_3O_4) = 6.2 mA/cm²). The difference in operating current is reduced with decreasing intensity, such that at 0.156 sun illumination both devices employing the different catalyst systems show a similar operating current (J_{OP}(Pt/RuO_2) = 1.2 mA/cm² and J_{OP}(Ni/Co_3O_4) = 1.15 mA/cm², see Figure 7.4). The slight improvement of the fill factor values measured for triple junction solar cells under reduced illumination intensity could cause the similar operating currents for both devices at low intensities. Therefore, the requirements for catalyst systems appear to be slightly more relaxed for the application under low intensity illumination.[55]

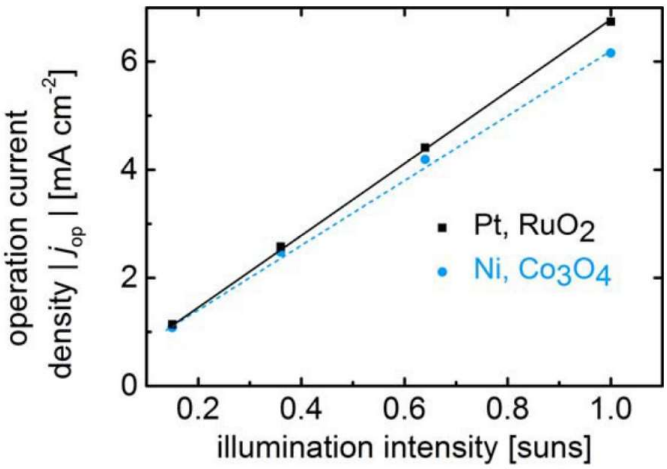

Figure 7.4: Operating current densities of PV-EC devices employing two different catalyst systems ((i) Pt/RuO_2 and (ii) Ni/Co_3O_4) plotted versus the illumination intensity. The operating current densities are extracted of the current-voltage curves of PV-EC devices under varied illumination intensities, taken from reference[55].

8.1.4 The influence of the illumination intensity and operating temperature

In the next section, both parameters, the illumination intensity and the operating temperature, were combined and the system was investigated under variation of both. As described in the introduction to this chapter, high illumination intensities can probably lead to high operating temperatures, whereas low illumination intensities could be attended by lower operating temperatures.

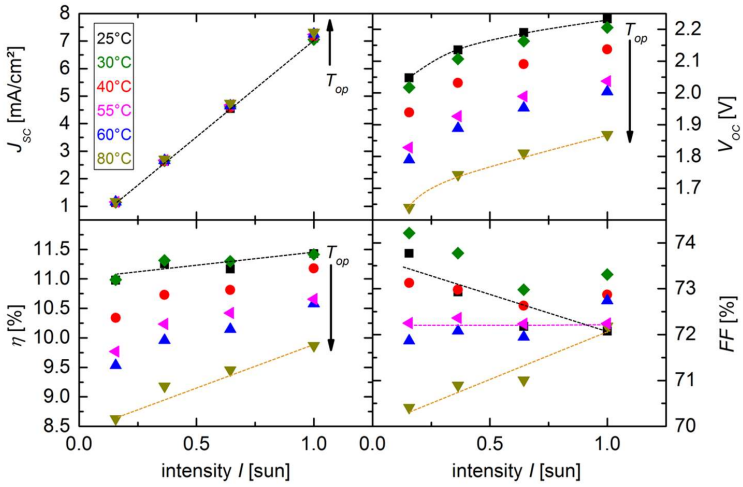

Figure 7.5: Photovoltaic parameters measured for an a-Si:H/a-Si:H/µc-Si:H triple junction cell under varied intensities and varied operating temperatures. The lines are only guides to the eye.

Figure 7.5 shows the PV parameters measured under the varied conditions. The lines shown in Figure 7.5 do not represent any fit and should only serve as guidelines for the reader. As described in chapter (3.4) and seen in the prior section, the short circuit current density increases with increasing intensity, since J_{SC} depends on the number of incident photons. Additionally, the short circuit current density increases slightly with increasing

temperature, due to the decrease of the band gap energy with increasing temperature. The open circuit voltage increases with increasing intensity. According to equation (28) the open circuit voltage depends logarithmically on the illumination intensity, which is shown in the appendix (Figure A8). The temperature increase leads to a reduction in open circuit voltage, due to the mentioned decrease in band gap energy and changed recombination kinetics caused by the higher temperatures.[127,128] For a temperature increase, the efficiency is decreased due to the stronger decrease in open circuit voltage, which cannot be compensated by the increase in short circuit current density.[60,61] The fill factor does not show a clear trend upon the variation in intensities and temperatures investigated. For temperatures below 55 °C, the fill factor is decreased with increasing intensity (e.g. from 73.8 % (0.156 sun) to 72.1 % (1 sun) for 25 °C), while this effect is inverted for temperatures above 55 °C (e.g. 70.4 % (0.156 sun) to 72.2 % (1 sun) for 80 °C). For a temperature of 55 °C, the fill factor is nearly constant over the investigated intensity range (72.2 ± 0.1 %). Possible reasons for the observed behavior of the fill factor could be due to an altered built-in field in the device and changed charge carrier recombination kinetics influenced by the temperature variation.[127,128]

Combining the measured current-voltage curves for the a-Si:H/a-Si:H/µc-Si:H triple junction cell at different intensities and temperatures with the measured current-voltage characteristics for the electrolysis reaction employing platinum and iridium oxide as electrodes under varied operating temperatures, Figure 7.6 is obtained. The positive current measured for the electrochemical cell in the range from 0 – 1.3 V is unexpected and no convincing explanation can be given to fully understand this observed effect.

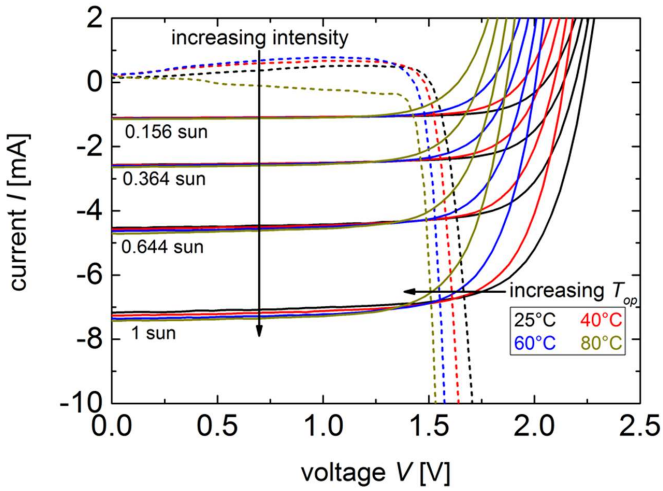

Figure 7.6: Current-voltage curves of an a-Si:H/a-Si:H/µc-Si:H triple junction solar cell measured under varied intensities and varied operating temperatures plotted with the current-voltage behavior of the electrolysis (Pt/IrOx) measured for different operating temperatures. The intersection point between PV cell and EC cell IV curve represents the operating current of the water splitting device at the respective intensity and temperature.

As described and discussed in the previous sections on the temperature (8.1.2) and intensity influences (8.1.3), similar effects can be observed for Figure 7.6. Increasing temperatures are beneficial for the electrolysis, but detrimental for the solar cell performance; and reduced intensities lead to reduced short circuit current densities and reduced open circuit voltages. Using Figure 7.6, the currents at the operating points for a given intensity and temperature can be extracted, which are shown in Figure 7.7. For each intensity, the currents measured for the different temperatures were normalized to the current obtained at 25°C (Figure 7.7). This current ratio is plotted versus the system temperature $T_{syst.}$, assuming a perfect thermal coupling between the photovoltaic and the electrolysis cell, resulting in $T_{elect.} = T_{photo.} = T_{syst.}$. In contrast to industrial electrolysers, which are typically temperature controlled and operate at 80 °C[20,192], in the present work the assumption is made that the increase in temperature is only due to heating effects caused by the illumination.

Figure 7.7 shows that for illumination intensities above 0.644 sun, a wide range of operating temperatures (25 – 60 °C) is beneficial, leading to a stable operating current in this range. If the illumination intensity is below 0.364 sun, low system temperatures (~25 °C) lead to the best PV-EC device performances. High system temperatures at low irradiation intensities result in a significant decrease of the normalized operating current (down to 0.86 for 0.156 sun at 80 °C).

Heating effects of the entire device, which are assumed to be caused in this case by the illumination above 0.644 sun, should be considered as a beneficial aspect for light induced PV-EC device operation if 60 °C are not exceeded. In the case of low irradiation intensities, the number of generated charge carriers in the solar cell is reduced due to the decreased amount of incident photons (reduced intensity). This reduction in generated charge carriers cannot be compensated by the slight increase of current density due to the reduced band gap energy for increased temperatures. Additionally, the open circuit voltage is reduced by both effects, the decreased intensities and the increased operating temperature. Therefore, the photovoltaic performance is decreased, such that the enhanced processes in the electrochemical cell cannot compensate the performance reduction.

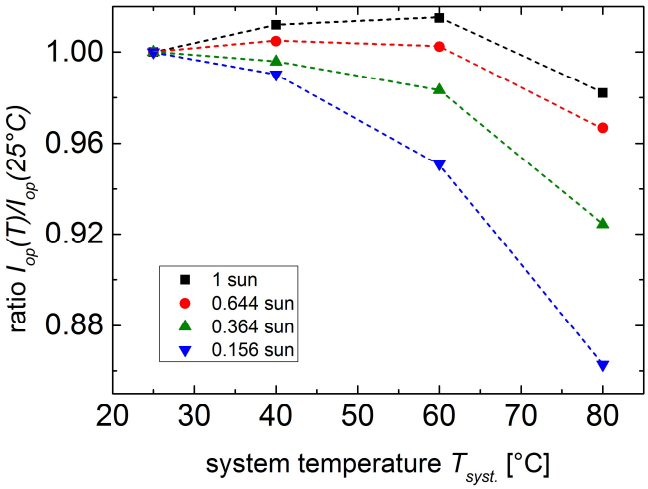

Figure 7.7: Normalized current I_{OP} over system temperature $T_{syst.}$. For each intensity investigated, the current at the operating point of the device was normalized to the current extracted for the lowest investigated system temperature of 25 °C.

Comparing the cost-effectiveness of different systems for solar hydrogen production, the heating effect due to the illumination intensity can be considered as an advantage for combined PV-EC devices over decoupled PV+EC systems without thermal coupling between PV and EC cell. In the case of a PV+EC system, the performance of the photovoltaic cell could be reduced due to heating caused by the illumination, while the electrolyser needs to be heated in order to operate at its full potential. By integrating both technologies into a PV-EC device, no additional heating/cooling of the individual parts would be necessary for the operation.

8.2 The influence of the incident illumination angle

Besides the previously investigated operating temperature and illumination intensity, the incident illumination angle can influence the PV-EC device performance. The incident illumination angle is subject to seasonal and daily variation. The seasonal variation depends on the degree of latitude, such that in Munich (Germany), for example, the difference between the incident angle at noon (12:00) on June 21st (65.3°) and on December 21st (18.5°) accounts for approximately 47°.

Regarding the outdoor application of photovoltaic cells, a variation in incident illumination angle leads to a reduction in output power due to the reduced number of incident photons per area and due to reflection losses, as reported in the literature.[53,131–134] However, as mentioned in the introduction to this chapter, it is possible to draw power out of the system at all points of the illuminated current-voltage curve as long as the product $|J| \cdot V \cdot FF > 0$. In the case of PV-EC devices, a variation in incident illumination angle leads to a decreased amount of hydrogen produced and in the worst case could switch the system off. Two major effects should be considered that can possibly influence the device performance under varying illumination angles. These are (i) the reduced effective illuminated device area, which results in a reduced intensity, and (ii) optical effects occurring at the interfaces (for example: glass/air and between silicon sub layers). In the following, the influence of both effects on the solar-to-hydrogen efficiency are evaluated in detail. An additional factor that has to be considered in further investigations of PV-EC devices for the outdoor application is the tilted mounting of the PV-EC device in order to ensure approximately perpendicular illumination angles. In contrast to the outdoor application, PV-EC devices characterized under laboratory conditions are either in vertical or horizontal measurement position. This additional point has to be considered regarding the PV-EC device construction and engineering (e.g. for gas and electrolyte transports), but will not be addressed further in the present work.

In order to evaluate the performance of the integrated PV-EC device based on an a-Si:H/a-Si:H/µc-Si:H triple junction solar cell under varying incident angles, the current-voltage curves of the photovoltaic cell obtained under varied illumination angles were combined in the electrical series model[124,125,149] (see chapter (4.5)) with linear sweep voltammetry curves using platinum and iridium oxide as electrodes.

8.2.1 Experimental details

External quantum efficiency measurements (EQE) under varied angles:

The external quantum efficiency setup is described in detail in chapter (4.2.2). For the angular dependent measurements, the monochromatic light was focused using a lens, forming a light spot of 3 mm width, which is considerably smaller than the solar cell area (A_0=1 cm²) under all incident angles as shown in Figure 7.8. Bias light was used in addition, to saturate the respective other sub cells in the solar cell stack (top cell: 590 nm, middle cell: 780 nm and 400 nm, bottom cell: 525 nm). Different angles of the incident illumination varying from 0° to 60° were realized. The resulting external quantum efficiencies were convoluted with the air mass (AM) 1.5G spectrum in the respective wavelength ranges to calculate the individual sub cell current densities J_{QE} (see also chapter (4.2.2)). [132]

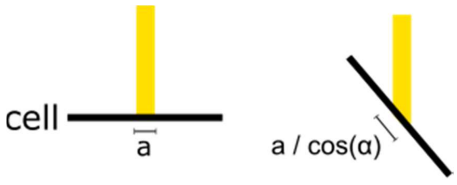

Figure 7.8: Illumination conditions at the external quantum efficiency measurement setup for the evaluation of the influence of varied incident angles, taken from reference[132].

Angular and intensity dependent current-voltage measurements (JV):

The current-voltage (JV) measurements were performed under different incident illumination angles (range of 0° to 60°) of the incident AM1.5G illumination provided by a class AAA sun simulator (setup described in chapter (4.2.1), Wacom sun simulator WXS-140S-Super). The sun simulator illuminates a total area of 100 cm², which is therefore 100 times the size of the illuminated solar cell area under 0° incident angle (A_0 = 1 cm²). A schematic sketch of the illumination conditions for the current-voltage setup is shown in Figure 7.9. The effect of an increasing incident illumination angle is described in the following in terms of an "effective illuminated device area", which follows cosine law and is equivalent to a description in terms of a reduced photon flux (reduced intensity) per unit area under angle of incidence α (see Figure 7.9)[131,132]:

$$A(\alpha)=A_0\cos(\alpha) \tag{44}$$

Area corrections are performed according to the cosine law.

JV measurements varying the illumination intensities are described in chapter (8.1.1). The results obtained in chapter (8.1) were used for comparison here.

In all cases, 0° and 1 sun illumination corresponds to normal incidence.

Figure 7.9: Illumination conditions at the current-voltage measurement setup for the evaluation of the influence of varied incident angles. The effective illuminated device area changes according to cosine law (44), taken from reference[132].

Electrochemical measurements:

To investigate the current-voltage behavior of the catalyst system consisting of platinum (HER, 99.95% purity, supplied by Goodfellow GmbH, Germany) and iridium oxide (OER, 12 g Ir/m^2 on Ti electrode, METAKEM GmbH, Usingen, Germany), linear sweep voltammetry measurements (LSV) were performed in 1M potassium hydroxide solution using a Gamry Reference 600 potentiostat. The measurements were conducted at room temperature without stirring at a scan rate of 50 mV/s.

8.2.2 The influence of the incident illumination angle

Figure 7.10 shows the photovoltaic parameters of the a-Si:H/a-Si:H/µc-Si:H triple junction solar cell obtained through the JV measurements under varied illumination angles (for JV curves see Figure A9). In order to illustrate the changes due to the variation in incident angle, all values were normalized to the values obtained under an incident illumination angle of 0° (normal incidence) and plotted versus the incident angle. The shown PV parameters are efficiency η, fill factor FF, open circuit voltage V_{OC}, short circuit current density J_{SC}, voltage at the maximum power point V_{MPP}, and current density at the maximum power point J_{MPP}. Figure 7.10 depicts the case that the effective illuminated area changes upon angle variation according to cosine law (44) influencing the shown photovoltaic parameters.

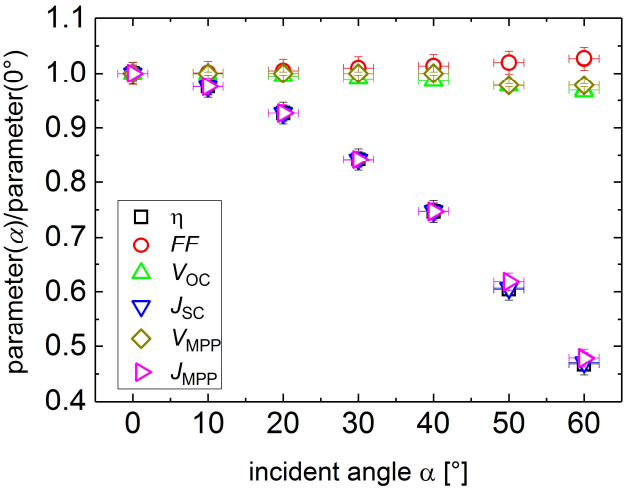

Figure 7.10: Normalized parameters obtained by JV measurements under varied illumination angles plotted versus the incident illumination angle. For all parameters the normalization was executed to the value measured at normal incidence (0°). No area correction according to cosine law (44) was performed.

The open circuit voltage V_{OC} (green triangles) is slightly reduced with increasing angle, while the voltage at the maximum power point V_{MPP} (dark yellow squares) is nearly constant over the range of angles investigated. The *FF* values (red circles) increase slightly with increasing incident angle. The strongest effect of an increased illumination angle can be seen for the photocurrent density (short circuit current density J_{SC} (blue triangles) and current density at the maximum power point J_{MPP} (magenta triangles)), which is reduced by about 52% for an angle of 60° (see Figure 7.10). The efficiency η (black rectangles) follows the trend of reduction with increasing angle as seen for the photocurrent density. A slight decrease in open circuit voltage accompanied by a high decrease in short circuit current density was also observed in the previous chapter discussing the influence of varied illumination intensities on the current-voltage characteristics. In the case of the reduced intensity, the decrease of J_{SC} is attributed to the reduced number of photons reaching the solar cell, while the slight reduction in V_{OC} is caused by reduced quasi-Fermi level splitting under reduced intensities.[60,128] An increase in *FF* can be expected with an increasing angle, similar to the case of reduction in the illumination intensity previously reported. An increase in *FF* values is generally attributed to the improvement in the built-in field in the device and reduced recombination of photogenerated charge carriers in the absorber layers.[193,194]

As mentioned in the introduction to this section, two possible effects should be considered that can possibly influence the device performance under varying illumination angles. These are (i) the reduced effective illuminated device area (according to cosine law (44) in section (8.2.1)) and (ii) optical effects occurring at the interfaces (for example: glass/air and between silicon sub layers). A possible reflection between the silicon sub layers could for example lead to a strong decrease in sub cell current density causing a limitation of the stack current density and therefore the overall performance. In the following, the influences of both effects are investigated separately. The influence of the reduced effective illuminated area (effect (i)) and thus a decreased number of photons reaching the device area for parameters obtained in the JV measurement under varied illumination angles is eliminated by performing area corrections according to the cosine law[131] (44), leaving only effect (ii) to reduce the device performance (see Figure 7.12).

In order to investigate the optical effects (ii) onto the device performance, external quantum efficiency (EQE) measurements were performed. In the case of EQE measurements, the effective illuminated area of the solar cell and the number of incident photons reaching the device are not reduced upon angular variation, since the illumination spot is considerably smaller than the solar cell area of 1 cm² (see Figure 7.8). Therefore, the spot is within the solar cell area under all investigated incident angles, ensuring a constant number of incident

photons for each wavelength in the investigated range. Hence, effect (i) is eliminated, allowing to investigate only effect (ii).

The external quantum efficiency EQE curves versus the wavelength λ measured for the three different sub cells under various incident angles (between 0° and 60°) can be found in the appendix (see Figure A10). Figure 7.11(a) shows the individual sub cell current densities J_{QE} (a-Si:H top cell, a-Si:H middle cell and µc-Si:H bottom cell) extracted from the EQE measurements under varied incident angles. The external quantum efficiencies are convoluted with the air mass (AM) 1.5G spectrum in the respective wavelength ranges in order to obtain the sub cell current densities (description see chapter (4.2.2)). In the case of the three sub cells, the current densities are reduced with an increasing incident illumination angle. This reduction is due to the optical effects (ii), the increased reflection at increased incident angles. One would expect the highest reflection increase on the air/glass interface, as suggested in the literature.[53,131] A multi-junction cell can be electrically described as a series connection of the different sub cells.[24] Therefore, the current density of the whole device is limited by the lowest sub cell current density. For this triple junction solar cell, the a-Si:H middle cell shows the lowest current density J_{QE} and thus limits the device current density under all investigated incident angles. The sub cell current densities were normalized to the respective values at normal incidence (0°) as shown in Figure 7.11(b), to illustrate the reduction trends observed for the individual sub cells.

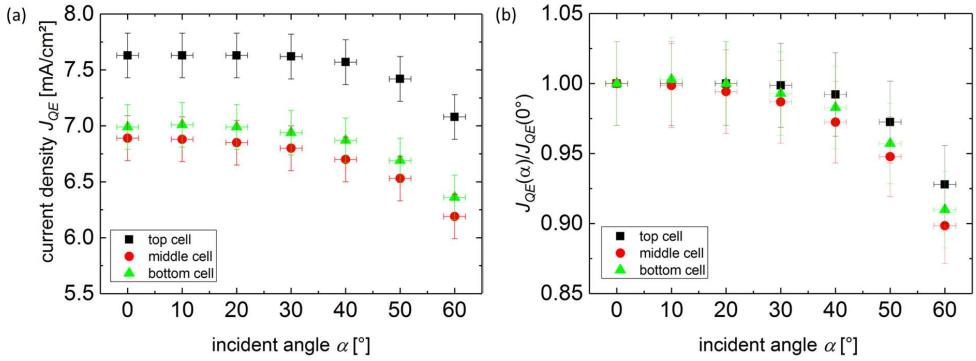

Figure 7.11: (a) Sub cell current densities J_{QE} evaluated from the EQE measurement under varied illumination angles plotted versus the incident illumination angle. (b) Normalized sub cell current densities J_{QE} versus the incident illumination angle for each sub cell. The normalization was carried out with respect to the values obtained at normal incidence (0°).

Similar reduction trends for all normalized sub cell current densities with increasing incident angles are found. The differences between the trends observed for the sub cells are within the error ranges. One possible reason for the slightly enhanced reduction of ~10% of the sub cell current densities at an incident angle of 60° for the middle and bottom sub cells compared with 5% reduction in the top cell could be related to the increased light path and therefore an increased absorption in the top cell.[131,132] Overall, the increased reflection at the interfaces under increased illumination angle accounts for a loss of approximately 10% of the cell stack current.

In order to investigate effect (i) (the reduced effective illuminated area of the photovoltaic current-voltage source), the illuminated area was corrected according to the cosine law (44) ($A(\alpha) = A_0 \cdot \cos(\alpha)$), leaving only the increased reflection losses to reduce the device performance. Figure 7.12 shows the area dependent parameters of short circuit current density (black curve) and current density at the maximum power point (red curve) with and without area correction (without: black squares, red triangle; with: black dots, red upside down triangle) plotted versus the incident illumination angle.

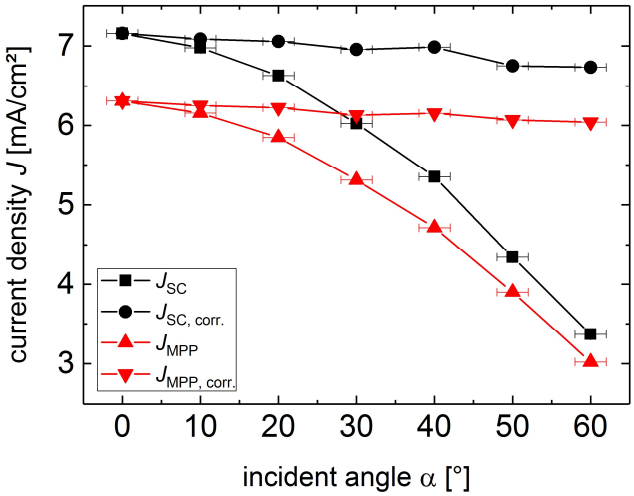

Figure 7.12: Current density versus incident illumination angle for the short circuit current density and the current density at the maximum power point. Black squares and red triangles are indicating the curves without area correction and black dots and red upside down triangles show the curves with area correction.

After performing the area correction according to cosine law (44), the current density at the maximum power point shows a decrease of -0.3 mA/cm² (-5 %). The short circuit current density is reduced by approximately 6 % (7.1 to 6.7 mA/cm²). This reduction could probably be due to the reflection losses as discussed in the previous section, where a reduction of up to 10 % was obtained for the limiting sub cell current density. Comparing the curves without area correction for the short circuit current density and the current density at the maximum power point shows that J_{SC} is more affected by the reduced effective illuminated area than J_{MPP}, which is indicated through a higher slope and decrease (black squares and red triangles). Overall, Figure 7.12 shows that the performance reduction observed in Figure 7.10 is mostly due to the reduced effective illuminated device area (effect (ii)), while the optical losses (effect (i)) play a minor role.

Solar-to-hydrogen efficiency under varied incident illumination angles

In order to investigate the effect of increasing illumination angles on the behavior of the integrated PV-EC device, the current-voltage curves (see Figure A9) were combined with the linear sweep voltammetry curve of platinum as HER electrode and iridium oxide as OER electrode according to the model described in chapter (4.5).[124,125,149] The resulting JV curves for the integrated PV-EC device depending on the incident angle are shown in Figure 7.13. The operating current density at bias-free conditions ($V = 0$ V) can be extracted and used to evaluate the solar-to-hydrogen efficiency η_{STH} according to equation (40).

The modelled current density-voltage curves of the PV-EC device based on an a-Si:H/a-Si:H/µc-Si:H triple junction solar cell in combination with platinum and iridium oxide in alkaline media (PV-EC device configuration also used in section (8.1)) show decreasing current densities and voltages for increasing incident illumination angles. The operating current density ($V = 0$ V) decreases for the range of angles investigated, but can be extracted in all cases. Thus, hydrogen can be generated using this PV-EC device configuration and the device is not switched off under all investigated illumination angles due to the excessive voltage provided by the a-Si:H/a-Si:H/µc-Si:H triple junction solar cell.

To distinguish between the influences of the optical effects and of the reduced effective illuminated area on the device performance, the operating current density and the resulting solar-to-hydrogen efficiency are plotted versus the incident angle in Figure 7.14 with and without area correction according to cosine law (44). By performing the area correction only optical effects are left to reduce the device performance. If the area

correction is not performed, the operating current density at bias-free conditions is reduced with increasing angle similar to the short circuit current density and the current density at the maximum power point. This directly affects the solar-to-hydrogen efficiency η_{STH}, which is reduced by about 52 % (from 8.2 % at 0° to 3.9 % at 60°) and accordingly, the hydrogen output is decreased. In the case of the performed area correction, the operating current density as well as the solar-to-hydrogen efficiency, and thus the hydrogen output, are nearly constant over the range of incident illumination angles investigated.

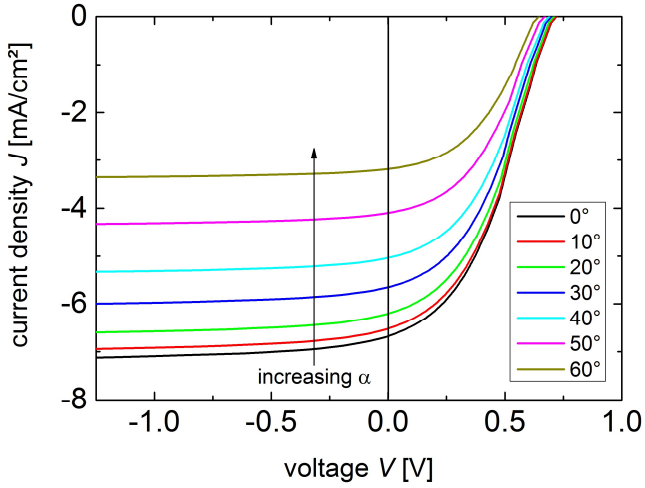

Figure 7.13: Current density-voltage curves of the integrated PV-EC device (a-Si:H/a-Si:H/µc-Si:H/Pt/KOH/IrO_X, same cell and configuration as used in section (8.1)) obtained under varying incident illumination angles using the electrical series connection model.[124,125,149] The operating current density at zero bias is indicated as well as the increasing illumination angles.

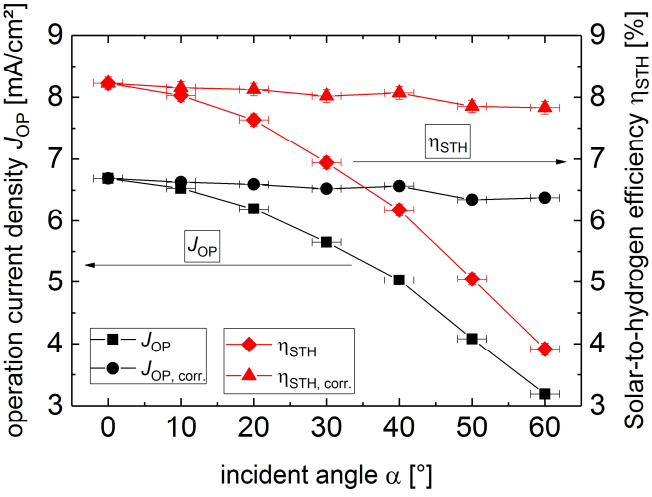

Figure 7.14: Extracted operating current density and solar-to-hydrogen efficiency calculated for bias-free conditions (V = 0 V, J_{OP}) plotted versus the incident illumination angle for a PV-EC device (a-Si:H/a-Si:H/µc-Si:H/Pt/KOH/IrO_X) without (black squares, red diamonds) and with (black dots, red triangles) area correction.

Overall, hydrogen can be generated by the PV-EC device consisting of an a-Si:H/a-Si:H/µc-Si:H triple junction solar cell in combination with platinum and iridium oxide in alkaline media for the range of incident illumination angles investigated in the present study (0 – 60°), since an operating current density could be extracted under all investigated angles. The PV-EC device is consequently not switched off by the illumination

under varied illumination angles (0 – 60°). The reduced effective illuminated device area can be understood as a decreased intensity due to the reduced number of photons per area. Thus, the variation of incident illumination angles represents an additional intensity loss path, which is added to the natural intensity losses, reducing the device performance and the hydrogen output. Optical losses due to reflection do not have a major influence on the device performance. An additional point that has to be considered for further device engineering, is the tilted mounting of the PV-EC device in order to ensure approximately perpendicular illumination angles. In contrast to the outdoor application, PV-EC devices characterized under laboratory conditions are either in vertical or horizontal measurement position. The tilted mounting position of the PV-EC devices has to be considered for instance regarding electrolyte and gas transport within the device.

8.3 The influence of the spectral quality

As described before, thin film silicon multi-junction based PV-EC devices are influenced by the operating conditions investigated, so far illumination intensity, operating temperature and incident illumination angle. In the following, the influence of the spectral quality on the device performance will be investigated. Multi-junction cells consist of sub cells with different electrical and optical properties. The sub cells absorb in different wavelength regions due to the different band gaps. As described in chapter (3.1.2), if the sub cells of the multi-junction cell stack are current matched under standard test conditions, then the illumination with a modified spectrum can lead to a current mismatch between the sub cells. This mismatch can potentially increase or decrease the device performance, depending on which sub cell is enhanced by the illumination.[195]

The spectral quality is frequently described and qualified in terms of average photon energy (APE), which is defined as the total energy in a spectrum (spectral irradiance) divided by the total number of photons it contains (photon flux density), see equation (29) in chapter (3.4.4).[44,51,196,197] Regarding the outdoor application, spectra measured in the northern hemisphere in winter appear to have lower average photon energies, since the share of the long wavelength region is increased, while in summer the share of short wavelengths is higher, resulting in a higher APE.[45] The average photon energies can vary for different locations as reported in literature (e.g. 1.90 – 1.95 eV for Shiga (Japan) and 1.59 – 1.72 eV for Rome (Italy)).[44,45,198] Note that this variation is not only due to the different geographical location but also to the different wavelength ranges of the incident spectrum considered to calculate the APE values (350 – 1050 nm for Shiga and 350 – 1700 nm for Rome).[44,45] Changes in the shape of a spectrum can also be caused, for example, if the photoabsorber material is illuminated through the electrolyte or the catalyst layer, respectively[41,199,200].

The experimental modification of the AM 1.5G spectrum towards higher/lower average photon energies was realized using a set of high power LEDs with respective wavelengths in the range of 465 – 850 nm. The current-voltage curves of the PV-EC device based on an a-Si:H/a-Si:H/µc-Si:H triple junction cell (also used in sections (8.1) and (8.2)) were studied under the modified spectra with an APE range of 1.69 – 1.75 V (calculated in the wavelength range from 300 to 1100 nm). The APE range realized here, is similar to the annual variation of APE reported in the literature[44]. Note that the spectra applied here simulate varied APE spectra as reported in literature but do not replicate any spectral shape reported for a given location. The purpose of the study is to investigate the trends of changes in the PV-EC device performance operating under conditions representing the annual changes between blue rich (summer) and red rich (winter) spectra. Different catalyst systems are applied in the PV-EC devices and investigated under varied illumination spectra to determine the influence of the electrochemical part of the device. Depending on the catalyst system, the operating point of the PV-EC device varies and can be influenced by varying spectral illumination conditions. System (A) consists of platinum as hydrogen evolution reaction catalyst and iridium oxide as oxygen evolution reaction catalyst and represents the noble metal reference system (also used in sections (8.1) and (8.2)). Two different earth-abundant catalyst systems were used for comparison. System (B) is made of nickel molybdenum nitride ($Ni_XMo_YN_Z$) (HER) and cobalt-iron layered double hydroxide (Co-Fe LDH, OER); both catalysts were deposited on porous nickel foam (for further information see chapter (7.3.1)). The third system used consists of the catalyst system presented in chapter (7.3.2), nickel molybdenum (NiMo) as HER and nickel iron oxide

($NiFeO_X$) as OER. In order to predict the PV-EC device performance and the resulting solar-to-hydrogen efficiencies under varied spectral quality conditions, the individually measured current-voltage characteristics (JV curve of the photovoltaic cell and LSV curves of the catalyst systems) were combined using the electrical series connection model described in chapter (4.5). The solar-to-hydrogen efficiencies of the PV-EC devices employing various catalyst systems were extracted at zero bias and calculated according to equation (40).

8.3.1 Experimental details

External quantum efficiency measurements were performed as described in chapter (4.2.2). The resulting sub cell current densities J_{QE} and quantum efficiency curves are shown in Figure 7.15(a). Current-voltage curves of the a-Si:H/a-Si:H/µc-Si:H triple junction solar cell were measured under AM 1.5G illumination provided by a class AAA sun simulator (see chapter (4.2.1)) and under modified spectra. Figure 7.15(b) shows the wavelength ranges of the high power LEDs, which were used for the spectral modification. The LED wavelength ranges were chosen such that the individual triple junction sub cells are addressed (top cell: blue + green, middle cell: green + red, bottom cell: red + infra-red, see Figure 7.15(b)). The modified spectra cover an APE range of 1.69 eV (red rich) to 1.75 eV (blue rich). For accurate comparison of the solar cell performance under varied spectral quality used here and to distinguish the influence of the spectral modification on the PV-EC device performance, the incident illumination intensity, incident angle and operating temperature were kept constant for all spectra investigated (25 °C and perpendicular illumination with 1000 W/m² equal to the light intensity under STC), although during the outdoor application changes in the spectral composition can be accompanied by a variation in intensity.[46] Two different power settings (either max. power 100 % or half of max. power 50 %) could be realized for each LED, allowing to cover the range of investigated APEs with finer steps. As an example, a blue modified spectrum with an APE of 1.75 eV is shown in Figure 7.16 as blue dashed curve. The initial AM1.5G spectrum is shown for comparison (black solid curve) and has an APE of 1.71 eV.

Electrochemical measurements:

The current-voltage behavior of the catalyst system consisting of platinum (HER, 99.95 % purity, supplied by Goodfellow GmbH, Germany) and iridium oxide (OER, 12 g Ir/m^2 on Ti electrode, METAKEM GmbH, Usingen, Germany) was determined using linear sweep voltammetry measurements (LSV), which were performed in 1 M potassium hydroxide solution using a Gamry Reference 600 potentiostat. The measurements were conducted at room temperature without stirring at a scan rate of 50 mV/s.

The current-voltage characterizations of the different earth-abundant catalyst systems are described in detail in section (7.3.1) for $Ni_XMo_YN_Z$/Co-Fe LDH and in chapter (7.3.2) for NiMo/$NiFeO_X$.

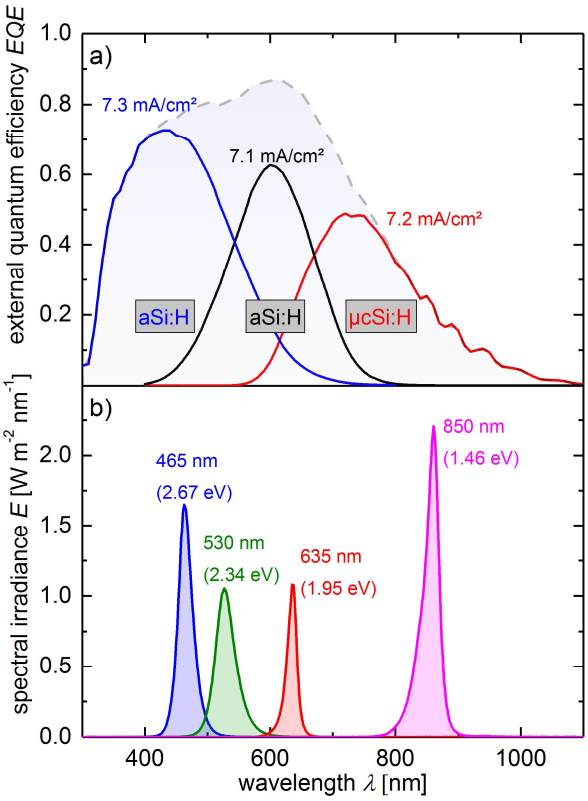

Figure 7.15: (a) EQE measured for the a-Si:H/a-Si:H/µc-Si:H solar cell (also used in section 7.1 and 7.2), J_{QE} values calculated for each sub cell are indicated, showing that the device current density J_{SC} under STC is limited by is the middle sub cell (lowest sub cell current density of J_{QE} = 7.1 mA/cm²). (b) Spectral irradiance of a set of high power LEDs with different wavelengths to vary the average photon energy of the spectrum. The different sub cells in the triple cell stack are addressed by the LED wavelengths.

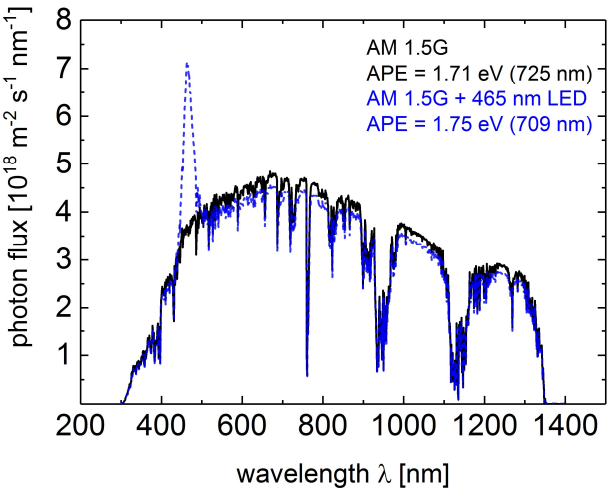

Figure 7.16: Blue modified spectrum (blue dashed curve) with an increased average photon energy of 1.75 eV compared to the AM1.5G spectrum (black solid curve) with an APE of 1.71 eV. The incident power of both spectra is 1000 W/m². Operating temperature and incident illumination angle were constant at 25 °C and 0° respectively.

8.3.2 The influence of the spectral quality

Photovoltaic parameters under varied APE spectra

Figure 7.17 shows the current density-voltage curves of an a-Si:H/a-Si:H/µc-Si:H triple junction solar cell (same cell as used in sections (8.1) and (8.2)) measured under varied spectral illumination. In the case of Figure 7.17(a), the illumination spectra were enhanced in the short wavelength range by using the additional blue LED (465 nm) on maximum power setting (APE = 1.75 eV) and on 50% of maximum power setting (APE = 1.73 eV). For Figure 7.17(b), the spectral shape was modified in the long wavelength region by applying additional infra-red light using the 850 nm LED at maximum power (APE = 1.69 eV) and for the APE of 1.70 eV the IR LED on half maximum power settings. The spectral modifications shown in Figure 7.17(a) and (b) represent the highest and lowest average photon energies investigated in this section (1.75 eV and 1.69 eV). In both cases, the JV curve measured under AM1.5G conditions (APE = 1.71 eV) is shown for comparison. The PV parameters obtained for the a-Si:H/a-Si:H/µc-Si:H triple junction cell measured under the varied spectral illumination are listed in Table 7.1.

Table 7.1: Overview of the photovoltaic parameters measured for the a-Si:H/a-Si:H/µc-Si:H triple junction cell under varied illumination spectra in the APE range of 1.69 – 1.75 eV. The total incident power was constant (1000 W/m²).

APE [eV]	LED λ [nm]	LED intensity	η_{PV} [%]	*FF* [%]	V_{OC} [V]	J_{SC} [mA/cm²]
1.69	850	100%	11.0	73.3	2.24	6.7
1.70	850	50%	11.4	73.3	2.24	6.9
1.73	465	50%	12.1	75.3	2.24	7.2
1.75	465	100%	11.5	74.9	2.24	7.0
1.71	Ref. AM1.5G		11.5	71.9	2.24	7.2

The open circuit voltage V_{OC} measured is constant (2.24 V) for the APE range of 1.69 – 1.75 eV as depicted in Figure 7.17 and shown in Table 7.1. As mentioned in the experimental details to this section, in the case of the spectral variation, operating temperature and illumination intensity were kept constant.

In contrast to the open circuit voltage, the short circuit current density J_{SC} is affected by the spectral composition of the incident illumination spectrum. For an enhancement in the short wavelength range by applying the blue LED on 50 % of maximum power (APE = 1.73 eV), the short circuit current density (J_{SC} = 7.2 mA/cm²) is similar to the J_{SC} obtained under standard test conditions (APE = 1.71 eV). The spectra with other varied APEs lead to a reduction of the short circuit current density for this particular triple junction solar cell, down to 6.7 mA/cm² measured for the spectrum with an average photon energy of 1.69 eV (infra-red LED on maximum power). The fill factor is generally increased for the spectral modifications investigated. The photovoltaic efficiency is reduced for red rich spectra (APE below 1.71 eV) and increased for blue rich spectra (APE above 1.71 eV).

The observed trends for the changes in short circuit current density can be explained by the structure of the multi-junction cell used in the present study. In the cell stack, the sub cells are connected in series, hence the total device voltage is the sum of all sub cell voltages and the total device current is limited by the lowest sub cell current (see also chapter (3.1.2)). The sub cells are electrically and optically optimized towards different wavelengths in order to make full use of the incident solar spectrum.[24,34] Therefore, the sub cells respond differently to the spectral modification with particular LEDs (see also Figure 7.15), which can be expected from the external quantum efficiency measurements. For example, for short wavelength enriched spectra (blue shifted, APEs of 1.73 eV and 1.75 eV) the a-Si:H top and middle sub cells show an enhanced light absorption, thus the respective sub cell current densities J_{QE} are increased. Due to the constant illumination intensity of 1000 W/m², an enrichment in the short wavelength range, compared to the AM1.5G spectrum, results in a reduction of the contribution in the long wavelength range (570 – 1100 nm) for the spectra with an APE of 1.73 eV and 1.75 eV (see also Figure 7.16).

The µc-Si:H bottom cell shows its highest spectral response in the wavelength range of 600 – 1100 nm. A reduced share in the long wavelength ranges thus leads to a decreased bottom cell current for blue rich spectra, which then limits the total cell stack current density ($J_{SC,APE1.75}$ = 7.0 mA/cm² and $J_{SC,APE1.73}$ = 7.2 mA/cm²). In the case of the strongly blue shifted spectra with an APE of 1.75, the reduction in the long wavelength range is more severe than for the spectra with 1.73 eV, thus the measured short circuit current density $J_{SC,APE1.75}$ is lower than $J_{SC,APE1.73}$.

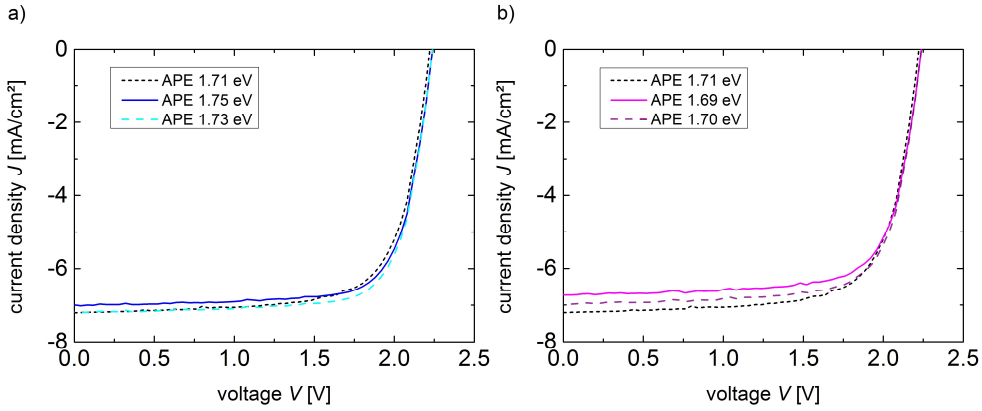

Figure 7.17: Measured current density-voltage curves for an a-Si:H/a-Si:H/µc-Si:H triple junction solar cell (same cell as used in sections (8.1) and (8.2)) under AM1.5G illumination (APE = 1.71 eV, dotted black curve) and (a) with additional 465 nm wavelength light (enriched in short wavelength range) and (b) with additional 850 nm wavelength light (enriched in long wavelength range). For finer APE steps, the LED power settings were (i) maximum power (APE = 1.75 eV and APE = 1.69 eV) and (ii) 50% of maximum power (APE = 1.73 eV and APE = 1.70 eV).

For the enhancement in the long wavelength range by applying the 850 nm LED, the µc-Si:H bottom cell shows an increased absorption and therefore an increased sub cell current density J_{QE}. In this case, the incident light in the short wavelength range is reduced, leading to reduced sub cell current densities in the a-Si:H top and middle cell, which then limit the device current ($J_{SC,APE1.70}$ = 6.9 mA/cm²; $J_{SC,APE1.69}$ = 6.7 mA/cm²).

For all spectral modifications, the increased current mismatch due to the varied illumination composition is reflected in the increase of the fill factor *FF* (71.9 → 75.3 %). The effect of an increasing fill factor with current mismatch for thin film silicon multi-junction solar cells is well described in literature.[51,52,136,201] The results obtained here indicate that mainly the short circuit current density (-7 % in the case of lowest APE spectrum) and the fill factor (+3.4 % absolute) of the a-Si:H/a-Si:H/µc-Si:H triple junction cell are influenced by the spectral modification, while the open circuit voltage remains constant (2.24 V) under these spectral modifications.

PV-EC device performance and solar-to-hydrogen efficiency under varied APE spectra

In the following section, the influence of the varied spectral illumination conditions on the performance of the entire PV-EC device will be discussed. The spectral modifications can possibly influence the choice of catalyst materials for the PV-EC device, since the device operating point is shifted depending on the catalyst overpotential. To evaluate the performance of the complete PV-EC device under varied spectral illumination composition, the current density-voltage curves of the PV-EC devices were calculated using the electrical series connection model described in chapter (4.5).

From the obtained current density-voltage curves of the combined PV-EC devices, the solar-to-hydrogen efficiencies under varied spectral illumination conditions, thus depending on the average photon energies, were concluded. The LSV curves of the catalyst systems used, can be found in the previous sections (see section (8.1) for Pt/IrO_X, section (7.3.1) for Co-Fe LDH/$Ni_XMo_YN_Z$ and section (7.3.2) for $NiMo/NiFeO_X$).

Figure 7.18 shows the resulting calculated current density-voltage curves for the PV-EC devices employing different catalyst systems under varied spectral composition for the incident illumination ((a) blue rich, high APEs of 1.73 eV and 1.75 eV; (b) red rich, low APEs of 1.69 eV and 1.70 eV).

Comparing the different catalyst systems in the PV-EC device under STC, the earth-abundant systems (B) (J_{OP}(B) = -6.76 mA/cm²) and (C) (J_{OP}(C) = -6.82 mA/cm²) show higher current densitiy values at the operating point than the noble metal system (A) (J_{OP}(A) = -6.64 mA/cm²) (for detailed discussion and further information see also chapter (7)). Regarding the performance of the PV-EC devices under varied average photon energy spectra, the same trend can be observed as for the current density-voltage curves of the photovoltaic cell shown in Figure 7.17. For the particular PV-EC device investigated in the present study, decreased average photon energies (1.70 and 1.69 eV) lead to a reduced current density at the operating point and thus a reduced solar-to-hydrogen efficiency η_{STH}. For an average photon energy of 1.73 eV, the operating current densities are increased compared to AM1.5G for all devices investigated. If the average photon energy is further increased to 1.75 eV, the operating current density is increased for Pt/IrO_X (A) and decreased for the earth-abundant catalyst systems ((B), (C)) compared to the operating current density under AM1.5G conditions.

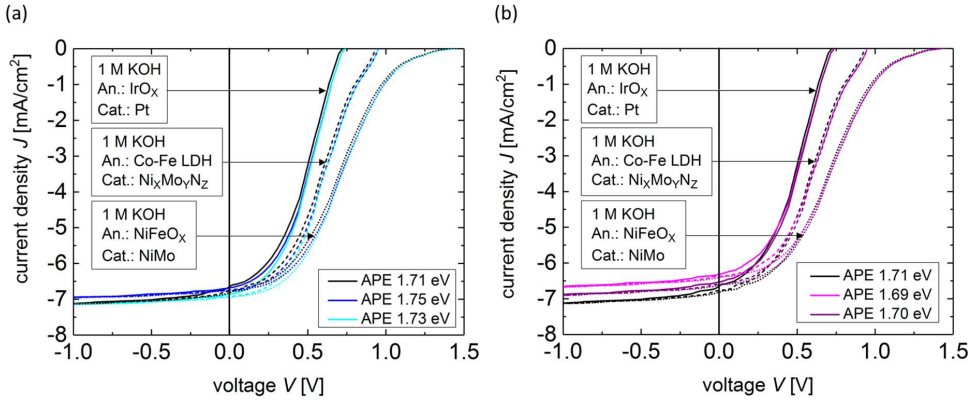

Figure 7.18: Calculated current density-voltage curves of an a-Si:H/a-Si:H/µc-Si:H triple junction solar cell based PV-EC device employing different catalyst systems (A, solid lines) Pt/IrO_X, (B, dashed lines) $Ni_XMo_YN_Z$/Co-Fe LDH and (C, dotted lines) NiMo/$NiFeO_X$ under standard test conditions (STC, AM1.5G, APE = 1.71 eV, black line) and under modified spectra: (a) high APEs (blue rich) and (b) low APEs (red rich). 1 M potassium hydroxide was used as electrolyte in all cases. The operating voltage for unbiased light induced water splitting is indicated at zero volts.

The solar-to-hydrogen efficiencies for the PV-EC devices investigated employing the particular a-Si:H/a-Si:H/µc-Si:H triple junction solar cell and the catalyst systems (A)-(C) are extracted from the calculated current density-voltage curves under varied illumination spectra at zero bias (Figure 7.18) and plotted versus the average photon energy as shown in Figure 7.19(a)-(c). The solar-to-hydrogen efficiencies obtained under STC are indicated using a horizontal guideline, while the trends for the solar-to-hydrogen efficiencies depending on the average photon energies are indicated by the grey dashed guidelines.

All catalyst systems employed with the a-Si:H/a-Si:/µc-Si:H triple junction solar cell show very similar trends for the solar-to-hydrogen efficiency plotted versus the average photon energy, shown in Figure 7.19(a)-(c). Average photon energies below 1.71 eV lead in all cases to reduced solar-to-hydrogen efficiencies. The maximum solar-to-hydrogen efficiencies are obtained for average photon energies around 1.71 – 1.72 eV for spectral modifications using the LEDs with 530 nm and 635 nm, respectively, followed by a decrease in solar-to-hydrogen efficiency. For the highly active catalyst system (C), the maximum solar-to-hydrogen efficiency is obtained at a lower average photon energy (1.71 eV, modified with red LED) as compared to system (A) ($\eta_{STH,max}$ at APE = 1.72 eV). Depending on the catalyst systems, it was observed that for high average photon energies, such as 1.75 eV, the solar-to-hydrogen efficiency can be lower than the STH efficiency yielded under AM1.5G (see catalyst systems (B) and (C)). Additionally, differences for the three catalyst systems investigated are found regarding the absolute solar-to-hydrogen efficiency values. All systems (A-C) show

changes of less than 1% absolute in solar-to-hydrogen efficiency over the range of average photon energies investigated (system (A): 7.76 – 8.57 %; system (B): 7.83 – 8.67 %; system (C): 7.87 – 8.71 %).

Under standard test conditions, the middle sub cell shows the lowest sub cell current density and thus limits the overall cell stack current density for the here used triple junction solar cell (see also Figure 7.15). By applying modified spectra of average photon energies of 1.71 eV (not AM1.5G) or 1.72 eV, respectively, the current limitation of the middle cell is resolved, since the middle sub cell responds with an increased sub cell current density to the modified spectra. The effect of the resolved current limitation is also reflected in the maximum solar-to-hydrogen efficiencies measured under spectra enhanced in the wavelength region between 500 – 700 nm (green LED 530 nm, red LED 635 nm), in which the middle sub cell absorbs (see Figure 7.15). The observed shift for the average photon energy at which the maximum solar-to-hydrogen efficiency is obtained, is due to the operating point of the PV-EC device, which depends on the used catalyst system. For highly active catalyst systems, as for example (C), the operating point is in a more flat region as for system (A) (see black lines in Figure 7.18). Decreased average photon energy spectra (e.g. during winter time) lead to an increased bottom sub cell current density due to the enrichment in the long wavelength region. Additionally, the sub cell current densities in the top and middle sub cells are decreased because of the reduced contribution in the short wavelength range and the top/middle cell then limits the device current and the solar-to-hydrogen efficiencies are reduced. For spectra enriched in the short wavelength region (high APE, e.g. during summer time), the opposite effect is observed: the top sub cell current densities are enhanced and the device current is limited by the bottom sub cell current (see solar-to-hydrogen efficiencies of system (B) and (C) for spectra with an APE of 1.75 eV).

Overall, the results shown in this section indicate that changes in the APE values within the range of 0.06 eV can substantially influence the device performance and affect the solar-to-hydrogen efficiency. In all spectral illumination compositions, the device current is limited by one sub cell current, which can alter depending on the average photon energy and shape of the incident illumination spectrum. Hence, multi-junction thin film silicon solar cells used for the application in light induced PV-EC devices should ideally be optimized with respect to the spectral conditions at the operating site, which are most likely different from STC. Comparing the different catalyst systems, similar trends were observed for the solar-to-hydrogen efficiency depending on the average photon energy. A detailed analysis of the spectral illumination compositions at the operating site could be beneficial prior to the installation of the thin film silicon multi-junction based PV-EC device.

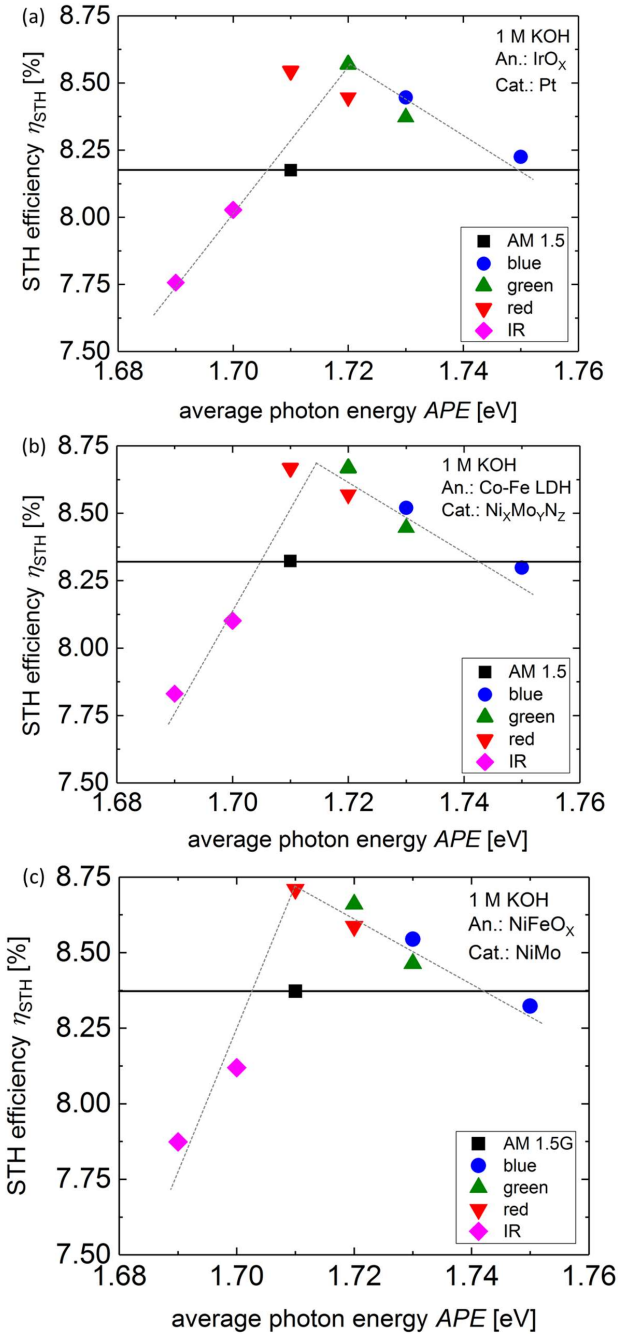

Figure 7.19: Solar-to-hydrogen efficiency plotted versus the average photon energy of the incident spectrum for a PV-EC device based on an a-Si:H/a-Si:H/µc-Si triple junction solar cell and different catalyst systems: a) Pt/IrO_X, b) $Ni_XMo_YN_Z$/Co-Fe LDH and c) NiMo/$NiFeO_X$. The colors illustrate, which LED was used to modify the spectrum and to achieve the respective APE.

8.4 Estimation of the annual hydrogen yield of multi-junction based PV-EC devices

In the following section, an estimation of the annual hydrogen output of multi-junction based PV-EC devices will be given. Different types of multi-junction cells from tandem to quadruple junctions (sub cells with different band gap energies[24,34]) will be compared regarding their preparation process and the amount of hydrogen generated under different spectral conditions. Based on the results of the previous sections, three different catalyst systems will be compared and combined with the different multi-junction cells in PV-EC devices. Regarding possible influences on the device performance due to the illumination investigated previously for an a-Si:H/a-Si:H/µc-Si:H triple junction cell, the assumption is made that other multi-junction cells show similar behavior regarding the illumination intensity and operating temperature as well as the incident illumination angle. Hence, the PV-EC devices employing different multi-junction cells will only be influenced by the spectral variation. One could for example imagine a testing site, where the PV-EC devices using different multi-junction cells are placed side-by-side, such that the influences in temperature, intensity and angle are equal. The active device areas are assumed to equal 1 m². Considering the results obtained in chapter (7.2), the 1 m² active area could be envisioned as consisting of several identical multi-junction cell parts connected in parallel.

The annual hydrogen output will be estimated for a real measured spectrum in a given location, which was reported in literature, where the maximum irradiance is reported for an APE above the average photon energy of the AM1.5G spectrum.[42] The current density-voltage curves of the different multi-junction solar cells were measured in an APE range of -0.26 – +0.18 eV difference to AM1.5G. The estimation process is exemplarily shown in detail for the a-Si:H/a-Si:H/µc-Si:H triple junction cell, which was also used in the previous sections. The estimation process was also applied for the other types of multi-junction cells.

8.4.1 Experimental details

The variation of the incident illumination spectra by using a set of high power LEDs is described in chapter (8.3). The results obtained in chapter (8.3) for the a-Si:H/a-Si:H/µc-Si:H triple junction cell were used for the calculation of the annual hydrogen output. Additionally, the APE range was increased by altering the share of the two light sources, a xenon and a halogen lamp, in the class AAA sun simulator (Wacom sun simulator WXS-140S-Super). To employ low APEs, the intensity of the xenon lamp was reduced, while the intensity of the halogen lamp was increased. For high APEs, the intensity share was inverted. The corresponding spectra can be found in the appendix (see Figure A12). Also in this case, the overall intensity of the incident illumination spectrum was kept constant at 1000 W/m² under perpendicular illumination angle and a temperature of 25 °C. The spectral quality is described in terms of average photon energy, the definition is given in chapter (3.4.4). By altering the share of the light sources and applying the additional LED light, the average photon energy range used in this section covers a range of ΔAPE = 0.44 eV and is presented as a difference to the average photon energy of the AM1.5G spectrum (1.71 eV $APE_{AM1.5G}$ = 0 eV ΔAPE). A possible contribution of changes for other operating conditions than the APE spectra during the outdoor application can be neglected due to the assumption that intensity, temperature and incident angle are equal for all devices investigated and have similar effects on the devices.

Calculation of the annual hydrogen yield:

The estimation of the annual hydrogen yield was performed according to the six following steps, which will be elaborated on in the following (section (8.4.2)).

1. The current density-voltage curves of the PV-EC devices were determined under AM1.5G and varied APE illumination spectra for 1 sun intensity (1000 W/m²).

2. The solar-to-hydrogen efficiencies were calculated for illumination under AM1.5G and varied APE illumination spectra for 1 sun intensity using the current density-voltage curves measured in point (1.) combined with the current-voltage characteristics (LSV measurements) for different catalyst systems. The electrical series connection model described in chapter (4.5) was used for the solar-to-hydrogen efficiency calculation.

3. Spectral data containing the annual irradiance depending on the average photon energy was taken from literature[44] and fitted using a Gaussian fit function yielding irradiance depending on average photon energy. The reported spectral data (1050 W/m²) is rescaled to an incident illumination intensity of 1000 W/m².

4. Using the fit function generated in point (3.), the solar-to-hydrogen efficiencies depending on the APE, calculated in point (2.), can be assigned to an irradiance for that specific APE. The solar-to-hydrogen efficiencies in dependence of the APE were convoluted with the irradiance depending on the APE.

5. Integration of all convoluted solar-to-hydrogen efficiencies with irradiance over the entire average photon energy range, resulting in the total value for the spectrum.

6. Multiplication of the total value obtained for the spectrum (point (5.)) with an experimentally determined factor of 2.5 L/m² for the hydrogen volume produced at 1% solar-to-hydrogen efficiency[35] leads to the hydrogen volume yield for the respective spectrum and device. The determination of the factor of 2.5 L/m² is shown in detail in the appendix (see Figure A11).

$$V_{annual}(Hydrogen) = 1\,m^2 \cdot 2.5\,L/m^2 \int_{APE1}^{APE2} P(APE)\,STH(APE)dAPE \tag{45}$$

8.4.2 Estimation of annual hydrogen yield for various multi-junction based devices employing different catalyst systems

The annual hydrogen estimation procedure described above will be exemplarily executed for a PV-EC device based on an a-Si:H/a-Si:H/µc-Si:H triple junction cell combined with platinum and iridium oxide as catalyst system.

1. Determination of current density-voltage curves under AM1.5G and varied APE spectra

Figure 7.20 shows the current density-voltage curves measured under the highest and lowest average photon energy realized by altering the share of the light sources. In both cases, the short circuit current density is significantly reduced compared to the current density-voltage curve measured under standard test conditions (AM1.5G, ΔAPE = 0 eV). For further discussion on the effects due to the varied illumination spectra, see section (8.3). Additionally, the current density-voltage curves obtained in the previous section (8.3) for the illumination with blue and red shifted spectra are used for the estimation of the annual hydrogen yield depending on the average photon energy (see Figure 7.17). For all current density-voltage measurements under varied APE spectra, the operating temperature (25 °C), illumination intensity (1000 W/m²) and incident illumination angle (0°) were kept constant.

2. Calculation of solar-to-hydrogen efficiencies under AM1.5G and varied APE spectral illumination

According to the second step of the estimation process, the solar-to-hydrogen efficiencies for various average photon energy spectra were calculated. Therefore, the current density-voltage curves measured in the first step were combined with the linear sweep voltammetry measurement of platinum and iridium oxide as catalyst system in the electrical series connection model described in chapter (4.5). The resulting solar-to-hydrogen efficiencies were plotted versus the differences of average photon energies related to AM1.5G, which is equal to zero difference in APE (Figure 7.21). As described in chapter (8.3.2) for this particular solar cell, average photon energies below AM1.5G (ΔAPE < 0 eV) lead to decreased solar-to-hydrogen efficiencies compared to

the solar-to-hydrogen efficiency obtained under AM1.5G illumination conditions. For average photon energies above AM1.5G (ΔAPE > 0 eV), the solar-to-hydrogen efficiencies are first increased with a maximum value at ΔAPE = +0.02 eV. For average photon energies above ΔAPE = +0.02 eV, the solar-to-hydrogen efficiency is decreased down to 7.3 %. For detailed description of the various effects occuring for the solar-to-hydrogen efficiency under varied spectral illumination quality see chapter (8.3.2). These steps were also carried out for the devices based on other multi-junction cells investigated in this section (tandem, quadruple and a-Si:H/µc-Si:H/µc-Si:H triple junction cells), combined with platinum and iridium oxide. The corresponding figures (current density-voltage curves and solar-to-hydrogen efficiency versus average photon energy difference) can be found in the appendix (see Figure A13, Figure A14, Figure A15 and Figure A16).

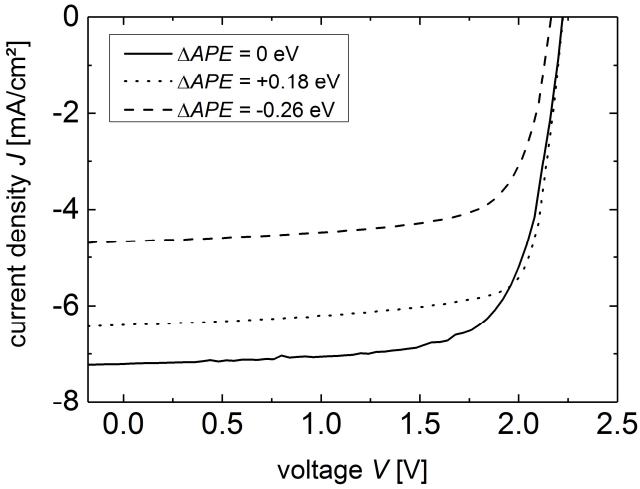

Figure 7.20: Current density-voltage curves for a-Si:H/a-Si:H/µc-Si:H triple junction solar cell (same as used in sections (8.3)-(8.1)) measured under AM1.5G illumination (solid line, ΔAPE = 0 eV) and under varied APE spectra. Shown here are the spectrum with highest APE (ΔAPE = +0.18 eV) and lowest APE (ΔAPE = -0.26 eV) realized. The operating temperature (25 °C), illumination intensity (1000 W/m²) and incident illumination angle (0°) were kept constant for all spectra.

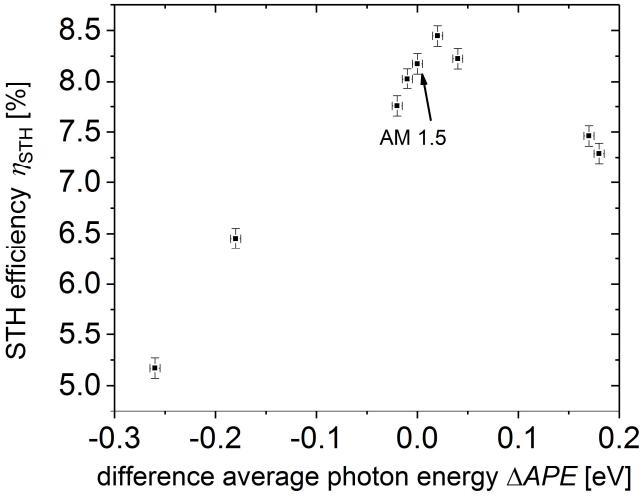

Figure 7.21: Solar-to-hydrogen efficiencies plotted versus the difference average photon energies for the PV-EC device (a-Si:H/a-Si:H/µc-Si:H/Pt/KOH/IrO_X), where AM1.5G is equal to zero difference in APE.

3. Literature data on spectral irradiance depending on the average photon energy

The data shown in Figure 7.22 were reported in the literature for Shiga in Japan and depict the irradiance measured over a year time depending on the average photon energy. The original data was rescaled in a way that AM1.5G conditions equal zero difference in average photon energy (ΔAPE = 0 eV). The maximum irradiance measured for this location is found at ΔAPE = +0.05 eV, thus most of the spectra recorded during one year are blue shifted compared to AM1.5G conditions. The spectral shape was fitted using a Gaussian function as depicted in red. The following function was obtained for the Gaussian fit with a mean root square of 0.988, using OriginPro:

$$y = (10.33 \pm 3.04) + \frac{(8.75 \pm 0.44)}{((0.06 \pm 0.01)\sqrt{\frac{\pi}{4\ln(2)}}} e^{\left(\frac{-4\cdot\ln(2)(x-0.04)^2}{(0.06\pm0.01)^2}\right)} \quad (46)$$

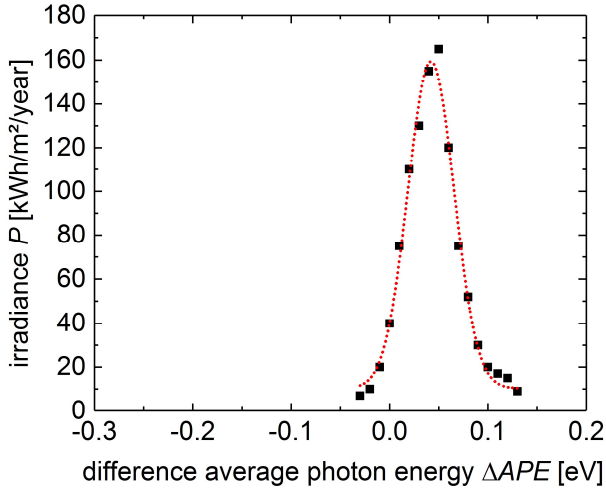

Figure 7.22: Irradiance versus difference in average photon energy. The original data was taken from reference[42] for Shiga, Japan. The data was rescaled such that AM1.5G resembles ΔAPE = 0 eV. The spectral shape was fitted using a Gaussian function in OriginPro.

4. Extraction of the irradiance for average photon energies used in the experiment

The average photon energy difference values used in the present study (e.g. ΔAPE = +0.02 eV was used) differ slightly from the average photon energy difference values reported in literature data concerning the annual irradiance (e.g. only ΔAPE = +0.01 eV and ΔAPE = +0.03 eV are available in reported data). Therefore, the Gaussian fit function is used to determine the irradiance at the average photon energy difference values for which the solar-to-hydrogen efficiencies were calculated (total intensity of the spectra 1000 W/m²). The solar-to-hydrogen efficiencies were convoluted with the irradiances at the respective average photon energy differences.

5. & 6. Integration of the convoluted values & multiplication with experimental factor for hydrogen yield

The values obtained from the convolution of the solar-to-hydrogen efficiencies and the irradiances at the respective average photon energies were integrated over the entire APE range investigated. The resulting factor was then multiplied with the experimentally obtained factor of the hydrogen volume at 1 % solar-to-hydrogen efficiency (2.5 L/m²). For a detailed explanation on the determination of the factor, see the appendix Figure A11.

$$V_{annual}(Hydrogen) = 1\,m^2 \cdot 2.5\,L/m^2 \int_{APE1}^{APE2} P(APE)\,STH(APE)\,dAPE \quad (47)$$

The resulting values of the annual hydrogen yield for the different multi-junction cells employed in PV-EC devices with platinum and iridium oxide as catalyst system under the reported literature spectrum can be seen in Figure 7.23.

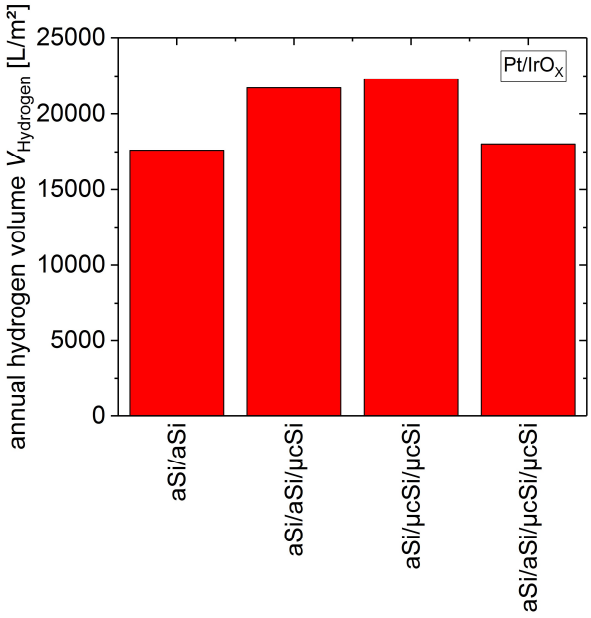

Figure 7.23: Annual hydrogen yield for different multi-junction cells employed in a PV-EC device with platinum and iridium oxide as catalyst system under the reported literature spectrum, which is shown in Figure 7.22[42].

Comparing the tandem and quadruple junction cells, one can see that both multi-junction cells yield a similar amount of hydrogen under these applied illumination conditions, therefore the production of the quadruple junction, which is time-intensive, would not be required, since the easier to prepare tandem junction yields an equal amount of hydrogen. The PV-EC device employing a-Si:H/µc-Si:H/µc-Si:H triple junction cells would produce the most hydrogen under these illumination conditions. However, the amount of hydrogen produced is only slightly increased compared to the use of a-Si:H/a-Si:H/µc-Si:H triple junction cells, which need lower deposition times to be prepared. The slightly higher amount of hydrogen produced does probably not compensate for the preparation process. Thus, under the reported illumination conditions over a year time in the combination with platinum and iridium oxide as catalyst system, a-Si:H/a-Si:H/µc-Si:H triple junction cells would preferably be used, considering ease of preparation and hydrogen yield.

Influence of the catalyst system on the annual hydrogen volume

In the previous chapters (7.3)-(7.6), it was shown that earth-abundant catalyst systems can outperfom noble metal catalyst systems employed in PV-EC devices based on triple junction thin film solar cells. Additionally, the results of chapter (8.3) indicate that the choice of the catalyst system influences the PV-EC device performance under varied spectral quality. Therefore, in the following section, the influence of the catalyst system on the annual hydrogen yield of PV-EC devices employing various multi-junction cells is investigated under the reported spectral conditions for Shiga (Japan). The calculation of the annual hygrogen yield was

performed according to the presented sequence in this chapter employing different catalyst system LSV curves for the solar-to-hydrogen efficiency calculation.

Figure 7.24 shows the annual hydrogen volume calculated for PV-EC devices based on different multi-junction cells applying different catalyst systems for the illumination conditions reported in Shiga (Japan) over a year time[42]. For the tandem junction, both earth-abundant catalyst systems yield considerably more hydrogen than the noble metal catalyst system. For the a-Si:H/a-Si:H/µc-Si:H triple junction cell, the difference between the catalyst systems is not as significant, whereas for the a-Si:H/µc-Si:H/µc-Si:H the hydrogen yield for the earth-abundant systems is increased. In the case of the quadruple junction cell only a slight difference between the hydrogen volumes produced employing different catalyst systems is observed for the reported illumination conditions[42].

If the different multi-junction cells are compared regarding their hydrogen yield, the most hydrogen is produced employing the a-Si:H/µc-Si:H/µc-Si:H triple junction cell. However, as mentioned before, these multi-junction cells are rather complex to prepare. In the case of the earth-abundant catalysts, the overpotential is significantly reduced, thus tandem junction cells can also be successfully employed in the PV-EC devices. Comparing the tandem junction cells to the triple junction cells, the annual amount of hydrogen produced for the PV-EC device (a-Si:H/a-Si:H/NiMo/KOH/$NiFeO_X$) exceeds the amount of hydrogen produced for a-Si:H/a-Si:H/µc-Si:H triple junction based PV-EC devices for the reported spectral conditions. The amount of hydrogen produced in the configuration a-Si:H/a-Si:H/NiMo/KOH/$NiFeO_X$ is the third highest calculated and only exceeded by the devices employing earth-abundant catalysts and the a-Si:H/µc-Si:H/µc-Si:H triple junction cells. The results indicate that for these spectral conditions at the operating site[42], the tandem based PV-EC device employing NiMo/$NiFeO_X$ should be favored for the outdoor application due to the easier preparation process.

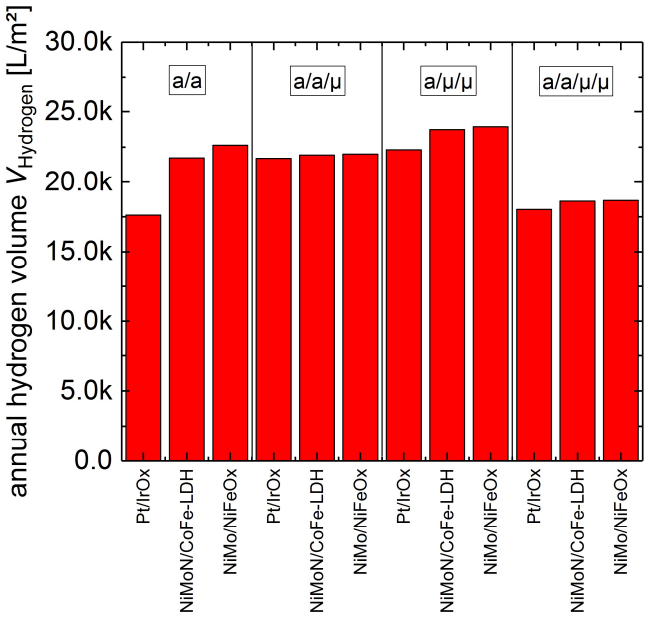

Figure 7.24: Annual hydrogen volume calculated according to the procedure described in this chapter for different multi-junction cells and various catalyst systems for spectral conditions measured over a year time in Shiga (Japan).

8.5 Summary

In this chapter, the varying illumination conditions and the resulting influences on the PV-EC device performance were investigated. It was found that operating temperatures up to 60 °C are beneficial for the PV-EC device performance, since the enhancement in the electrochemical reactions fully compensates the performance loss of the photovoltaic cell. Regarding the influence of the illumination intensity, the hydrogen output by the solar driven water splitting devices is reduced upon intensity decrease. If temperature and intensity variations are combined, as it is probably the case during the outdoor application, it was found that a wide range of operating temperatures is applicable for high illumination intensities, whereas low operating temperatures (~25 °C) are most beneficial for low illumination intensities. Assuming that high illumination intensities could cause enhanced system temperatures and a good thermal conductivity in the PV-EC device, the observed performance increase for high system temperatures can be advantageous for an integrated device compared to a decoupled system. In a decoupled system the solar cell and the electrolyser are connected by wires and placed several meters apart. Regarding the highest operating potential of the decoupled system, the solar cell temperature should not be increased, while the electrolyser is heated to operating temperatures around 80 °C. Concerning the incident illumination angle, it was found that optical effects, such as reflection, play a minor role, while the device performance is mainly reduced due to the reduced effective illuminated area, which is an additional illumination intensity loss path. It was found that hydrogen can be generated under all angles investigated. Additionally, the PV-EC device installation under a certain angle requires further device engineering regarding the gas and electrolyte transport through the PV-EC device. The variations in the spectral quality showed that red shifted spectra lead to reduced solar-to-hydrogen efficiencies for the PV-EC device investigated in the present study, while slight blue shifts increase the solar-to-hydrogen efficiencies. If the spectrum is strongly blue shifted, the PV-EC device performance also depends on the catalyst system used. For highly active catalyst systems, a strong blue shift leads to a reduced solar-to-hydrogen efficiency. Generally, the choice of the catalyst system influences the PV-EC device performance under varied spectral quality, since the catalyst system determines the PV-EC device's operating point, which can be shifted into a region that is more effected by the spectral modification.

Finally, the annual hydrogen yield for different PV-EC devices was estimated for an operating site reported in literature[42] under the assumption that operating temperature, illumination intensity and incident illumination angle lead to the same effects in the PV-EC devices and can thus be neglected. The only variation left in that case would be the spectral quality. Different multi-junction cells and catalyst systems were investigated under spectral conditions reported in the literature for Shiga, Japan. It was found that the highest hydrogen yield can be expected for a system consisting of a-Si:H/µc-Si:H/µc-Si:H/NiMo/KOH/$NiFeO_X$. However, due to the cost-intensive preparation process of the a-Si:H/µc-Si:H/µc-Si:H triple junction solar cell, this might not be the most favored system. Alternatively, the system based on tandem junction cells (a-Si:H/a-Si:H/NiMo/KOH/$NiFeO_X$) yields an only slightly lower (95 % from the a-Si:H/µc-Si:H/µc-Si:H triple junction cell device) amount of hydrogen, while the tandem cell is easier to prepare. For the estimation of the annual hydrogen yield, light induced degradation effects, which are observed for thin film silicon solar cells, have not been taken into account.[34] Overall, the catalyst system and multi-junction cell used in the PV-EC device should ideally be adjusted towards the illumination and operating conditions found at the operating site in order to gain the maximum amount of hydrogen. All effects investigated here have to be taken into account prior to installing the light induced water splitting device at the desired operating location. The PV-EC devices shown in the present work allow a high flexibility towards the use and exchange of photovoltaic cells and catalyst systems. This modularity would also be needed for the application of the technique at different operating sites, which require the use of various system combinations.

9 Summary and further prospects

Photovoltaic-biased electrochemical (PV-EC) devices represent one possible approach for the sustainable generation of hydrogen from renewable energy sources. Besides PV-EC devices, which are on an intermediate cost and technology readiness level, the use of photoabsorber materials emerged in electrolyte (PEC, low costs expected, low technology readiness level)[26] and the use of photovoltaic cells wired to electrolyser systems (PV+EC, higher costs expected, high technology readiness level)[26] are investigated as other possible alternatives.

The scope of this work was to further investigate the promising multi-junction thin film silicon based PV-EC devices regarding their potential for an applicable outdoor technology. Therefore, special emphasis was put on the device construction, such that it provides a maximum range of modularity and stability for the individual components, the upscaling beyond laboratory scale of the individual earth-abundant part, and the device characterization was expanded to non-standard test conditions similar to those obtained outdoors. In a previous work, multi-junction thin film silicon based PV-EC devices have been shown to work quite efficiently under laboratory conditions (η_{STH} = 9.5 %). These devices consisted of an a-Si:H/a-Si:H/µc-Si:H triple junction solar cell, platinum as hydrogen evolution reaction catalyst, ruthenium oxide as oxygen evolution reaction catalyst and had an active area below 1 cm². The efficiency target of 10 % for solar driven water splitting declared by the U.S. department of energy was nearly achieved. Thus, the idea of this work was to further investigate the device potential regarding its application and the use of earth-abundant components rather than to further increase the solar-to-hydrogen efficiency. The present work was embedded in the second period of a joint project between the Technical University of Darmstadt (Department of Material Science) and the Forschungszentrum Jülich GmbH (Institute for Energy and Climate Research – 5 Photovoltaics) and funded by the Deutsche Forschungsgemeinschaft (DFG, Priority Program SPP 1613). During the first funding period, valuable knowledge transfer between both partners was established, such that a profound electrochemical expertise was gathered at the IEK-5, which this work could rely on. Additionally, samples were exchanged between the two project partners, allowing for example a more detailed material characterization, leading to a better understanding of the processes during the electrochemical reactions.

Most of the multi-junction thin film solar cell configurations used in this work have been previously developed to their nearly full potential.[34] However, the potential of a-Si:H/µc-Si:H/µc-Si:H triple junction cells was not fully exploited, since the current density for this cell type is expected to exceed the current density measured for a-Si:H/a-Si:H/µc-Si:H triple junction cells, while providing lower voltages. In the present work, the investigation of the a-Si:H/µc-Si:H/µc-Si:H triple junction cells was pursued further to increase the current density by varying the cell thickness without decreasing the output voltage. The increase in cell thickness by 1800 nm resulted in an increase in the sum of the sub cell current densities by +1.1 mA/cm² and an increase in short circuit current density by +0.5 mA/cm² (J_{SC} = 8.4 mA/cm²) at nearly constant open circuit voltages (V_{OC} ~1.91 V). The results presented in chapter (5) show that both types of triple junction cells can drive the water splitting reaction equally well in PV-EC devices, if the overpotential for the catalyst system does not exceed 400 mV. As shown in chapter (8), devices based on a-Si:H/µc-Si:H/µc-Si:H triple junction cells are calculated to generate the highest annual amount of hydrogen under the conditions applied. The usage of a-Si:H/µc-Si:H/µc-Si:H triple junction cells is however a trade-off between the amount of hydrogen expected, preparation costs and the ease of preparation.

An electrochemical measurement workplace was set up, allowing to measure devices of various sizes, different electrode materials under variable measurement conditions (e.g. stationary versus flow state, gas separation and quantification). PV-EC devices fulfilling all points for the implementation into the workplace were developed and tested in the setup, as described in chapter (6) and (7.1). Each device is modularly built, enabling the easy exchange and the individual characterization of every component. The device for sample sizes up to 1.5 x1.5 cm² is mainly used for evaluating the electrochemical performance of the materials considered for the upscaling process. The modular design of the large area device (100 cm²) facilitates the separate upscaling of the solar cell and the respective gas evolution reaction catalysts. Long term operation using these devices is

accommodated by using sheet metal electrodes, which also serve as protection layer. Additionally, the performance of the used solar cell combined with a sheet metal electrode is not decreased as if it could be the case for the implementation of protection layers, which requires the removal of the solar cell rear contact.

In the following the individual PV-EC device components were investigated regarding their upscaling potential and the usage in the 100 cm² device. One challenge occurring during the upscaling process in the case of thin film silicon based technology, is the efficient current collection through the front contact TCO layer. Hence, different front contact patterns using laser processing and evaporated metal front grids were investigated to increase the active solar cell area beyond 1 cm². The thin film silicon solar cell finally employed for solar driven water splitting in the device has an active area of 64 cm² created by using a laser patterning approach, which ensured low resistive losses as well as a decreased chance for entire solar cell failure. Additionally, a module consisting of three shingled crystalline silicon solar cells has been tested in the PV-EC device to show its potential for the water splitting application as well as the modularity of the device towards different solar cell technologies.

One of the main requirements for solar water splitting in order to compete with the fossil fuel based hydrogen production, is cost efficiency, which is to a large extent related to the catalyst materials. Thus, mainly earth-abundant, low cost materials should be implemented as catalyst materials. The existing literature on earth-abundant catalyst materials for the water splitting reaction in alkaline media has been extensively studied and the synthesis of different catalyst materials was successfully established. Nanosheets of Ni_3S_2 were hydrothermally deposited onto nickel foam electrodes, which can probably be used in a second upscaling approach based on the lateral interconnection of identical sub cells (side-by-side approach), described in the literature[157]. Nickel molybdenum and nickel iron oxide were chosen as candidates for the deposition on nickel sheets and the implementation into the 100 cm² PV-EC device. Both catalysts were prepared on small sheets of 1.5x1.5cm² size and tested in the small PV-EC device in order to determine the best conditions for the electroplating on 50.3 cm² electrodes. Prior to the implementation into the PV-EC device, the performance of different upscaled catalyst systems was evaluated and NiMo/$NiFeO_X$ shows a similar performance compared to the noble metal reference system Pt/IrO_X with an overpotential as low as 455 mV at 10 mA/cm² (η(Pt/IrO_X) = 450 mV).

The upscaled thin film silicon solar cell was combined with the earth-abundant NiMo/$NiFeO_X$ catalyst system. The solar-to-hydrogen efficiency measured for this large scale combined system equals 5.1 %. Thus, the earth-abundant PV-EC device slightly outperforms the PV-EC device consisting of the same thin film silicon solar cell combined with platinum and iridium oxide (4.8 %). Additionally, the solar-to-hydrogen efficiency was doubled using NiMo/$NiFeO_X$ as catalysts compared to the use of Ni/Ni catalyst system. For the PV-EC device consisting of NiMo/$NiFeO_X$ combined with the module of shingled crystalline solar cells, the solar-to-hydrogen efficiency measured was 6.3 %. The earth-abundant catalyst system NiMo/$NiFeO_X$ showed an excellent stable performance for several days during a simulated day-night-cycle. Thus, NiMo/$NiFeO_X$ is an excellent system for the long-term application in solar driven water splitting devices and their upscaling to larger areas.

In order to determine the influences of different outdoor illumination conditions on the hydrogen production, the device characterization was extended to conditions similar to those obtained outdoors, such that the influences of varied operating temperature, incident illumination intensity as well as spectral composition on the device performance could be illustrated and the possible performance losses under real conditions could be indicated. It was shown that an operating temperature increase up to 60 °C leads to a decreased solar cell performance which is fully compensated by the enhanced electrochemical transport and reaction kinetics. Varied operating temperatures and illumination intensity were combined in order to investigate the device performance, assuming that high irradiation intensities would lead to increased operating temperatures. It was observed that for high illumination intensities increased operating temperatures are most beneficial, while for low illumination intensities lower operating temperatures yield the highest device performance. By variation of the incident illumination angle, it was found that hydrogen could be produced using the PV-EC device employing an a-Si:H/a-Si:H/µc-Si:H triple junction solar cell in combination with platinum and iridium oxide

as catalyst system in alkaline media under all incident illumination angles investigated (0 – 60°). It was additionally found that the reduced effective illuminated area is an additional intensity loss path, while optical effects, such as reflection, play a minor role. For further device engineering, the tilted mounting of the PV-EC devices has to be considered regarding the gas and electrolyte transport within the device. Due to the variation of the spectral quality, which is observed over year and day time and expressed in terms of average photon energy, an absolute difference in solar-to-hydrogen efficiency of 1% was measured. Generally, the performance of the investigated PV-EC device in the present study under low average photon energy spectra (winter) is reduced. In order to maximize the output of the hydrogen production, the catalyst and solar cells have to be chosen or optimized regarding the illumination conditions found at the operating site rather than with regards to laboratory conditions.

The insights gained in the characterization under non-standard test conditions were used to perform an estimation of the annually produced hydrogen depending on the annual average photon energy range for a given location, comparing different solar cells and catalyst systems employed in the devices. The calculation suggests that for well-developed highly performing earth-abundant catalysts, the voltage generated by a tandem junction can be sufficient for the light induced water splitting reaction producing the second highest amount of hydrogen under the reported conditions for the given location. The highest hydrogen production is found for the device consisting of the a-Si:H/µc-Si:H/µc-Si:H triple junction solar cell combined with $NiMo/NiFeO_X$. However, the preparation of a-Si:H/µc-Si:H/µc-Si:H triple junction solar cells requires a longer, and thus probably also more expensive process as compared to tandem or a-Si:H/a-Si:H/µc-Si triple junction solar cells. The calculation for the annually produced amount of hydrogen can be also used for devices based on other absorber technologies.

For further investigation of the light induced integrated water splitting devices, the device area has to be upscaled even further, ideally beyond m² limits, which can be achieved for the thin film silicon technology. Therefore, the different components as well as the device itself have to be increased in size. Furthermore, an advanced device that handles increased amounts of electrolyte, hydrogen and current has to be designed. The different technologies for hydrogen evolution, such as PEC, PV-EC and PV+EC will be compared in the future regarding their potential applications, cost and ease of preparation and maintenance.

An additional field that benefits from the knowledge gained by investigating light induced water splitting and has attracted substantial interest over the past years, is the light induced CO_2 reduction. By reducing CO_2, valuable products can be obtained that can be used for different purposes (e.g. methanol for fuel cells). However, if the carbon dioxide reduction is performed using solar cells in integrated devices, the potential difference that has to be overcome is approximately 2 V for the reduction half-cell, due to multi-electron transfer reactions and high overpotentials occurring. Thus, for the CO_2 reduction also multi-junctions are needed to overcome the required potential difference. Additionally, catalyst selectivity has to be ensured in order to produce only one (max. two) products. Since CO_2 is gaseous, ideally gas diffusion electrodes should be used in the integrated device, such that either the photocathode can be permeated by carbon dioxide or a photoanode is used in combination with a gas diffusion electrode as cathode. In order to use thin film silicon multi-junction solar cells as photoanodes, the layers have to be deposited in the n-i-p configuration. The preparation of multi-junction n-i-p cells is still under investigation.

Overall, this work provides further insight into the future application of multi-junction thin film silicon based, fully earth-abundant PV-EC devices of upscaled area under outdoor conditions as well as the challenges and limitations occurring during this application. Different paths to overcome these challenges are suggested. In the future, the research on light induced hydrogen generation has to be combined with research activities in hydrogen storage and fuel cell technology. This could provide a sustainable energy infrastructure based on renewable solar energy, hydrogen and electricity for the future.

10 Bibliography

[1] BP, *Stat. Rev. World Energy* **2018**, 1–56.

[2] M. Sato, in *Fluid-Mineral Interact. A Tribut. to H. P. Eugster*, **1990**.

[3] P. Mann, L. Gahagan, M. B. Gordon, in *Giant Oil Gas Fields Decad. 1990-1999 Michel T. Halbouty*, American Association Of Petroleum Geologists, Tulsa, Okla., **2003**.

[4] E. A. Wrigley, *Cambridge Univ. Press* **2010**, 978-0-521-76693–7.

[5] J. G. Singer, *Combustion. Fossil Power*, Windsor, CT (USA); ABB/Combustion Engineering, Inc., United States, **1991**.

[6] D. G. H. Herzog, *Encycl. Energy* **2004**, *1*, 1–11.

[7] G. S. Booras, S. C. Smelser, *Energy* **1991**, *16*, 1295–1305.

[8] C. D. Keeling, S. C. Piper, R. B. Bacastow, M. Wahlen, T. P. Whorf, M. Heimann, H. A. Meijer, *Scripps Inst. Oceanogr.* **2001**, *21*, 1–29.

[9] D. M. Etheridge, L. P. Steele, R. L. Langenfelds, R. J. Francey, J. M. Barnola, V. I. Morgan, *J. Geophys. Res. Atmos.* **1996**, *101*, 4115–4128.

[10] R. F. Keeling, C. D. Keeling, *Scripps CO2 Progr. Data. UC San Diego Libr. Digit. Collect.* **2017**, *doi.org/10*, Accessed on [*16.12.2018].

[11] S. Solomon, G. Plattner, R. Knutti, P. Friedlingstein, *PNAS* **2009**, *106*, 1704–1709.

[12] J. C. G. Walker, *Orig. Life* **1985**, *16*, 117–127.

[13] A. A. Pavlov, J. F. Kasting, L. L. Brown, K. A. Rages, R. Freedman, *J. Geophys. Res.* **2000**, *105*, 11981–11990.

[14] G. W. Crabtree, M. S. Dresselhaus, M. V. Buchanan, *Phys. Today* **2004**, *57*, 324–327.

[15] P. Jena, *J. Phys. Chem. Lett.* **2011**, *2*, 206–211.

[16] D. K. Ross, *Vacuum* **2006**, *80*, 1084–1089.

[17] J. A. Turner, *Science (80-.).* **2004**, *305*, 972 LP – 974.

[18] B. C. R. Ewan, R. W. K. Allen, *Int. J. Hydrogen Energy* **2005**, *30*, 809–819.

[19] A. Hauch, S. D. Ebbesen, S. H. Jensen, M. Mogensen, *J. Mater. Chem.* **2008**, *18*, 2331–2340.

[20] D. Stolten, *Hydrogen Science and Engineering: Materials, Processes, Systems and Technology*, Wiley VCH, **2016**.

[21] R. M. Navarro Yerga, M. C. Álvarez Galván, F. del Valle, J. A. Villoria de la Mano, J. L. G. Fierro, *ChemSusChem* **2009**, *2*, 471–485.

[22] R. T. Ross, *J. Chem. Phys.* **1966**, *45*, 1–7.

[23] M. F. Weber, M. J. Dignam, *J. Electrochem. Soc.* **1984**, *131*, 1258–1265.

[24] F. Urbain, V. Smirnov, J. P. Becker, A. Lambertz, F. Yang, J. Ziegler, B. Kaiser, W. Jaegermann, U. Rau, F. Finger, *Energy Environ. Sci.* **2016**, *9*, 145–154.

[25] A. Fujishima, K. Honda, *Nature* **1972**, *238*, 37–38.

[26] S. Ardo, D. Fernandez Rivas, M. A. Modestino, V. Schulze Greiving, F. F. Abdi, E. Alarcon Llado, V. Artero, K. Ayers, C. Battaglia, J. P. Becker, et al., *Energy Environ. Sci.* **2018**, *11*, 2768–2783.

[27] J.-W. Schüttauf, M. A. Modestino, E. Chinello, D. Lambelet, A. Delfino, D. Dominé, A. Faes, M. Despeisse, J. Bailat, D. Psaltis, et al., *J. Electrochem. Soc.* **2016**, *163*, 1177–1181.

[28] T. Kubo, H. Sachs, S. Nadel, *OPPORTUNITIES FOR NEW APPLIANCE AND EQUIPMENT EFFICIENCY STANDARDS: ENERGY AND ECONOMIC SAVINGS BEYOND CURRENT STANDARDS PROGRAMS*, **2001**.

[29] S. Nordmann, B. Berghoff, A. Hessel, B. Zielinsk, J. John, S. Starschich, J. Knoch, *Sol. Energy Mater. Sol. Cells* **2019**, *191*, 422–426.

[30] T. J. Jacobsson, V. Fjällström, M. Edoff, T. Edvinsson, *Sol. Energy Mater. Sol. Cells* **2015**, *138*, 86–95.

[31] S. Licht, B. Wang, S. Mukerji, T. Soga, M. Umeno, H. Tributsch, *J. Phys. Chem. B* **2000**, *104*, 8920–8924.

[32] W. H. Cheng, M. H. Richter, M. M. May, J. Ohlmann, D. Lackner, F. Dimroth, T. Hannappel, H. A. Atwater, H. J. Lewerenz, *ACS Energy Lett.* **2018**, *3*, 1795–1800.

[33] J. Jia, L. C. Seitz, J. D. Benck, Y. Huo, Y. Chen, J. W. D. Ng, T. Bilir, J. S. Harris, T. F. Jaramillo, *Nat. Commun.* **2016**, *7*, 13237.

[34] F. Urbain, Light Induced Water Splitting Using Multijunction Thin Film Silicon Solar Cells, RWTH Aachen, ISBN: 9783958061484, **2016**.

[35] J. P. Becker, B. Turan, V. Smirnov, K. Welter, F. Urbain, J. Wolff, S. Haas, F. Finger, *J. Mater. Chem. A* **2017**, *5*, 4818–4826.

[36] M. Shalom, D. Ressnig, X. Yang, G. Clavel, T. P. Fellinger, M. Antonietti, *J. Mater. Chem. A* **2015**, *3*, 8171–8177.

[37] L. L. Feng, G. Yu, Y. Wu, G. D. Li, H. Li, Y. Sun, T. Asefa, W. Chen, X. Zou, *J. Am. Chem. Soc.* **2015**, *137*, 14023–14026.

[38] C. Tang, Z. Pu, Q. Liu, A. M. Asiri, Y. Luo, X. Sun, *Int. J. Hydrogen Energy* **2015**, *40*, 4727–4732.

[39] A. S. Batchellor, S. W. Boettcher, *ACS Catal.* **2015**, *5*, 6680–6689.

[40] C. Fan, *J. Electrochem. Soc.* **1994**, *141*, 382.

[41] J. W. Ager, M. R. Shaner, K. A. Walczak, I. D. Sharp, S. Ardo, *Energy Environ. Sci.* **2015**, *8*, 2811–2824.

[42] T. Minemoto, S. Nagae, H. Takakura, *Sol. Energy Mater. Sol. Cells* **2007**, *91*, 919–923.

[43] T. Minemoto, S. Fukushige, H. Takakura, *Sol. Energy Mater. Sol. Cells* **2009**, *93*, 1062–1065.

[44] S. Nagae, M. Toda, T. Minemoto, H. Takakura, Y. Hamakawa, *Sol. Energy Mater. Sol. Cells* **2006**, *90*, 3568–3575.

[45] C. Cornaro, A. Andreotti, *Prog. Photovolt Res. Appl.* **2013**, *21*, 996–1003.

[46] L. Mutiara, K. Pegels, A. Reinders, *2015 IEEE 42nd Photovolt. Spec. Conf. PVSC 2015* **2015**, DOI 10.1109/PVSC.2015.7356209.

[47] J. Merten, J. Andreu, *Sol. Energy Mater. Sol. Cells* **1998**, *52*, 11–25.

[48] R. Gottschalg, T. R. Betts, D. G. Infield, M. J. Kearney, *Conf. Rec. IEEE Photovolt. Spec. Conf.* **2002**, 1138–1141.

[49] R. Gottschalg, T. R. Betts, D. G. Infield, M. J. Kearney, *Sol. Energy Mater. Sol. Cells* **2005**, *85*, 415–428.

[50] S. N. Agbo, T. Merdzhanova, U. Rau, O. Astakhov, *Sol. Energy Mater. Sol. Cells* **2017**, *159*, 427–434.

[51] S. Reynolds, V. Smirnov, *Energy Procedia* **2015**, *84*, 251–260.

[52] C. Ulbrich, C. Zahren, A. Gerber, B. Blank, T. Merdzhanova, A. Gordijn, U. Rau, *Int. J. Photoenergy* **2013**, *2013*, DOI 10.1155/2013/314097.

[53] C. Ulbrich, Spectral and Directional Dependence of Light-Trapping in Solar Cells, Rheinisch-Westfälische Technische Hochschule Aachen, **2011**.

[54] F. Urbain, J. P. Becker, V. Smirnov, J. Ziegler, F. Yang, B. Kaiser, W. Jaegermann, S. Hoch, A. Maljusch, U. Rau, et al., *Mater. Sci. Semicond. Process.* **2016**, *42*, 142–146.

[55] V. Smirnov, K. Welter, J. P. Becker, F. Urbain, W. Jaegermann, F. Finger, *Energy Procedia* **2016**, *102*, 36–42.

[56] K. Welter, V. Smirnov, J. P. Becker, P. Borowski, S. Hoch, A. Maljusch, W. Jaegermann, F. Finger, *ChemElectroChem* **2017**, *4*, 2099–2108.

[57] P. Yu, M. Cardona, *Fundamentals of Semiconductors: Physics and Materials Properties*, Springer-Verlag, Berlin, Heidelberg, **2010**.

[58] R. A. Smith, *Semiconductors*, Cambridge University Press, New York, USA, **1979**.

[59] C. Kittel, *Introduction to Solid State Physics*, Wiley, New York, USA, **2005**.

[60] J. Nelson, *The Physics of Solar Cells*, Imperial College Press, London, **2003**.

[61] P. Würfel, *Physics of Solar Cells: From Basic Principles to Advances Concepts*, Wiley VCH, Weinheim, Germany, **2009**.

[62] R. Memming, *Semiconductor Electrochemistry*, Wiley VCH, Weinheim, Germany, **2001**.

[63] W. Shockley, W. T. Read, *Phys. Rev.* **1952**, *87*, 835–842.

[64] R. N. Hall, *Phys. Rev.* **1952**, *87*, 387–387.

[65] M. A. Green, *IEEE Trans. Electron Devices* **1984**, *31*, 671–678.

[66] C. Sah, R. N. Noyce, W. Shockley, *Proc. IRE* **1957**, *45*, 1228–1243.

[67] S. De Wolf, A. Descoeudres, Z. C. Holman, C. Ballif, *green* **2012**, *2*, 7–24.

[68] R. Street, *Technology and Applications of Amorphous Silicon*, Springer-Verlag, Berlin, Heidelberg, **2000**.

[69] F. Gaspari, in *Optoelectron. - Mater. Tech.* (Ed.: P. Predeep), IntechOpen, **2006**.

[70] O. Vetterl, A. Dasgupta, A. Lambertz, H. Stiebig, F. Finger, H. Wagner, *MRS Proc.* **2001**, *664*, A25.8.1.

[71] O. Vetterl, F. Finger, R. Carius, P. Hapke, L. Houben, O. Kluth, A. Lambertz, A. Mück, B. Rech, H. Wagner, *Sol. Energy Mater. Sol. Cells* **2000**, *62*, 97–108.

[72] W. B. Jackson, N. M. Amer, *Phys. Rev. B* **1982**, *25*, 5559–5562.

[73] S. Klein, F. Finger, R. Carius, T. Dylla, J. Klomfass, *J. Appl. Phys.* **2007**, *102*, DOI 10.1063/1.2815645.

[74] M. A. Green, M. J. Keevers, *Prog. Photovoltaics Res. Appl.* **1995**, *3*, 189–192.

[75] J. K. Rath, *Sol. Energy Mater. Sol. Cells* **2003**, *76*, 431–487.

[76] R. E. I. Schropp, M. Zeman, *Amorphous and Microcrystalline Silicon Solar Cells: Modeling, Materials and Device Technology*, Springer US, New York, USA, **1998**.

[77] T. Soga, *Nanostructured Materials for Solar Energy Conversion*, Elsevier Science, Oxford, UK, **2006**.

[78] F. Urbain, K. Wilken, V. Smirnov, O. Astakhov, A. Lambertz, J. P. Becker, U. Rau, J. Ziegler, B. Kaiser, W. Jaegermann, et al., *Int. J. Photoenergy* **2014**, *2014*, DOI 10.1155/2014/249317.

[79] K. Wilken, Tandem Cells Providing High Open Circuit Voltages for Photoelectrochemical Water Splitting, Technische Universität Darmstadt, Germany, **2013**.

[80] R. Carius, *Philos. Mag. B* **2000**, *80*, 741–753.

[81] V. Smirnov, A. Lambertz, S. Moll, M. Bär, D. E. Starr, R. G. Wilks, M. Gorgoi, A. Heidt, M. Luysberg, B. Holländer, et al., *Phys. status solidi A* **2016**, *213*, 1814–1820.

[82] S. Wang, V. Smirnov, T. Chen, B. Holländer, X. Zhang, S. Xiong, Y. Zhao, F. Finger, *Jpn. J. Appl. Phys.* **2015**, *54*, 11401.

[83] W. Böttler, Light Scattering and Trapping in Thin Film Silicon Solar Cells with an N-i-p Configuration, Rheinisch Westfälische Technische Hochschule Aachen, Germany, ISBN 978-3-95806-023-4, **2015**.

[84] W. Böttler, V. Smirnov, J. Hüpkes, F. Finger, *J. Non. Cryst. Solids* **2012**, *358*, 2474–2477.

[85] S. Reynolds, R. Carius, F. Finger, V. Smirnov, *Thin Solid Films* **2009**, *517*, 6392–6395.

[86] W. Böttler, V. Smirnov, J. Hüpkes, F. Finger, *Phys. status solidi A* **2012**, *209*, 1144–1149.

[87] F. Urbain, V. Smirnov, J. P. Becker, U. Rau, F. Finger, J. Ziegler, B. Kaiser, W. Jaegermann, *J. Mater. Res.* **2014**, *29*, 2605–2614.

[88] F. Urbain, V. Smirnov, J. P. Becker, A. Lambertz, U. Rau, F. Finger, *Sol. Energy Mater. Sol. Cells* **2016**, *145*, 142–147.

[89] The figure was created using empirical data from Reference Solar Spectral Irradiance: Air Mass 1.5 https://www.nrel.gov/grid/solar-resource/spectra-am1.5.html accessed June 2019, **2019**.

[90] A. De Vos, *J. Phys. D Appl. Phys.* **1980**, *13*, 839–846.

[91] O. Isabella, A. H. M. Smets, M. Zeman, *Sol. Energy Mater. Sol. Cells* **2014**, *129*, 82–89.

[92] M. A. Green, *Third Generation Photovoltaics: Advanced Solar Energy Conversion*, Springer-Verlag, Berlin, Heidelberg, **2003**.

[93] S. Schicho, Amorphous and Microcrystalline Silicon Applied in Very Thin Tandem Solar Cells, Rheinisch Westfälische Technische Hochschule Aachen, Germany, ISBN: 9783893366934, **2011**.

[94] B. Bills, X. Liao, D. Galipeau, Q. Fan, *IEEE Trans. Electron Devices* **2012**, *59*, 2327–2330.

[95] J. Kwak, S. W. Kwon, K. S. Lim, *J. Non-Cryst. Solids* **2004**, *352*, 1847–1850.

[96] G.-J. Li, G.-F. Hou, X.-Y. Han, Y.-J. Yuan, C.-C. Wei, J. Sun, Y. Zhao, X.-H. Geng, *Chinese Phys. B* **2009**, *18*, 1674.

[97] R. W. Impey, P. A. Madden, I. R. McDonald, *J. Phys. Chem.* **1983**, *87*, 5071–5083.

[98] F. J. Morin, J. P. Maita, *Phys. Rev.* **1954**, *96*, 28–35.

[99] C. Canali, C. Jacoboni, F. Nava, G. Ottaviani, A. Alberigi-Quaranta, *Phys. Rev. B* **1975**, *12*, 2265–2284.

[100] Z. Chen, T. F. Jaramillo, T. G. Deutsch, A. Kleiman-Shwarsctein, A. J. Forman, N. Gaillard, R. Garland, K. Takanabe, C. Heske, M. Sunkara, et al., *J. Mater. Res.* **2010**, *25*, 3–16.

[101] Z. Chen, H. Dinh, E. Miller, *Photoelectrochemical Water Splitting: Standards, Experimental Methods, and Protocols*, Springer-Verlag, New York, USA, **2013**.

[102] V. S. Bagotsky, *Fundamentals of Electrochemistry*, Wiley, **2005**.

[103] A. D. McNaught, A. Wilkinson, *IUPAC. Compendium of Chemical Terminology*, Blackwell Scientific Publications, Oxford, **1997**.

[104] A. J. Bard, L. R. Faulkner, *Electrochemical Methods: Fundamentals and Applications*, Wiley, New York, USA, **2001**.

[105] A. Hamnett, *Handb. Fuel Cells* **2010**, DOI 10.1002/9780470974001.f101005.

[106] P. Quaino, F. Juarez, E. Santos, W. Schmickler, *Beilstein J. Nanotechnol.* **2014**, *5*, 846–854.

[107] S. Trasatti, *J. Electroanal. Chem.* **1972**, *39*, 163–184.

[108] C. C. L. McCrory, S. Jung, I. M. Ferrer, S. M. Chatman, J. C. Peters, T. F. Jaramillo, *J. Am. Chem. Soc.* **2015**, *137*, 4347–4357.

[109] M. Fang, W. Gao, G. Dong, Z. Xia, S. P. Yip, Y. Qin, Y. Qu, J. C. Ho, *Nano Energy* **2016**, *27*, 247–254.

[110] R. Williams, *J. Chem. Phys.* **1960**, *32*, 1505–1514.

[111] A. B. Ellis, S. W. Kaiser, J. M. Bolts, M. S. Wrighton, *J. Am. Chem. Soc.* **1977**, *99*, 2839–2848.

[112] M. G. Walter, E. L. Warren, J. R. McKone, S. W. Boettcher, Q. Mi, E. A. Santori, N. S. Lewis, *Chem. Rev.* **2010**, *110*, 6446–6473.

[113] R. van de Krol, M. Grätzel, *Photoelectrochemical Hydrogen Production*, Springer US, **2012**.

[114] M. G. Kast, L. J. Enman, N. J. Gurnon, A. Nadarajah, S. W. Boettcher, *ACS Appl. Mater. Interfaces* **2014**, *6*, 22830–22837.

[115] B. Mei, T. Pedersen, P. Malacrida, D. Bae, R. Frydendal, O. Hansen, P. C. K. Vesborg, B. Seger, I. Chorkendorff, *J. Phys. Chem. C* **2015**, *119*, 15019–15027.

[116] J. Ziegler, F. Yang, S. Wagner, B. Kaiser, W. Jaegermann, F. Urbain, J.-P. Becker, V. Smirnov, F. Finger, *Appl. Surf. Sci.* **2016**, *389*, 73–79.

[117] J. Ziegler, Photoelektrosynthese von Wasserstoff Mit Silizium-Dünnschicht-Tandemsolarzellen, Technische Universität Darmstadt, urn:nbn:de:tuda-tuprints-46954, **2015**.

[118] F. Urbain, V. Smirnov, J. P. Becker, U. Rau, J. Ziegler, F. Yang, B. Kaiser, W. Jaegermann, S. Hoch, M. Blug, et al., *Chem. Phys. Lett.* **2015**, *638*, 25–30.

[119] H. Helmholtz, *Ann. Phys.* **1853**, *165*, 211–233.

[120] K. Rajeshwar, *Encycl. Electrochem.* **2007**, DOI 10.1002/9783527610426.bard060001.

[121] M. Nakamura, N. Sato, N. Hoshi, O. Sakata, *ChemPhysChem* **2011**, *12*, 1430–1434.

[122] L. Pilon, H. Wang, A. d'Entremont, *J. Electrochem. Soc.* **2015**, *162*, 5158–5178.

[123] J. Klett, J. Ziegler, A. Radetinac, B. Kaiser, R. Schäfer, W. Jaegermann, F. Urbain, J.-P. Becker, V. Smirnov, F. Finger, *Phys. Chem. Chem. Phys.* **2016**, *18*, 10751–10757.

[124] F. Urbain, V. Smirnov, J. P. Becker, U. Rau, J. Ziegler, B. Kaiser, W. Jaegermann, F. Finger, *Sol. Energy Mater. Sol. Cells* **2015**, *140*, 275–280.

[125] J. P. Becker, F. Urbain, V. Smirnov, U. Rau, J. Ziegler, B. Kaiser, W. Jaegermann, F. Finger, *Phys. status solidi A* **2016**, *213*, 1738–1746.

[126] B. Parkinson, *Acc. Chem. Res.* **1984**, *17*, 431–437.

[127] O. Dupré, R. Vaillon, M. A. Green, *Thermal Behavior of Photovoltaic Devices: Physics and Engineering*, Springer International Publishing, **2017**.

[128] D. Abou-Ras, T. Kirchartz, U. Rau, *Advanced Characterization Techniques for Thin Film Solar Cells*, Wiley VCH, Weinheim, Germany, **2011**.

[129] D. M. Tobnaghi, R. Madatov, P. Farhadi, *Electr. POWER Eng. Control Syst.* **2013**, 90–93.

[130] E. Cuce, P. M. Cuce, T. Bali, *Appl. Energy* **2013**, *111*, 374–382.

[131] K. Wilken, U. W. Paetzold, M. Meier, M. Smeets, N. Prager, M. Fahland, F. Finger, V. Smirnov, *IEEE J. Photovoltaics* **2015**, *5*, 1646–1653.

[132] K. Wilken, Low Temperature Thin-Film Silicon Solar Cells on Flexible Plastic Substrates, Rheinisch Westfälisch Technische Hochschule Aachen, Germany, ISBN: 978-3-95806-235-1, **2016**.

[133] M. Smeets, V. Smirnov, K. Bittkau, M. Meier, R. Carius, U. Rau, U. W. Paetzold, *Opt. Express* **2015**, *23*, A1575.

[134] J. L. Balenzategui, F. Chenlo, *Sol. Energy Mater. Sol. Cells* **2005**, *86*, 53–83.

[135] A. K. Yadav, S. S. Chandel, *Renew. Sustain. Energy Rev.* **2013**, *23*, 503–513.

[136] C. Ulbrich, C. Zahren, J. Noll, B. Blank, A. Gerber, A. Gordijn, U. Rau, *Proc. 26th Photovolt. Sol. Energy Conf. Exhib.* **2011**, 302–305.

[137] J. Müller, O. Kluth, S. Wieder, H. Siekmann, G. Schöpe, W. Reetz, O. Vetterl, D. Lundszien, A. Lambertz, F. Finger, et al., *Sol. Energy Mater. Sol. Cells* **2001**, *66*, 275–281.

[138] B. Rech, J. Müller, T. Repmann, O. Kluth, T. Roschek, J. Hüpkes, H. Stiebig, W. Appenzeller, *MRS Proc.* **2003**, *762*, A3.1.

[139] O. Vetterl, On the Physics of Microcrystalline Silicon Thin Film Solar Cells - From the Material to Devices with High Conversion Efficiencies, Heinrich-Heine-Universität Düsseldorf, **2001**.

[140] T. Grundler, Silicon Oxide as an Intermediate Reflector in Silicon Thin Film Solar Cells, Rheinisch Westfälische Technische Hochschule Aachen, **2009**.

[141] A. Lambertz, F. Finger, R. E. I. Schropp, U. Rau, V. Smirnov, *Prog. Photovoltaics Res. Appl.* **2015**, *23*, 939–948.

[142] W. Reetz, H. Stiebig, T. Brammer, B. Rech, J. Fölsch, *Proc. 2nd ISEC-Europe Sol. Congr. Eurosun98* **1999**, *1.5-1*.

[143] V. Huhn, Quantitative Luminescence Imaging of Solar Cells, Rheinisch Westfälisch Technische Hochschule Aachen, Germany, ISBN: 978-3-95806-363-1, **2018**.

[144] R. T. Coyle, J. A. Switzer, *Electrochemical Synthesis of Ceramic Films and Powders*, **1989**, US 4882014; A.

[145] L. Gal-Or, I. Silberman, R. Chaim, *J. Electrochem. Soc.* **1991**, *138*, 1939–1942.

[146] H. Ju, J. K. Lee, J. Lee, J. Lee, *Curr. Appl. Phys.* **2012**, *12*, 60–64.

[147] I. Gurrappa, L. Binder, *Sci. Technol. Adv. Mater.* **2008**, *9*, DOI 10.1088/1468-6996/9/4/043001.

[148] S.-I. Pyun, H.-C. Shin, J.-W. Lee, J.-Y. Go, *Electrochemistry of Insertion Materials for Hydrogen and Lithium*, Springer Berlin Heidelberg, Berlin, Heidelberg, **2012**.

[149] J. Ziegler, B. Kaiser, W. Jaegermann, F. Urbain, J.-P. Becker, V. Smirnov, F. Finger, *ChemPhysChem* **2014**, *15*, 4026–4031.

[150] D. Long, *Raman Spectroscopy*, Mcraw-Hill International Book Company, New York, USA, **1977**.

[151] Y. Liang, Q. Liu, A. M. Asiri, X. Sun, Y. He, *Int. J. Hydrogen Energy* **2015**, *40*, 13258–13263.

[152] *Hydrogen Europe: European Hydrogen & Fuel Cell Project Database - Project PECSYS*, Europe, **2017**.

[153] Fraunhofer Institute for Solar Energy Systems, *Photovoltaics Report*, Freiburg, **2018**.

[154] J. J. Hanak, *Sol. Energy* **1979**, *23*, 145–147.

[155] S. Nakano, T. Matsuoka, S. Kiyama, H. Kawata, N. Nakamura, Y. Nakashima, S. Tsuda, H. Nishiwaki, M. Ohnishi, I. Nagaoka, et al., *Jpn. J. Appl. Phys.* **1986**, *25*, 1936–1943.

[156] S. Haas, A. Gordijn, H. Stiebig, *Prog. Photovoltaics Res. Appl.* **2008**, *16*, 195–203.

[157] B. Turan, J. P. Becker, F. Urbain, F. Finger, U. Rau, S. Haas, *Nat. Commun.* **2016**, *7*, 1–9.

[158] B. Rech, T. Roschek, T. Repmann, J. Müller, R. Schmitz, W. Appenzeller, *Thin Solid Films* **2003**, *427*, 157–165.

[159] C. Battaglia, A. Cuevas, S. De Wolf, *Energy Environ. Sci.* **2016**, *9*, 1552–1576.

[160] J. Geissbühler, S. De Wolf, A. Faes, N. Badel, Q. Jeangros, A. Tomasi, L. Barraud, A. Descoeudres, M. Despeisse, C. Ballif, *IEEE J. Photovoltaics* **2014**, *4*, 1055–1062.

[161] M. W. Denhoff, N. Drolet, *Sol. Energy Mater. Sol. Cells* **2009**, *93*, 1499–1506.

[162] A. Richter, V. Smirnov, A. Lambertz, K. Nomoto, K. Welter, K. Ding, *Sol. Energy Mater. Sol. Cells* **2018**, *174*, 196–201.

[163] A. Descoeudres, C. Allebé, N. Badel, L. Barraud, J. Champliaud, F. Debrot, A. Faes, A. Lachowicz, J. Levrat, S. Nicolay, et al., *Energy Procedia* **2015**, *77*, 508–514.

[164] I. H. Kwak, H. S. Im, D. M. Jang, Y. W. Kim, K. Park, Y. R. Lim, E. H. Cha, J. Park, *ACS Appl. Mater. Interfaces* **2016**, *8*, 5327–5334.

[165] N. Jiang, Q. Tang, M. Sheng, B. You, D. Jiang, Y. Sun, *Catal. Sci. Technol.* **2016**, *6*, 1077–1084.

[166] A. Irshad, N. Munichandraiah, *ACS Appl. Mater. Interfaces* **2017**, *9*, 19746–19755.

[167] M. Gong, D. Wang, C. Chen, B. Hwang, H. Dai, *Nano Res.* **2016**, *9*, 28–46.

[168] L. Trotochaud, S. L. Young, J. K. Ranney, S. W. Boettcher, *J. Am. Chem. Soc.* **2014**, *136*, 6744–6753.

[169] F. M. Sapountzi, J. M. Gracia, C. J. Weststrate, H. O. A. Fredriksson, J. W. Niemantsverdriet, *Prog. Energy Combust. Sci.* **2017**, *58*, 1–35.

[170] C. Tang, N. Cheng, Z. Pu, W. Xing, X. Sun, *Angew. Chemie - Int. Ed.* **2015**, *54*, 9351–9355.

[171] L. Xiao, S. Zhang, J. Pan, C. Yang, M. He, L. Zhuang, J. Lu, *Energy Environ. Sci.* **2012**, *5*, 7869–7871.

[172] F. Dionigi, P. Strasser, *Adv. Energy Mater.* **2016**, *1600621*, 1600621.

[173] J. R. McKone, B. F. Sadtler, C. A. Werlang, N. S. Lewis, H. B. Gray, *ACS Catal.* **2013**, *3*, 166–169.

[174] S. Klaus, Y. Cai, M. W. Louie, L. Trotochaud, A. T. Bell, *J. Phys. Chem. C* **2015**, *119*, 7243–7254.

[175] H. Bode, K. Dehmelt, J. Witte, *Electrochim. Acta* **1966**, *11*, 1079-IN1.

[176] M. Muhler, W. Schuhmann, *Edelmetallfreie Katalysatoren Für Die Wasserstoffproduktion Aus Erneuerbaren Energiequellen – Sustainable Hydrogen*, Bochum, **2016**.

[177] M. Beller, A. Brückner, A. Martin, *Edelmetallfreie Katalysatoren Für Die Wasserstoffproduktion Aus Erneuerbaren Energiequellen – Sustainable Hydrogen*, Rostock, **2016**.

[178] J. Xie, S. Li, X. Zhang, J. Zhang, R. Wang, H. Zhang, B. Pan, Y. Xie, *Chem. Sci.* **2014**, *5*, 4615–4620.

[179] K. Joya, X. Sala, *Phys. Chem. Chem. Phys.* **2015**, *17*, DOI 10.1039/C4CP05053C.

[180] N. Hamzelui, Electrodeposition of Nickel Based Catalysts for Photoelectrochemical Water Splitting, Rheinisch Westfälische Technische Hochschule Aachen, **2017**.

[181] D. A. Corrigan, *J. Electrochem. Soc.* **1987**, *134*, 377.

[182] M. D. Merrill, R. C. Dougherty, *J. Phys. Chem. C* **2008**, *112*, 3655–3666.

[183] M. W. Louie, A. T. Bell, *J. Am. Chem. Soc.* **2013**, *135*, 12329–12337.

[184] XPS, International, *Handbooks of Monochromatic XPS Spectra - 5 Volume Series*, Marlborough, Massachusetts, USA, **1997**.

[185] B. V. Crist, *Handbooks of Monochromatic XPS Spectra*, XPS International, Ames, Iowa, USA, **1999**.

[186] S. Tengeler, M. Fingerle, W. Calvet, B. Kaiser, T. Mayer, W. Jaegermann, *J. Electrochem. Soc.* **2018**, *165*, 3122–3131.

[187] M. C. Biesinger, B. P. Payne, L. W. M. Lau, A. Gernson, R. St, R. S. C. Smart, *Surf. Interface Anal.* **2009**, *41*, 324–332.

[188] M. Lee, H. S. Jeon, S. Y. Lee, H. Kim, S. J. Sim, Y. J. Hwang, B. K. Min, *J. Mater. Chem. A* **2017**, *5*, 19210–19219.

[189] D. S. Hall, C. Bock, B. R. MacDougall, *J. Electrochem. Soc.* **2013**, *160*, F235–F243.

[190] R. Gottschalg, D. G. Infield, M. J. Kearney, *Sol. Energy Mater. Sol. Cells* **2003**, *79*, 527–537.

[191] R. Gottschalg, T. R. Betts, D. G. Infield, M. J. Kearney, *Meas. Sci. Technol.* **2004**, *15*, 460–466.

[192] K. Lohrberg, P. Kohl, *Electrochim. Acta* **1984**, *29*, 1557–1561.

[193] I. Afdi Yunaz, S. Kasashima, S. Inthisang, T. Krajangsang, S. Miyajima, A. Yamada, M. Konagai, *Conf. Rec. IEEE Photovolt. Spec. Conf.* **2009**, 000153–000157.

[194] S. Kasashima, R. Uzawa, B. Janthong, S. Inthisang, T. Krajangsang, P. Sichanugrist, M. Konagai, *Proc. IEEE 37th Photovolt. Spec. Conf.* **2011**, 634–637.

[195] S. Reynolds, F. Urbain, V. Smirnov, *J. Phys. Conf. Ser.* **2017**, *794*, 012025.

[196] T. R. Betts, C. N. Jardine, R. Gottschalg, D. G. Infield, K. Lane, *3rd World Conf. Photovolt. Energy Convers.* **2003**, 1756–1759.

[197] M. Norton, A. M. G. Amillo, R. Galleano, *Sol. Energy* **2015**, *120*, 337–344.

[198] M. C. Peel, B. L. Finlayson, T. A. McMahon, *Hydrol. Earth Syst. Sci.* **2007**, *11*, 1633–1644.

[199] L. Trotochaud, T. J. Mills, S. W. Boettcher, *J. Phys. Chem. Lett.* **2013**, *4*, 931–935.

[200] P. Bogdanoff, D. Stellmach, O. Gabriel, B. Stannowski, R. Schlatmann, R. van de Krol, S. Fiechter, *Energy Technol.* **2016**, *00*, 1–13.

[201] B. Yan, G. Yue, J. Yang, S. Guha, *2008 33rd IEEE Photovolt. Spec. Conf.* **2008**, DOI 10.1109/PVSC.2008.4922607.

11 Appendix

Appendix-Chapter 4

Table A1: Sample list of the deposited a-Si:H/µc-Si:H/µc-Si:H triple junction solar cells.

Sample name	top [nm]	middle [nm]	bottom [nm]	total [nm]	total J_{QE} [mA/cm²]	J_{SC} [mA/cm²]
15B-097	140	1000	1600	2740	24.9	7.85
15B-131	140	1300	2100	3540	25.8	8.17
16B-053	140	1300	2100	3540	25.1	7.05
16B-083	140	1600	2100	3840	24.1	7.34
16B-123	140	1900	2500	4540	26.0	8.32
16B-141	170	1900	2500	4570	25.0	8.22
16B-166	140	1900	2500	4540	25.4	6.99
16B-169	140	1600	2500	4240	26.0	8.09
16B-173	140	1300	2500	3940	25.6	8.02
16B-179	140	1920	2500	4560	25.8	8.41
16B-182	140	1920	2300	4360	24.4	7.96

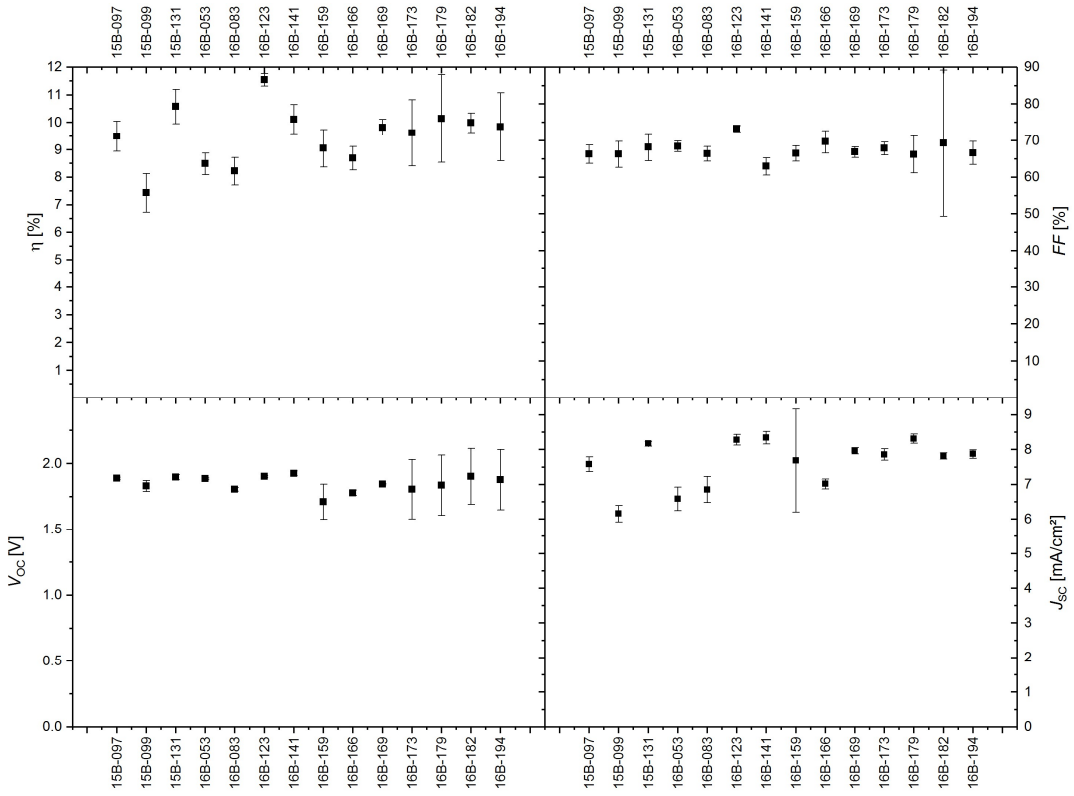

Figure A1: Overview of the photovoltaic parameters evaluated for the deposited a-Si:H/µc-Si:H/µc-Si:H triple junction solar cells listed in Table A1.

Appendix-Chapter 5

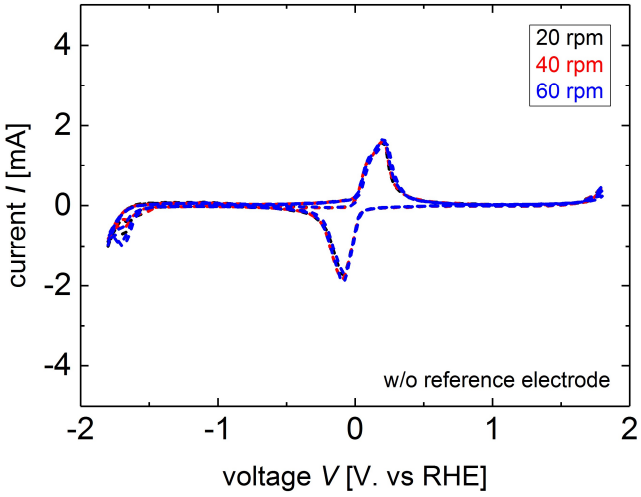

Figure A2: Current-voltage curve in two electrode configuration for different pumping speeds, employing nickel/nickel as electrodes and 1 M KOH as electrolyte.

Appendix-Chapter 6

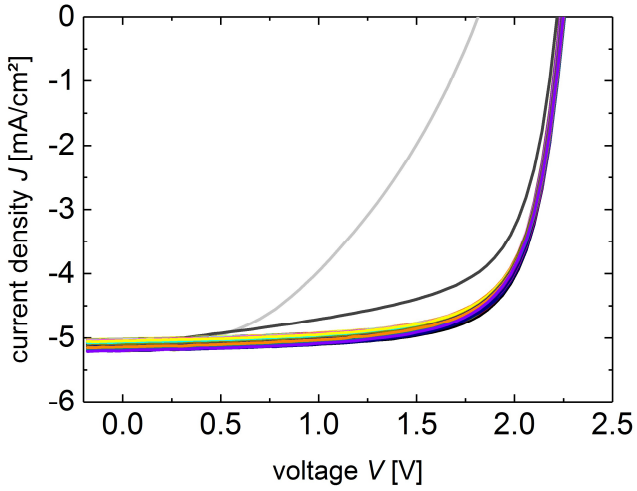

Figure A3: Current density-voltage curves of the 64 individual parts of the 64 cm² solar cell with laser processed front contact modification.

Figure A4: Ampoule prior to opening. The CMB complex, which initially had no color, has turned brown during the reaction. The nickel foam shows a black brown color after to reaction (compared to metallic before). A black, brownish accumulation of material, partially containing crystals, is found at the top of the ampoule.

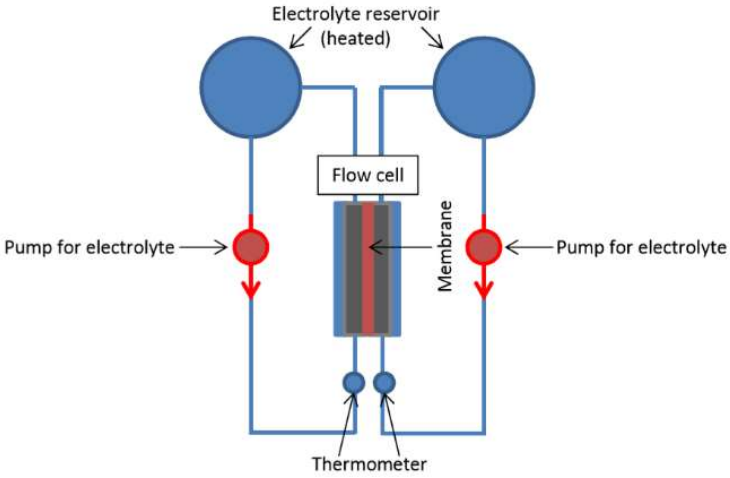

Figure A5: Schematics (not to scale) of a setup (as used by Evonik Creavis GmbH) to measure the temperature dependence of a flow (PV)-EC cell, including a membrane for gas separation, heated electrolyte reservoirs, and temperature control in the electrolyte flow circuit controlled by a peristaltic pump. The flow EC cell in zero gap configuration consisting of porous electrodes (grey) and a membrane (100µm, red). In order to form a PV-EC device, a PV cell can be electrically attached to the cathode side of the EC cell.

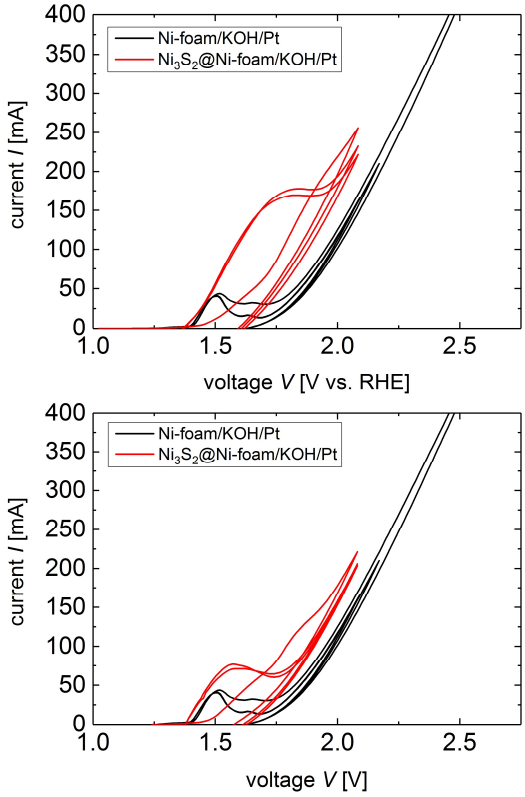

Figure A6: The electrochemical performance obtained by means of cyclic voltammetry (CV) measurements for Ni_3S_2 coated nickel foam. A hydrothermally untreated nickel foam reference is shown for comparison. The measurements were performed in 1 M potassium hydroxide solution and platinum served as counter electrode.

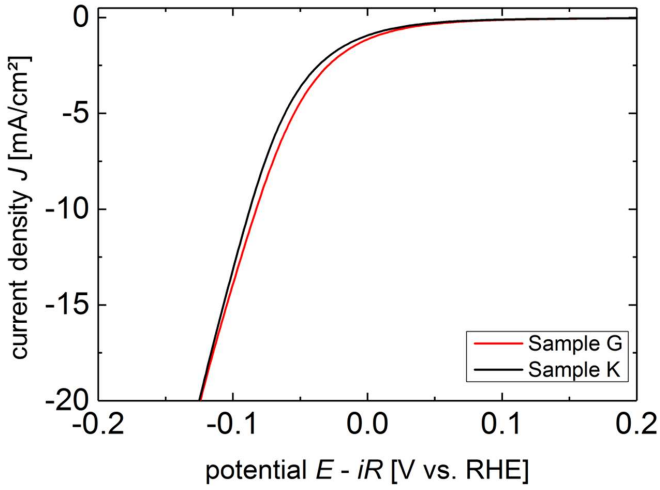

Figure A7: Current density-voltage curves of the NiMo samples G and K deposited under constant charge density conditions. Both curves show a similar potential at a current density of -10 mA/cm².

Appendix-Chapter 7

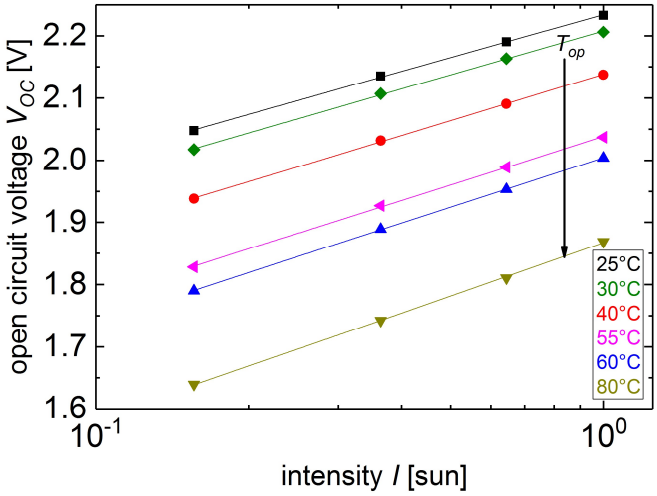

Figure A8: Open circuit voltage plotted versus the illumination intensity on logarithmic scale. The linear fits were performed using Origin and show the logarithmic dependence of the open circuit voltage.

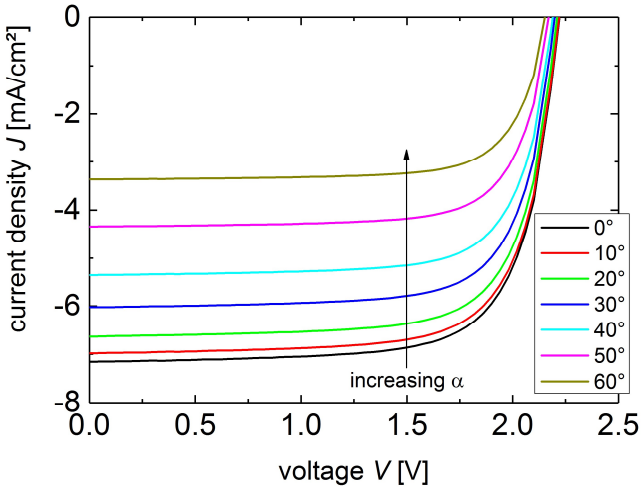

Figure A9: Current density-voltage curves measured under varied incident illumination angles for an a-Si:H/a-Si:H/µc-Si:H triple junction solar cell.

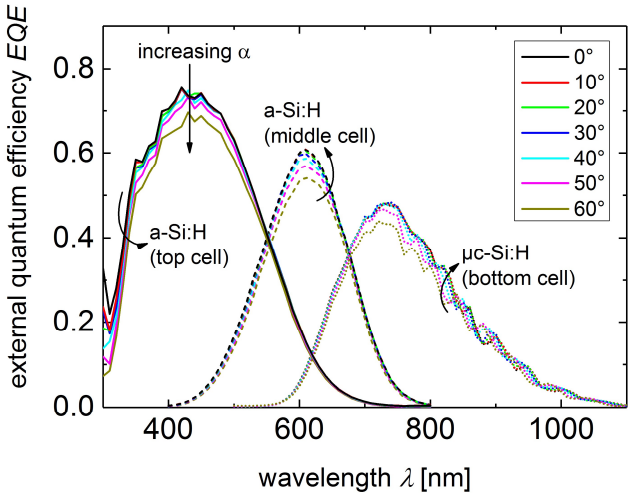

Figure A10: External quantum efficiency at various incident illumination angles plotted versus wavelength (solid lines: top cell, dashed lines: middle cell, dotted lines: bottom cell). The highest EQEs are obtained under 0° incident illumination angle and decrease for an increase of the illumination angle over the entire wavelength range investigated. Comparing the individual sub cells, the most prominent reduction for the top cell is observed in the range from 350 – 500 nm and is possibly due to increased reflection at the air/glass interface. The EQE for the middle cell shows the highest reduction for wavelengths between 550 – 650 nm. The external quantum efficiency of the μc-Si:H bottom cell is mainly affected in the wavelength range from 700 – 850 nm. Here, the interference patterns observed in the long wavelength range (800 – 1000 nm under 0° angle) shift towards shorter wavelength under increased illumination angle (750 – 1000 nm for 60°). The interference patterns are caused by the reflection of the incident light at the metal back contact of the solar cell. Due to the variation of the incident angle, the reflection at the rear side changes and causes the observed shift of the interference patterns.

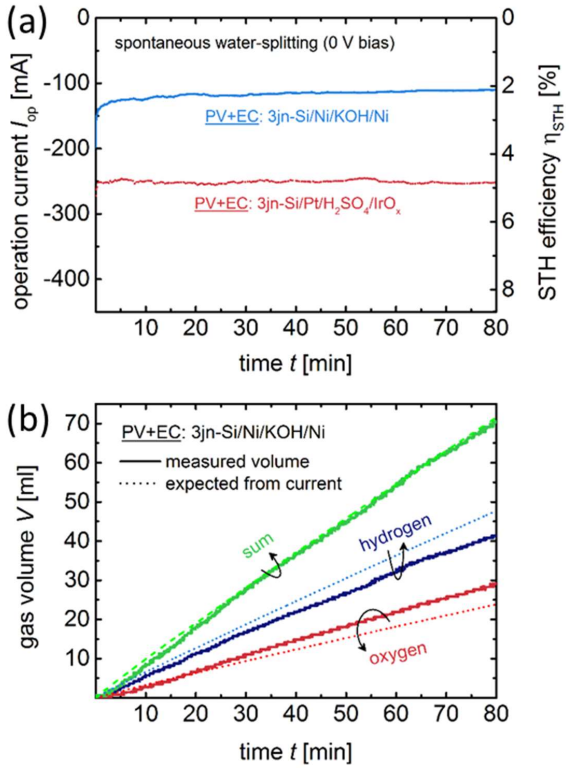

Figure A11: Experimental data used to determine the factor of 2.5 L/m² for hydrogen generation. 2.1 % solar-to-hydrogen efficiency equal to 33 mL of hydrogen produced in one hour for an active area of 64 cm² (0.016 L equal 1% for 0.0064 cm²). Thus, 2.5 L/m² of hydrogen are produced for 1 % of solar-to-hydrogen efficiency.

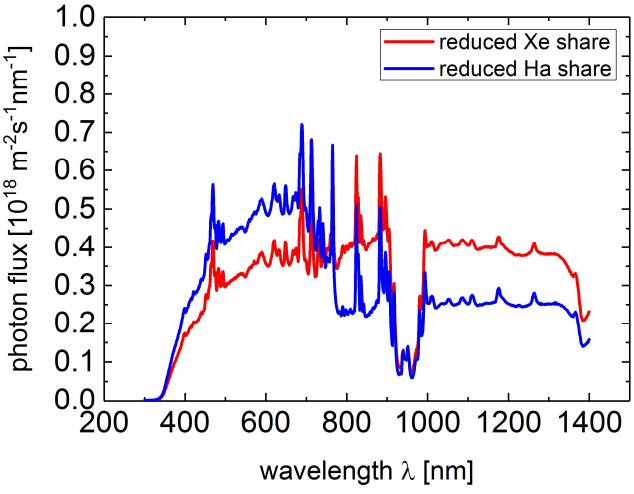

Figure A12: Spectra with altered lamp intensity variation. A reduced xenon lamp share results in a red shifted spectrum, while a reduced halogene lamp share leads to a blue shift of the spectrum. The overall spectral irradiance accounts for 1000 W/m².

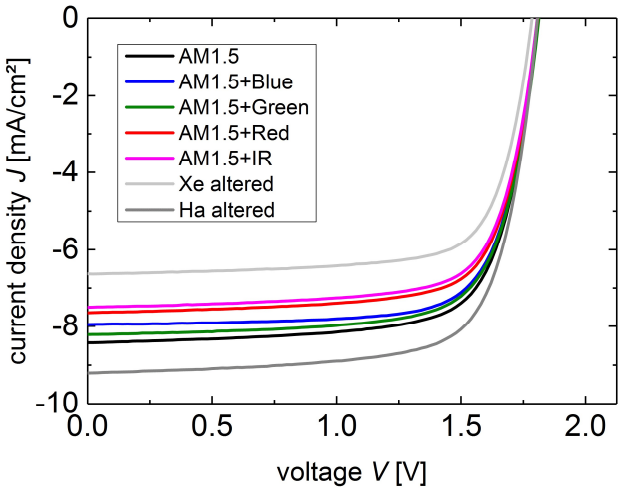

Figure A13: Current density-voltage curves for a tandem junction cell measured under spectra with varied average photon energy. Temperature (25 °C), intensity (1000 W/m²) and angle (0°) were kept constant.

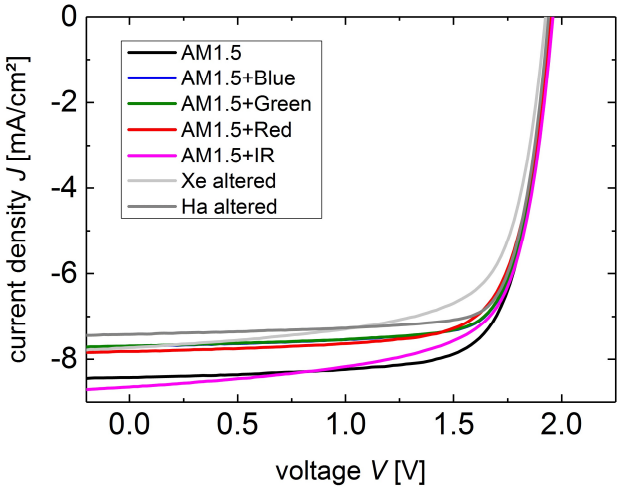

Figure A14: Current density-voltage curves for an a-Si:H/µc-Si:H/µc-Si:H triple junction cell measured under spectra with varied average photon energy. Temperature (25 °C), intensity (1000 W/m²) and angle (0°) were kept constant.

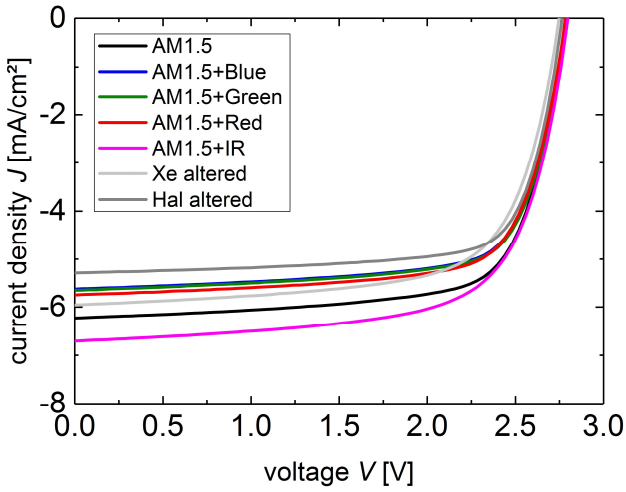

Figure A15: Current density-voltage curves for a quadruple junction cell measured under spectra with varied average photon energy. Temperature (25 °C), intensity (1000 W/m²) and angle (0°) were kept constant.

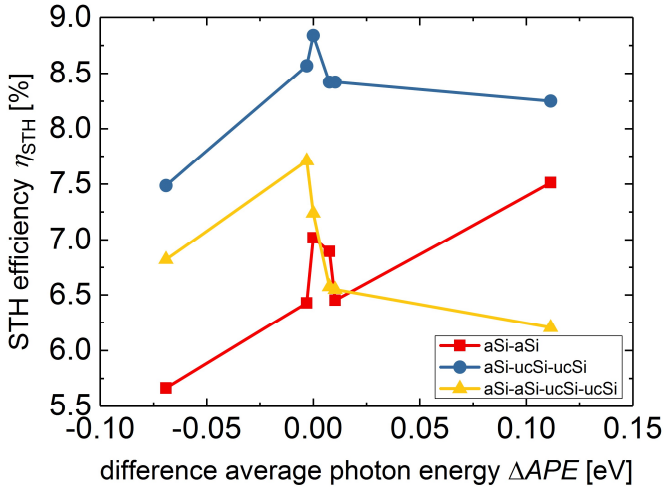

Figure A16: Solar-to-hydrogen efficiencies plotted versus difference in average photon energy for different types of multi-junction cells.

Abbreviations

AC	alternating current
AM	air mass
APE	average photon energy
BMBF	Bundesministerium für Bildung und Forschung
CA	chronoamperometric
CE	counter electrode
CMB	cyanuric acid – melamine – barbituric acid
CP	chronopotentiometric
c-SHJ	crystalline silicon heterojunction
CSM	chlorosulfonated synthetic rubber
CV	cyclic voltammetry
DC	direct current
DFG	Deutsche Forschungsgemeinschaft
DI	deionized
DSR	differential spectral response
EC	electrochemical cell
ECSA	electrochemically active surface area
EIS	electrical impedance spectroscopy
EQE	external quantum efficiency
FWHM	full width at half maximum
GC	glassy carbon
HER	hydrogen evolution reaction
ICS-TAK	Institute of Complex Systems -Technische und Administrative Infrastruktur Konstruktion
IEK-5	Institut für Energie und Klimaforschung 5
IHL	inner Helmholtz layer
IR	infra-red
ITO	indium tin oxide
JV	current-voltage
LDH	layered double hydroxide
LED	light-emitting diode
LP	laser processing
LSV	linear sweep voltammetry
MPP	maximum power point
OC	open circuit
OCP	open circuit potential
OER	oxygen evolution reaction
OHL	outer Helmholtz layer
Ox	oxidation
PEC	photoelectrochemical cell
PEEK	polyether ether ketone
PEM	proton exchange membrane
PMMA	poly(methyl methacrylate)
PV	photovoltaic
PV-EC	photovoltaic-biased electrochemical cell
PV+EC	photovoltaic cell + electrolyser
QE	quantum efficiency
RE	reference electrode
Red	reduction
RF	radio frequency

RHE	reversible hydrogen electrode
RT	room temperature
SC	short circuit
SEM	scanning electron microscope
SHE	standard hydrogen electrode
SMU	source measurement unit
STC	standard test conditions
STH	solar-to-hydrogen
TCO	transparent conductive oxide
TF	thin film
TMB	trimethylborane
UHV	ultra-high vacuum
UV	ultraviolet
VHF	very high frequency
WE	working electrode
XPS	X-ray photoelectron spectroscopy

List of publications

Journal publications in the framework of the present thesis:

K. Welter, N. Hamzelui, V. Smirnov, J.-P. Becker, W. Jaegermann, F. Finger, *J. Mater. Chem. A*, **2018**, *6*, 15968. *Catalysts from earth abundant materials in a scalable, stand-alone photovoltaic-electrochemical module for solar water splitting*

K. Welter, V. Smirnov, J.-P. Becker, P. Borowski, S. Hoch, A. Maljusch, W. Jaegermann, F. Finger, *ChemElectroChem*, **2017**, *4*, 2099-2108. *The influence of operation temperature and variations of the illumination on the performance of integrated photoelectrochemical water-splitting devices*

V. Smirnov, K. Welter, F. Finger, F. Urbain, J.R. Morante, B. Kaiser, W. Jaegermann, 'Photoelectrochemical Solar Cells' (ed. by Nurdan Demirci Sankir and Mehmet Sankir, **2019**, Scrivener Publishing LLC, 351-384. *Implementation of multijunction solar cells in integrated devices for the generation of solar fuels*

S. Reynolds, K. Welter, V. Smirnov, *Phys. Status Solidi A*, **2019**, *216*, 1800847. *Silicon Thin Films: Functional Materials for Energy, Healthcare, and IT Applications*

S. M. Thalluri, B. Wei, K. Welter, R. Thomas, V. Smirnov, L. Qiao, Z. Wang, F. Finger, L. Liu, *ACS Energy Lett.*, **2019**, *4*, 1755 – 1762. *Inverted Pyramid Textured p-Silicon Covered with Co_2P as an Efficient and Stable Solar Hydrogen Evolution Photocathode*

F. Urbain, P. Tang, V. Smirnov, K. Welter, T. Andreu, F. Finger, J. Arbiol, J. R. Morante, *ChemSusChem*, **2019**, *12*, 1428 – 1436. *Multilayered Hematite Nanowires with Thin-Film Silicon Photovoltaics in an All-Earth-Abundant Hybrid Tandem Device for Solar Water Splitting*

F. Urbain, S. Murcia-López, N. Nembhard, J. Vázquez-Galván, C. Flox, V. Smirnov, K. Welter, T. Andreu, F. Finger, J. R. Morante, *J. Phys. D. Appl. Phys.*, **2019**, *52*, 044001. *Solar vanadium redox-flow battery powered by thin-film silicon photovoltaics for efficient photoelectrochemical energy storage*

A. Richter, V. Smirnov, A. Lambertz, K. Nomoto, K. Welter, K. Ding, *Sol. Energy Mater. Sol. Cells*, **2018**, *174*, 196-201. *Versatility of doped nanocrystalline silicon oxide for applications in silicon thin-film and heterojunction solar cells*

J.-P. Becker, B. Turan, V. Smirnov, K. Welter, F. Urbain, J. Wolff, S. Haas, F. Finger, *J. Mater. Chem. A*, **2017**, *5*, 4818. *A modular device for large area integrated photoelectrochemical water-splitting as a versatile tool to evaluate photoabsorbers and catalysts*

V. Smirnov, K. Welter, J. Becker, F. Urbain, W. Jaegermann, F. Finger, *Energy Procedia*, **2016**, *102*, 36-42. *The effect of the illumination intensity on the performance of Si multijunction based integrated photoelectrochemical water splitting devices*

Other journal publications:

C. Stieghorst, G. Hampel, B. Karches, P. Krenckel, P. Kudějová, C. Plonka, Z. Révay, S. Riepe, K. Welter, N. Wiehl, *J. Radioanal. Nucl. Chem.*, **2018**, *317*, 307-313. *Determination of boron and hydrogen in materials for multicrystalline solar cell production with prompt gamma activation analysis*

B. Karches, K. Welter, C. Stieghorst, N. Wiehl, T. Reich, S. Riepe, P. Krenckel, H. Gerstenberg, C. Plonka, *J. Radioanal. Nucl. Chem.*, **2017**, *311*, 541-548. *Instrumental determination of phosphorus in silicon for photovoltaics by β spectroscopy: a new approach*

Conference presentations

Manfred-Eigen-Gespräche für Nachwuchswissenschaftler (Mülheim, Germany, 2016)
Synthesis and application of NiX@Nickel- foam co-catalysts for photoelectrochemical water splitting (Poster)

Summer School „Solar H_2“ (Berlin, Germany, 2016)
Photoelectrochemical water splitting using adapted silicon based semiconductor multijunction cell structures (Poster)

European Materials Research Society Spring Meeting (Straßburg, France, 2017)
Approaches for the upscaling of solar water splitting photocathodes (Poster)
Incident angular and intensity illumination dependence of integrated photoelectrochemical water splitting devices (Oral presentation)
Long-term hydrogen production through integrated silicon based photoelectrochemial water splitting devices (Oral Presentation)

Materials Research Society Fall Meeting (Boston, United States of America, 2017)
Development of Catalysts for an Integrated Photovoltaic-biased Electrosynthetic Device for Solar Water Splitting on Large Area (Oral presentation)

NanoGe Fall Meeting (Torremolinos, Spain, 2018)
Catalysts from earth abundant materials in a stand-alone photovoltaic-electrochemical module for solar water splitting (Poster)

International Bunsen-Discussion-Meeting (Taormina, Italy, 2019)
Earth abundant catalysts in a stand-alone, scalable photovoltaic-electrochemical solar water splitting module (Poster, Poster Prize by *Journal of Materials Chemistry A, B & C and Materials Horizons*)

Acknowledgements

It is my great pleasure to thank the people who have helped me making this thesis possible.

First of all, I would like to express my deepest gratitude to Prof. Dr. Jaegermann for supervising my thesis and giving me the opportunity to pursue my research with all possibilities and freedom. He supported me with valuable discussions and always made time for me, when I needed it.

I also kindly thank Prof. Dr. Rau for his willingness to review my thesis and for showing such great interest in my work, supporting me with intense discussion and ideas.

I am deeply thankful to Dr. Friedhelm Finger for being a great group leader. He always found the right way of guidance, criticism, confidence in me and encouragement. He always asked the right questions to make me think about my work and supported me in my goals.

I would like to express my deepest gratitude to my two supervisors Dr. Vladimir Smirnov and Dr. Jan-Philipp Becker for being the best possible supervisors. Dr. Vladimir Smirnov constantly supported, encouraged me and was awalys available for discussion and questions. He provided me knowledge about thin film solar cells, about paper writing, spend hours on proof reading and helped me to improve myself a lot. The time he spent on my education is uncountable. Dr. Jan-Philipp Becker was always available for discussion and feedback even after he had already moved. He introduced me into the world of water splitting, provided me with valuable knowledge and always made time for me when I needed it.

I would also like to thank Niloofar Hamzelui for doing such excellent work as master student, building the basis on which I could further elaborate the catalyst systems.

I thank me colleagues from the Technical University Darmstadt for their support and many discussions: Thorsten Cottre, Florian Neuberger, Dr. Florent Yang, Leslie Frotscher and Dr. Bernd Kaiser.

I specially thank all those who helped me with device construction, sample preparation and characterization: Hilde Siekmann, Sandra Moll, Joachim Kirchhoff Andreas Lambertz, Gunnar Schöpe, Andreas Bauer, Markus Hülsbeck, Sabine Kasper, Christoph Zahren, Wilfried Reetz, Daniel Weigand, Vito Huhn and Thomas Birrenbach, the people working at the Institute of Complex Systems - Technische und Administrative Infrastruktur Konstruktion und Werkstatt. And last but not least Andrea Mülheims, Petra Lorbach and Astrid Nogga for assistance with administrative tasks.

Special thanks to Sabine Kasper, Manuela Meyer, Sandra Moll, Daniel Weigand, Markus Hülsbeck and Joachim Kirchhoff for always being there for me and listening to me talking about my problems, my personal life and laughing about my bad jokes. You made life at work so much fun.

I would also like to acknowledge the financial support of the Deutsche Forschungsgemeinschaft (DFG), Priority Program 1613 (Fuels Produced Regeneratively Through Light-Driven Water Splitting: Clarification of the Elemental Processes Involved and Prospects for Implementation in Technological Concepts) and the joint project “Sustainable Hydrogen” (FKZ 03X3581 of the German Bundesministerium für Bildung und Forschung (BMBF)), for which I am grateful.

I would like to thank my parents and all my friends from Köln and Mainz for making me laugh and successfully distracting me from work in my free time. Special thanks to Marie Kerkloh for reading my thesis and for finding so many small mistakes that I would not have noticed otherwise.

Finally, I am deeply grateful to Marcel Schotten for always being there for me, helping me through my work and thesis, taking care of me in the best possible way, giving me confidence when I was lacking it, making me laugh although I was in a bad mood and providing me with energy even though you hardly had any. This work and my life would have not been possible without you.

Band / Volume 495
Measurements of Atmospheric OH and HO_2 Radicals by Laser-Induced Fluorescence on the HALO Aircraft during the OMO-ASIA 2015 Campaign
C. Künstler (2020), 156 pp
ISBN: 978-3-95806-477-5

Band / Volume 496
Tomographic observations of gravity waves with the infrared limb imager GLORIA
I. Krisch (2020), vii, 187 pp
ISBN: 978-3-95806-481-2

Band / Volume 497
Aquisition of temporally and spatially highly resolved data sets of relevant trace substances for model development and model evaluation purposes using a mobile measuring laboratory
D. Klemp, R. Wegener, R. Dubus, U. Javed (2020), 110 pp
ISBN: 978-3-95806-465-2

Band / Volume 498
Charakterisierung des Werkstoffverhaltens während des Kosinterns einer neuartigen, inert gestützten Festoxidbrennstoffzelle
F. Grimm (2020), ix, 168 pp
ISBN: 978-3-95806-482-9

Band / Volume 499
WEGE FÜR DIE ENERGIEWENDE
Kosteneffiziente und klimagerechte Transformationsstrategien für das deutsche Energiesystem bis zum Jahr 2050
M. Robinius et al (2020), VIII, 141 pp
ISBN: 978-3-95806-483-6

Band / Volume 500
Mechanical Behavior of Solid Electrolyte Materials for Lithium-ion Batteries
G. Yan (2020), x, 139 pp
ISBN: 978-3-95806-484-3

Band / Volume 501
Retrieval of atmospheric quantities from remote sensing measurements of nightglow emissions in the MLT region
Q. Chen (2020), 208 pp
ISBN: 978-3-95806-485-0

Band / Volume 502
Auswirkungen der Energiewende auf das deutsche Gastransportsystem
B. Gillessen (2020), XVII, 186
ISBN: 978-3-95806-487-4

Band / Volume 503
Lagrangian Simulation of Stratospheric Water Vapour: Impact of Large-Scale Circulation and Small-Scale Transport Processes
L. Poshyvailo (2020), 126 pp
ISBN: 978-3-95806-488-1

Band / Volume 504
Water Management in Automotive Polymer-Electrolyte-Membrane Fuel Cell Stacks
S. Asanin (2020), XVIII, 172 pp
ISBN: 978-3-95806-491-1

Band / Volume 505
Towards a new real-time irrigation scheduling method: observation, modelling and their integration by data assimilation
D. Li (2020), viii, 94 pp
ISBN: 978-3-95806-492-8

Band / Volume 506
Modellgestützte Analyse kosteneffizienter CO_2-Reduktionsstrategien
P. M. Lopion (2020), XIV, 269 pp
ISBN: 978-3-95806-493-5

Band / Volume 507
Integration of Renewable Energy Sources into the Future European Power System Using a Verified Dispatch Model with High Spatiotemporal Resolution
C. Syranidou (2020), VIII, 242 pp
ISBN: 978-3-95806-494-2

Band / Volume 508
Solar driven water electrolysis based on silicon solar cells and earth-abundant catalysts
K. Welter (2020), iv, 165 pp
ISBN: 978-3-95806-495-9

Weitere ***Schriften des Verlags im Forschungszentrum Jülich*** unter
http://wwwzb1.fz-juelich.de/verlagextern1/index.asp

Energie & Umwelt / Energy & Environment
Band / Volume 508
ISBN 978-3-95806-495-9

Mitglied der Helmholtz-Gemeinschaft

JÜLICH
Forschungszentrum